Technische Universität München
Institut für Energietechnik

Lehrstuhl für Thermodynamik

On the Determination of Local Reverse Osmosis Membrane Properties from Optical Boundary Layer Measurements

Alexander Kroiß

Vollständiger Abdruck der von der Fakultät für Maschinenwesen der Technischen Universität München zur Erlangung des akademischen Grades eines

DOKTOR – INGENIEURS

genehmigten Dissertation.

Vorsitzender:
    Prof. Dr.-Ing. Harald Klein
Prüfer der Dissertation:
    Prof. Dr.-Ing. Thomas Sattelmayer
    Prof. Dr. rer. nat. Stephan Leyer

Die Dissertation wurde am 17.05.2019 bei der Technischen Universität München eingereicht und durch die Fakultät für Maschinenwesen am 08.10.2019 angenommen.

To my students.

Preface

This work was conducted during my time as research and teaching assistant at Institute of Thermodynamics, Technical University of Munich.

During my master studies in 2009, my long-standing supervisor, supporter, colleague and friend Dr.-Ing. Markus Spinnler introduced me to solar desalination. I would like to thank him from the bottom of my heart, both personally and professionally, for the time spent together since then, the experiences we shared and the cheerful memories.

It all started with my first term paper about Reverse Osmosis (RO) plants powered by hybrid photovoltaic/thermal systems. Two years later, Markus and I were filing the first project proposal, which gave me the opportunity to do research at the institute. Solarenergieförderverein Bayern e.V. was the first who financially supported the project to build up the infrastructure for the new research field about membrane desalination at the institute. In addition, Trunz Water Systems AG made it possible for us to gain first experimental experience with membrane desalination plants by lending a brackish water RO plant for free. The financing of further activities was guaranteed by a research grant (02WA1299) of a joint German-Israeli Water Technology Research Program funded by the German Federal Ministry of Education and Research (BMBF) and the Israeli Ministry of Science and Technology (MOST). I would like to thank all sponsors and associated industry partners for their great support.

I want to express my special thanks to my supervisor, Prof. Dr.-Ing. Thomas Sattelmayer, not only for his scientific supervision but also for his confidence in me and my work over many years. It was an honor for me to be part of the institute as coordinator of the research group Transport Phenomena as well as teaching assistant and lecturer over many years.

I thank Prof. Dr. rer. nat. Stephan Leyer for being the co-examiner of my thesis and Prof. Dr.-Ing. Harald Klein for taking over the examination presidency as well as for allowing us to use his laboratories to determine fluid properties. Let me express my heartfelt thanks to his employees Mrs. Danuta Styrnik und Dr.-Ing. Sebastian Rehfeldt for their always generous and kind support during the experiments. In this context, many thanks also go to Anton Paar GmbH for lending a multi-wavelength refractometer for free.

I would like to thank the co-workers of our electrical and mechanical workshop for their support during the development of the membrane test rig with the high pressure membrane test cell, especially for the fast realization of short-term requests.

For the many valuable discussions and the nice time together at the institute with many cheerful moments, I would like to thank my colleagues. For their time and good advice, special thanks go to the proofreaders of this thesis: Bernd Heithorst, Florian Kiefer, Alexander Präbst, Dr.-Ing. Markus Spinnler and Diana Wollmann. I thank Dr.-Ing. Christoph Hirsch for his scientific advice, especially in my final year at the institute. Many heartfelt thanks go to Prof. em. Dr.-Ing. Dr.-Ing. E.h. Franz Mayinger for his strategic and scientific advice not only about optical methods.

What made me proud and full of joy throughout all the years was the collegial cooperation with my students. With the so-called Grubenteam, I went through thick and thin. The team spirit and the personal commitment from everyone were exemplary in my eyes. In deep gratitude I dedicate this thesis to them. Everybody is personally named in the end of this thesis. As representatives for the entire team, my sincere thanks go to Maximilian Altnöder, Daniel Appel, Sebastian Eyerer, Bernd Heithorst, Michael Hofmann, Moritz Link, Stefan Körber, Julian Kuczaty, Alexander Präbst, Matthias Schreyer, Cornelius Thies, Stephan Wolf and Kilian Zörntlein.

Who I can always rely on are my family and friends. They gave me strength and support through all the years, for which I cannot thank them enough.

Aalen, 2019 Alexander Kroiß

Abstract

The performance data of Reverse Osmosis (RO) membranes can vary significantly. The main reasons are local variations of material properties and membrane testing conditions. To determine membrane performance parameters with high local resolution, a new methodology was developed and validated. The inverse method combines conventional lab-scale membrane tests with optical boundary layer measurements visualizing mass transfer through the membrane. The combination of the experimental methods with computational fluid dynamics and optical ray tracing makes the investigation of local mass transport phenomena possible.

The developed inverse method is applicable in the full RO operating range. It is applied to determine the performance of a Thin-Film Composite aromatic polyamide RO membrane. The investigations were carried out at elevated pressures (up to 60 bar), at brackish as well as sea water salinity conditions (NaCl salt mass fractions at the membrane up to 80 g/kg) and at elevated temperature (30 °C). Limitations of the developed inverse method caused by obstructive optical phenomena (e.g. diffraction, significant light deflection, spherical aberration) are overcome by the combination of multiple optical measurement techniques and optical ray tracing simulations.

The RO membrane performance results indicate that the salt permeability constant is sensitive to salinity. The results are confirmed by a Maxwell-Stefan modeling approach taking membrane charge effects into account.

Table of Content

Nomenclature

Latin Characters

A	Water permeability constant	[m s^{-1} bar^{-1}]
a_i	Coefficients in empirical correlation	[-]
a	Activity	[-]
a	Amplitude	[-]
B	Salt permeability constant	[m s^{-1}]
b	Constant parameter in osmotic pressure equation	[bar]
b_i	Coefficients in empirical correlation	[-]
c_P	Specific heat capacity	[J kg^{-1} K^{-1}]
c	Molar concentration	[mol m^{-3}]
c	Speed of light	[m s^{-1}]
D	Diffusivity	[m^2 s^{-1}]
$\mathfrak{D}$	Maxwell-Stefan diffusivity	[m^2 s^{-1}]
Đ	Manipulated Maxwell-Stefan diffusivity	[m^2 s^{-1}]
d_h	Hydraulic diameter	[m]
d_i	Diffusional driving force for species i	[m^{-1}]
d	Thickness	[m]
e_rel	Relative deviation, $e_{y_i,\mathrm{rel}} = \frac{y_i - y_{i,\mathrm{ref}}}{y_{i,\mathrm{ref}}}$	[-]
f_i	Terms in diffusivity correlation	[A.U.]
f	Focal length of a lens	[m]
f	Frequency	[s^{-1}]
GCI	Grid convergence index	[-]
GPL	Geometric path length	[m]
g	Gravitational acceleration	[m s^{-2}]
h	Planck's quantum of action	[J s]
I	Dimensionless intensity	[-]

I_n	Normalized intensity	[-]
ID	Identifier	[-]
i	Species or component i	[-]
j	Mass flux	[kg m^{-2} s^{-1}]
$\bar{j}_P$	Mean permeate flux of entire membrane	[kg m^{-2} s^{-1}]
j	Species or component j	[-]
K_S	Salt solubility / salt distribution coefficient	[-]
$K_{\mathrm{S},\infty}$	Salt solubility asymptote	[-]
K_W	Water solubility / water distribution coefficient	[-]
$K_{\mathrm{W},\gamma}$	Activity related part of water solubility	[-]
L	Length of investigated test section	[m]
l^M	Thickness of thin-film active layer of membrane	[m]
l	Length	[m]
$\bar{M}$	Molar mass	[kg mol^{-1}]
m	Mass	[kg]
m	Molality	[mol kg^{-1}]
NDP	Net driving pressure	[bar]
N	Number of nodes	[-]
N	Molecular refractivity	[m^{-3} mol^{-1}]
n	Refractive index	[-]
n	Length for distribution of nodes	[m]
n	Hydration number	[-]
OPL	Optical path length	[m]
P	Permeability	[m^{2} s^{-1}]
p	Pressure	[bar]
p_i	Coefficients in empirical correlation	[-]
q_i	Coefficients in empirical correlation	[-]
$\mathbf{r}$	Position vector in Cartesian coordinates	[m]
$\mathbf{r}$	Residual vector in multi-objective optimization	[-]
Δr	Light ray deflection	[m]
r	Radius	[m]
r_S	Source term	[kg m^{-3} s^{-1}]
R	Universal gas constant	[J mol^{-1} K^{-1}]
R	Correlation coefficient	[-]

R	Residual	[-]
Sp	Mesh spacing	[-]
SR	Salt rejection	[-]
s	Ray coordinate	[m]
T	Temperature	[K]
t	Time	[s]
t_c	Thickness of lens	[m]
u	Velocity	[m s^{-1}]
V_F	Feed Volume Flow Rate	[l h^{-1}]
$\bar{V}$	Molar volume	[m^3 mol^{-1}]
w	Mass fraction	[-]
w_i^M	Mass fraction of component i inside the membrane phase which consists of three components salt, water and the membrane itself	[-]
w_i^E	Mass fraction of component i in the external solution outside the membrane phase (index E is omitted when it is clear that the solution outside the membrane is meant)	[-]
$w_{i,\mathrm{F}}^\mathrm{E}$	Mass fraction of component i in the external solution on the feed side	[-]
$w_{i,\mathrm{F},0}^\mathrm{E}$	Mass fraction of component i in the external solution on the feed side at the test cell inlet	[-]
$w_{i,\mathrm{F,M}}^\mathrm{E}$	Mass fraction of component i in the external solution on the feed side on the membrane surface	[-]
$\bar{w}_{i,\mathrm{F,M}}^\mathrm{E}$	Mean mass fraction of component i in the external solution on the feed side on the surface of the entire membrane	[-]
x	Molar fraction	[-]
x, y	Placeholder variable	[A.U.]
x, y, z	Cartesian coordinates	[m]

Greek Characters

α	Coefficient for water permeability constant	[-]
α	Light ray angle	[-]
β	Coefficient for salt permeability constant	[-]

β	Trapezoid angle	[-]
β	Mass transport coefficient	[$\mathrm{m\ s^{-1}}$]
χ	Electrical charge density	[$\mathrm{mol\ l^{-1}}$]
Δ_1, Δ_2	Electrophoretic correction terms	[$\mathrm{m^2\ s^{-1}}$]
δ_{ij}	Kronecker delta	[-]
δ_C	Concentration boundary layer height	[m]
δ	Light ray deflection at Schlieren filter position	[m]
η	Non-dimensional length scale	[-]
ϵ	Factor in a correlation	[$\mathrm{m^{-1}}$]
Γ	Thermodynamic correction factor	[-]
γ	Activity coefficient	[-]
κ	Volume (or bulk) viscosity	[Pa s]
λ	Thermal conductivity	[$\mathrm{W\ m^{-1}\ K^{-1}}$]
λ	Wavelength	[m]
μ	Chemical potential	[$\mathrm{J\ mol^{-1}}$]
μ	Dynamic viscosity	[Pa s]
ν	Stoichiometric coefficient	[]
Ω	Non-dimensional salt mass fraction	[-]
ω	Inclination angle relative to horizontal plane	[-]
π	Osmotic pressure	[bar]
ϕ	Phase of electromagnetic wave (light)	[-]
ϕ	Practical osmotic coefficient	[-]
ρ_i	Mass concentration of component i	[$\mathrm{kg\ m^{-3}}$]
ρ	(Solution) density	[$\mathrm{kg\ m^{-3}}$]
τ	Transmittance	[-]
θ	Half aperture angle of first lens in light path behind test cell	[-]

Superscripts

-	Mean
0	Infinite dilution
CFD	Computational Fluid Dynamics
cc	With membrane charge and coupled mass transport
cd	With membrane charge and decoupled mass transport

E	Outside the membrane phase in the external solution (no matter of inside or outside the boundary layer)
EXP	Experimental data
it	Salt permeability constant is determined iteratively
LMPM	With assumptions of the Local Membrane Parameter Method
M	Inside the membrane phase which consists of the three components salt, water and the membrane itself
MS	Maxwell-Stefan
nc	Without membrane charge and coupled mass transport
noD	No diffusivity term included
PA	Polyamide
ref	Reference state
SDM	CFD results based on Solution-Diffusion Model
T	Thermal
ws	Salt permeability constant modeled as a function of w_S

Subscripts

∞	Ambient
$\pm$	Average property of an electrolyte
0	Reference state (inlet / initial / vaccum / ...)
adj	Adjusted
c	Compacted
Δ_1, Δ_2	Electrophoretic correction
Δ	Term in density correlation
D	Diffusive
δ_C	Bulk phase
eff	Effective
F	On the feed side
Γ	Thermodynamic correction
i, j	Counter
in	In
ini	Initial
λ	Thermal diffusion (Fourier)

λ	Wavelength specific
M	On the surface of the membrane phase (thin-film active layer)
M	Membrane component
lim	Limit
lb	Lower bound
max	Maximum
min	Minimum
out	Out
P	On the permeate side
p	Pressure
Rob.-Sto.	Robinson and Stokes [141]
R	Result
ref	Reference
rel	relative
rgh	Pseudo hydrostatic
SPart	Salt related part in formula
SFL	Second field lense
S	Salt
th	Threshold
TC	Test cell channel (inside)
T	Temperature
ub	Upper bound
WPart	Water related part in formula
W	Water

Non-Dimensional Numbers

Pe	Peclet number	$\frac{j_{\mathrm{P}} d_{\mathrm{h}}}{\rho D}$
Sh	Sherwood number	$\frac{\beta d_{\mathrm{h}}}{D}$

Abbreviations

AFM	Atomic Force Microscopy
BE	Beam Expander
BS	Beam Splitter
BW	Brackish Water
CA	Cellulose Acetat
CAD	Computer Aided Design
CAM	Camera
CFD	Computational Fluid Dynamics
CH	Channel Height
CL	Condenser Lens
DHI	Digital Holographic Interferometry
DMP	Double Membrane Piston
EXP	Experimental
F	Fanning
FFT	Fast Fourier Transformation
GCI	Grid Convergence Index
HI	Holographic Interferometry
I	Interferometry
IL	Imaging Lens
IL	Information Loss
LF	Low Fouling
LMPM	Local Membrane Parameter Method
LS	Light Source
L	Local
M	Mirror
M	Mean
MF	Microfiltration
MPD	m-Phenylenediamine
NF	Nanofiltration
NMR	Nulcear Magnetic Resonance
OB	Object Beam
PA	Polyamide

RB	Reference Beam
RBS	Rutherford Backscattering Spectrometry
RO	Reverse Osmosis
SC	Schlieren
SH	Shadowgraphy
SDM	Solution-Diffusion Model
SF	Schlieren Filter
SFL	Second Field Lens
SW	Sea Water
TC	Test Cell
TEM	Transmission Electron Microscopy
TFC	Thin-Film Composite
TMC	Trimesoyl Chloride
UF	Ultrafiltration
V	Valve

List of Figures

List of Tables

1 Introduction

The Latin word *membrana* intends to describe *membranes* in a biological sense. Human body cell walls or pig bladders are good examples. The latter ones were scientifically investigated by the pioneer of membrane science, Abbé Nollet [40, p. 6]. He discovered the osmosis phenomenon and attributed membranes a semi-permeable character [40, p. 6]. The term *semi-permeable* originates from Latin as well: While the membrane is a barrier for one half (*semi*) of species, it is permeable (*permeare*) for the other half. This means that membranes are able to separate pure substances from a mixture. As this property makes membranes interesting for various research and technical applications, synthetic membranes have been engineered taking biological solutions as an example. In the application field of desalination, fresh water is separated from brackish or sea water. Today, the most energy efficient desalination technology is Reverse Osmosis (RO) membrane desalination [58, p. 201]. For RO plant design, detailed knowledge about the membrane performance is necessary. The goal of the present study is the development of a new inverse methodology to characterize RO membranes on a local scale by means of optical boundary layer measurements. This goal is based on the literature reviewed in the following section.

1.1 Motivation

Membrane Transport

Since the beginning of RO desalination in 1959 [40, p. 7] different membrane transport models, e.g. [82, 102, 108, 111, 158, 162], have been developed providing valuable insight in membrane theory as well as tools to predict membrane performance. The modeling approach based on solution and diffusion of water and salt in dense membranes is widely accepted in RO desalination [9, 107, 109, 135] and described by the so-called Solution-Diffusion Model (SDM) [102]. Membrane models are usually calibrated by experimental data. For cellulose acetate (CA) membranes, the first membrane generation, much experimental data exist to describe the solubility and diffusivity of water and salt, compare e.g. LONSDALE ET AL. [102]. For complex Thin-Film Composite (TFC) membranes, the second membrane generation, a similar database is not available according to PAUL [127, p. 373]. Therefore, a TFC membrane is studied in the present thesis. As the SDM was developed during the time of the first membrane generation, it is worth to review the SDM assumptions later in this study (section 2.1).

Membrane Manufacturing

The thickness of the so-called thin-film active layer is responsible for the separation characteristic of the TFC membrane. It is in the order of 30 nm [109, p. 43]. The paths through which species diffuse in this layer have a nominal pore diameter in the sub-nanometer range [9, p. 17]. Although manufacturing processes faced great advance during the past decades, it is still not trivial to produce a defect-free membrane with constant quality as sheets of several square meters, which are packed in standard, spiral-wound RO modules. In 2010, CORONELL ET AL. [24] studied three fully aromatic polyamide TFC RO membranes and measured the active layer thickness of three membrane samples. A mean standard deviation of ±48.3% related to the average thickness [24] shows quite impressively the need for membrane manufacturing process optimization.

Local variations of membrane properties affect also membrane module performance. Membrane manufacturers indicate in their product specifications that the individual membrane module permeate production flow rate can vary between +20%/-20% [32], +20%/-15% [86] and +33%/-15% [120], to give a quantitative impression for brackish water membrane modules. What is seen as prerequisite for manufacturing process optimization is a suitable analysis tool for local membrane characterization.

Membrane Testing

Different membrane module manufacturers specify their product data at different testing conditions, e.g. different salinity levels of 1500 ppm [120] or 2000 ppm [32, 86]. There is no standard for membrane testing on which either industry or research agree on. A standard testing protocol would be advantageous as membrane performance is sensitive to operating conditions. The most important parameters are pressures, temperatures and salt mass fractions [109, 135] on both sides of the membrane. Also the pH-value [25, 178], pretreatment of the testing fluid and of the membrane itself is important. Temporal influences exist as well and mostly go back to membrane compaction [73, 103, 131, 135] and/or membrane fouling [50, 81, 144].

In 2006, SCHIPOLOWSKI ET AL. [149] investigated the variance of experimental lab-scale results based on samples from a membrane module sheet. They quantified the maximum (and average) deviation of a single test cell sample from the average properties of the entire RO membrane sheet. The result was 44% (12%) for the water permeability and to 120% (23%) for the salt permeability [149, p. 76]. In 2013, CATH ET AL. [20] presented the results of a round-robin test for osmotically driven TFC polyamide membranes by seven independent laboratories. The results for the permeabilities appear to have also a much higher variation for salt, +100%/-66%, than for water, +4%/-4%. This shows the difficulty of achieving consistent, reliable data, especially for salt separation membrane characteristics.

In 2009, VAN WAGNER ET AL. [178] drew the attention to the experimental conditions at which membrane data are gained. They point out one general problem inherent to the common membrane tests: "Although polarization effects can be minimized in cross-flow mode by operating at low pressure and higher cross-flow velocity, they can never be completely eliminated and should be accounted for [...]", [178, p. 98]. There are different strategies to take the concentration boundary layer, i.e. concentration polarization, into account.

Commonly, a mass transfer coefficient is determined and fed into a boundary layer model. A Sh-correlation is needed to derive the transfer coefficient. Depending on the flow regime (laminar / turbulent, with / without suction, undeveloped / developed) and the channel geometry (rectangular, slit, tubular, radial, with / without spacer, et cetera) a large number of correlations exist. GERALDES and ALFONSO [57] provide a good overview for RO applications.

Common membrane test cells used in RO lab-scale experiments have rather complex channel geometries. The channels are filled with spacers taken from RO modules. In this way it is guaranteed that the membrane is tested under the same flow conditions as in a membrane module. The spacers are eddy-promoters and reduce the concentration boundary layer within the channel. For these complex geometries, the typical approach to determine the Sh-correlation is to vary one or more operating parameters (feed velocity, pressure, concentration or permeate flux) and to fit a boundary layer model to the gained data. The latter often needs to be combined with a membrane model. SUTZKOVER ET AL. [164] provide a compact overview on the different experimental protocols.

The main disadvantage of the membrane performance measurement in the described or a similar way is that results for the mass transfer coefficient can be misleading. The reason are inherent modeling uncertainties either of the boundary layer model or the membrane model. MURTHY and GUPTA [118], for example, combined two different membrane models with the same boundary layer model and came to significantly different results for the mass transfer coefficient [118, p. 47].

A different approach is to work with simple channel geometries: In this case, first-principle approaches can be applied to take account for the concentration boundary layer, compare e.g. [13, 14, 62]. Rotating disk experiments with laminar flow are to be mentioned in this context, referring to SHERWOOD ET AL. [159, p. 240]. For their boundary conditions, an exact solution to the Navier-Stokes equations exists [159, p. 240]. The laminar flow is "uniformly accessible" and the local mass transfer coefficient is the same everywhere on the disk [159, p. 240]. The disadvantage here is still that local membrane characteristics cannot be determined. However, the principle idea to determine the boundary layer as exact as possible is picked up in the present study.

Boundary Layer Measurements

Direct quantitative concentration boundary layer measurements cannot only provide valuable data to identify the best suited boundary layer model for a given geometry. They can provide data even on a local scale. The highest quality of quantitative data is achieved in a non-invasive way, in-situ and in real-time. The measurement data should have high local resolution. The data analysis should not depend on a model of the phenomenon studied. This categorization goes back to CHEN ET AL. [21], who provide a good review on non-invasive observation methods in membrane science. The experimental methods to quantify boundary layer phenomena which are truly non-invasive but are still only moderately complex are based on optics [21]. This is one of the reasons why non-invasive optical boundary layer characterization plays a major role in this study. There are further benefits, which are outlined later in section 2.2.4. Before, a brief overview of the application of optical methods in literature with a focus on membrane science is given.

Broadly speaking, the investigated channel geometries became more complex with continuous improvement of the applied measurement techniques. Great efforts have been made to push boundary layer investigations from simple to more realistic but complex flow conditions. In the 1970/80s, boundary layer investigations in membrane desalination began with classic Shadowgraphy and Interferometry [78, 105, 176, 177], and were continued, from 1998 on, with classic Holographic Interferometry (HI) [23, 41, 43, 46] and, starting in 2010, with Digital Holographic Interferometry (DHI) [44, 146]. After dead-end unstirred batch-cell experiments with ultrafiltration (UF) [41, 43, 46, 61, 176, 177] and RO membranes [42, 45, 105], the research focus went on to cross-flow experiments with nanofiltration (NF) and RO membranes in test cells with rectangular channels [44, 142, 145, 146]. In 2016, the first membrane (NF) test cell with a channel filled with spacer-like obstacles [23] was investigated with HI, similar to the work of TAUSCHER [167] about heat transfer in heat exchangers with turbulence-promotors in 2000. With an optical method based on thermochromic liquid crystals, TABURINI ET AL. [166] started research on temperature boundary layer measurements in spacer-filled channels in the field of membrane distillation in 2013.

The classical RO module operating window ranges to maximum 40°C fluid temperature limited by the material properties of the glue used in membrane modules. Literature data for concentration boundary layer experiments in combination with RO membranes are available only up to a temperature of 26°C [44]. Furthermore, experimental data exist up to pressures of 7 to 8 bar for cross-flow conditions [41, 43, 44, 46, 142, 145, 146] and up to 30 bar for batch experiments [105]. Due to the low hydrostatic pressure level, the investigated osmotic pressure levels and, consequently, the salt concentration levels are also limited. Experiments can be found for brackish water conditions with bulk concentrations of maximum 7 g/kg [44]. There are not experimental data for sea water conditions with salt concentrations around 70 to 80 g/kg and osmotic pressures around 60 bar.

Low pressure and concentration levels have experimental advantages: The design of a membrane test cell with optical access can be kept rather simple (due to the low pressures). The measurement quantity of the mentioned optical method is the refractive index, which depends on both, concentration and temperature (besides wavelength and pressure). Therefore, the refractive index gradients caused by the boundary layer are weaker for a generally lower feed concentration level at otherwise identical operating conditions. For refractive index measurements this is an advantage as from strong refractive index gradients obstructive optical phenomena arise, which have to be compensated by higher experimental effort (advanced optical setups and subsequent data analysis). In 2013, RODRIGUES ET AL. [142] provided data which allow to quantify this advantage. They determined the relative deviation of the salt concentration on the membrane measured with Holographic Interferometry from Computational Fluid Dynamics (CFD) results. With classical data analyses, deviations of up to 60% were obtained for strong refractive index gradients, compared to 20% at comparably weak gradients [142, fig. 8]. Improving the optical data evaluation, the maximum relative deviation could be reduced to <35% for the strong refractive index gradients [142, fig. 8]. Note that the terms *strong* and *weak* in context with the refractive index gradient are specified later in this thesis (section 2.2.3 on page 55).

In studies with focus on boundary layer theory, experimental data are not necessarily needed for the entire RO operating window. Similarity solutions allow extrapolations to different temperatures, concentrations and pressures when the flow regime does not change. However, the membrane characteristic itself depends on these operating conditions also affecting the boundary layer development. In the present study, this sensitivity of the concentration boundary layer to the membrane performance is to be exploited.

Based on the presented brief literature review, the goal and the associated scope of the thesis are described in the following.

1.2 Goal and Scope of the Thesis

The principal goal of the thesis is to develop an inverse methodology for membrane characterization which allows the determination of membrane parameters with a significantly higher local resolution compared to conventional lab-scale membrane tests, see figure 1.1.

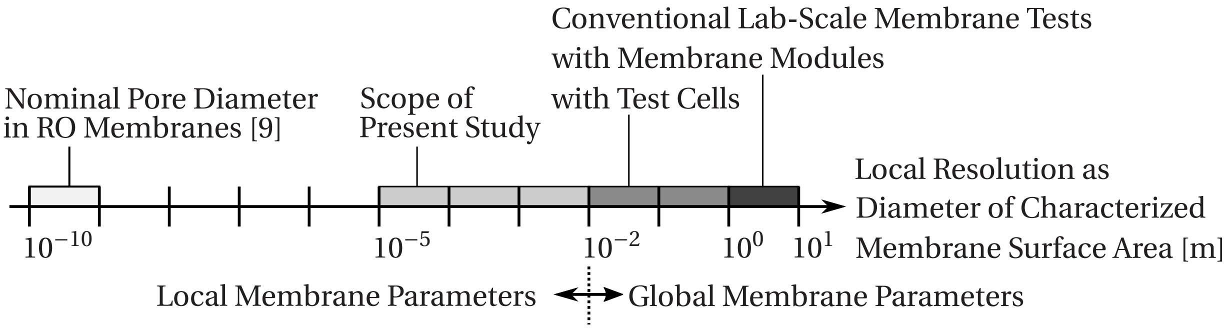

Figure 1.1: Local resolution of membrane characterisation methods.

In figure 1.1, the local resolution is estimated by the diameter of membrane surface area used to determine membrane performance data. Conventional lab-scale tests result in global membrane parameters based on surface-averaged performance data of entire membrane sheets. The length scale of such membrane sheets ranges between centimeters in test cells or meters in membrane modules. The goal of this thesis is to determine local membrane parameters of small parts of the tested membrane sheet. The length scale of the smallest parts will range between 10^{-5} m and 10^{-4} m. Local resolutions in the order of magnitude of the nominal pore diameter of RO membranes [9] are not scope of the present study.

Besides the goal of high local resolution, membrane characterization should be possible in-situ under real operating conditions. The method should be applicable in the full RO operating window for brackish and sea water conditions, including elevated pressures and temperatures. Misleading results due to uncertainties introduced by the buildup of concentration boundary layers during material separation are to be avoided.

In figure 1.2, an illustrative overview of the goal and the abstracted outline of the thesis is given. In the following, the outline is described in detail, starting with the selection of methods to achieve the pursued goal.

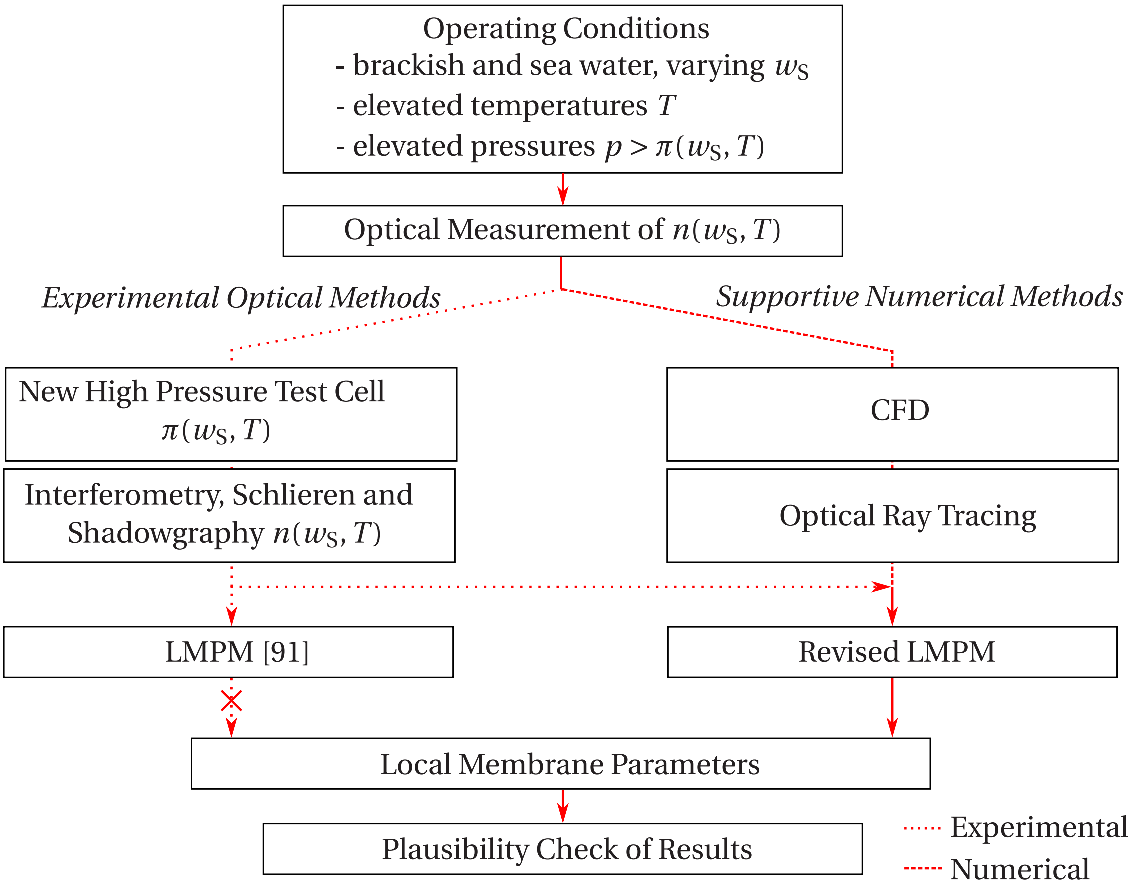

Figure 1.2: Outline of the thesis.

In 2015, a methodology for the determination of local membrane parameters (LMPM) from concentration boundary layers was published by the author [91]. By means of a salt mass balance it was shown how local permeate flux and local permeate salt mass fraction can be calculated directly from a concentration boundary layer profile. With the local feed salt mass fraction on the membrane, Solution-Diffusion model parameters can be derived. In the present study, the LMPM is tested in a proof of concept study to determine its accuracy (section 3.2). This method requires the characterization of the concentration boundary layer profile by measuring its zeroth, first and second order derivative. As it was introduced in the previous section, optical methods based on refractive index measurements are well suited for this purpose as the refractive index is sensitive to the salt concentration in the fluid.

As indicated in figure 1.2, the pursued determination of the refractive index n is based on two main methodological elements: experimental optical methods and supportive numerical methods. The experimental branch is described first.

As membrane characterization should be possible not only for brackish but also for sea water conditions (varying salt mass fraction w_S), for which high osmotic (π) and thus high hydrostatic operating pressures (p) are typical, state-of-the-art membrane test cells with optical access cannot be used. Therefore, the development of a new high pressure test cell is necessary (section 3.1.1). In order to be able to easily access the concentration boundary layer, the channel geometry should be kept as simple as possible, rectangular and without spacers.

For the determination of membrane performance at elevated operating temperatures T above typical ambient temperatures around 20°C in laboratories, it has to be guaranteed that the concentration boundary layer measurement is not corrupted by potential temperature boundary layers inside the optical test cell, as the refractive index is also sensitive to temperature. Temperature boundary layers are either taken into account as suggested in a previous publication [90] or they are avoided by controlling the ambient temperature in the laboratory to equal the temperature of the experimental apparatus $T = T_\infty$. In the present study, experiments are conducted at $T = 30°\mathrm{C}$.

As will be explained in more detail in section 2.2.4, the following three optical methods are tailored for the measurement of the derivatives of the concentration and thus the refractive index profile in the boundary layer: Interferometry (zeroth), Schlieren (first) and Shadowgraphy (second order derivative). These optical methods will be combined in one experimental setup (section 5.1) to allow two types of simultaneous measurements of the boundary layer inside the high pressure test cell. The combination of LMPM and these optical methods has a high potential to lead to an improvement of the local measurement resolution providing line-of-sight averaged membrane performance data instead of global, surface-averaged data, as it is the case for conventional membrane test cells.

However, anticipating the outcome of the proof of concept study of the LMPM (section 3.2), it will turn out that the combination of the LMPM and the proposed experimental methods is not accurate enough to derive local membrane performance. Therefore, the experimental methods will be expanded by supportive numerical methods in order to develop a revised version of the LMPM (section 3.3), see second branch in figure 1.2. This includes a 3D Computational Fluid Dynamics (CFD) model of the high pressure test cell (section 3.1). Numerically, local variations of the membrane performance can be modeled and their influence on the concentration boundary layer can be studied. The boundary layer measurements provide data for validation of the simulated boundary layer results. In order to make a validation of the CFD boundary layer data possible by means of the optical experiments, the CFD model is integrated in an optical ray tracing simulation (section 4.3). In this way, light propagation in the optical setup can be modeled. The result of the optical simulations will be numerically generated images with normalized light intensities. This will allow to compare experimentally and numerically determined intensity profiles directly instead of concentration profiles. Error propagation during the calculation of concentration boundary layer profiles from measurement data biased by obstructive optical phenomena like diffraction, significant light deflection and spherical aberration are avoided. This will be especially advantageous for the investigation boundary layers with strong concentration and, consequently, strong refractive index gradients when classical evaluation algorithms run in their limits.

The revised LMPM will be applied to evaluate the performance of a TFC brackish water RO membrane (chapter 6). For both brackish and sea water conditions, the same membrane sheet will be used. Both the water and the salt permeability constant are to be determined. However, the focus will be on the local investigation of the salt but not the water permeability constant, motivated by the comparably high scattering of literature data for permeability of salt. Applying the standard model for RO membrane performance analyses, the Solution-Diffusion Model (section 2.1.3), it will turn out that the salt permeability constant is not constant but depends on the operating conditions. In order to confirm the physical relevance of the membrane performance results and the validity of the new inverse methodology, the plausibility of the data is successfully checked by a different membrane modeling approach based on Maxwell-Stefan theory (section 2.1.5). As shown in figure 1.2, this plausibility check completes the scope of the present study.

1.3 Thesis Overview

The thesis is structured as follows: Subsequent to the introduction, the fundamentals for membrane transport are laid in chapter 2. A detailed look into boundary layer theory will reveal the experimental methods to be applied when investigating membrane transport phenomena. These are the measurements of the refractive index n by means of Interferometry, Schlieren and Shadowgraphy. In this context, the fundamentals on optical methods are presented. Important recurring terms like *weak* and *strong* refractive index gradients, *classical* optical methods and the *fanning* effect are defined in section 2.2.3. Furthermore, a brief overview of the previously published theoretical work about the LMPM [91] is included in chapter 2.

In chapter 3, the LMPM [91] is tested in a proof of concept study with CFD. After introducing the test cell design, the derived CFD model is described including the implemented membrane boundary condition based on the Solution-Diffusion Model (SDM). Chapter 3 concludes with a comprehensive revision of the LMPM. This step from the LMPM to the revised LMPM marks the switch from the left to the right branch in figure 1.2.

The revised LMPM combines the experimental methods with the CFD model and an optical ray tracing tool, which is presented in chapter 4. There the optical phenomena relevant for modeling are also explained.

Subsequently, the experimental methods are outlined in chapter 5. The implementation of the optical setup is described before an overview of the membrane test rig, the sensors and measurement accuracies is given. Information about the investigated membrane and the membrane testing procedure are provided in the end of chapter 5.

The results of the revised LMPM are presented in chapter 6. While the water permeability results are plausible, different hypotheses are tested to physically explain the results for the salt permeability constant. The successful plausibility check of these results proves the applicability of the new inverse methodology for membrane characterization.

The present study concludes with a summary and gives an outlook on future research topics.

2 Theory

In this chapter, the basics of RO membrane transport modeling are introduced. The standard model for RO membranes is explained. It is used for the analysis of the Thin-Film Composite (TFC) membrane investigated in this study. The presented model assumptions and considered physical phenomena are also relevant for the discussion of the results presented in chapter 6. There the plausibility of the results will be checked by means of a Maxwell-Stefan membrane modeling approach, which is outlined in detail at the end of chapter 2.1. After the membrane related fundamentals, a brief introduction on boundary layer theory and optical boundary layer measurement is provided. The focus lies on the film theory as its assumptions are also the basis for the local membrane parameter method (LMPM). Then, a compact overview on the previously published theoretical work on the LMPM [91] is presented. In this context, the connection between boundary layer theory and optical methods is elaborated. This is the basis for the subsequent chapter, where the LMPM is tested in a proof of concept study.

2.1 Membrane Transport

In the following, a review of the of the standard RO model, the Solution-Diffusion Model (SDM), is presented. For the discussion of the results presented in chapter 6, a detailed knowledge about the considered physical phenomena, the assumptions and the mathematical simplifications is necessary. As the historical context between model development and available membranes is relevant for the understanding of the membrane model design, it is included in the following section.

2.1.1 The Membrane

Membrane desalination dominates today's market [58, p. 198] mainly because of two major developments: For the first time, Reid and Bretion (1959) were able to separate salt from water with a synthetic membrane, which was based on cellulose acetate (CA) [40, p. 7]. Loeb and Sourirajan (1963) then achieved the breakthrough to manufacture this membrane with an asymmetric structure [37, p. 411], which resulted in practically relevant water fluxes. Cadotte and Petersen made the second major development step in 1978 [40, p. 9]: They solved the contradicting requirement for the membrane thickness to be as small as possible (high flux and selectivity) but to be large enough to provide mechanical strength (resistance to high operating pressures). They invented the so-called Thin-Film Composite (TFC) membranes, which are composed of different materials for different requirements on the membrane. The most important [40, p. 8] TFC membrane type consists of an aromatic polyamide (PA) thin-film layer (thickness in order of 30 nm [109, p. 43]). The PA layer is supported by a polysulfone polymer on top of a polyester backing [137, p. 2]. The film is formed by so-called interfacial polymerization, compare figure 2.1: The PA layer is the result of the reaction of Trimesoyl Chloride (TMC), also known as 1,3,5 benzenetri carboxylic acid chloride, and m-Phenylenediamine (MPD), also known as 1,3 diaminobenzene [160, p. 21]. Before the reaction takes place, a microporous polysulfone support is dipped into an aqueous MPD solution such that the pores located close to its surface are filled [97, p. 82]. Then this MPD coated polysolfone membrane is immersed in a water-immiscible solvent solution containing TMC [9, p. 116].

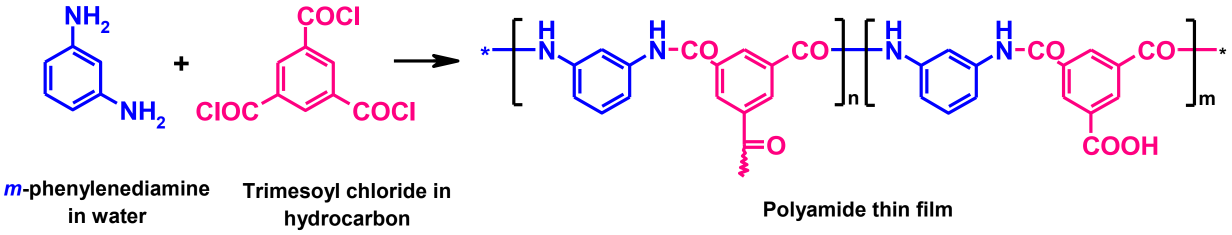

Figure 2.1: Interfacial polymerization reaction of MPD and TMC [98, fig. 1].

MPD and TMC react at the interface of the two immiscible solutions and a highly cross-linked thin-film layer is formed on the top of the polysulfone support [9, p. 117]. The cross-linking of the polymer chains improves the membrane separation characteristics [72]. For more detailed explanation please refer to e.g. RAUTENBACH and ALBRECHT [135]. At this point, it is important to understand that, due to incomplete reaction of the third carboxylic acid chloride group (the COCl-group in figure 2.1), the PA layer is negatively charged in an aqueous solution like salt water [160, p. 22]. Compared to CA membranes, the electrical charge density of PA TFC membranes is significantly higher [24, 30]. This will turn out to be important when interpreting the results presented in chapter 6.

The membrane investigated throughout this thesis is a cross-linked fully aromatic PA TFC brackish water membrane. It was manufactured by TORAY INDUSTRIES, INC. and it is labeled TML10D [174]. It has a modified membrane surface for improved fouling characteristics. The goals of such surface modifications are typically: increased hydrophilicity, reduced roughness and tailored electrical charge properties [81, p. 586]. As many foulants are hydrophobic, the probability of their adsorption on the membrane is lower when a pure water layer is formed on a highly hydrophilic surface [81, p. 586], see figure 2.2.

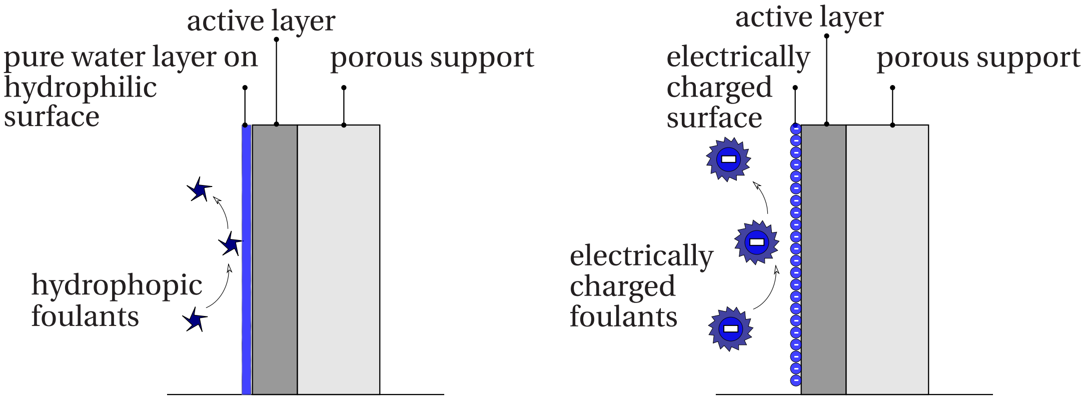

Figure 2.2: Anti-fouling mechanisms: hydrophilicity and surface charge modifications, adapted from [81, fig. 1].

A reduced surface roughness also lowers the probability that foulants are trapped by the membrane [81, p. 586]. Electrostatic repulsion is also beneficial as the foulants themselves are often electrically charged [87, p. 44]. Although the exact modifications of the TML10D membrane are not published by Toray, it can be stated that the goal of its development was the prevention of hydrophobic and electrostatic interactions with foulants [137, p. 19]. According to Henmi et al. [69, p. 2138], the focus of Toray was on achieving hydrophilic property on the membrane surface. Additionally, the surface roughness was also reduced via a cross-linked hydrophilic coating, compare figure 2.3.

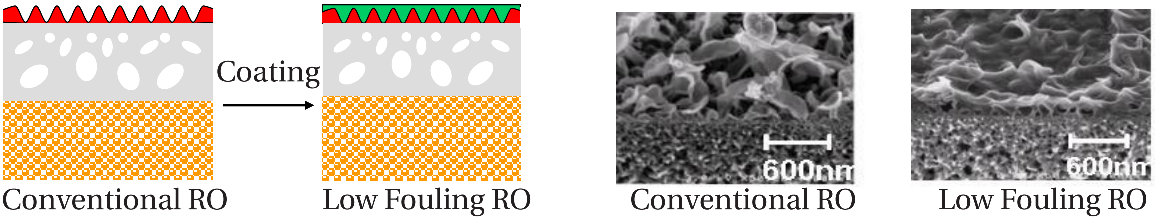

Figure 2.3: Design of a low fouling Toray membrane, adapted from [137, p. 21].

No detailed information could be found about surface charge modifications of the TML10D membrane except that the hydrophilic polymer coating is also seen as a countermeasure against electrostatic interaction [137, p. 20]. However, it is reported by Toray [137, p. 39] that the electrical charge density of the RO membrane has the greatest influence on the solute permeability.

2.1.2 Introduction of Membrane Transport Modeling

In the following, a brief overview of membrane transport modeling is given:

In 1958, Kedem and Katchalsky [82] published pioneering work on transport modeling for synthetic membranes. They present a phenomenological approach based on irreversible thermodynamics theory. Their approach was well received by the community, further developed [162] and is still applied today, e.g. [53]. One of its main advantages is that the modeling approach does not depend on the membrane type [109, p. 73].

Models which do depend on the membrane type can be divided in three main categories: pore models, pore-free models and intermediate ones [9, p. 17]. A classification is possible by means of the largest pore size of the membrane, as illustrated in figure 2.4. While microfiltration (MF) and ultrafiltration (UF) membranes clearly can be put in the pore model category [9, fig. 2.2], RO membranes are generally modeled as continuous, pore-free membranes. If RO membranes are specified with a pore size, it is usually indirectly estimated by the size of the molecules which diffuse through the membrane [9, p. 17]: It ranges between 0.2 nm and 0.5 nm [9, p. 17]. Nanofiltration membranes (NF) are an example for membranes in the transition region between RO and UF membranes [9, p. 17]. Such membranes are modeled by an intermediate approach between truly pore and truly pore-free models [9, p. 17].

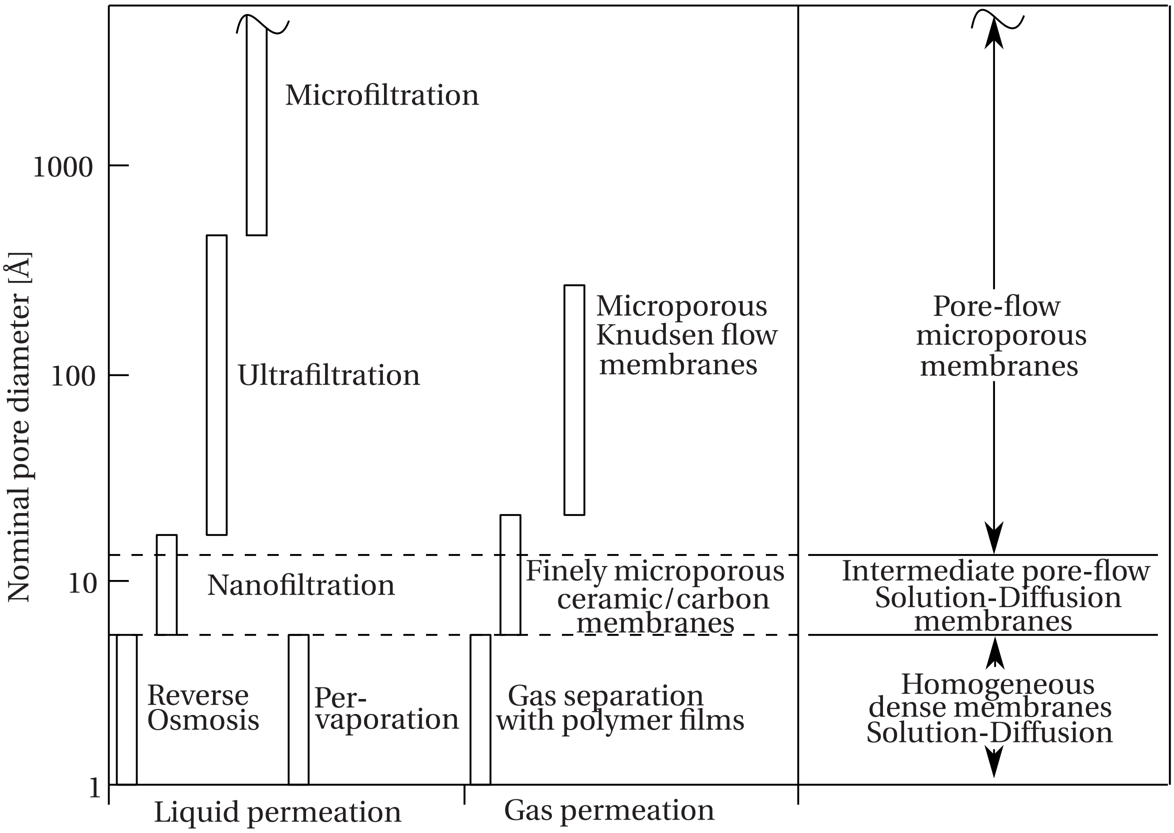

Figure 2.4: Pore size and membrane models, adapted from [9, fig. 2.2].

For a more extensive overview, it is referred to standard reference books like MELIN and RAUTENBACH [109] or BAKER [9]. In the next section, the used standard transport model for RO membranes is described in detail.

2.1.3 The Solution-Diffusion Modeling Approach

The Solution-Diffusion Model (SDM) goes back to LONDSALE ET AL. [102], who developed their theory based on experiments with CA membranes and aqueous NaCl solutions.

As already mentioned, the central assumption of the model is that the membrane is dense, homogenous and pore-free. Mass transport is determined by diffusion through a single phase [102, p. 1353], the thin-film active layer of the membrane.

To give a brief overview, the most important assumptions of the SDM are:

- The membrane is seen as a continuum without pores [109, p. 79].
- There is only diffusive mass transfer in the membrane [109, p. 79].
- Fick's law of diffusion can be applied [102, p. 1353].
- Binary diffusion is assumed for each solvent in the membrane due to small concentrations of the respective other solvents in membrane. This results from low solubilities of the solvents in the membrane [135, p. 52].
- The coupling of flows inside the membrane is negligible [109, p. 79].
- Chemical equilibrium at the interface between membrane and external solution can be assumed [109, p. 79].
- The chemical potential is modeled assuming an isothermal process and no external forces.
- The pressure level in the membrane is constant [109, p. 88] and corresponds to the feed pressure (illustrated later in figure 2.5(a)). The pressure drop between high and low pressure side takes place at the interface between thin-film active layer and support structure [135, fig. 3.1].

In figure 2.5, important physical quantities for RO membrane transport are illustrated. These are hydrostatic pressure p, salt and water mass fraction w_S and w_W, salt and water flux j_S and j_W, and chemical potential for water μ_W.

There are the phases of the external solutions (superscript E) and the one inside the thin-film active layer of the membrane (superscript M). Note that the superscript E is omitted later in this study when it is clear that the external solution outside the membrane is meant. In RO desalination, the feed side (subscript F) has typically a higher salt mass fraction than the permeate side (subscript P). The thin-film active layer is oriented towards the high pressure side (feed side) to avoid its detachment from the porous support layer. The porous support layer (low pressure side) provides not only mechanical strength but serves also as a diffusive barrier between active layer and permeate channel [135, p. 89]. This is the reason why, in contrast to e.g. gas permeation, the permeate salt mass fraction $w^{\mathrm{E}}_{\mathrm{S,P}}$ of an RO membrane (at the interface between active layer and porous support) is negligibly influenced by the flow conditions in the permeate channel [135, p. 89].

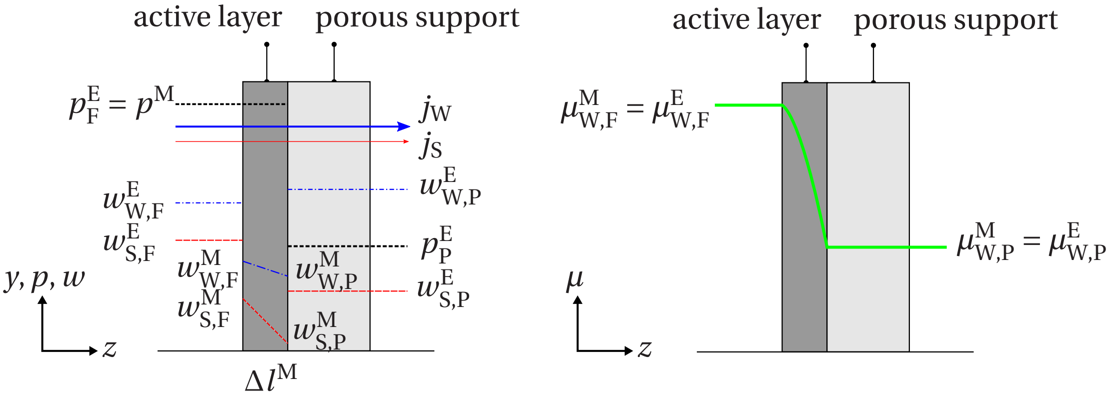

(a) Pressures, mass fractions and fluxes; adapted from [135, fig. 3.1].

(b) Chemical potential of water for linear activity gradient and zero pressure gradient in the active layer of the membrane.

Figure 2.5: Mass transport in RO membranes.

In figure 2.5(a), it is interesting to see the discontinuities of the salt and water mass fractions at the boundaries of the thin-film active layer. Here it helps to take the model designation *Solution-Diffusion* literally: Before diffusion of a species can take place inside the membrane, the species needs to dissolve in the membrane. The relation between quantities of the external solution and the corresponding ones of inside the active layer is expressed by the so-called solubility of the respective species.

After this brief generic overview, a quantitative description of the membrane mass transport is presented in the following. The two main equations for salt and water mass flux through the membrane j_S and j_W are derived. As already stated, emphasis is put on a presentation from scratch exposing which assumptions are made, which physical phenomena are neglected and which mathematical simplifications are required. The derivation begins with the diffusive mass transport inside the membrane.

Diffusive Mass Transport Inside the Membrane

Already in 1855, FICK investigated membrane transport experimentally [48, p. 81] stating that the pore theory is indefensible. His observations led to the famous Fick's law, a phenomenological approach [181, p. 19]. In its original form it is based on a concentration difference as driving force.

BIRD ET AL. [15, p. 565] provide a generalized description for diffusive transport: Besides the concentration gradient two other mechanical driving forces can be relevant, i.e. pressure gradients and external force differences [15, p. 564]. Additionally, the mass flux can be influenced by temperature gradients. Such coupling of driving forces goes back to irreversible thermodynamics theory [15, p. 564]. A general overview of coupling of driving forces and their influence on fluxes in a binary system is given in figure 2.6.

For the mass transport modeling according to the SDM, this means the following: As the SDM model assumes an isothermal process, an influence of a temperature gradient on the mass flux in the membrane is excluded. As the pressure gradient inside the membrane is assumed to be zero (discussed in detail later in section 2.1.5) and as external forces are neglected [109], pressure diffusion and forced diffusion are not taken into account in the SDM. In short, only Fickian diffusion is considered.

Driving forces Fluxes	Velocity gradients	Temperature gradient	Concentration gradient Pressure gradient External force differences
Momentum	Newton's law $[\mu, \kappa]$		
Energy		Fourier's law $[\lambda]$	Dufour effect $[D_i^{\mathrm{T}}]$
Mass		Soret effect $[D_i^{\mathrm{T}}]$	Fick's law $[D_{ij}]$

Figure 2.6: Schematic overview of fluxes and driving forces in a binary system, adapted from [15, fig. 18.4-1]. In brackets, the transport coefficients are given.

As Fick's law is defined in terms of fluxes [181, p. 5], different forms of the diffusion equation are possible. They are based on different reference frames (e.g. mass, molar, volume) [26, p. 60]. In membrane desalination, the mass-based one is common, compare e.g. [127].

According to Fick's law, the water flux $j_{\mathrm{W,D}}^{\mathrm{M}}$ reads [26, p. 60]:

$$j_{\mathrm{W,D}}^{\mathrm{M}} = -\rho^{\mathrm{M}} D_{\mathrm{WM}} \frac{\mathrm{d}w_{\mathrm{W}}^{\mathrm{M}}}{\mathrm{d}z} \tag{2.1}$$

This flux is defined relative to the centre of mass of all components in the system, in this case membrane and water. Note that the influence of the third component salt is not taken into account (no coupling of flows, low solubility in the membrane).

What is experimentally measurable is the water mass flux relative to a fixed coordinate system $j_{\mathrm{W}}^{\mathrm{M}}$ [135, p. 51]:

$$j_{\mathrm{W}}^{\mathrm{M}} = \rho_{\mathrm{W}}^{\mathrm{M}} u_{\mathrm{W}}^{\mathrm{M}} = j_{\mathrm{W,D}}^{\mathrm{M}} + \rho_{\mathrm{W}} u^{\mathrm{M}} \tag{2.2}$$

u^{M} denotes the velocity of the centre of mass of all components in the system. $u_{\mathrm{W}}^{\mathrm{M}}$ and $u_{\mathrm{M}}^{\mathrm{M}}$ are the velocities of the components water and membrane, respectively. As the velocity of the membrane is zero, it follows for u^{M}:

$$u^{\mathrm{M}} = \frac{\sum \rho_i u_i}{\sum \rho_i} = \frac{\overbrace{\rho_{\mathrm{W}}^{\mathrm{M}} u_{\mathrm{W}}^{\mathrm{M}}}^{j_{\mathrm{W}}^{\mathrm{M}}} + \rho_{\mathrm{M}}^{\mathrm{M}} \overbrace{u_{\mathrm{M}}^{\mathrm{M}}}^{=0}}{\rho_{\mathrm{W}}^{\mathrm{M}} + \rho_{\mathrm{M}}^{\mathrm{M}}} = \frac{j_{\mathrm{W}}^{\mathrm{M}}}{1 + \frac{\rho_{\mathrm{M}}^{\mathrm{M}}}{\rho_{\mathrm{W}}^{\mathrm{M}}}} \tag{2.3}$$

With $\rho_{\mathrm{M}}^{\mathrm{M}} = (1 - w_{\mathrm{W}}^{\mathrm{M}})\rho^{\mathrm{M}}$ the water mass flux reads as follows:

$$j_{\mathrm{W}}^{\mathrm{M}} = -\frac{1}{1 - w_{\mathrm{W}}^{\mathrm{M}}} \rho^{\mathrm{M}} D_{\mathrm{WM}} \frac{\mathrm{d} w_{\mathrm{W}}^{\mathrm{M}}}{\mathrm{d} z} \tag{2.4}$$

As the SDM approach assumes that the permeand solubility in the membrane is low, the term $1 - w_{\mathrm{W}}^{\mathrm{M}}$ is approximated by 1. Thus, the mass flux relative to fixed coordinates used in the SDM is an approximation [135, p. 52]:

$$j_{\mathrm{W}}^{\mathrm{M}} \approx j_{\mathrm{W,D}}^{\mathrm{M}} = -\rho^{\mathrm{M}} D_{\mathrm{WM}} \frac{\mathrm{d} w_{\mathrm{W}}^{\mathrm{M}}}{\mathrm{d} z} \tag{2.5}$$

Accordingly, the salt mass flux through the membrane $j_{\mathrm{S}}^{\mathrm{M}}$ is expressed:

$$j_{\mathrm{S}}^{\mathrm{M}} = -\rho^{\mathrm{M}} D_{\mathrm{SM}} \frac{\mathrm{d} w_{\mathrm{S}}^{\mathrm{M}}}{\mathrm{d} z} \tag{2.6}$$

Including the Concept of Solubility

As a next step, the hardly experimentally accessible quantities inside the membrane $w_{\mathrm{W}}^{\mathrm{M}}$ and $w_{\mathrm{S}}^{\mathrm{M}}$ are linked to measurable quantities of the external solution $w_{\mathrm{W}}^{\mathrm{E}}$ and $w_{\mathrm{S}}^{\mathrm{E}}$. This allows to quantify solubility in the following. It starts with an assumption for the chemical potential: Despite the irreversible character of the RO transport process [135, p. 53], the SDM is based on the assumption of an equilibrium between the respective chemical potentials at the phase interfaces, as illustrated above in figure 2.5(b) on page 19.

For isobaric, isothermal systems, the chemical potential of a component i μ_i, is a function of a pure substance term (A), a concentration-dependent term accounting also for non-ideality of the real solution (B) and a term taking the absolute pressure level into account (C), compare e.g. [135, p. 53]:

$$\mu_i(T,p,x_i) = \underbrace{\mu_i^{\mathrm{ref}}(T,p^{\mathrm{ref}})}_{\mathrm{A}} + \underbrace{RT\ln a_i(T,p^{\mathrm{ref}},x_i)}_{\mathrm{B}} + \underbrace{\bar{V}_i(p-p^{\mathrm{ref}})}_{\mathrm{C}} \tag{2.7}$$

In term B, activity $a_i = x_i\gamma_i$ is a measure for the effective concentration of component i in the non-ideal solution correcting concentration x_i by the activity coefficient γ_i. It follows for the molar fractions of water at the feed and permeate side $x_{\mathrm{W,F}}^{\mathrm{M}}$ and $x_{\mathrm{W,P}}^{\mathrm{M}}$:

$$x_{\mathrm{W,F}}^{\mathrm{M}} = \frac{\gamma_{\mathrm{W,F}}^{\mathrm{E}}}{\gamma_{\mathrm{W,F}}^{\mathrm{M}}} x_{\mathrm{W,F}}^{\mathrm{E}} \tag{2.8}$$

$$x_{\mathrm{W,P}}^{\mathrm{M}} = \frac{\gamma_{\mathrm{W,P}}^{\mathrm{E}}}{\gamma_{\mathrm{W,F}}^{\mathrm{M}}} x_{\mathrm{W,P}}^{\mathrm{E}} e^{-\frac{\bar{V}_{\mathrm{W}}}{RT}(p_{\mathrm{F}}-p_{\mathrm{P}})} \tag{2.9}$$

Note that equations (2.8) and (2.9) take the assumption for the pressure gradient across the membrane into account. Equilibrium of the chemical potential $\mu_{\mathrm{W}}^{\mathrm{M}} = \mu_{\mathrm{W}}^{\mathrm{E}}$ is assumed at the phase interfaces.

It is important to notice in equation (2.9) that the actual driving force for the water transport through the membrane, the hydrostatic pressure difference, comes in through the boundary conditions at the phase interface on the permeate side [127, p. 374]. This is called pressure-induced diffusion [127, 128]. In the case of RO, this makes the water concentration *decrease* from feed to permeate side. In figure 2.5(a) on page 19, an illustration of the development of the concentrations inside the membrane is included.

In equation (2.7) term (C) for the pressure influence is negligible for NaCl but not for water [109, p. 90]. From the boundary conditions at the phase interfaces, the molar fractions of salt at the feed and permeate side $x_{\mathrm{S,F}}^{\mathrm{M}}$ and $x_{\mathrm{S,P}}^{\mathrm{M}}$ result:

$$x_{\mathrm{S,F}}^{\mathrm{M}} = \frac{\gamma_{\mathrm{S,F}}^{\mathrm{E}} x_{\mathrm{S,F}}^{\mathrm{E}}}{\gamma_{\mathrm{S,F}}^{\mathrm{M}}} \tag{2.10}$$

$$x_{\mathrm{S,P}}^{\mathrm{M}} = \frac{\gamma_{\mathrm{S,P}}^{\mathrm{E}} x_{\mathrm{S,P}}^{\mathrm{E}}}{\gamma_{\mathrm{S,P}}^{\mathrm{M}}} \tag{2.11}$$

Introducing the equation for the osmotic pressure

$$\pi_i = -\frac{RT}{\bar{V}_i} \ln a_i \tag{2.12}$$

which originates in a simplified version from VAN'T HOFF [135, p. 5], the numerators of equations (2.10) and (2.11) $\gamma_i^{\mathrm{E}} x_i^{\mathrm{E}} = a_i^{\mathrm{E}}$ can be substituted by:

$$\gamma_i^{\mathrm{E}} x_i^{\mathrm{E}} = e^{-\frac{\bar{V}_i}{RT}\pi_i} \tag{2.13}$$

In the following, these results are integrated step by step in equations (2.5) and (2.6), ending up in equations for salt and water solubility.

The mass fractions are replaced by the molar fractions $w_i^{\mathrm{M}} = \frac{\bar{M}_i}{\bar{M}^{\mathrm{M}}} x_i^{\mathrm{M}}$. Additionally, a constant water activity coefficient $\gamma_{\mathrm{W}}^{\mathrm{M}}$ is assumed within the membrane:

$$\gamma_{\mathrm{W,F}}^{\mathrm{M}} = \gamma_{\mathrm{W,P}}^{\mathrm{M}} = \gamma_{\mathrm{W}}^{\mathrm{M}} \tag{2.14}$$

For salt, a constant ratio of the activity coefficients in the external solution and the membrane is assumed:

$$\frac{\gamma_{\mathrm{S,F}}^{\mathrm{E}}}{\gamma_{\mathrm{S,F}}^{\mathrm{M}}} = \frac{\gamma_{\mathrm{S,P}}^{\mathrm{E}}}{\gamma_{\mathrm{S,P}}^{\mathrm{M}}} = \frac{\gamma_{\mathrm{S}}^{\mathrm{E}}}{\gamma_{\mathrm{S}}^{\mathrm{M}}} \tag{2.15}$$

In section 6.3, the assumption made in equation (2.15) needs to be dropped in order to be able to quantify the influence of the electrical charge density of the PA TFC membrane on salt permeability.

After linearizing the molar fraction gradients of the respective components $i = \mathrm{W}$ and $i = \mathrm{S}$ inside the active layer of the membrane with a thickness Δl^{M},

$$\frac{\mathrm{d}x_i^{\mathrm{M}}}{\mathrm{d}z} \approx -\frac{x_{i,\mathrm{F}}^{\mathrm{M}} - x_{i,\mathrm{P}}^{\mathrm{M}}}{\Delta l^{\mathrm{M}}}, \tag{2.16}$$

the mass fluxes can be expressed as a function of concentration quantities in the external solution.

The water mass flux reads:

$$j_{\mathrm{W}}^{\mathrm{M}} = \frac{1}{\Delta l^{\mathrm{M}}} \rho^{\mathrm{M}} \underbrace{\frac{1}{\gamma_{\mathrm{W}}^{\mathrm{M}}} \frac{\bar{M}_{\mathrm{W}}}{\bar{M}^{\mathrm{M}}}}_{K_{\mathrm{W}}} D_{\mathrm{WM}} \left(e^{-\frac{\bar{V}_{\mathrm{W}}}{RT}\pi_{\mathrm{F}}} - e^{-\frac{\bar{V}_{\mathrm{W}}}{RT}(p_{\mathrm{F}} - p_{\mathrm{P}} + \pi_{\mathrm{P}})} \right) \tag{2.17}$$

K_W denotes water solubility, also known as the distribution coefficient for water. Note that the reciprocal of the water activity coefficient in the membrane $K_{W,\gamma} = \frac{1}{\gamma_W^M}$ becomes relevant later in section 6.3.

The salt flux results analogously:

$$j_S^M = \frac{1}{\Delta l^M} \underbrace{\frac{c^M}{c^E} \frac{\gamma_S^E}{\gamma_S^M}}_{K_S} D_{SM} (\rho_{S,F}^E - \rho_{S,P}^E) \tag{2.18}$$

$K_S = \frac{c^M}{c^E} \frac{\gamma_S^E}{\gamma_S^M}$ denotes the salt solubility, also known as distribution coefficient for salt.

Final Equation Set of the Solution-Diffusion Model

When the e-Function in equation (2.17) is approximated by series expansion, $e^x = \sum_{n=0}^{\infty} \frac{x^n}{n!} \approx 1 + x$, accepting an error around 4% for sea water conditions [135, p. 55], the standard SDM equation for the water flux results:

$$j_W = j_W^E = j_W^M = \rho_W A \underbrace{(p_F - p_P - (\pi_F - \pi_P))}_{NDP} \tag{2.19}$$

The difference between hydrostatic pressure difference $\Delta p = p_F - p_P$ and osmotic pressure difference $\Delta \pi = \pi_F - \pi_P$ is called net driving pressure NDP. The parameter A is the so-called water permeability constant:

$$A = \frac{1}{\Delta l^M} \frac{\rho^M}{\rho_W} \frac{1}{\gamma_W^M} \frac{\bar{M}_W}{\bar{M}^M} \frac{\bar{V}_W}{RT} D_{WM} \tag{2.20}$$

The standard SDM equation for the salt flux is expressed by:

$$j_S = j_S^E = j_S^M = B(\rho_{S,F}^E - \rho_{S,P}^E) \tag{2.21}$$

B denotes the salt permeability constant:

$$B = \frac{K_S D_{SM}}{\Delta l^M} \tag{2.22}$$

The permeate flux is the sum of water and salt flux:

$$\dot{j}_{\mathrm{P}} = \dot{j}_{\mathrm{P}}^{\mathrm{E}} = \dot{j}_{\mathrm{P}}^{\mathrm{M}} = \dot{j}_{\mathrm{S}}^{\mathrm{M}} + \dot{j}_{\mathrm{W}}^{\mathrm{M}} \tag{2.23}$$

A parameter to quantify the separation characteristic of the membrane is the Salt Rejection:

$$SR = \frac{w_{\mathrm{S,F,M}}^{\mathrm{E}} - w_{\mathrm{S,P,M}}^{\mathrm{E}}}{w_{\mathrm{S,F,M}}^{\mathrm{E}}} \tag{2.24}$$

To be exact, equation (2.24) describes the *True* Salt Rejection as concentration values on the membrane are used [135, p. 58]. When concentration values of the bulk phases are applied in, *SR* is called *Apparent* Salt Rejection [135, p. 58].

Summing up, the SDM was introduced with the focus on important assumptions. In the next section, the two main SDM parameters for membrane characterization, i.e. water and salt permeability constant, are discussed in more detail.

2.1.4 Membrane Parameters of the Solution-Diffusion Model

As already mentioned in the introduction (section 1.1), the water and salt permeability constants A and B are commonly determined experimentally [135, p. 56].

According to RAUTENBACH and ALBRECHT [135, p. 57] water and salt permeability constants depend on temperature. Additionally, the water permeability constant is dependent on pressure, while the salt permeability constant is almost pressure independent [135, p. 56]. The standard procedure is to measure the membrane performance in the parameter range of interest and to fit the measurement data to Arrhenius type equations [135, p. 57]. A brief theoretical basis for the applied equations is given in the following.

2.1.4.1 Influence of Temperature on Permeability Constants

Looking at equation (2.20) for the water permeability constant A, the greatest influence of temperature is expected from the diffusivity D_{WM} of water in the membrane. According to JIN ET AL. [77, p. 348], D_{WM} is proportional to the ratio of temperature T and dynamic viscosity μ:

$$D_{\mathrm{WM}} \propto \frac{T}{\mu} \tag{2.25}$$

Evaluating the correlation for viscosity of an aqueous NaCl solution provided by OZBEK ET AL. [126, p. 18], the main temperature influence on viscosity can be described by an exponential dependence on temperature:

$$\mu \propto \exp(-T) \tag{2.26}$$

Therefore, the temperature dependence for the water permeability constant (equation (2.20)) can be described as follows [135, p. 57]:

$$A = A_0 \cdot \exp\left(\alpha_{\mathrm{T}} \frac{T - T_0}{T_0}\right) \tag{2.27}$$

Note that the subscript 0 indicates an arbitrary reference state. For the salt permeability constant, also an Arrhenius type function is commonly assumed. However, the influence of temperature on the water permeability constant is expected to be stronger than on the salt permeability constant [135, p. 57]:

$$B = B_0 \cdot \exp\left(\beta_{\mathrm{T}} \frac{T - T_0}{T_0}\right) \tag{2.28}$$

To give an order of magnitude, $\alpha_{\mathrm{T}} = 7.1$ and $\beta_{\mathrm{T}} = 3.0$ are typical values for CA membranes [135, p. 57]. For the investigated PA TFC polyamide membrane, a similar result is achieved ($\alpha_{\mathrm{T}} = 6.6$) as it will be shown later when presenting the results (section 6.1). Note that β_{T} is not determined in the present study as the focus is on analyses of local membrane properties and not on the influence of temperature on B.

2.1.4.2 Influence of Pressure on Permeability Constants

The influence of pressure on the permeability constants is discussed in literature in the context of membrane compaction. The mechanisms of compaction and the design of membranes resistant to compaction are questions of ongoing research [131].

In 2010, PENDERGAST ET AL. [131] adapted a concept from LONDSDALE ET AL. [103, p. 115] for a mechanistic description of compaction. The main contribution of the phenomenon is attributed to the porous support structure which is compressed when the membrane is exposed to pressure differences [131, p. 2]. A compacted support structure results in an increased effective path length for permeating species: $\Delta l^{\mathrm{M}}_{\mathrm{eff,c}} > \Delta l^{\mathrm{M}}_{\mathrm{eff,ini}} > \Delta l^{\mathrm{M}}$ (see figure 2.7).

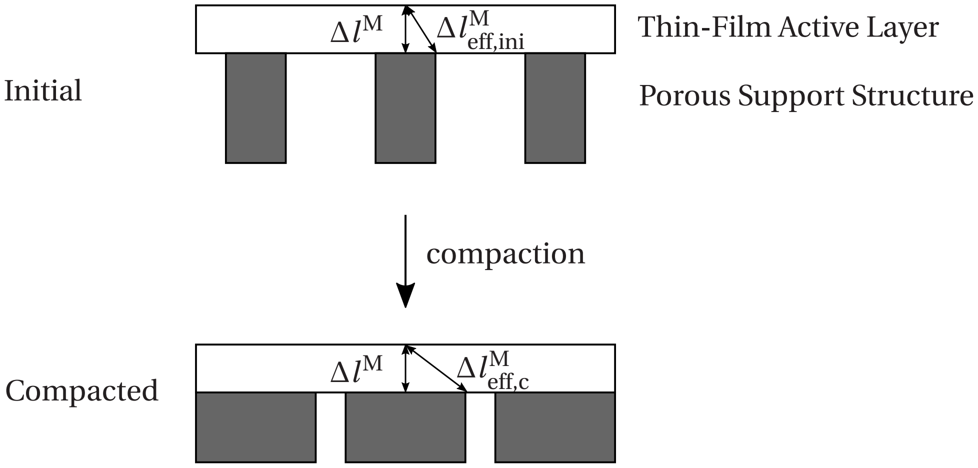

Figure 2.7: Increase of path length for diffusion due to compaction, adapted from [103, fig. 5] and [131, fig. 10].

As the relevant path length for diffusion only appears in the denominator of the permeability constants, the water and salt fluxes should decrease to the same amount during compaction. This, however, could not be experimentally confirmed by PENDERGAST ET AL. [131, p. 7]. Consequently, compaction effects are also likely to occur in the thin-film active layer [131, p. 7]. This is indicated by RAUTENBACH and ALBRECHT [135, p. 56], too. What can be generally observed in experiments is that the permeate flux through the membrane significantly decreases during the first operating hours when the membrane becomes compacted. The water permeability decreases with increasing pressure. The higher the pressure, the higher the compaction effect. Both, reversible and irreversible compaction, occur [135, p. 56]. The reversible part can be taken into account with the following empirical equations [135, p. 57]:

$$A = A_0 \cdot \exp\left(\alpha_\mathrm{p} \frac{p - p_0}{p_0}\right) \tag{2.29}$$

$$B = B_0 \cdot \exp\left(\beta_\mathrm{p} \frac{p - p_0}{p_0}\right) \tag{2.30}$$

The pressure dependence of the water permeability constant is in the order of magnitude of $\alpha_\mathrm{p} = -0.003$ to $\alpha_\mathrm{p} = -0.005$ for CA membranes [135, p. 57]. For the investigated TFC polyamide membrane, a similar result is achieved, $\alpha_\mathrm{p} = -0.0027$, as it will be shown later when presenting the results (chapter 6.1). As mentioned above, the salt permeability constant should be almost independent of pressure [135, p. 56], i.e. $\beta_\mathrm{p} \approx 0$.

2.1.4.3 Superposition of the Influences of Temperature and Pressure on Permeability Constants

Combining equation (2.27) with (2.29) and equation (2.28) with (2.30), respectively, the temperature and pressure dependence of water and salt permeability constant of an RO membrane can be described by the following two equations:

$$A = A_0 \cdot \exp\left(\alpha_\mathrm{p} \frac{p - p_0}{p_0} + \alpha_\mathrm{T} \frac{T - T_0}{T_0}\right) \tag{2.31}$$

$$B = B_0 \cdot \exp\left(\beta_\mathrm{p} \frac{p - p_0}{p_0} + \beta_\mathrm{T} \frac{T - T_0}{T_0}\right) \tag{2.32}$$

2.1.4.4 Influence of Salinity on Permeability Constants

It is not common to standardly take into account the influence of salinity on the permeability constants of RO membranes. According to RAUTENBACH and ALBRECHT [135, p. 56] (1989) water and salt permeability constants of RO membranes do not dependent on the salt mass fractions on both sides of the membrane [135, p. 56]. For CA membranes, this was shown by KIMURA and SOURIRAJAN [84] in 1967.

However, in 2005 BARTELS ET AL. [10, fig. 8] measured a dependence of the salt permeability constant B on the feed salinity. They investigated PA TFC membranes for brackish water applications. Their results are depicted in figure 2.8.

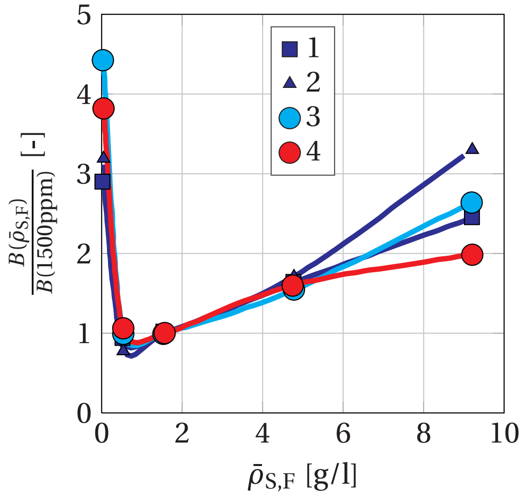

Figure 2.8: Manufacturer data for four membrane samples 1 to 4 on the influence of salinity on B for $T = 25°C$, $u_P = 25.5\ l/m^2h$ and pH = 7 [10].

BARTELS ET AL. [10] determined a minimum of B around $\bar{\rho}_S = 0.5$ g/l in standard test cell experiments. They could not explain the large decrease of B for salinities between $\bar{\rho}_S = 0...0.5$ g/l [10, p. 192]. But they claim that membrane charge and the resulting Donnan potential are the reason for the increase of B up to a factor of 4 for salinities between $\bar{\rho}_S = 0.5...10$ g/l.

Another potential reason for a salinity dependence of the permeability constants is the use of Fick's diffusitity in the model. Fick's diffusivity linearly contributes to the permeability constants, see equations (2.20) and (2.22). BITTER [17, p. 31] emphasizes that strong composition and concentration dependencies of Fick's diffusivity D can appear, especially in liquid mixtures. This dependence can partly be described by the thermodynamic correction factor Γ_{ij} [136]:

$$D = \Gamma_{ij} \cdot \mathfrak{D} \tag{2.33}$$

$$\Gamma_{ij} = \delta_{ij} + \frac{\partial \ln \gamma_i}{\partial \ln x_i} \tag{2.34}$$

The concentration dependent correction factor Γ is shown in figure 2.9 for the diffusivity of NaCl in water at two different temperature levels 25°C and 30°C.

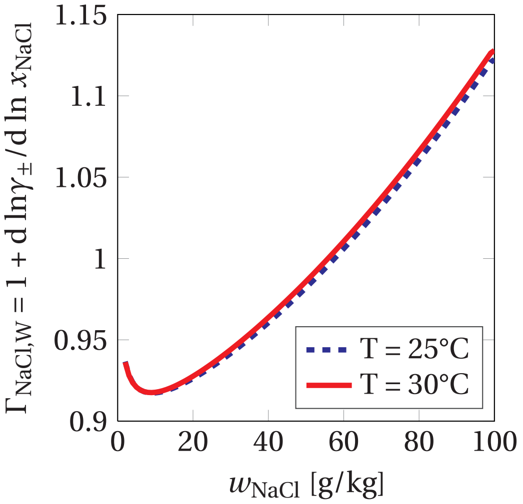

Figure 2.9: Thermodynamic correction factor for NaCl diffusivity in water. Activity coefficient data $\gamma_\pm$ are taken from CLARKE and GLEW [22].

At a first sight, the curves of B and Γ shown in figures 2.8 and 2.9 look similar. However, the relative change of Γ with w_S is less significant than the one of B. In addition, Γ has its minimum at $w_S \approx 10$ g/kg instead at $w_S \approx 0.5$ g/kg. Furthermore, in case of Γ the initial decrease of its curve is well understood. A decrease of $\gamma_\pm$ and consequently of Γ with w_S is characteristic for dilute, strong electrolytic solutions like NaCl in water [104, p. 135]. At low ion concentrations, the distance between ions is large and long range Coulomb attractive forces make oppositely charged ions group around an ion shielding its charge [104, p. 135]. This shield makes the ion interact less with other ions resulting in a lower effective ion concentration and a drop of the activity coefficient $\gamma_\pm$. For dilute solutions, the decrease of $\gamma_\pm$ with w_S is quantitatively described by the DEBYE-HÜCKEL equation [29] and extended versions [104, p. 136]. For more concentrated solutions, the intermolecular distances decrease such that short range, mainly repulsive forces become dominant which result in an increase of $\gamma_\pm$ [104, p. 136]. At high ion concentrations, this trend is additionally supported by Coulomb repulsion [104, p. 136].

Another reason for a salinity dependence of permeability can be the coupling of salt and water transport through the membrane. Not taking mass transport coupling into account in the SDM model is critizied by BITTER [17, p. 32-33] as well as by PAUL [127, p. 374]. However, PAUL [127, p. 380, p. 383] recognizes that the success of the SDM indicates that coupling effects in RO desalination might not be dominant. But he also attests that hardly any data exist in literature providing estimations about the magnitude of frictional coupling effects.

In addition to that, GEISE ET AL. [54, p. 1706] strengthen that already the basic equations for diffusive transport in RO membranes do not take its multi-component character into account. Modeling of multi-component diffusion would be necessary involving membrane, water and salt or even membrane, water, salt and cations and anions.

The focus in chapter 6.3 will be on the salinity dependence of the salt permeability constant. To better understand the physics, a membrane model different from the SDM will be needed. A modeling approach which allows to take all transport phenomena discussed above into account is based on the Maxwell-Stefan approach for diffusion. It is introduced in the following.

2.1.5 The Maxwell-Stefan Modeling Approach

BIRD ET AL. [15, p. 570] introduced the Maxwell-Stefan equations for diffusion problems in multi-component gases at low density. BITTER [17, p. 33] took this approach to describe multi-component diffusion in membranes. Also PAUL [127, p. 374] uses it for his reformulation of the Solution-Diffusion theory for RO membranes.

The main advantages of the Maxwell-Stefan approach are as follows:

- In contrast to Fick's diffusivities, Maxwell-Stefan diffusivities have a binary meaning also in multi-component diffusion [181, p. 19]. This link between binary and multi-component diffusion does not exist for Fick's law.
- As Fick's law is a phenomenological approach based only on concentration gradients, thermodynamic, electric and mechanical influences on diffusion are hidden in Fick's diffusivity. Instead, the Maxwell-Stefan approach is a physical approach taking multiple driving forces into account. This allows to clearly attribute Maxwell-Stefan diffusivities to a physical phenomenon [181, p. 18].
- While Fick's diffusivities are only valid within a certain reference frame (e.g. mass, molar, volume), Maxwell-Stefan diffusivities do not face that problem as their definition goes back to absolute velocities and not to fluxes [181, p. 18].
- While a ternary-component approach based on Fick needs four diffusivities, Maxwell-Stefan models need only three independent parameters (the fourth Fick's diffusivity can be interpreted as thermodynamic information [181, p. 17]).
- Model extension taking charge effects into account is possible, see e.g. GEISE ET AL. [54, p. 1706].

Especially the fact that diffusivity is independent of composition and concentration makes the Maxwell-Stefan modeling approach interesting. BITTER [17,

p. 35] puts this into perspective. The derivation of the Mawell-Stefan equations implies that during a collision between two different molecules no other molecules are involved [17, p. 35]. However, it has to be stated that this might describe reality better in gas mixtures, for which the Maxwell-Stefan theory was originally derived, than in liquids [17, p. 35], as illustrated in figure 2.10. BITTER [17, p. 33] emphasises to be aware of the assumption inherent to the theory: "The average friction exerted on molecules i in a multi-component system equals the molar average friction experienced by i in binary mixtures of i and the individual components of the former mixture". WILD [181, p. 3] also mentions that this strong molecular interaction between molecules makes diffusion modeling in liquids much more difficult than in gas.

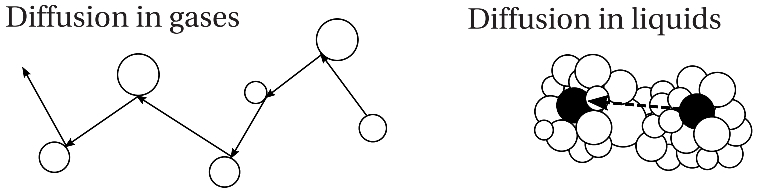

Figure 2.10: Collision of molecules in gases and liquids, adopted from BITTER [17, p. 35].

All in all, with the Maxwell-Stefan approach it is possible to develop a model which is based on three, almost concentration independent diffusivities. What might often remain as an uncertainty is the knowledge of the thermodynamic correction factors relating ideal and real material properties with each other. Note that ideal means that interaction between molecules of the same type is the same as the interaction between molecules of a different type [181, p. 2]. There is mechanical interaction like movement, friction and collision as well as thermodynamic interaction like attraction and repulsion [181, p. 1].

In the following, the Maxwell-Stefan theory is applied to the membrane problem, similar to the work of PAUL [127] in 2004. With PAUL as co-author, GEISE ET AL. [54] extended the model's application to charged membranes in 2010. Their work is the basis for the following description of the Maxwell-Stefan theory applied to RO membranes.

Membrane Modeling with Maxwell-Stefan Theory

The Maxwell-Stefan theory is based on the assumption that for steady-state diffusion an equilibrium exists between driving forces and frictional forces [16, 17, 181]:

$$\underbrace{d_i}_{\text{driving force}} = \underbrace{-\sum_{j\neq i} \frac{x_i x_j}{\mathfrak{D}_{ij}}(u_i - u_j)}_{\text{frictional forces}} \tag{2.35}$$

Note that equation (2.35) assumes isothermal conditions. The velocities u of the components i and j are to be seen relative to a fixed coordinate system. Following PAUL [127, p. 374] the driving force inside the membrane is expressed as

$$d_i = \frac{1}{c^{\mathrm{M}} RT} \cdot (c_i^{\mathrm{M}} \nabla \mu_i^{\mathrm{M}} - w_i \nabla p^{\mathrm{M}}), \tag{2.36}$$

with the chemical potential gradient in the membrane

$$\nabla \mu_i^{\mathrm{M}} = RT \nabla \ln a_i^{\mathrm{M}} + \bar{V}_i \nabla p^{\mathrm{M}}. \tag{2.37}$$

A central assumption of the Solution-Diffusion Model was a zero pressure gradient inside the membrane (section 2.1.3). According to MELIN and RAUTENBACH [109, p. 88] the question if the pressure gradient in the membrane is negligible or constant is expendable as both assumptions lead to the same result. Also PAUL and EBRA-LIMA [128, p. 2207] investigated different assumptions for the pressure distribution in the membrane and came to conclusion that a membrane pressure equal to the feed pressure is a good approximation. They support their finding with experimental results from ROSENBAUM and COTTON [143]. Therefore, also in the present study the pressure gradient within the membrane is neglected:

$$\nabla p^{\mathrm{M}} = 0 \tag{2.38}$$

In order to keep the model complexity at a moderate level, a ternary system of membrane, water and salt (NaCl) is considered, considering Na^+ and Cl^- separately only when needed, i.e. when focusing on solubility. The modeling is continued with only three components and therefore three transport equations for water W, salt S and membrane M. Note that the index S still denotes NaCl, however, whenever needed for clarity, the subscript NaCl is used within this study.

Putting equations (2.35) to (2.38) together, substituting the velocities of the components by the experimentally accessible mass fluxes $u_i = \frac{j_i}{w_i^{\mathrm{M}} \cdot \rho^{\mathrm{M}}}$ and substituting molar fractions by mass fractions $x_i^{\mathrm{M}} = \frac{\bar{M}^{\mathrm{M}}}{\bar{M}_i} w_i^{\mathrm{M}}$ the basis for the Maxwell-Stefan model is obtained:

$$-\nabla \ln a_{\mathrm{W}}^{\mathrm{M}} = \frac{1}{\mathfrak{D}_{\mathrm{WS}}} \frac{\bar{M}^{\mathrm{M}}}{\bar{M}_{\mathrm{S}}} w_{\mathrm{S}}^{\mathrm{M}} \left(\frac{j_{\mathrm{W}}}{w_{\mathrm{W}}^{\mathrm{M}} \cdot \rho^{\mathrm{M}}} - \frac{j_{\mathrm{S}}}{w_{\mathrm{S}}^{\mathrm{M}} \cdot \rho^{\mathrm{M}}}\right) + \frac{1}{\mathfrak{D}_{\mathrm{WM}}} \frac{\bar{M}^{\mathrm{M}}}{\bar{M}_{\mathrm{M}}} w_{\mathrm{M}}^{\mathrm{M}} \left(\frac{j_{\mathrm{W}}}{w_{\mathrm{W}}^{\mathrm{M}} \cdot \rho^{\mathrm{M}}} - \frac{j_{\mathrm{M}}}{w_{\mathrm{M}}^{\mathrm{M}} \cdot \rho^{\mathrm{M}}}\right) \tag{2.39}$$

$$-\nabla \ln a_{\mathrm{S}}^{\mathrm{M}} = \frac{1}{\mathfrak{D}_{\mathrm{WM}}} \frac{\bar{M}^{\mathrm{M}}}{\bar{M}_{\mathrm{M}}} w_{\mathrm{W}}^{\mathrm{M}} \left(\frac{j_{\mathrm{S}}}{w_{\mathrm{S}}^{\mathrm{M}} \cdot \rho^{\mathrm{M}}} - \frac{j_{\mathrm{W}}}{w_{\mathrm{W}}^{\mathrm{M}} \cdot \rho^{\mathrm{M}}}\right) + \frac{1}{\mathfrak{D}_{\mathrm{SM}}} \frac{\bar{M}^{\mathrm{M}}}{\bar{M}_{\mathrm{M}}} w_{\mathrm{M}}^{\mathrm{M}} \left(\frac{j_{\mathrm{S}}}{w_{\mathrm{S}}^{\mathrm{M}} \cdot \rho^{\mathrm{M}}} - \frac{j_{\mathrm{M}}}{w_{\mathrm{M}}^{\mathrm{M}} \cdot \rho^{\mathrm{M}}}\right) \tag{2.40}$$

$$-\nabla \ln a_{\mathrm{M}}^{\mathrm{M}} = \frac{1}{\mathfrak{D}_{\mathrm{MW}}} \frac{\bar{M}^{\mathrm{M}}}{\bar{M}_{\mathrm{W}}} w_{\mathrm{W}}^{\mathrm{M}} \left(\frac{j_{\mathrm{M}}}{w_{\mathrm{M}}^{\mathrm{M}} \cdot \rho^{\mathrm{M}}} - \frac{j_{\mathrm{W}}}{w_{\mathrm{W}}^{\mathrm{M}} \cdot \rho^{\mathrm{M}}}\right) + \frac{1}{\mathfrak{D}_{\mathrm{MS}}} \frac{\bar{M}^{\mathrm{M}}}{\bar{M}_{\mathrm{S}}} w_{\mathrm{S}}^{\mathrm{M}} \left(\frac{j_{\mathrm{M}}}{w_{\mathrm{M}}^{\mathrm{M}} \cdot \rho^{\mathrm{M}}} - \frac{j_{\mathrm{S}}}{w_{\mathrm{S}}^{\mathrm{M}} \cdot \rho^{\mathrm{M}}}\right) \tag{2.41}$$

As the membrane component is fixed, its velocity and flux is zero yielding $j_{\mathrm{M}} = 0$. Thus, the mass transfer of the ternary system can be described only with two equations. In the following, equations (2.39) and (2.40) are used.

The molar mass of the membrane component $\bar{M}_{\mathrm{M}}$ and the one of the solution membrane-water-salt $\bar{M}^{\mathrm{M}} = (\sum \frac{w_i}{\bar{M}_i})^{-1}$ are usually not known. Theoretically, the molecular weight and the molar mass of a cross-linked polymer is even infinite [127, p. 375]. PAUL [127] switches therefore from molar fractions to mass fractions, substituting the Maxwell-Stefan diffusivities by

$$\text{Đ}_{ij} = \mathfrak{D}_{ij} \frac{\bar{M}_i}{\bar{M}^{\mathrm{M}}} \tag{2.42}$$

hiding the unknown molar masses in manipulated Maxwell-Stefan diffusivities. In this work, such manipulations of the diffusivities are to be avoided, i.e. the molar mass is to be a model input later in section 6.3.

In order to come to an applicable set of equations, the following simplifications are made, according to PAUL [127]:

- Transport parameters like the manipulated diffusivities Đ_{ij} are constants independent of concentration [127, p. 379]. This means that thermodynamic correction factors Γ_{ij} are neglected, i.e. they are assumed to equal one).

- Linear concentration profiles within the membrane are assumed. This means that average values correspond to the arithmetic mean values $\bar{w}_i^{\mathrm{M}} = \frac{1}{2}(w_{i,\mathrm{F}}^{\mathrm{M}} + w_{i,\mathrm{P}}^{\mathrm{M}})$.

Putting everything together, the following equations result for the water and the salt flux:

$$\epsilon_{\mathrm{W}} = \frac{1}{\bar{w}_{\mathrm{M}}^{\mathrm{M}} \cdot \Delta l^{\mathrm{M}} \cdot (1 + \frac{\text{Đ}_{\mathrm{WM}}}{\text{Đ}_{\mathrm{WS}}} \frac{\bar{w}_{\mathrm{S}}^{\mathrm{M}}}{\bar{w}_{\mathrm{M}}^{\mathrm{M}}} + \frac{\text{Đ}_{\mathrm{SM}}}{\text{Đ}_{\mathrm{WS}}} \frac{\bar{M}_{\mathrm{S}}}{\bar{M}_{\mathrm{W}}} \frac{\bar{w}_{\mathrm{W}}^{\mathrm{M}}}{\bar{w}_{\mathrm{M}}^{\mathrm{M}}})} \tag{2.43}$$

$$\epsilon_{\mathrm{S}} = \epsilon_{\mathrm{W}} \tag{2.44}$$

$$j_{\mathrm{W,WPart}} = \epsilon_{\mathrm{W}} \cdot \rho^{\mathrm{M}} \cdot \text{Đ}_{\mathrm{WM}} \cdot (1 + \frac{\text{Đ}_{\mathrm{SM}}}{\text{Đ}_{\mathrm{WS}}} \frac{\bar{M}_{\mathrm{S}}}{\bar{M}_{\mathrm{W}}} \frac{\bar{w}_{\mathrm{W}}^{\mathrm{M}}}{\bar{w}_{\mathrm{M}}^{\mathrm{M}}})(w_{\mathrm{W,F}}^{\mathrm{M}} - w_{\mathrm{W,P}}^{\mathrm{M}}) \tag{2.45}$$

$$j_{\mathrm{W,SPart}} = \epsilon_{\mathrm{W}} \cdot \rho^{\mathrm{M}} \cdot \text{Đ}_{\mathrm{SM}} \cdot \frac{\text{Đ}_{\mathrm{WM}}}{\text{Đ}_{\mathrm{WS}}} \frac{\bar{w}_{\mathrm{W}}^{\mathrm{M}}}{\bar{w}_{\mathrm{M}}^{\mathrm{M}}}(w_{\mathrm{S,F}}^{\mathrm{M}} - w_{\mathrm{S,P}}^{\mathrm{M}}) \tag{2.46}$$

$$j_{\mathrm{S,WPart}} = \epsilon_{\mathrm{S}} \cdot \rho^{\mathrm{M}} \cdot \text{Đ}_{\mathrm{WM}} \cdot \frac{\text{Đ}_{\mathrm{SM}}}{\text{Đ}_{\mathrm{WS}}} \frac{\bar{M}_{\mathrm{S}}}{\bar{M}_{\mathrm{W}}} \frac{\bar{w}_{\mathrm{S}}^{\mathrm{M}}}{\bar{w}_{\mathrm{M}}^{\mathrm{M}}}(w_{\mathrm{W,F}}^{\mathrm{M}} - w_{\mathrm{W,P}}^{\mathrm{M}}) \tag{2.47}$$

$$j_{\mathrm{S,SPart}} = \epsilon_{\mathrm{S}} \cdot \rho^{\mathrm{M}} \cdot \text{Đ}_{\mathrm{SM}} \cdot (1 + \frac{\text{Đ}_{\mathrm{WM}}}{\text{Đ}_{\mathrm{WS}}} \frac{\bar{w}_{\mathrm{S}}^{\mathrm{M}}}{\bar{w}_{\mathrm{M}}^{\mathrm{M}}})(w_{\mathrm{S,F}}^{\mathrm{M}} - w_{\mathrm{S,P}}^{\mathrm{M}}) \tag{2.48}$$

$$j_{\mathrm{W}} = j_{\mathrm{W,WPart}} + j_{\mathrm{W,SPart}} \tag{2.49}$$

$$j_{\mathrm{S}} = j_{\mathrm{S,WPart}} + j_{\mathrm{S,SPart}} \tag{2.50}$$

The impact of mass transport coupling on the total flux can be quantified by the proportion of $j_{\mathrm{S,WPart}}$ and $j_{\mathrm{W,SPart}}$ in j_{S} and j_{W}, respectively.

Until now, only the mass transport within the membrane was discussed. In accordance with the SDM theory, solubility of water and salt connects the parameters of the external solution with the ones inside the membrane. The concept of solubility is taken from the SDM model. Water and salt solubility can be calculated by means of equations (2.8) to (2.11).

What is still required is a modeling approach for membrane charge effects. These will be integrated into the Maxwell-Stefan model by a salinity dependent salt solubility.

Already in 1966, MERTEN [111] provided a correlation for salt sorption in selective membranes taking membrane charge effects into account and GEISE ET AL. [54, p. 1706] applied his expression. In the present study, it is avoided to work with the correlation of MERTEN [111] as it implicitly assumes that molar concentrations of the solution are the same for feed phase and membrane phase. Note that this is explained in more detail in appendix A. In this study the modeling is continued following BIRD ET AL. [16, p. 792]. Assuming continuity of the chemical potential at the membrane interface between external solution and the membrane, a relationship between salt concentration in the external solution and in the membrane can be derived step by step:

$$RT\ \ln(\underbrace{a^{\mathrm{E}}_{\mathrm{Na^+}} \cdot a^{\mathrm{E}}_{\mathrm{Cl^-}}}_{a^{\mathrm{E}}_{\mathrm{S}}}) + \bar{V}_{\mathrm{S}} \cdot (p^{\mathrm{E}} - p^{\mathrm{ref}}) = RT \ln(\underbrace{a^{\mathrm{M}}_{\mathrm{Na^+}} \cdot a^{\mathrm{M}}_{\mathrm{Cl^-}}}_{a^{\mathrm{M}}_{\mathrm{S}}}) + \bar{V}_{\mathrm{S}} \cdot (p^{\mathrm{M}} - p^{\mathrm{ref}}) \tag{2.51}$$

$$\frac{a^{\mathrm{E}}_{\mathrm{Na^+}} \cdot a^{\mathrm{E}}_{\mathrm{Cl^-}}}{a^{\mathrm{M}}_{\mathrm{Na^+}} \cdot a^{\mathrm{M}}_{\mathrm{Cl^-}}} = e^{\frac{\bar{V}_{\mathrm{S}}}{RT} \cdot (p^{\mathrm{M}} - p^{\mathrm{E}})} \tag{2.52}$$

$$\frac{x^{\mathrm{E}}_{\mathrm{Na^+}} \cdot x^{\mathrm{E}}_{\mathrm{Cl^-}} \cdot \gamma^{\mathrm{E}2}_{\pm}}{x^{\mathrm{M}}_{\mathrm{Na^+}} \cdot x^{\mathrm{M}}_{\mathrm{Cl^-}} \cdot \gamma^{\mathrm{M}2}_{\pm}} = e^{\frac{\bar{V}_{\mathrm{S}}}{RT} \cdot (p^{\mathrm{M}} - p^{\mathrm{E}})} \tag{2.53}$$

$$\frac{c^{\mathrm{E}}_{\mathrm{Na^+}} \cdot c^{\mathrm{E}}_{\mathrm{Cl^-}} \cdot c^{\mathrm{M}2} \cdot \gamma^{\mathrm{E}2}_{\pm}}{c^{\mathrm{M}}_{\mathrm{Na^+}} \cdot c^{\mathrm{M}}_{\mathrm{Cl^-}} \cdot c^{\mathrm{E}2} \cdot \gamma^{\mathrm{M}2}_{\pm}} = e^{\frac{\bar{V}_{\mathrm{S}}}{RT} \cdot (p^{\mathrm{M}} - p^{\mathrm{E}})} \tag{2.54}$$

The intermediate result of equation (2.54) is combined with the assumption of charge neutrality in the membrane [111, p. 31]. Charge neutrality means that the charges of the mobile ions in the membrane counterbalance the fixed charges of the membrane. For a negatively charged membrane with an electrical charge density χ $[\frac{\mathrm{mol}}{\mathrm{m}^3}]$ it follows:

$$c^{\mathrm{M}}_{\mathrm{Na^+}} = \chi + c^{\mathrm{M}}_{\mathrm{Cl^-}} \tag{2.55}$$

This means that inside the membrane there are more counter-ions ($\mathrm{Na^+}$-ions) than co-ions ($\mathrm{Cl^-}$-ion). Some of the counter-ions are attracted by the fixed charges of the membrane. The remaining counter-ions travel together with the co-ions through the membrane. As the charges of the ions travelling through the membrane balance each other, no electrical net current is generated [25, p. 422]. As a consequence, the effective salt concentration, which is relevant for the salt mass transfer through the membrane, is the same as the concentration of the co-ions $c_\mathrm{S}^\mathrm{M} = c_{\mathrm{Cl}^-}^\mathrm{M}$, see e.g. GEISE ET AL. [54, p. 1705]. Note that a counterexample for a membrane process with electrical net currents would be electrodialysis.

Finally, the following equation results linking the salt concentrations of external solution and membrane, see also [16, p. 792]:

$$\frac{c_\mathrm{S}^{\mathrm{E}2}}{(c_\mathrm{S}^\mathrm{M} + \chi) \cdot c_\mathrm{S}^\mathrm{M}} = \frac{\gamma_\pm^{\mathrm{M}2}}{\gamma_\pm^{\mathrm{E}2}} \cdot \frac{c^{\mathrm{E}2}}{c^{\mathrm{M}2}} \cdot e^{\frac{\bar{V}_\mathrm{S}}{RT} \cdot (p^\mathrm{M} - p^\mathrm{E})} \tag{2.56}$$

$$x_\mathrm{S}^{\mathrm{M}2} + x_\mathrm{S}^\mathrm{M} \cdot \frac{\chi}{c^\mathrm{M}} - \frac{\gamma_\pm^{\mathrm{E}2}}{\gamma_\pm^{\mathrm{M}2}} \cdot x_\mathrm{S}^{\mathrm{E}2} \cdot e^{-\frac{\bar{V}_\mathrm{S}}{RT} \cdot (p^\mathrm{M} - p^\mathrm{E})} = 0 \tag{2.57}$$

Equation (2.57) is a quadratic equation in x_S^M (with $c^\mathrm{M} = \frac{\rho^\mathrm{M}}{\sum x_i^\mathrm{M} \bar{M}_i}$) and can be solved analytically. According to the assumption for the pressure gradient inside the membrane (equation 2.38), the pressure difference at the membrane surface, $p^\mathrm{M} - p^\mathrm{E}$, is assumed to be zero at the feed side and equal to the hydrostatic pressure difference between feed and permeate $p_\mathrm{F} - p_\mathrm{P}$ at the permeate side.

GEISE ET AL. [54, p. 1706] come to the conclusion that the ratio of the activity coefficients outside and inside the membrane $\frac{\gamma_\pm^\mathrm{E}}{\gamma_\pm^\mathrm{M}}$ is the upper limit for the solubility of salt K_S when the salt concentrations in the external solution c_S^E are much higher than the membrane electrical charge density χ:

$$K_\mathrm{S} \rightarrow K_{\mathrm{S},\infty} = \frac{\gamma_\pm^\mathrm{E}}{\gamma_\pm^\mathrm{M}} \text{ for } c_\mathrm{S}^\mathrm{E} >> \chi \tag{2.58}$$

This finding is interesting as this means there is a salinity dependence of the solubility of salt and also a saturation level at salinities much higher than the electrical charge density of the membrane, see GEISE ET AL. [54, fig. 28, p. 1706] for illustration.

2.1.6 Membrane Parameters of the Maxwell-Stefan Model

In table 2.1, a compact overview of the literature review of the Maxwell-Stefan model parameters is presented. Only data relevant for both the modeling approach and the investigated membrane type are included.

The results for the most important membrane model parameters presented in table 2.1 are commented in the following:

- **Maxwell-Stefan diffusivities:** Measurement data for ternary Maxwell-Stefan diffusivities are rare. However, as Maxwell-Stefan diffusivities have a binary meaning [181, p. 19], their values can be estimated by binary Fickian diffusivities data. In the binary case, Maxwell-Stefan and Fickian diffusivities are in the same order of magnitude as long as the thermodynamic correction factor is close to one, see equation (2.33). This can be assumed in our case as the concentration of one component of the binary solution is always low (salt in water, water in membrane, salt in membrane). For the salt-water diffusivity estimate, the results of the Fickian diffusivity experiments summarized in appendix B are used. For the water-membrane and salt-membrane diffusivity estimates, the literature data presented in table 2.1 are taken.
- **Salt solubility**: In 2003, GHUI [59] stated that the salt solubility K_S is independent of concentration for polyamide membranes. He cited STRATHMANN and MICHAELS [163] and FROMMER ET AL. [52]. While STRATHMANN and MICHAELS [163] provide data only for one concentration level w_{NaCl} = 10 g/kg, FROMMER ET AL. [52] present results for w_{NaCl} = 100 g/kg. They mention that two concentration levels were investigated, w_{NaCl} = 10 g/kg and w_{NaCl} = 100 g/kg, but only the latter is presented. There is a difference of one order of magnitude between the data of STRATHMANN and MICHAELS [163] and Frommer et al. [52]. KOROS ET AL. [88] derived $K_S = 0.024$ from the data of STRATHMANN and MICHAELS. $K_S = 0.23$ is the result of FROMMER ET AL. [52]. Therefore, it is difficult to retrace the statement of GHUI [59] about the concentration independence of salt solubility for polyamide membranes. This is to be investigated further in section 6.3.2 of chapter 6.

Table 2.1: Literature review of membrane model parameters.

Parameter	Symbol	Unit	Reference	Method of Reference and Comments	Value of Reference
Maxwell-Stefan Diffusivities					
Salt in water	$\mathfrak{D}_{\mathrm{SW}}$	$\frac{\mathrm{m}^2}{\mathrm{s}}$	N.N.	N.N.	N.N.
Salt in membrane	$\mathfrak{D}_{\mathrm{SM}}$	$\frac{\mathrm{m}^2}{\mathrm{s}}$	N.N.	N.N.	N.N.
Water in membrane	$\mathfrak{D}_{\mathrm{WM}}$	$\frac{\mathrm{m}^2}{\mathrm{s}}$	Scattergood and Lightfoot [148]	Ion-exchange membrane (sulphonated polystyrene imbedded in polytethylene), $T = 25°\mathrm{C}$	$2.02 \cdot 10^{-10} \pm 9\%$
Binary Diffusivities					
Salt in water	D_{SW}	$\frac{\mathrm{m}^2}{\mathrm{s}}$	This study, see appendix B	Digital Finite Fringe Interferometry, $T = 30°\mathrm{C}$, $w_{\mathrm{S}} = 50$ g/kg	$1.6119 \cdot 10^{-9}$
Salt in membrane	D_{SM}	$\frac{\mathrm{m}^2}{\mathrm{s}}$	Koros et al. [88] using data from Strathmann and Michaels [163]	Calculated, $T = 25°\mathrm{C}$	$10.7 \cdot 10^{-14}$
			Frommer et al. [52]	Elution experiment, $T = 30°C$, $w_{\mathrm{S}} = 100$ g/kg	$1.5 \pm 0.3 \cdot 10^{-14}$
			Frommer et al. [52]	Elution experiment, $T = 30°C$, $w_{\mathrm{S}} = 10$ g/kg	$0.8 \pm 0.04 \cdot 10^{-14}$
Water in membrane	D_{WM}	$\frac{\mathrm{m}^2}{\mathrm{s}}$	Koros et al. [88] using data from Strathmann and Michaels [163]	Calculated, $T = 25°\mathrm{C}$	$1.44 \cdot 10^{-10}$
			Frommer et al. [52]	Determination of self-diffusion-coefficient of water (i.e. lower limit for an operation with osmotic flow), Nulcear Magnetic Resonance (NMR), at 25°C	$1.5 \pm 0.3 \cdot 10^{-10}$
			Zhang et al. [185, p. 150]	Membrane type FT30 RO, extrapolating exponential depedency of diffusivity	$8 \cdot 10^{-10}$
Partition Coefficients					
Water	K_{W}	-	Koros et al. [88] using data from Strathmann and Michaels [163]	A vacuum quartz mass sorption spring balance, $T = 25°\mathrm{C}$	0.23
			Frommer et al. [52]	Estimation based on a good guess for the water content in the membrane and the density of the dry polymer	0.49
Salt	K_{S}	–	Koros et al. [88] using data from Strathmann and Michaels [163]	ashing, $T = 25°\mathrm{C}$, $w_{\mathrm{S}} = 10$ g/kg	0.024
			Frommer et al. [52]	Elution experiment, $T = 30°\mathrm{C}$, $w_{\mathrm{S}} = 100$ g/kg	0.23 ± 0.1
Densitites					
Membrane	ρ^{M}	$\frac{\mathrm{kg}}{\mathrm{m}^3}$	Wei et al. [179, fig. 2(A)]	Atomistic molecular dynamic simulation, polyamide membrane	≈ 1.22...1.31
	$\rho^{\mathrm{M}}_{\mathrm{M}}$	$\frac{\mathrm{kg}}{\mathrm{m}^3}$	Zhang et al. [185, p. 147]	Membrane types FT30 RO and LF10	1.24
Polymer	ρ^{PA}	$\frac{\mathrm{kg}}{\mathrm{m}^3}$	Koros et al. [88, p. 386]	N.N.	1.3...1.4
			Mark et al. [106, p. 403]	Dry aromatic polyamide; Frommer et al. [52] refer to this reference	1.39
			Wei et al. [179, p. 6]	Dry polyamide membrane	1.28

Parameter	Symbol	Unit	Reference	Method of Reference and Comments	Value of Reference
Molar Mass					
Membrane	$\bar{M}^{\mathrm{M}}$	$\frac{\mathrm{g}}{\mathrm{mol}}$	N.N.	N.N.	N.N.
Polymer	$\bar{M}_{\mathrm{M}}$	$\frac{\mathrm{g}}{\mathrm{mol}}$	ZHANG ET AL. [185, p. 149]	Membrane type FT30 RO, molar mass of the structural repeating unit of the active layer polymer, calculated from polyamide active layer composition data and group contribution theory (necessary in free volume theory)	642.08
Membrane Charge					
Charge density	χ	$\frac{\mathrm{mol}}{\mathrm{l}}$	CORONELL ET AL. [25],[24]	Membrane type LF10 RO from Nitto Denko, low fouling membrane, fully aromatic polyamide without coating, negatively charged, Rutherford Backscattering Spectrometry	0.23...0.5 for pH = 6.3...10.2
			CORONELL ET AL. [25],[24]	Membrane type FT30 RO from Dow Liquid Separation, fully aromatic polyamide with coating, negatively charged, Rutherford Backscattering Spectrometry	0.11...0.51 for pH = 6.3...10.2
			CORONELL ET AL. [25],[24]	Membrane type TFC-S NF from Koch Membrane Systems, fully aromatic polyamide without coating, negatively charged, Rutherford Backscattering Spectrometry	0.16...0.53 for pH = 6.3...10.2
		$\frac{\mathrm{meq}}{\mathrm{g}}$	DEMISCH AND PUSCH [30]	Membrane type cellulose acetate, negatively charged, method of Heymann and Rabinov.	0.0034
		$\frac{\mathrm{meq}}{\mathrm{g}}$	BAKER [9, p. 400]	Typical concentration of fixed ionic groups in ion exchange membranes	3-4 or more
Thickness					
Active layer	Δl^{M}	nm	CORONELL ET AL. [24, p. 6810]	Membrane type LF10 RO from Nitto Denko, low fouling membrane, fully aromatic polyamide without coating, negatively charged, Rutherford Backscattering Spectrometry	$116, \sigma = \pm 55$
			CORONELL ET AL. [24, p. 6810]	Membrane type FT30 RO from Dow Liquid Separation, fully aromatic polyamide with coating, negatively charged, Rutherford Backscattering Spectrometry	$120, \sigma = \pm 47$
			MELIN AND RAUTENBACH [109, p. 40]		≈ 30
			RIGWAY ET AL. [138, p. 7]	Conclusion of RIGWAY ET AL.: Rough peaks (protuberances) in active layer visualized by transmission electron microscopy (TEM) and atomic force microscopy (AFM) are an indicator for the polyamide thickness, relevant for solute partitioning, to be much thinner than previously assumed	$5 - 10$

- **Water solubility**: STRATHMANN and MICHAELS [163] and Frommer et al. [52] provide also data for the water solubility K_W. The data of STRATHMANN and MICHAELS [163] are based on experiments with a vacuum quartz mass sorption spring balance, while the data of FROMMER ET AL. [52] are more an estimate.

- **Electrical charge density**: In recent years, researchers from University of Illinois published data about electrical charge density of TFC membranes: In 2010, CORONELL ET AL. [24] investigated six RO/NF membranes employing Rutherford backscattering spectrometry (RBS). Five of them had fully aromatic polyamide active layers. One of them was a coated low fouling brackish water RO membrane very similar to the membrane investigated in the present work. The concentration of the measured negative membrane charges caused by the carboxylic functional groups (R-COOH/R-COO$^-$) is very similar for all fully aromatic polyamide membrane types [24, tab. 1]. There was no significant difference between BW/SW membranes or RO/NF membranes [24, tab. 1]. This allows to assume that the electrical charge density of the membrane investigated in the present study might have similar values. In figure 2.11, data for a brackish water low fouling RO membrane are shown.

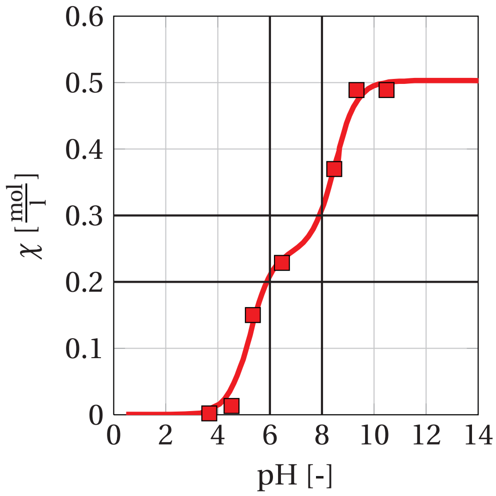

Figure 2.11: Electrical charge density as a function of pH-value for a fully aromatic polyamide low fouling RO membrane (LF10 from Nitto Denko). Data extracted from CORONELL ET AL. [24, fig. 1a].

It can be seen that the negative membrane charge density significantly depends on the pH-value. It ranges between 0.23 and 0.31 $\frac{\text{mol}}{\text{l}}$ at pH-values of 6.3 and 8, respectively. Note that the pH-value was approximately 7.1 in the experiments of the present study, see appendix B.

In 1976, DEMISCH and PUSCH [30] determined the electrical charge density of CA membranes. With a value of 0.0034 $\frac{\text{meq}}{\text{g}}$ ($1\frac{\text{meq}}{\text{g}} \approx 1\frac{\text{mol}}{\text{l}}$) the electrical charge density of CA membranes is two orders of magnitudes lower than the one of PA membranes. This might explain why charge effects where not taken into account during the development of the SDM model.

- **Thin-film active layer thickness**: The order of magnitude of the thin-film active layer thickness is known from reference-books like MELIN and RAUTENBACH [109, p. 40]. In a comprehensive study with the Rutherford Backscattering Spectrometry method, CORONELL ET AL. [24] determined the thickness of the thin-film active layer. They observed a high standard deviation of the results. For example, the average thickness of their low fouling membrane was $\Delta l^{\text{M}} = 116$ nm with $\sigma = \pm 55$ nm.

- **Membrane density**: The total membrane density ρ^{M} in the SDM is usually approximated by the external solution density. While various references give values for the dry polyamide density ρ^{PA} ranging within ρ^{PA} =1.28 and 1.4 $\frac{\text{kg}}{\text{m}^3}$ [163, 179], the solution density of the wet membrane ρ^{M} might be slightly lower, which is in agreement with the findings of WEI ET AL. [179]. To account for the influence of temperature and salinity on the solution density it will be avoided to assume a constant membrane solution density later in section 6.3.2. Instead, the ratio of the between the solution density of the external solution and the membrane will be used.

- **Molar mass**: The molar mass of a cross-linked polymer is hardly known. PAUL emphasizes that the molecular weight is theoretically even infinite due to the cross-linking [127, p. 375]. ZHANG ET AL. provide a value for molar mass of the "structural repeating unit of the polymer" [185] of a FT30 RO membrane. It is $\bar{M}_{\text{M}} = 642.08\frac{\text{g}}{\text{mol}}$. Data for the investigated TML10D [174] membrane were not found. The result of ZHANG ET AL. will be used later in section 6.3.2 to set an upper constraint for $K_{\text{W},\gamma} = \frac{1}{\gamma_{\text{W}}^{\text{M}}}$.

2.2 Concentration Boundary Layers

After the introduction of membrane transport the focus will be drawn to concentration boundary layers in the following.

The knowledge of the salt concentration at the membrane surface is essential for the description of transport phenomena in the membrane. The purpose of the RO membrane is to separate different substances from each other. In desalination, these are water and salt. As described in section 2.1, a positive net driving pressure results in a diffusive flux of permeate through the membrane along the pressure gradient. On the high pressure side, the permeate flux induces a convective transport of species from bulk region of the surrounding fluid towards the membrane [135, p. 77]. Due to the separation characteristics of the RO membrane, mainly salt is rejected at the membrane surface [135, p. 77]. Therefore the salt mass fraction at the membrane is higher than in the bulk region resulting in a diffusive back transport of salt from the membrane surface to the bulk [135, p. 77]. In steady-state, the diffusive and the convective force balance each other [135, p. 77]. A characteristic concentration profile, the so-called concentration boundary layer, develops from the membrane to the bulk region as illustrated in figure 2.12. Note that membrane transport theory in section 2.1 is based on a z-axis oriented in permeate flow direction to obtain positive permeate fluxes. Starting with boundary layer theory, the z-axis is turned in the following part of the thesis.

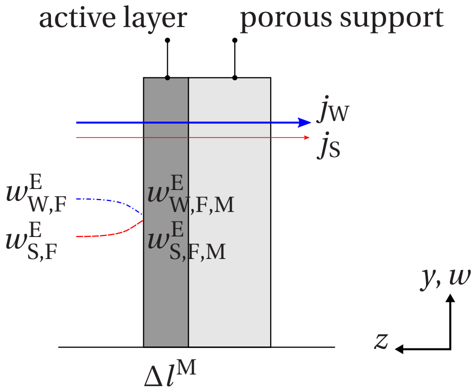

Figure 2.12: Concentration boundary layer for water and salt. Adapted from [135, fig. 3].

The concentration boundary layer adjacent to an RO membrane depends on flow regime, fluid properties, temperature, bulk concentration and pressure on both sides of the membrane as well as the material properties of the membrane. The dependence of the boundary layer on these influencing parameters will be exploited in this study to determine the mass transfer properties of the membrane.

In the following section, the film theory for modeling boundary layers is briefly explained. This allows a short introduction of the main model parameters which characterize boundary layers. The assumptions of the film model are also the basis of the LMPM, which is presented afterwards. Before the present chapter concludes with a recommendation for optical methods for boundary layer measurements, necessary fundamentals on optics are introduced.

2.2.1 Film Theory

According to MERSMANN [110, p. 91], the film theory was originally developed by LEWIS and WHITMAN [99] investigating principles of gas absorption in 1924. In RO desalination this model is often applied [109, 135].

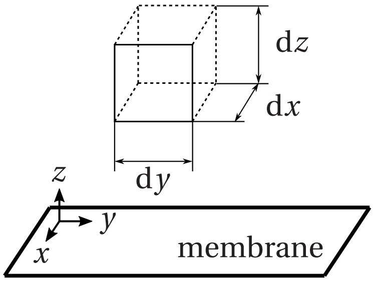

Figure 2.13: Finite volume element for salt mass balance.

The mathematical derivation of the film model [135, p. 78] starts with a salt mass balance for a finite volume in the fluid outside the membrane (figure 2.13):

$$\frac{\partial \rho_S}{\partial t} = -\nabla \cdot (\rho_S \cdot \mathbf{u}) + \nabla(\rho D_{SW} \nabla w_S) + r_S \tag{2.59}$$

ρ_S is the mass concentration of salt. $\mathbf{u}$ is the velocity vector of the volume element. For the diffusive mass transport, Fickian diffusion with diffusivity D_SW is assumed. r_S represents a source term for chemical reactions. Note that the superscript E is omitted in this section as it is clear that the external solution is considered.

The following assumptions are made for the film model [135, p. 79]:

1. Steady-state: $\frac{\partial}{\partial t} = 0$, $j_\mathrm{P} = \text{const.} = u_\mathrm{P}\rho_\mathrm{P}$
2. Comparing concentration gradients orthogonal and parallel to the membrane, the latter ones can be neglected, $\frac{\partial}{\partial x} << \frac{\partial}{\partial z}$ and $\frac{\partial}{\partial y} << \frac{\partial}{\partial z}$.
3. No source term: $r_\mathrm{S} = 0$
4. Fickian diffusion.
5. Permeate flux equals net mass transfer in z-direction: $j_\mathrm{P} = -\rho(z)u_z(z) = u_\mathrm{P}\rho_\mathrm{P}$
6. Constant density and diffusivity.

Taking assumptions (1) to (5) into account, equation (2.59) turns into:

$$0 = -\frac{\partial}{\partial z}(\rho_\mathrm{S}(z)u_z(z)) + \frac{\partial}{\partial z}(\rho(z)D_\mathrm{SW}(z)\frac{\partial w_\mathrm{S}}{\partial z}(z)) \tag{2.60}$$

Integrating equation 2.60, leads to:

$$0 = -w_\mathrm{S}(z)\underbrace{\rho(z)u_z(z)}_{-j_\mathrm{P}} + \rho(z)D_\mathrm{SW}(z)\frac{\partial w_\mathrm{S}}{\partial z}(z) + C \tag{2.61}$$

Due to steady-state and the reduction of the 3D problem to a 1D problem, we can proceeded with absolute differentials.

With a salt balance across the membrane, the following is obtained:

$$0 = -w_\mathrm{S}(z)\underbrace{\rho(z)u_z(z)}_{-j_\mathrm{P}} + \rho(z)D_\mathrm{SW}(z)\frac{\mathrm{d}w_\mathrm{S}}{\mathrm{d}z}(z) + \underbrace{C}_{-j_\mathrm{S,P}=-w_\mathrm{S,P}j_\mathrm{P}} \tag{2.62}$$

$$j_{\mathrm{P}}(w_{\mathrm{S}}(z) - w_{\mathrm{S,P}}) = -\rho(z) D_{\mathrm{SW}}(z) \frac{\mathrm{d}w_{\mathrm{S}}}{\mathrm{d}z}(z) \tag{2.63}$$

Note that a rearranged version of equation (2.63) with $z = 0$ mm will become relevant for the membrane boundary condition in the CFD model, discussed later in section 3.1.4:

$$\frac{u_z(0)}{D_{\mathrm{SW}}(0)}(w_{\mathrm{S}}(0) - w_{\mathrm{S,P}}) = \frac{\mathrm{d}w_{\mathrm{S}}}{\mathrm{d}z}(0) \tag{2.64}$$

To obtain the film model equation, equation (2.63) is integrated from the membrane surface to the distance z:

$$\int_{w_{\mathrm{S,M}}}^{w_{\mathrm{S}}(z)} \frac{1}{w_{\mathrm{S}}(z) - w_{\mathrm{S,P}}} \mathrm{d}w_{\mathrm{S}}(z) = -j_{\mathrm{P}} \int_0^z \frac{1}{\rho(z) D_{\mathrm{SW}}(z)} \mathrm{d}z \tag{2.65}$$

$$\frac{w_{\mathrm{S}}(z) - w_{\mathrm{S,P}}}{w_{\mathrm{S,M}} - w_{\mathrm{S,P}}} = e^{-j_{\mathrm{P}} \cdot \int_0^z \frac{\mathrm{d}z}{\rho(z) D_{\mathrm{SW}}(z)}} \tag{2.66}$$

For constant density and diffusivity (assumption (6)), an evaluation of equation (2.66) at the transition of the concentration boundary layer to the bulk $z = \delta_{\mathrm{C}}$ results in:

$$\frac{w_{\mathrm{S},\delta_{\mathrm{C}}} - w_{\mathrm{S,P}}}{w_{\mathrm{S,F,M}} - w_{\mathrm{S,P}}} = e^{-\frac{j_{\mathrm{P}}}{\rho} \cdot \frac{\delta_{\mathrm{C}}}{D_{\mathrm{SW}}}} \tag{2.67}$$

The ratio $\frac{D_{\mathrm{SW}}}{\delta_{\mathrm{C}}}$ can be substituted by the mass transport coefficient β (for vanishing flux) [135, p. 80]. With this definition, the exponent of the e-function in equation (2.67) can be expressed in dimensionless form by means of two main parameters, the Sherwood and the Peclet number:

$$\frac{w_{\mathrm{S},\delta_{\mathrm{C}}} - w_{\mathrm{S,P}}}{w_{\mathrm{S,M}} - w_{\mathrm{S,P}}} = e^{-\frac{\mathrm{Pe}}{\mathrm{Sh}}} \tag{2.68}$$

A good overview of Sh-correlations relevant for RO applications is provided by GERALDES and ALFONSO [57], as mentioned already in section 1.1.

Based on this introduction of the film theory, the LMPM is developed in the following section.

2.2.2 Local Membrane Parameter Method (LMPM)

Looking at the set of equations (2.60) to (2.63) from a different perspective, a method can be developed to determine local transport parameters (j_P and $w_\mathrm{S,P}$) from the boundary layer shape.

The assumptions (1) to (5) listed on page 47, which are necessary for the film model, are assumed to be valid also in this section.

Equation (2.60) can be rewritten as follows:

$$0 = -\frac{\mathrm{d}\rho_\mathrm{S}}{\mathrm{d}z}u_z - \rho_\mathrm{S}\frac{\mathrm{d}u_z}{\mathrm{d}z} + \frac{\mathrm{d}\rho}{\mathrm{d}z}D_\mathrm{SW}\frac{\mathrm{d}w_\mathrm{S}}{\mathrm{d}z} + \rho\,\frac{\mathrm{d}D_\mathrm{SW}}{\mathrm{d}z}\frac{\mathrm{d}w_\mathrm{S}}{\mathrm{d}z} + \rho D_\mathrm{SW}\frac{\mathrm{d}^2 w_\mathrm{S}}{\mathrm{d}z^2} \tag{2.69}$$

With assumption (5) and some algebra, the following equation is obtained:

$$j_\mathrm{P} = -\underbrace{\rho(z)}_{0.}\,D_\mathrm{SW}(z)\cdot\left(\underbrace{\frac{1}{\rho(z)}\frac{\mathrm{d}\rho}{\mathrm{d}z}(z)}_{1.} + \frac{1}{D_\mathrm{SW}(z)}\frac{\mathrm{d}D_\mathrm{SW}}{\mathrm{d}z}(z) + \underbrace{\frac{1}{\frac{\mathrm{d}w_\mathrm{S}}{\mathrm{d}z}(z)}\frac{\mathrm{d}^2 w_\mathrm{S}}{\mathrm{d}z^2}(z)}_{2.}\right) \tag{2.70}$$

Note that equation (2.70) looks slightly different from the one presented in [91]. Equation (2.70) is derived without the restricting assumption on the dependence of the solution density ρ on the salt mass fraction w_S.

Looking at equation (2.70) and neglecting the term with the diffusivity derivative (discussed later in section 3.2), the dependence of the permeate flux on the boundary layer shape becomes visible. The *boundary layer shape* is represented by the zeroth (0.) and first (1.) order derivative of density and second (2.) order derivative of the salt mass fraction. Equation (2.70) is of utmost importance for the present thesis: It is not only an equation for the determination of a local permeate flux but it contains also a recommendation for the optical methods to be applied in this thesis (section 2.2.4).

Rearranging equation (2.63) provides an expression for the permeate salt mass fraction:

$$w_\mathrm{S,P} = w_\mathrm{S}(z) + \frac{\rho(z)D_\mathrm{SW}(z)}{j_\mathrm{P}}\frac{\mathrm{d}w_\mathrm{S}}{\mathrm{d}z}(z) \tag{2.71}$$

The combination of the two local mass transport equations (2.70) and (2.71) with the ones for water and salt flux of RO membranes (2.19) and (2.21) allows the determination of local membrane parameters like A and B, see equation (2.20) and (2.22).

The proposed LMPM is used in the present study to determine local measurement data for transport (j_P and $w_\mathrm{S,P}$) and membrane (A and B) parameters.

2.2.3 Optical Measurement Methods

In order to be able to understand which optical measurement methods are well suited for the LMPM, a brief introduction of optical fundamentals is necessary. The introduction of the theory will be specifically tailored to the boundary characterization problem of this study.

2.2.3.1 Light Propagation through a Refractive Index Gradient Medium

Figure 2.14 illustrates the cross-section of a spacer-free, rectangular channel with a membrane. An aqueous NaCl solution flows along the membrane in negative y-direction. Permeate diffuses through the membrane in negative

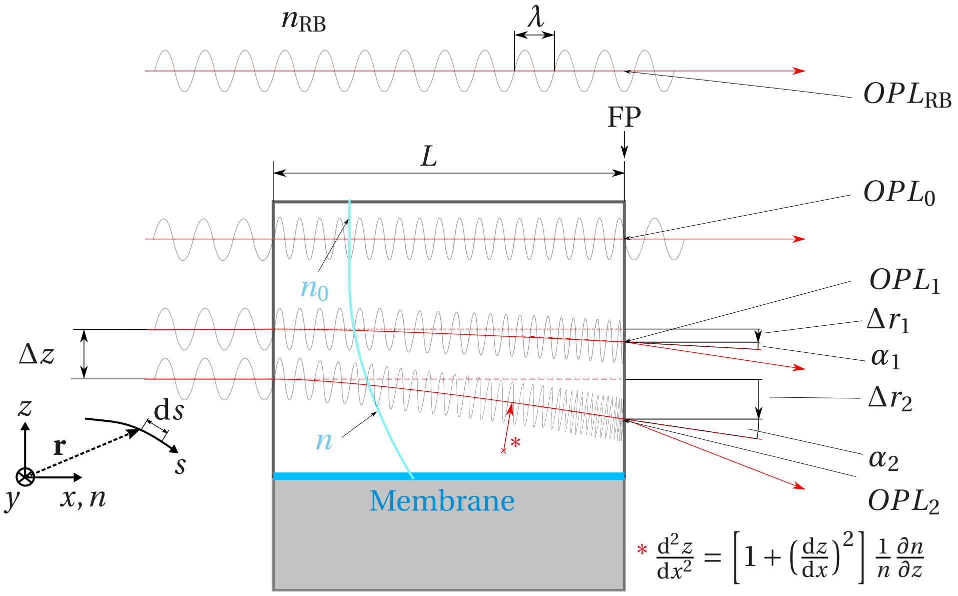

Figure 2.14: Basic principle of light propagation through a medium with a refractive index gradient in a membrane test cell.

z-direction, while a concentration boundary layer profile develops in positive z-direction resulting in the refractive index profile n. Normal to the refractive index gradient of the boundary layer light rays enter the channel in positive x-direction. The rays face a deflection towards the membrane as the direction of the refractive index gradient points in negative z-direction. The ray path through an inhomogeneous medium can be described as follows [180, p. 3]:

$$\frac{\mathrm{d}}{\mathrm{d}s}\left(n\frac{\mathrm{d}\mathbf{r}}{\mathrm{d}s}\right)=\nabla n \tag{2.72}$$

s denotes the ray coordinate (see figure 2.14). $\mathbf{r}$ is the position vector of the ray in Cartesian coordinates (x,y,z). $\mathrm{d}s$ is the infinitesimal change of the ray path and can be expressed in cartesian coordinates by

$$\mathrm{d}s=\sqrt{\mathrm{d}x^2+\mathrm{d}y^2+\mathrm{d}z^2}=\sqrt{1+\left(\frac{\mathrm{d}y}{\mathrm{d}x}\right)^2+\left(\frac{\mathrm{d}z}{\mathrm{d}x}\right)^2}\,\mathrm{d}x, \tag{2.73}$$

which turns equation (2.72) into [180, p. 8]:

$$\frac{\mathrm{d}^2z}{\mathrm{d}x^2}=\left[1+\left(\frac{\mathrm{d}y}{\mathrm{d}x}\right)^2+\left(\frac{\mathrm{d}z}{\mathrm{d}x}\right)^2\right]\left[\frac{1}{n}\frac{\partial n}{\partial z}-\frac{\mathrm{d}z}{\mathrm{d}x}\frac{1}{n}\frac{\partial n}{\partial x}\right] \tag{2.74}$$

Like in film theory (section 2.2.1), it is assumed that refractive index gradients parallel to the membrane are negligible compared to the orthogonal ones ($\frac{\partial n}{\partial x} << \frac{\partial n}{\partial z}$ and $\frac{\partial n}{\partial y} << \frac{\partial n}{\partial z}$). Therefore, the influence of the refractive index gradient on the ray path in cross-flow direction y is small, i.e. the slope of the ray $\frac{\mathrm{d}y}{\mathrm{d}x}$ in this direction becomes negligible. Light deflection in the direction orthogonal to the membrane can become significant in the present study. But the measured ray angles $\frac{\mathrm{d}z}{\mathrm{d}x}$ are always smaller than unity. Thus the term $\frac{\mathrm{d}z}{\mathrm{d}x}\frac{1}{n}\frac{\partial n}{\partial x}$ is negligible as well. With these assumptions, equation (2.74) reduces to:

$$\frac{\mathrm{d}^2z}{\mathrm{d}x^2}=\left[1+\left(\frac{\mathrm{d}z}{\mathrm{d}x}\right)^2\right]\frac{1}{n}\frac{\partial n}{\partial z} \tag{2.75}$$

Equation (2.75) is integrated in the optical ray tracing model presented later in chapter 4. In literature about boundary layer characterization by means of optical methods, a further simplified version of equation (2.74) is often found, neglecting the term $\left(\frac{\mathrm{d}z}{\mathrm{d}x}\right)^2$, see e.g. [36, p. 201] , [66, p. 34] or [112, p. 125]. In these cases, light deflections in z-direction are assumed to be negligibly small in general.

When light is not modeled via geometric but wave optics, electromagnetic waves are to propagate through the medium, instead of rays. The ray coordinate s denotes then the direction of the normal of a wave front and the refractive index manipulates the wavelength λ. What is conserved during propagation is the energy of the wave $E = hf$ [67, p. 12]. As Planck's quantum of action h is a constant, the frequency of the wave f is constant as well. The frequency of the light can be expressed as a function of the speed of light c and its wavelength λ:

$$f = \frac{c}{\lambda} = \frac{c_0}{n\lambda} \tag{2.76}$$

The refractive index relates the actual speed of light in the medium c to its constant speed in vacuum c_0. To maintain a constant frequency f, the dominator $n\lambda$ in equation (2.76) must not change as well i.e. in a medium with higher refractive index the wavelength is reduced. The integral of the refractive index along the ray path is called optical path length $OPL = \int n(s)\mathrm{d}s$.

2.2.3.2 Interferometry

Interferometry aims to measure the differences of optical path lengths. It contains the information of the phase ϕ of the electromagnetic wave:

$$OPL = \frac{\phi}{2\pi}\lambda \tag{2.77}$$

When two electromagnetic waves are superimposed, the amplitude a of the resulting new wave depends on the intensities of the two waves and on the difference of their phases [152, p. 8] as well. The light intensity I is a measure of its wave amplitude, $I = |a|^2$ [152, p. 7], and can be visualized on a screen or digitally recorded via a camera chip. The maximum intensity is reached when two waves which are in phase interfere, i.e. when their phases differ only in integer multiples of 2π, known as constructive inference. In case of the boundary layer experiment in figure 2.14, multiple intensity maxima may be observed when the reference beam with subscript RB in figure 2.14 interferes with the object beam with subscripts $i = 0, 1, 2...$, which propagated through the refractive index gradient field. The difference between two neighbouring intensity maxima corresponds to the fixed optical path length difference:

$$\Delta OPL = OPL_{i+1} - OPL_i = \lambda \tag{2.78}$$

Let us assume that the geometric path of both beams $GPL = \int \mathrm{d}s$ is identical. Moreover, the reference beam may propagates in the same medium, except from the boundary layer test section (length L). Then, the difference between the neighbouring intensity maxima stands also for a fixed refractive index difference:

$$\Delta n = n_{i+1} - n_i = \frac{\lambda}{L} \tag{2.79}$$

The goal of an Interferometry experiment is to relate the intensity variations in the recorded image caused by such differences in the optical path length ΔOPL or the refractive index Δn unambiguously to the optical phenomenon of interest. This means that Interferometry aims to directly measure the refractive index. However, the difference in the optical path length $\Delta OPL = OPL_i - OPL_{\mathrm{RB}}$ contains the information about any difference between reference and object beam. In case of the present study, this difference is not only caused by the boundary layer but also by test cell components like glass windows. The target measurement quantity is $\Delta OPL = OPL_i - OPL_0$ or, to be more specific, $\Delta n = n_i - n_0$. To eliminate the difference between the reference beam and the beam representing the state without boundary layer, different interferometer types can be an option. The Mach-Zehnder-Interferometer setup needs an exact duplicate of the test section in the path of the reference beam path so that OPL_{RB} turns into OPL_0, compare e.g. MERZKIRCH [112][p. 164, fig. 3.30]. Holographic Interferometry is another option which requires two records called holograms, one of the test section with and one without the boundary layer. The two holograms are superimposed, i.e. interferred, afterwards. Via substraction of the phases and thus the optical length information in the respective hologram, the measured quantity is then the desired one: $\Delta OPL = OPL_i - OPL_{\mathrm{RB}} - (OPL_0 - OPL_{\mathrm{RB}}) = OPL_i - OPL_0$. Digital Holographic Interferometry has been applied in preliminary experiments, compare KROISS ET AL. [90]. However, process inherent, unavoidable vibrations of the RO test section make it difficult to record two holograms at exactly the same state. In the present study, a Finite Fringe Interferometry approach is applied in combination with a Fourier Transform method according to TAKEDA ET AL. [165]. In Infinite Fringe Interferometry, reference RB and object beam OB are aligned such that a uniform intensity distribution results in the reference image which is recorded without a boundary layer present. This means the phase difference between both beams is constant across the overall image. In contrast, in Finite Fringe Interferometry a constant fringe pattern is introduced already in the reference image [80, fig. 16]. For illustration see figure 5.2 on page 111, which shows a Finite Fringe raw image of a concentration boundary layer measurement. More details on the interferometry setup and evaluation algorithms will be provided later in chapter 5.

2.2.3.3 Schlieren

For the introduction of the Schlieren method, the assumption of ray optics is sufficient. In figures 2.14 and 2.15, the most important quantities described in the following are included.

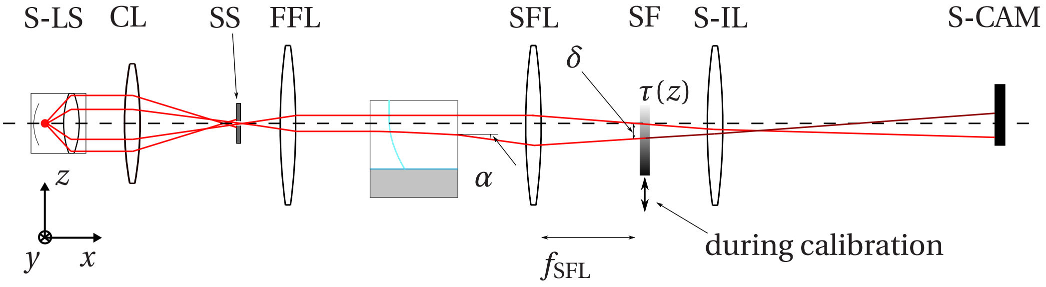

Legend:
Schliere S, Light Source LS, Condenser Lens CL, Source Slit SS, First Field Lens FFL
Second Field Lens SFL, Schlieren Filter SF, Imaging Lens IL, Camera CAM

Figure 2.15: Scheme of a Schlieren setup.

The term Schliere denotes a refractive index gradient. In the present study, this gradient is caused by the concentration boundary layer. The measurement quantity is the ray angle α in the end of the test section where the focal plane FP of the Schieren optics is set, see figure 2.14. It can be directly derived from the ray path equation (2.75):

$$\alpha = \arctan\frac{\mathrm{d}z}{\mathrm{d}x} \approx \frac{\mathrm{d}z}{\mathrm{d}x} = \int_0^L \left(\frac{\mathrm{d}^2 z}{\mathrm{d}x^2}\right)\mathrm{d}x = \int_0^L \left[1 + \underbrace{\left(\frac{\mathrm{d}z}{\mathrm{d}x}\right)^2}_{\ll 1}\right] \underbrace{\frac{1}{n}\frac{\partial n}{\partial z}}_{\approx \text{const.}} \mathrm{d}x \approx \frac{1}{n}\frac{\partial n}{\partial z} L \quad (2.80)$$

Equation (2.80) shows how the Schlieren measurement is related to the first derivative of the refractive index. The assumptions inherent in equation (2.80) are the basis for many Schlieren evaluation algorithms, compare e.g. [66, p. 34] or [155, p. 27]. Subsequently, the term *classical Schlieren* is used when these assumptions apply: As ray deflection in z-direction within the Schliere is assumed to be negligibly small ($|\frac{\mathrm{d}z}{\mathrm{d}x}| << 1$), a small angle approximation can be applied and the squared value $\left(\frac{\mathrm{d}z}{\mathrm{d}x}\right)^2$ can be entirely neglected. For the same reason, it is can be assumed that the term $\frac{1}{n}\frac{\partial n}{\partial z}$ is constant along the ray path. In the present study, refractive index gradients are called *weak* when the influence of ray deflection on the measured quantity is negligible. Otherwise refractive index gradients are *strong*.

The ray angle α is measured as follows: After the Schliere, a condensing lens is positioned, see figure 2.15. Parallel light not obstructed by the Schliere is focussed on the focal point behind the lens SFL in distance of the focal length f_{SFL}. At this position, non-parallel obstructed rays do not pass the focal point of the lens. A ray shift δ in z-direction results, which can be measured by means of a so-called Schlieren filter SF. In the present study, this filter has a transmittance $\tau(z)$ with a continuous transmittance gradient in z-direction. The filter is positioned normal to the optical axis in distance f_{SFL} after the lens SFL. The intensity of the light ray is attenuated by the filter depending on δ. To obtain a correlation between light intensity and deflection, a calibration step is necessary before the actual measurement. During calibration, images are recorded for different z-positions of the filter while no boundary layer is present. During measurements, the filter position is fixed but the rays might be deflected depending on the refractive index gradient in the test cell. With the correlation between image intensity and Schlieren filter, δ can be determined. For known properties of the optical components and media between Schliere and Schlieren filter, α can be derived from δ.

2.2.3.4 Shadowgraphy

For Shadowgraphy experiments, the Schlieren filter SF is omitted in the setup shown in figure 2.15. This results in a loss of information as the angle α_i cannot be quantified anymore. What is left for quantification is the ray deflection Δr_i as shown in figure 2.14. A brief example is given of how the measurement works in principle in the following.

Light intensity I quantifies power of light per unit area. In the 1D sketch in figure 2.14, the area is represented by Δz. The power of light is represented by the two rays framing Δz. After the test section, these two rays are distributed over a larger area $\Delta z + \Delta r_2 - \Delta r_1$. As the power of light does not change, light intensity decreases from I_0 to I_1 along the test section. Assuming that the relative intensity change is equal to the relative area change [36, p. 204], it can be estimated as follows:

$$\frac{\Delta I}{I_\text{o}} = \frac{\Delta r_2 - \Delta r_1}{\Delta z} \approx \frac{\alpha_2 \cdot L - \alpha_1 \cdot L}{\Delta z} = \frac{\Delta \alpha}{\Delta z} \cdot L \tag{2.81}$$

$$\frac{\Delta \alpha}{\Delta z} \cdot L \rightarrow \frac{\mathrm{d}\alpha}{\mathrm{d}z} \cdot L \approx \frac{\mathrm{d}}{\mathrm{d}z}\left(\frac{1}{n}\frac{\partial n}{\partial z} L\right) \cdot L \tag{2.82}$$

Equations (2.81) and (2.82) contain the following two assumptions:

1. The shift Δr_i of can be approximated by the angles α_i and the length of the test section L:
$$\Delta r_i = \int_0^L \alpha_i(x)\mathrm{d}x \approx \alpha_i(L) \cdot L \tag{2.83}$$
2. Equation (2.80) can be used to substitute α_i. By means of these two assumptions, the connection between the second derivative of the refractive index and the actual measured quantity $\frac{\Delta I}{I_0}$ of the Shadowgraphy method becomes visible.

However, in this work these two restrictive assumptions are avoided for the evaluation of Shadowgraphy measurements. In contrast to classical Shadowgraphy (see ECKELMANN [36]), the focal plane FP of the Shadowgraphy optics will be identical with the one of the Schlieren optics as depicted in figure 2.14.

If ray deflection were negligible, no intensity changes could be measured in this way. In the present study, the actual unwanted effect of significant ray deflection within the test section, subsequently called *the fanning effect*, will be used to quantify strong refractive index gradients. In this case, Shadowgraphy can be applied as quantitative measurement but needs an advanced evaluation method like optical ray tracing, which is introduced later in chapter 4.

2.2.3.5 Summary

In this brief introduction of Interferometry, Schlieren and Shadowgraphy, it was explained that they stand for the measurement of the zeroth, first and second order of the refractive index gradient. This is the link to the equations underlying the LMPM (2.70) and (2.71), which will be outlined in more detail in the next section.

2.2.4 The Link between Boundary Layer Theory and Optical Methods

In section 1.1, the general suitability of optical methods for the non-invasive characterization of boundary layers was described. Equations (2.70) and (2.71) allow a more detailed specification of the optical methods for an application in the present study.

The target measurement quantity of the optical methods is the refractive index. It is sensitive to both salt mass fraction and temperature. For the investigated aqueous NaCl solution, there is a linear dependence of the refractive index n on the salt mass fraction w_S, see equation (B.1) on page 160. In addition, for each wavelength of light λ, the refractive index n and solution density ρ of component i are coupled by molecular refractivity N and molar mass $\bar{M}$ in the Lorentz-Lorenz equation [66, p. 217]:

$$N_{i,\lambda} = \frac{n_{i,\lambda}^2 - 1}{n_{i,\lambda}^2 + 2} \frac{\bar{M}_i}{\rho_i} \tag{2.84}$$

As a consequence, the three previously highlighted terms of equation (2.70) can be linked to refractive index substitutes, as indicated in figure 2.16. The three optical methods presented above can be related to to these terms based on the zeroth, first and second refractive index gradient [35].

$$\begin{array}{llcll}
\rho(z) & \propto & n(z) & \rightarrow & \text{Interferometry} \\
\frac{1}{\rho(z)}\frac{\mathrm{d}\rho}{\mathrm{d}z}(z) & \propto & \frac{1}{n(z)}\frac{\mathrm{d}n}{\mathrm{d}z}(z) & \rightarrow & \text{Schlieren} \\
\frac{1}{\frac{\mathrm{d}w_\mathrm{S}}{\mathrm{d}z}(z)}\frac{\mathrm{d}^2 w_\mathrm{S}}{\mathrm{d}z^2} & \propto & \frac{\mathrm{d}}{\mathrm{d}z}\left(\frac{1}{n(z)}\frac{\mathrm{d}n}{\mathrm{d}z}(z)\right) & \rightarrow & \text{Shadowgraphy}
\end{array}$$

Figure 2.16: Link between film theory and optical methods.

In theory, one of the three method seems to be sufficient to measure either the zeroth, first or second derivative of the refractive index. The other two quantities could be calculated. However, thinking about measurement noise and possible error propagation during integration or derivation of a noisy measurement signal, the coupling of these three optical methods will be beneficial.

Error propagation is not only an issue for the determination of the terms of equation (2.70). The determination of the permeate salt mass fraction $w_{\mathrm{S,P}}$ (equation (2.71)) depends itself on an accurate value for the permeate flux j_P which is the outcome of equation (2.70). In turn, accurate data for $w_{\mathrm{S,P}}$ and j_P are the basis for the correct calculation of the water and salt permeability constants. Therefore, it is necessary that also the fluid properties, which are direct input parameters to equations (2.70) and (2.71), are precisely known. Thus, it was decided to experimentally determine density ρ and diffusivity D_{SW} of the aqueous NaCl solution deployed in this study. Their dependence on salt mass fraction w_S and temperature T is important as it is the link to the actual measurement quantity, the refractive index n. In appendix B, the results of the experimental analyses of these fluid properties $(\rho, D_{\mathrm{SW}}, n)$ are briefly summarized.

The choice of the three optical methods to determine the parameters of equations (2.70) and (2.71) introduce also limitations to the LMPM. Theoretically, the term *local* could mean one spot on the membrane. Practically, the optical methods will provide a line-of-sight averaged result defined by the path length of light within the membrane test cell, as described by means of figure 2.14.

In the end, the question about the achievable accuracy of the LMPM needs to be addressed . This will be investigated in more detail in the following chapter 3.

3 Method Development with Computational Fluid Dynamics (CFD)

In the following chapter, the LMPM is analyzed and further developed by means of Computational Fluid Dynamics (CFD). First of all, the CFD model is described. Second, the model is used to perform a proof of concept study for the LMPM. At the end of this chapter, a revision of the LMPM is presented describing how the CFD model will be integrated in the revised LMPM.

3.1 CFD Modeling

First, the high pressure membrane test cell design is described (section 3.1.1) before geometry and mesh of the modeled fluid domain are derived (section 3.1.2). The OpenFOAM solver is outline afterwards. Subsequently, a description of boundary conditions and applied thermo-physical properties is provided.

3.1.1 Design of the Membrane Test Cell

The membrane test cell is designed to optically access the concentration boundary layer on the feed side of a horizontally aligned flat sheet membrane in a spacer-free rectangular channel. In figure 3.1(a), an illustrative overview of the assembled test cell is given. Note that geometrical dimensions relevant for CFD modeling will be provided later in section 3.1.2. The test cell consists of a permeate channel module on the bottom of the membrane, a feed channel module on the top of the membrane and two side lids. Each side lid has three glass windows for optical access. Two of these glass windows are made of replaceable step glasses with external flanges for mounting. The third glass window is permanently glued in the pocked of the side lid. To have proper optical access normal to a uniformly flat membrane surface, the membrane is tightened with fixing rods on the vertical walls of the permeate channel module as shown in the cross-sectional view of the text cell in figure 3.1(b).

Only below the horizontally aligned part of the membrane a permeate spacer is put, which is taken from the same RO module as the membrane itself. Therefore, during test cell operation only the horizontal part of the membrane sheet can face a hydrostatic pressure difference. This design was inspired by the work of Mahlab et al. [105].

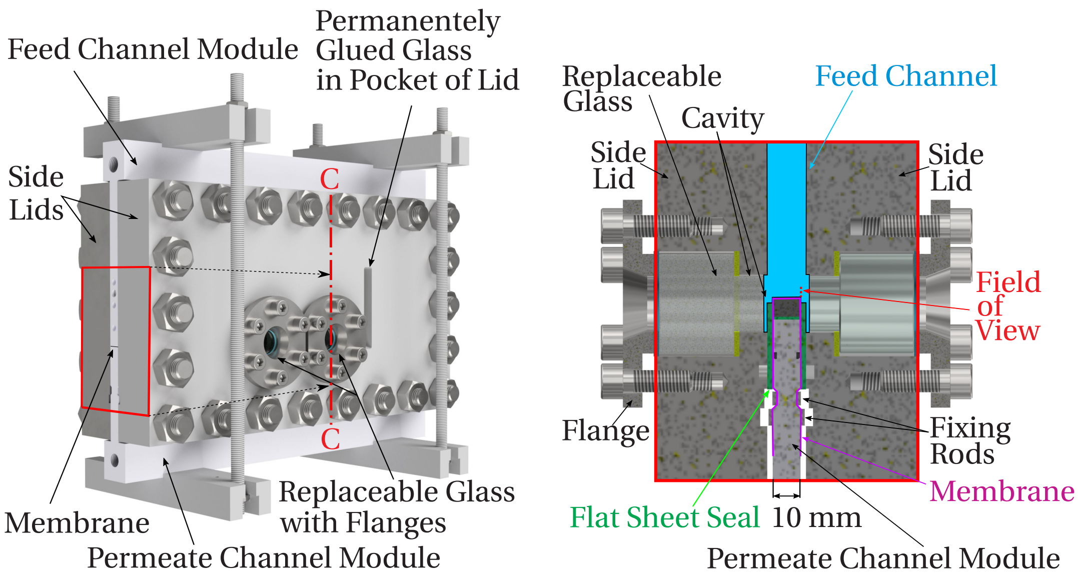

(a) Developed test cell with optical accesses.

(b) Cross section at measurement position C-C.

Figure 3.1: High pressure membrane test cell with optical access.

Further important design solutions, which meet the requirements on the high pressure membrane test cell, are briefly described in the following by means of figures 3.1(b) and 3.2.

1. **Sealing:** In order to avoid membrane damage, the sealing concept of the test cell is decisive. The best practice for a leakage free assembly of the

test cell was to use a Teflon sealing (not illustrated in figure 3.1(b)) between the vertical part of the membrane and the permeate channel module. Furthermore, flat sheet seals were installed between the permeate and feed channel modules and the side lids, see figure 3.1(b). A sealing concept based on O-rings failed as these change their shape depending on the pressure inside the test cell, which can result in membrane damage. To double-check the integrity of the installed membrane in the test cell with optical access, it was operated in series with a state-of-the-art membrane test cell (section 5.2.3) in a pure water experiment before conducting the actual boundary layer experiments (section 6.1).

2. **Optical Access:** The two design solutions for the optical access were already briefly introduced above. The first design solution with replaceable glasses has the option for realignment but the disadvantage of a small cavity in the fluid domain, which is depicted in figure 3.1(b). At this cylindrical cavity a fluid recirculation zone develops which expands with rising feed flow velocities, see HEITHORST ET AL. [68] for detailed analyses. To minimize any influence of the cavity geometry on the concentration boundary layer in the present study, the feed flow rate was set to the minimum flow rate of the membrane test rig $V_F \approx 3$ l/h. Such cavities are avoided by the second design solution using a permanentely glued optical glass. But this design does not have the option for realignment or easy exchange. Both configurations were implemented successfully. No leakage occurred even at maximum pressure levels.

3. **Feed channel:** The feed channel module is designed such that both channel height as well as channel inlet and outlet geometry can be modified to adjust the flow profile inside the test cell. In figure 3.2, an overview of the module is given. It consists of the main feed channel module, the height adapter and the channel adapters for inlet and outlet, which are designed identical. By means of different height adapters made from stainless steel different channel heights can be realized. The height adapter shown was selected in the present study to set the maximum channel height of 60 mm to be able to do experiments at minimum feed flow velocities because of the cavity problem. The channel inlet and outlet

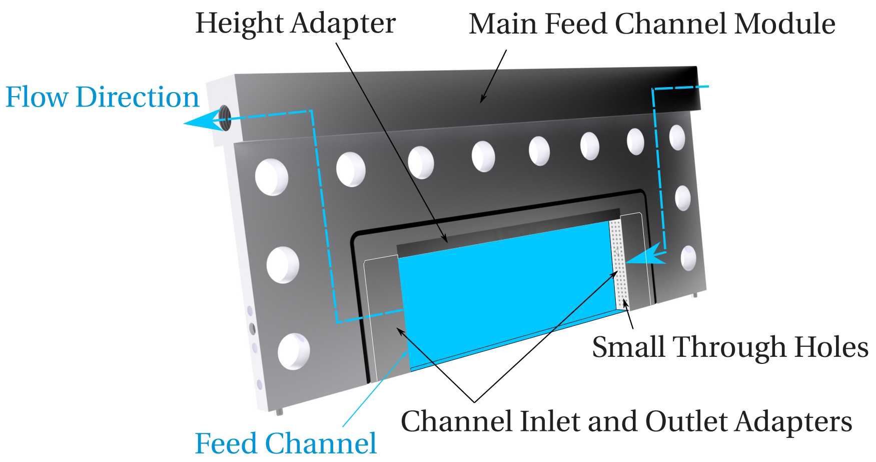

Figure 3.2: Feed channel module with channel inlet and outlet adapters and variable channel height.

adapters depicted in figure 3.2 were designed by SCHMIDT ET AL. [150]. As it was not possible to manufacture the adapter geometry from steel due to its small through holes with a radius of 0.6 mm, they were 3D printed and made of polyamide.

4. **Pressure resistance and material:** Austenitic steel of the type 1.4571 is chosen as test cell material due to its high resistance to corrosion. The material of all optical glasses is fused silica with SQ1 quality. The wall thickness of the windows and the four main test cell parts (permeate channel module, feed channel module, two side lids with glass windows) were determined via a FEM analyses. To give an order of magnitude, the side lids have a thickness of around 40 mm.

For more details on the design of the high pressure membrane test cell see WOLF ET AL. [184].

3.1.2 Geometry and Mesh of the Fluid Domain

The geometry of the fluid domain is derived from the Computer-Aided Design (CAD) drawings of the membrane test cell. The following simplifications were made:

- Small unevennesses caused by the imperfect adhesive surrounding of the optical access with glued glass or by screw heads are neglected.
- Cavities at the step glasses are taken into account as sketched in figure 3.1(b).
- The thickness of the flat sheet seal between the channel modules and the side lids is assumed to be uniform and constant.
- The geometries in front of and after the channel inlet and outlet flow adapters are not taken into account.

In order to keep required computational capacity low but computational accuracy high, it was decided to model the fluid domain with a multiple-block [47, p. 33] structured mesh and refinements wherever necessary. The mesh is generated with ANSYS ICEM CFD 14.0. In figures 3.3 and 3.4, the frontal view as well as three cross-sections of the 3D mesh are illustrated. For better illustration, both halfs of the channel geometry are depicted. Only one half of the symmetrical geometry is computed.

Round geometries like the inlet and outlet pipes as well as the windows for optical access were modeled with O-grids. The mesh refinement is carried out for each block separately. The mesh in the concentration boundary layer region is designed via a bi-exponential bunching law in z-direction defined by two spacings $Sp1$ and $Sp2$, the ratios $R1$ and $R2$ and the number of nodes N for length n [5]. Information about these mesh parameters are included in figure 3.4 and table 3.1.

The mesh on the membrane has 312 nodes along its 180 mm length and 40 nodes along 5 mm width, which is only half of the actual membrane width to account for test cell symmetry. The spacing in x-direction ranges from

50 μm in the center of windows to 1.6 mm in regions far away from geometrical changes inside the channel. The spacing in y-direction ranges from 150 μm in the membrane center to 50 μm in the outer region.

In order to prove mesh independence, a study based on the grid convergence index GCI [139, 140] was carried out with three grid solutions (fine, medium and coarse). The CFD boundary conditions were taken from the experiment with the strongest refractive index gradient measured in the present study. The experimental conditions are presented later in table 3.6 on page 76 (experiment BW-P60). The focus lies on the calculation of the GCI for parameters relevant for boundary layer investigations: local permeate flux j_{P}, local salt mass fraction at the membrane $w_{\mathrm{S,F,M}}$ and boundary layer height $\delta = \delta_{99.5\%}$ located in close vicinity of the channel center at the measurement position. Additionally, mean permeate flux $\bar{j}_{\mathrm{P}}$ and mean salt mass fraction on the membrane $\bar{w}_{\mathrm{S,F,M}}$ were selected as both become important in chapter 6. According to FIMBRES-WEIHS and WILEY [49, p. 766], meshes with grid convergence indices GCI below a threshold of typically 5 to 10% can be accepted. The GCI of each investigated parameter of the medium coarse grid with about 2.37 million cells meets this threshold with a safety factor of F_{S} =1.25 [139, p. 136]. For the finest grid, a significant improvement of the GCI of any investigated parameter was not observed. Therefore, the medium coarse grid is chosen for further analyses.

Note that a 2D mesh was derived from the symmetry plane of the selected 3D mesh. Thus a similar grid quality can be assumed. This 2D mesh will be used only for preliminary analyses presented later in figure 6.2(a).

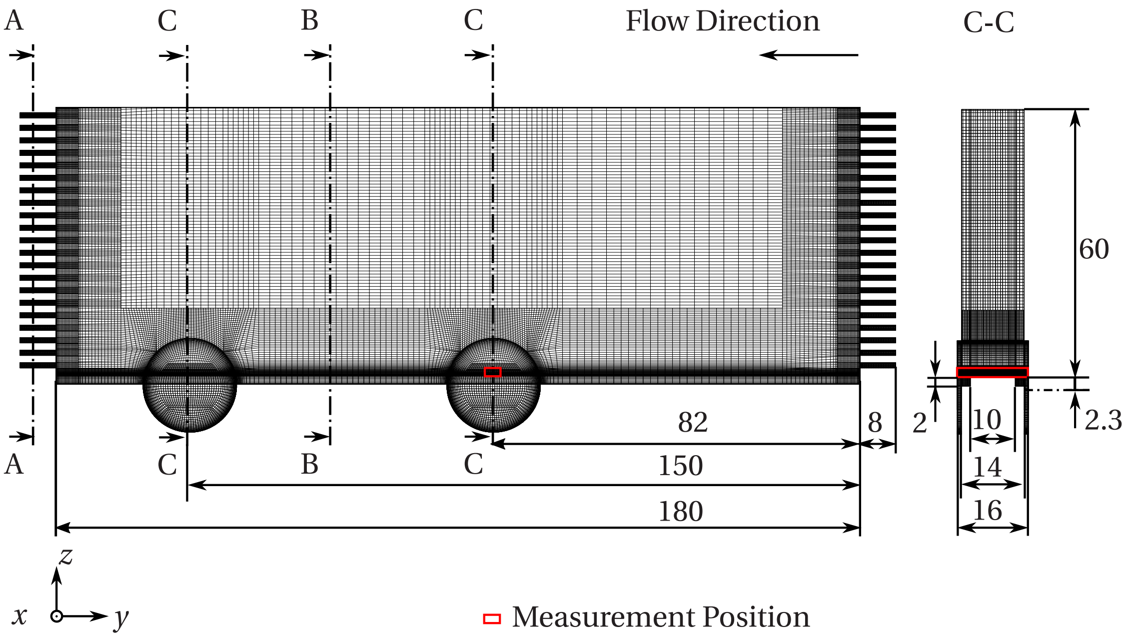

Figure 3.3: Structured mesh: front view and cross section at the measurement position.

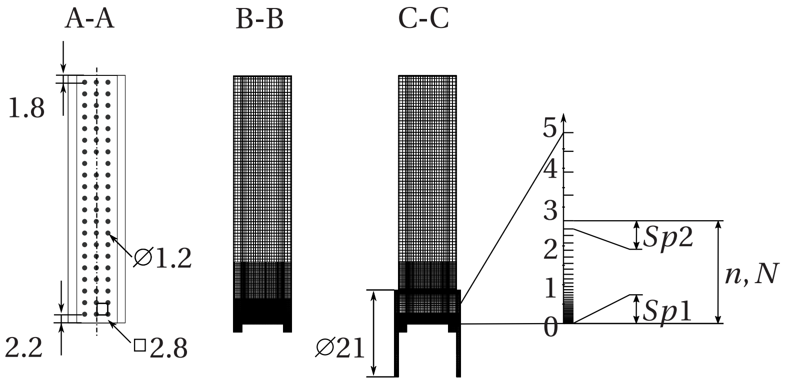

Figure 3.4: Structured mesh: cross-sections A-A, B-B and C-C.

Table 3.1: Mesh parameters.

Cross-Section	$Sp1$ [mm]	$R1$ [-]	$Sp2$ [mm]	$R2$ [-]	n [mm]	N [-]	Comment
B-B	0.0075	1.5	0.5	1	6.12	41	channel region without O-grids
C-C	0.00364	1.5	0.186	1	2.65	41	channel region with O-grids

3.1.3 Solver

The open-source software OpenFOAM 2.1.x was chosen as simulation platform due to its high flexibility. Different solvers designed for specific problems are available and can be modified by the user to meet specific requirements. In the present study, the steady-state solver *buoyantSimpleFoam,* originally developed for heat transfer and buoyancy-driven flows [122], is taken as basis. According to FLETCHER and WILEY [51], the influence of graviation is not relevant for our experiments conducted with a horizontally aligned membrane at the channel bottom. However, buoyancy effects have been observed in preliminary experiments e.g. when an RO experiment was stopped and the natural osmosis processes started. Therefore, it was decided to modify a solver which already had the option of taking gravitational effects into account. Even though they are not relevant for the present study, this might be helpful for future work.

In accordance with FLECTCHER and WILEY [51], the thermo-physical properties density, viscosity, diffusivity, heat capacity and thermal conductivity are allowed to be dependent on temperature and salt mass fraction but to be independent of pressure.

The **governing equations** solved via the Finite Volume method by the steady-state solver ($\frac{\partial}{\partial t} = 0$) are:

Conservation of mass:

$$\nabla \cdot (\rho \mathbf{u}) = 0 \tag{3.1}$$

Conservation of energy (with Fourier's law for thermal diffusion):

$$c_\mathrm{P} \nabla \cdot (\mathbf{u} \rho T) = \nabla \cdot (\lambda \nabla T) \tag{3.2}$$

Conservation of salt (with Fick's law for mass diffusion):

$$\nabla \cdot (\mathbf{u} \rho w_\mathrm{S}) = \nabla \cdot (D_\mathrm{SW} \rho \nabla w_\mathrm{S}) \tag{3.3}$$

Conservation of momentum (Newton's second law):

$$\nabla \cdot (\rho \mathbf{u}\mathbf{u}) = -\nabla p + \nabla \cdot \left[\mu(\nabla \mathbf{u} + (\nabla \mathbf{u})^\mathrm{T}) - \tfrac{2}{3}\mu(\nabla \cdot \mathbf{u})\mathbf{I}\right] + \rho \mathbf{g} \tag{3.4}$$

The *buoyantSimpleFoam* solver [125] was modified by adding the conservation equation for the salt transport as well as the thermo-physical properties for an aqueous NaCl solution. Moreover, instead of the enthalpy equation, the temperature equation was implemented in accordance with MOUKALLED ET AL. [117, p. 62]. This made an easy integrating of the thermo-physical properties possible. Relying on the temperature instead of the enthaly equation does not have a negative influence on the quality of the CFD results as the enthalpy of mixing of an aqueous NaCl solution can be neglected. This can be estimated by means of enthalpy data from PITZER ET AL. [132]. Furthermore, during the experiments analysed in the present study, fluid and ambient temperatures were kept constant anyway.

The momentum equation (3.4) was rearranged [121] for implementation in OpenFOAM introducing the modified pressure $p_{\mathrm{rgh}} = p - \rho \mathbf{g} \cdot \mathbf{r}$ [124] :

$$-\nabla p + \rho \mathbf{g} = -\nabla (p_{\mathrm{rgh}} + \rho \mathbf{g} \cdot \mathbf{r}) + \rho \mathbf{g} = -\nabla p_{\mathrm{rgh}} - (\mathbf{g} \cdot \mathbf{r}) \nabla \rho - \rho \mathbf{g} + \rho \mathbf{g} = -\nabla p_{\mathrm{rgh}} - (\mathbf{g} \cdot \mathbf{r}) \nabla \rho \tag{3.5}$$

According to the release announcements of OpenFOAM [124], solving for the p_{rgh} instead for the static pressure p was made to "avoid deficiencies in the handling of the pressure force / buoyant force balance on non-orthogonal and distorted meshes", [124].

For an overview of the numerical schemes applied in the CFD analyses of the present study, see table 3.2.

Table 3.2: Applied numerical schemes.

Scheme	**Term**	**OpenFOAM Keyword**	**Order of Accuracy**	**Reference**
gradient (∇)	any	`Gauss linear`	2	[71] [47, p. 90]

divergence ($\nabla\cdot$)	scalar transport
	$\nabla \cdot (\rho \mathbf{uu})$
	any other
		`Gauss vanLeer`
		`Gauss vanLeerV`
		`Gauss linear`
			2
			2
			2
				[71] [47, p. 90]
				[71, 123] [47, p. 90]
				[71] [47, p. 90]

Laplacian (∇^2)	any	`Gauss linear corrected`	$1-2$	[71] [47, p. 90]
cell to face interpolations of values	any	`linear`	2	[71] [47, p. 90]

3.1.4 Boundary Conditions

The boundary conditions for the computational domain are summarized in table 3.3 and briefly explained below.

Table 3.3: Boundary conditions for computational domain.

Boundary	**Velocity**	**Pressure**	**Temperature**	**Salt Mass Fraction**
Inlet	$\mathbf{u}_\mathrm{F} = \mathbf{u}_\mathrm{F,0}$	$\nabla p = 0$	$T = T_0$	$w_\mathrm{S,F} = w_\mathrm{S,F,0}$
Outlet	$\nabla \mathbf{u}_\mathrm{F} = 0$	$p_\mathrm{rgh} = 0$	$\nabla T = 0$	$\nabla w_\mathrm{S,F} = 0$
Walls	$\mathbf{u}_\mathrm{F} = 0$	$\nabla p = 0$	$\nabla T = 0$	$\nabla w_\mathrm{S,F} = 0$
Membrane (Type L)	$\mathbf{u}_\mathrm{n,F} = \frac{j_\mathrm{P}}{\rho_\mathrm{F,M}} \cdot \mathbf{n}$	$\nabla p = 0$	$\nabla T = 0$	$\nabla_\mathrm{n} w_\mathrm{S,F} = \frac{\mathbf{u}_\mathrm{n,F}}{D_\mathrm{SW}} (w_\mathrm{S,F,M} - w_\mathrm{S,P})$
Membrane (Type M)	$\mathbf{u}_\mathrm{n,F} = \frac{j_\mathrm{P}}{\rho_\mathrm{F,M}} \cdot \mathbf{n}$	$\nabla p = 0$	$\nabla T = 0$	$\nabla_\mathrm{n} w_\mathrm{S,F} = \frac{\mathbf{u}_\mathrm{n,F}}{D_\mathrm{SW}} (w_\mathrm{S,F,M} - \bar{w}_\mathrm{S,P})$

The velocity boundary conditions apply to the small pipes of the flow distribution adapter (shown in figures 3.3 and 3.4). The flow is assumed to be evenly distributed over all small inlet pipes.

The pressure boundary condition $\nabla p = 0$ is realized with the OpenFOAM boundary condition `buoyantPressure`. For the outlet pressure condition, the `fixedValue` boundary condition can be used when neglecting gravity ($\mathbf{g} = \mathbf{0}$), otherwise `fixedMeanValue` is recommended ($\mathbf{g} \neq \mathbf{0}$).

For the CFD analyses carried out in this study, constant fluid and ambient temperatures can be assumed and thus zero temperature gradients on the channel walls.

The membrane boundary condition is based on the SDM, as described in section 2.1.3. For the permeation velocity, a Dirichlet boundary condition is chosen. The velocity component at the feed water side normal to the membrane $u_\mathrm{n,F} = u_\mathrm{z,F}$ is the ratio of permeate flux j_P and the feed solution density on the membrane surface $\rho_\mathrm{F,M}$. For the salt mass fraction at the membrane, a Neumann boundary condition is chosen. The salt mass fraction gradient is a function of diffusivity D_SW and the permeation velocity $u_\mathrm{n,F} = u_\mathrm{z,F}$ as defined by equation (2.64) in section 2.2.1.

In contrast to many other studies, e.g. [2, 23, 146, 182], the boundary condition for the salt mass fraction is not calculated with the salt rejection as constant input parameter. This would result in

$$\frac{\mathrm{d}w_{\mathrm{S,F}}}{\mathrm{d}z} = \frac{u_{\mathrm{z,F}} SR\, w_{\mathrm{S,F,M}}}{D_{\mathrm{SW}}} \tag{3.6}$$

or in a similar correlation, when the apparent instead of the true salt rejection is used, e.g. by COMPLETO ET AL. [23].

Of course, an equation of type (3.6) might be very simple to implement. However, what it implies is the fact that the ratio of feed salt mass concentration and permeate salt mass concentration is fixed. This simplification means that the membrane characteristics need to change such along the feed channel that a constant ratio between feed and permeate salt concentration results. In this way, a dependence of the membrane characteristic on salinity is implemented. A simplification which implies such a strong assumption on membrane characteristics is not seen as applicable for the goal of the present study. Instead, salt transport through the membrane is to be defined only by one model input parameter, namely the salt permeability constant B.

Figure 3.5 shows how the membrane boundary condition is implemented. It can be noticed that the permeate salt mass fraction $w_{\mathrm{S,P}}$ is not a model input parameter. Instead, the permeate salt mass fraction is calculated for each cell from a cubic function in $w_{\mathrm{S,P}}$, which results when all necessary parameters $(u_{\mathrm{n,F}}, \rho_{\mathrm{F,M}}, w_{\mathrm{S,F,M}}, T, B)$ are expressed as a function of the salt mass fraction. The cubic equation is solved by the bisection method. This allows to numerically access the *local* permeate salt mass fraction on the permeate side of the thin-film active layer. This is possible as for RO membranes, an "unhindered" permeate flux [135, p. 89] can be assumed, see section 2.1.3 on page 19. Due to the porous support structure of the RO membrane, the influence of the flow conditions in permeate channel on the salt mass fraction at the permeate side of the thin-film active layer can be neglected [27, 109, 135]. Note that we have co-current flow in the permeate channel.

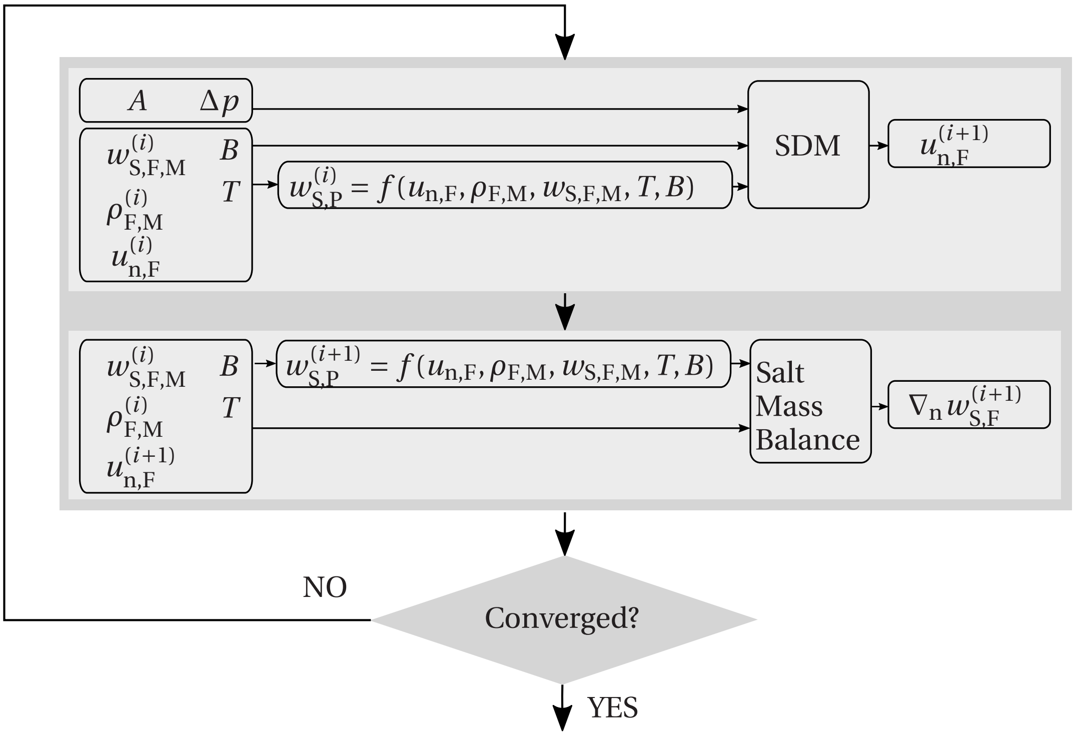

Figure 3.5: Membrane boundary condition.

In table 3.3 on page 70, two different membrane boundary conditions (L and M) were presented. L stands for *local* denoting the boundary condition exactly as described above, whereas M stands for *mean*. The latter was implemented to achieve better convergence behaviour. In accordance with PRÄBST ET AL. [133], ideal mixing of the permeate produced is assumed for the membrane boundary condition M. Instead of the local permeate salt mass fraction its averaged value is input to the equations for permeate osmotic pressure (equation (2.12)), salt mass flux (equation (2.21)) and salt mass fraction gradient (equation (2.64)). On the one hand, this diminishes the advantage of local permeate salt flux data. On the other hand, the convergence behaviour of the simulation is more robust, especially for cases where osmotic equilibrium is reached in parts of the test cell e.g. in the corners at the test cell outlet between membrane and channel wall. The results presented later in chapter 6 will be almost independent from the membrane boundary condition type (figure 6.8 on page 133).

3.1.5 Thermo-Physical Properties

An overview of the thermo-physical properties implemented in the CFD model and consistently used throughout the present study is given in table 3.4. A short explanation of the selected correlations is given below.

Table 3.4: Thermo-physical properties.

Fluid Property	**Parameter**	**Unit**	**Reference**
Density	$\rho(w_\mathrm{S}, T)$	$\frac{\mathrm{kg}}{\mathrm{m}^3}$	measurements (appendix B)
Mass diffusivity	$D_\mathrm{SW}(w_\mathrm{S}, T)$	$\frac{\mathrm{m}^2}{\mathrm{s}}$	ROBINSON and STOKES [141] and measurements (appendix B)
Practical osmotic coefficient	$\phi(w_\mathrm{S}, T)$	–	correlation built with data of CLARKE and GLEW [22] (equation (3.10))
Osmotic pressure	$\pi(w_\mathrm{S}, T, \phi, \rho)$	bar	ROBINSON and STOKES [141, p. 205]
Dynamic viscosity	$\mu(w_\mathrm{S}, T)$	Pas	SHARQAWY ET AL. [157]
Thermal conductivity	$\lambda(w_\mathrm{S}, T)$	$\frac{\mathrm{W}}{\mathrm{mK}}$	SHARQAWY ET AL. [157]
Specific heat capacity	$c_\mathrm{P}(w_\mathrm{S}, T)$	$\frac{\mathrm{J}}{\mathrm{kgK}}$	SHARQAWY ET AL. [157]

Both density and diffusivity of the aqueous NaCl solution were determined experimentally, see appendix B. The material properties relevant for momentum equation (dynamic viscosity) and energy conservation (thermal conductivity and specific heat capacity) are assumed to be satisfactorily modeled by the correlations taken from SHARQAWY ET AL. [157], which are often applied in desalination research.

SHARQAWY ET AL. [157] also provide a correlation for the osmotic pressure of standard sea water. A preliminary sensitivity study revealed that the difference between the osmotic pressure of standard sea water and the one of an aqueous NaCl solution can range in the order of 10% for a salinity typically measured at the end of seawater RO plants (≈ 70 g/kg). Moreover, in literature the simplified linear osmotic pressure equation $\pi = b \cdot w_\mathrm{S}$ is often used in CFD calculations [51, 56, 146]. However, in case of the present study it cannot be excluded that the non-ideal character of the investigated fluid might become relevant. This might especially be important when interpreting the experimental results for which low net driving pressures are characteristic (section 6.2). Therefore, exact modeling of the non-ideal fluid behaviour of the investigated aqueous NaCl solution is essential.

For this purpose, an osmotic pressure equation is applied, which is based on a relationship for the activity of the solvent provided by ROBINSON and STOKES [141, p. 205] and recommended by SOURIRAJAN [161, p. 160]:

$$\ln a_{\mathrm{W}} = -\nu m \bar{M}_{\mathrm{W}} \phi \tag{3.7}$$

For an aqueous NaCl solution, the stoichiometric coefficient ν is 2. Molality m relates the moles of the solute to the mass of the solvent and can be calculated as follows:

$$m = \frac{w_{\mathrm{S}}}{(1 - w_{\mathrm{S}})\bar{M}_{\mathrm{S}}} \tag{3.8}$$

In combination with equation (2.12), the osmotic pressure (in bar) reads:

$$\pi_{\mathrm{W}} = 10^{-5} \cdot \nu R T \underbrace{\frac{\bar{M}_{\mathrm{W}}}{\bar{V}_{\mathrm{W}}}}_{\rho_{\mathrm{W}}} m \phi \tag{3.9}$$

For the practical osmotic coefficient, an empirical correlation was developed for the range of $w_{\mathrm{S}} = 0 \ldots 0.1$ kg/kg and $T = 283.15 \ldots 323.15$ K:

$$\phi = \frac{q_1}{w_{\mathrm{S}} + q_2} - q_3 \cdot \frac{\sqrt{w_{\mathrm{S}}}}{q_4 + q_5\sqrt{w_{\mathrm{S}}}} + w_{\mathrm{S}} \cdot (q_6 + q_7 \cdot w_{\mathrm{S}} + q_8 \cdot w_{\mathrm{S}}^2) + q_{10} \cdot w_{\mathrm{S}} \cdot (T - q_9) \tag{3.10}$$

Some terms of equation (3.10) were inspired by parts of the ϕ-correlation of CLARKE and GLEW [22].

The empirical coefficients q_1 to q_{10} presented in table B.5 in appendix B were determined by a least square fit to data of CLARKE and GLEW [22].

The result of the parametrized correlation for ϕ is validated with randomly selected data based on activity experiments of an aqueous NaCl solution provided by ROBINSON and STOKES [141, p. 461, p. 465, p. 466]. Based on the results summarized in table 3.5, the error of equation (B.5) is in the order of 1% related to the experimental value.

Table 3.5: Comparison of practical osmotic coefficients calculated with equation (3.10) with experimental data of Robinson and Stokes [141].

m	w_S	T	$\phi_\text{Robinson-Stokes}$	$\phi_\text{This Study}$	$\frac{\phi_\text{This Stud}}{\phi_\text{Robinson-Stokes}}$
$\frac{\mathrm{mol}}{\mathrm{kg}}$	$\frac{\mathrm{kg}}{\mathrm{kg}}$	°C	–	–	–
0.1	0.0058	25	0.9324	0.9320	0.9996
1	0.0552	25	0.9355	0.9361	1.0007
1.4	0.0756	25	0.9513	0.9536	1.0024
2	0.1047	60	0.9990	1.0086	1.0096
0.1024	0.0059	35	0.9312	0.9321	1.0010

3.2 Local Membrane Parameter Method: Proof of Concept Study

The local membrane parameter method (LMPM) was introduced in section 2.2.2. In this section, the method is tested in a proof of concept study. The success of the LMPM mainly depends on the accuracy of the input parameters to the LMPM equations (2.70) and (2.71) and on the validity of the assumptions made in section 2.2.2. The main purpose of the following study is to check if the film model assumptions are a suitable basis for the LMPM. The membrane model will not be questioned relying on the SDM. In the end of this section, the accuracy of the LMPM is estimated and suitable fields of application are identified.

3.2.1 Methodology

To test the validity of the film model assumptions in the LMPM at the measurement position in the high pressure membrane test cell, concentration boundary layer data simulated with the 3D CFD model are used. In both LMPM and CFD, the SDM is used to model the membrane. If the assumptions made are valid, local transport (j_P and w_P) and membrane (A and B) parameters can be properly determined from the concentration boundary layer data (ρ, w_S, D_SW and its derivatives).

Using 3D CFD simulation data instead of experimental data has the advantage that the validity of the film model assumptions made can be tested independently of the accuracies of the membrane model and the input parameters of the LMPM. The latter depend on measurement noise, errors due to optical distortions and on the accuracies for thermo-physical and membrane property models.

Instead of using arbitrary CFD boundary conditions, they are taken from the test conditions of the boundary layer experiments presented in chapter 6.2. In this way, the CFD results presented here will be useful again when discussing the experimental results. In table 3.6, these test conditions are summarized for brackish (BW) and sea water (SW) experiments. Only the data of the BW experiments are needed in the present proof of concept study.

Table 3.6: Test conditions for brackish water (BW) and sea water (SW) for different pressure levels (P).

Case ID	Δp [bar]	$\bar{j}_\mathrm{P}$ [kg/m^{2}h]	$T_\mathrm{F} \approx T_\infty$ [°C]	V_F [l/h]	$\bar{u}_\mathrm{F}$ [mm/s]	$w_{\mathrm{S,F},0}$ [g/kg]
BW-P15	15.0	5.7	29.9	3.0	1.0	10.4
BW-P20	20.1	7.9	30.0	3.0	1.0	10.4
BW-P25	25.0	10.0	30.0	3.1	1.0	10.4
BW-P35	34.7	13.4	29.7	2.6	0.9	10.0
BW-P45	44.1	16.7	29.8	2.5	0.8	10.0
BW-P55	54.3	21.1	29.8	3.1	1.0	10.0
BW-P60	60.4	22.9	30.0	2.5	0.8	10.0
SW-P45	44.9	6.5	30.5	2.7	0.9	35.2
SW-P55	54.6	8.2	30.5	2.7	0.9	35.2
SW-P60	59.7	8.8	30.7	2.6	0.9	35.2

The proof of concept study is structured as follows: First, the test cell CFD results are introduced. Second, important LMPM assumptions are discussed by means of a test case. Third, the results are presented for the brackish water experiments.

3.2.2 Introduction of CFD Results

For demonstration of the CFD results relevant for the LMPM, the BW-P60 experiment is chosen. The membrane boundary condition L is used (see section 3.1.4) in combination with the permeability constants determined later in this study. The results for A are listed in table 6.1 and the ones for B are shown in figure 6.8.

The feed salt mass fraction distribution in the symmetry plane and on the membrane surface is illustrated in figures 3.6(a) and 3.6(b), respectively. Besides, three positions P1, P2 and P3 on the membrane are highlighted. They will become important later in the next section.

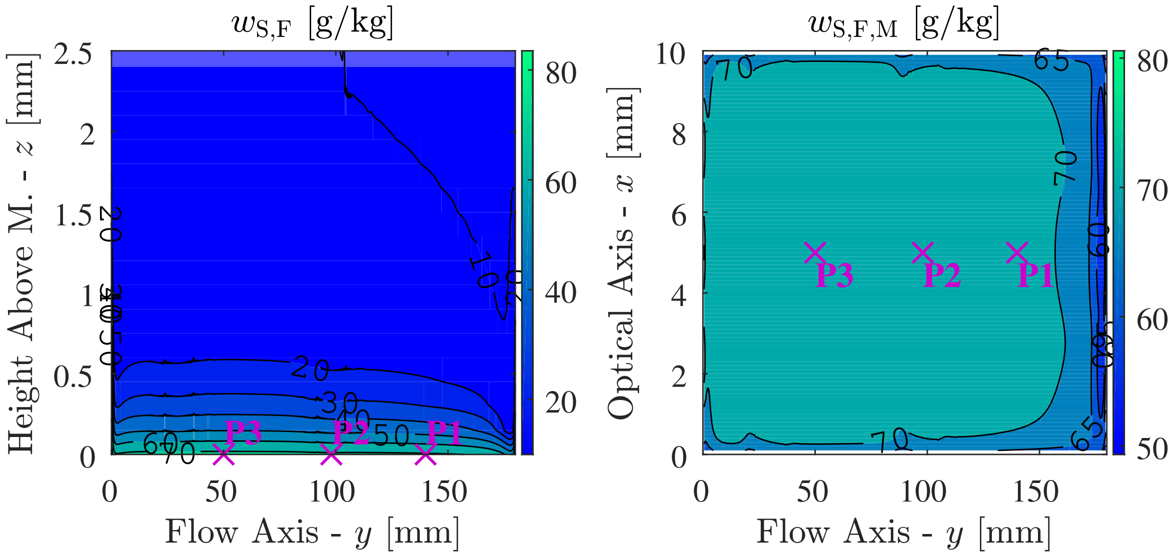

(a) Feed salt mass fraction in the symmetry plane.

(b) Feed salt mass fraction on the membrane surface.

Figure 3.6: 3D CFD results for salt mass fraction in feed channel for experiment BW-P60.

The aqueous NaCl solution enters the test cell at $y = 180$ mm. Flow direction is in negative y-direction. The salt mass fraction on the membrane increases very fast from its bulk value of about $w_{S,0} = 10$ g/kg. The maximum salt mass fraction value is reached in the corner between flow adapter and membrane surface at the test cell exit ($y = 0$ mm), where the fluid velocity tends towards zero. For the same reason, an elevated salt mass fraction can be observed at the test cell inlet (y = 180 mm), too. The influence of the test cell geometry on the salt mass fraction distribution on the membrane becomes also visible close to the channel walls parallel to the flow direction, especially where the windows for optical access are located. However, this influence is rather small. A small influence of the test cell geometry on the concentration boundary layer is good as the LMPM relies on line-of-sight integrated experimental data along the optical axis (x-direction).

In figures 3.7(a) and 3.7(b), permeate flux j_{P} and permeate salt mass fraction w_{P} are presented. The CFD results for j_{P} and w_{P} correspond well with the results for the feed salt mass fraction on the membrane $w_{\mathrm{S,F,M}}$ (figure 3.6). The fluxes are high where the feed salt mass fraction is low due to high net driving pressures. The permeate salt mass fractions is low where the fluxes are high and feed salt mass fractions on the membrane are low.

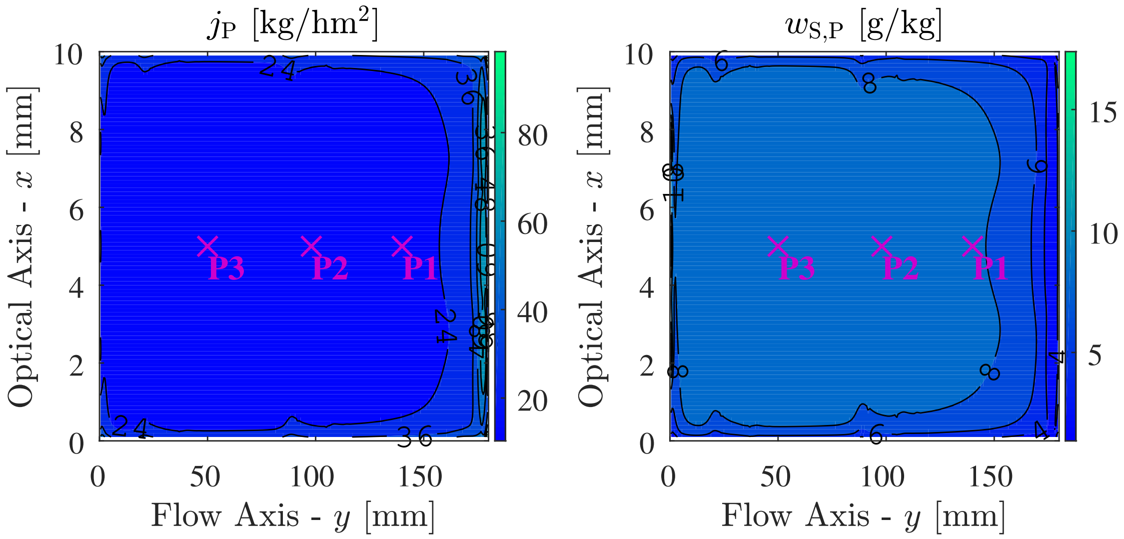

(a) Permeate mass flux. (b) Permeate salt mass fraction.

Figure 3.7: 3D CFD results for permeate flux and permeate salt mass fraction for experiment BW-P60.

For the further analysis, the three positions P1, P2 and P3 inside the test cell are selected, see figures 3.6(a) to 3.7(b). All of them are located on the symmetry plane. P1 and P3 are rather close to the test cell in- and outlet. In contrast to P2, they are far away from the windows for optical access. Note that during boundary layer experiments light propagates along the x-coordinate of P2.

3.2.3 Discussion of Assumptions

According to equations (2.70) and (2.71), any z-position of the boundary layer may theoretically be used for evaluation. Diffraction phenomena caused at the membrane and by strong refractive index gradients in the boundary layer (section 4.2) make measurements far away from the membrane preferable. What is decisive for the flexibility of LMPM is assumption (5) in section 2.2.1. The net mass transfer in z-direction $j_z(z) = -\rho(z)u_z(z)$ is assumed to be constant $j_z(z) = j_\mathrm{P}$ within the boundary layer for all z. In figure 3.8(a), the relative deviation of j_z from j_P is depicted for the BW experiments.

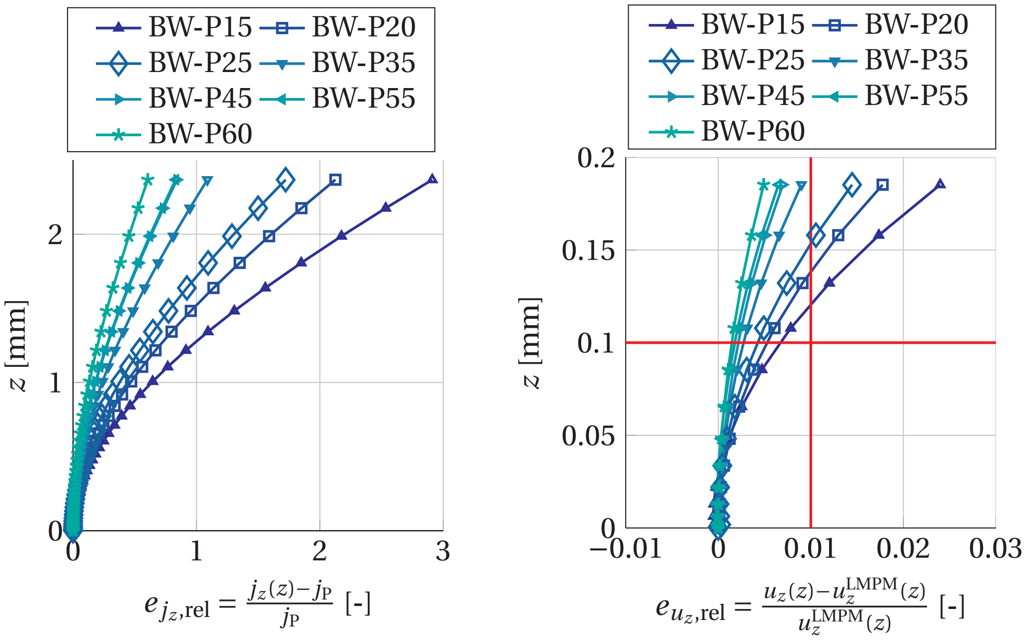

(a) Net mass transfer in z-direction.

(b) Velocity component in z-direction. In red: accuracy threshold of 1% (vertical) and height above membrane for further anaysis $z = 100\ \mu$m (horizontal).

Figure 3.8: Checking assumption (5) of the LMPM at position P2.

$e_{j_z,\mathrm{rel}}$ decreases with increasing fluxes from BW-P15 to BW-P60. Thus, for a stronger momentum in z-direction the validity of the assumption *constant net mass transfer in z-direction* is higher.

The second aspect of assumption (5) is that the z-component of the local fluid velocity in the boundary layer can be expressed as a function of permeate flux and fluid density. This is tested via the relative deviation between the calculated CFD values $u_z(z)$ and the ones resulting from the LMPM assumption $u_z^{\mathrm{LMPM}}(z) = \frac{-j_{\mathrm{P}}}{\rho(z)}$ shown in figure 3.8(b). That this assumption might be valid only in the close vicinity of the membrane was clear. By means of figure 3.8(b), this vicinity can be quantified. Accepting an error $e_{u_z,\mathrm{rel}} < 1\%$ (accuracy threshold), the assumption is valid up to $z = 100\ \mu$m. The question if this accuracy threshold is sufficiently low to get satisfactory LMPM results has to be answered in the following. However, it has to be kept in mind that a measurement closer than 100 μm to the membrane might be difficult due to diffraction phenomena. Thus, for the further analysis a z-position of 100 μm is seen as a good choice.

For the evaluation of the LMPM equations (2.70) and (2.71), the necessary input parameters are extracted from the CFD model.

Required first and second order derivatives of these parameters are numerically calculated by means of a second order accuracy forward differencing scheme for non-uniform grids, compare SCHREYER ET AL. [154, p. 41]. For illustration, the zeroth, first and second order derivative of the salt mass fraction is presented in a non-dimensional form in figure 3.9.

The non-dimensional salt mass fraction Ω is calculated as follows:

$$\Omega(w_{\mathrm{S,F}}) = \frac{w_{\mathrm{S,F}} - w_{\mathrm{S,F},\delta_{\mathrm{C}}}}{w_{\mathrm{S,F,M}} - w_{\mathrm{S,F},\delta_{\mathrm{C}}}} \tag{3.11}$$

And the spatial coordinate z turns into η:

$$\eta(z) = \frac{z}{\delta_{\mathrm{C}}} \tag{3.12}$$

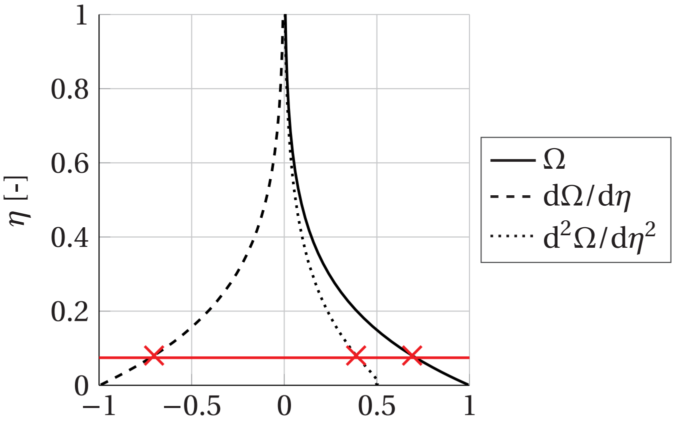

Figure 3.9: Non-dimensional form of zeroth, first and second order derivative of salt mass fraction (BW-P60). The position for data analysis is marked red.

In section 2.2.2, it was indicated that the term with the diffusivity derivative is negligible in equation (2.70). In order to support this statement $j_{\mathrm{P}}(z)$ is calculated once taking the diffusivity term into account and once neglecting it, $j_{\mathrm{P}}^{\mathrm{noD}}(z)$. The results depicted in figure 3.10 show a relative error less than 1% when neglecting the diffusivity derivative, which is reasonably small.

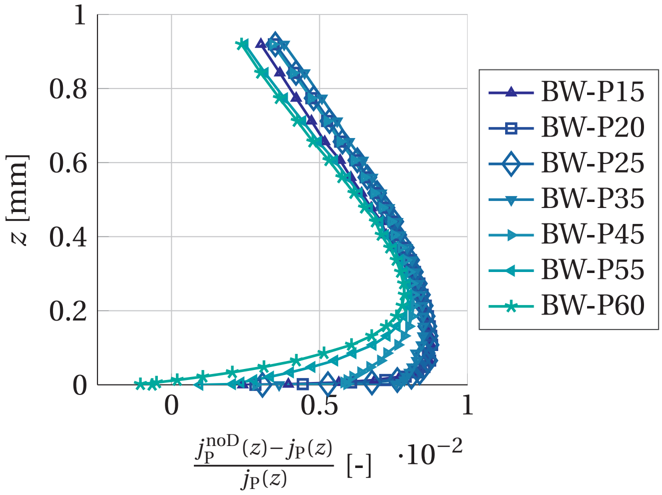

Figure 3.10: Hypothetical error of the permeate flux when neglecting the diffusivity derivative term in equation (2.70).

3.2.4 Results for Local Mass Transport

Now the LMPM is applied at $z = 100\ \mu$m. The results for the local transport parameters j_P and $w_{\mathrm{S,P}}$ are presented in figures 3.11(a) and 3.11(b). Note that the diffusivity derivative term was not neglected here even its impact on j_P proved to be low. This allows a discussion of the results with a focus on the film model assumptions in the LMPM.

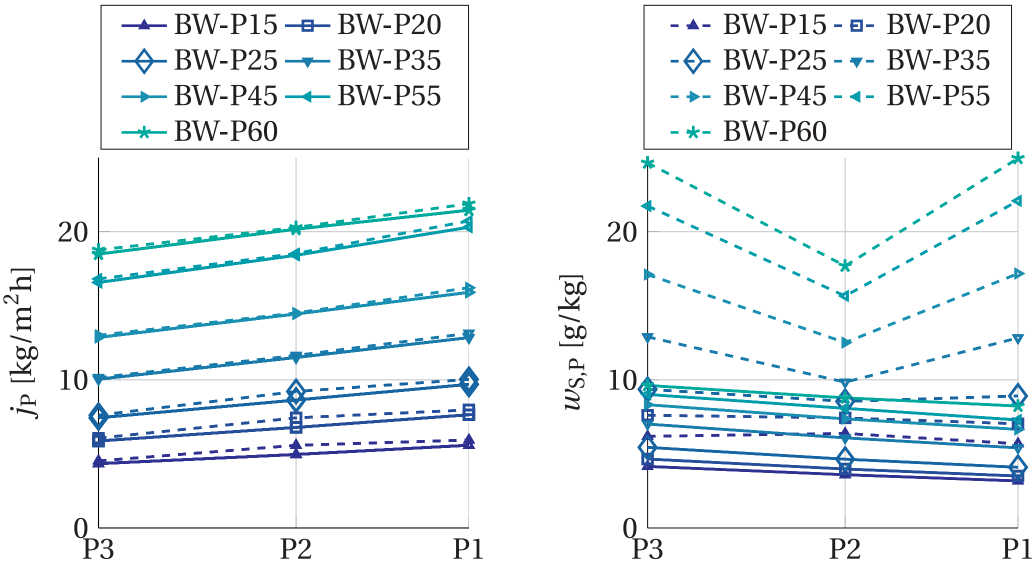

(a) Permeate mass flux. (b) Permeate salt mass fraction.

Figure 3.11: Local permeate mass flux and salt mass fraction: CFD data (solid lines) and LMPM results (dashed lines).

Referring to figure 3.11(a), it can be stated that the CFD data and the LMPM results for the local permeate flux are in very good agreement. This is true independent of position (P1, P2, P3) and pressure level (P15 to P60). The mean relative error $\bar{e}_{j_\mathrm{P},\mathrm{rel}}$ is 3.3%. For position P2, this value is 4.5% and thus only slightly higher. Therefore, the influence of the cavity due to the optical access is considered to be small for the investigated boundary layer profile taken from the channel center. Furthermore, strong refractive index gradients, which are characteristic especially for the experiments at the higher pressure levels, do not seem to have a negative impact on the permeate flux resulting from the LMPM.

The results for the permeate salt mass fraction (figure 3.11(b)) are not satisfactory. The mean relative error is $\bar{e}_{w_{S,P},\mathrm{rel}} = 107\%$. It has to be stated that the LMPM failed to quantitatively determine the permeate salt mass fraction. Possible reasons are discussed in the following:

As the diffusivity derivative term is included in the evaluation, no error was introducted by its neglection. An implementation error is also unlikely, as otherwise the permeate flux determination should fail as well.

As the permeate flux results are in good agreement, error propagation from the flux result (equation (2.70)) to the calculated salt mass fraction (equation (2.71)) is unlikely to cause the high mean relative error.

Errors can be introcuded by assumption (5) as stated in the previous section 3.2.3. However, the error was expected to be low due to $e_{u_z,\mathrm{rel}} < 1\%$ at $z = 100\mu\mathrm{m}$. An evaluation closer to the membrane is not considered because of the obstructing optical phenomena close to the membrane, see sections 4.2 and 6.2.2.

Furthermore, discussing figure 3.11(b), it looks like that there is a trend for a greater error towards higher pressures. The assumptions of the LMPM were taken from the film theory. Concentration gradients were neglected in both bulk flow direction (y-coordinate) and along the optical axis (x-coordinate). However, they could be a plausible explanation:

Considering gradients in bulk flow direction, they become more important with increasing pressure levels. For the experiments at higher pressure levels, not only an increased permeate flux is characteristic but also an increased overall level of salt mass fraction on the membrane, which starts to increase from the same bulk level for all experiments. This means that the salt mass fraction gradients in the boundary layer become stronger with increasing pressure levels.

Discussing gradients along the optical axis, attentions is drawn to the different salt mass fraction results for P2 compared P1 and P3, see figure 3.11(b). Instead of increasing from P1 to P3, the salt mass fraction drops at P2 for the cases BW-45 to BW-P60. The development of the concentration gradients around P2 is different from the one around P1 and P3 due to the change of the test cell geometry nearby optical access, which might be an explanation for the different P2 result.

The poor results of the LMPM for of the permeate salt mass fraction influence the calculation of net driving pressure and salt mass fraction difference across the membrane. This error propagation significantly corrupts the calculation of the membrane parameters A and B. Unfortunately, the determination of local membrane parameters seem to be out of reach in this case.

3.2.5 Conclusion

The study presented in the preceding section made clear that the great potential of the LMPM lies in the determination of the local permeate mass flux. The method is capable to predict its development along the membrane and to provide quantitative results.

The LMPM provides only poor results for the permeate salt mass fraction. Consequently, reliable membrane performance data cannot be acquired with satisfactory accuracy by the method.

The reason for this poor results is that the assumptions made in the LMPM seem to be not justified at the measurement position in the test cell. There are three ways to deal with this problem:

First, the assumptions on which the LMPM are based can be changed. Different boundary layer models with less restrictive assumptions than the film model can be tested as basis of the LMPM. The cost for dropping model assumptions will be the increase of the method's complexity.

Second, the test cell design can be changed such that it is tailored to meet the assumptions of the LMPM for example by avoiding cavities.

Even if one of the both ways just mentioned is successful, the LMPM still can fail. Modeling errors, the influence of measurement noise, optical distortions and the line-of-sight integration character of the optical measurement on the results of the LMPM has not been investigated yet. Therefore, it was decided to revise the LMPM.

3.3 Revised Local Membrane Parameter Method (LMPM)

Instead of taking a boundary layer model as basis and dealing with assumptions, which obviously can hardly be met experimentally in a satisfactory way, it was decided to integrate the developed CFD model into a revised version of the LMPM. The idea behind is as follows:

When modeling the fluid domain, care was taken to account for important influences of the test cell geometry on the boundary layer development inside the test cell. This includes the water inlet and outlet pipes of the flow adapter, the sealing geometry as well as small cavities at the glass windows. Furthermore, the for mass transport most important thermo-physical correlations for fluid density and NaCl diffusivity were experimentally validated before implemention, see appendix B. The membrane boundary condition was implemented such that the membrane is modeled by water and salt permeability constants A and B instead of A and salt rejection SR. This avoids nonphysical membrane characteristics as explained in section 3.1.4.

Assuming in addition

- negligible influence of the generally small mesh dependencies (section 3.1.2),
- a valid CFD solver accounting for all important physical phenomena for laminar flow (section 3.1.3),
- known experimental test conditions (table 3.6) and
- that the SDM is able to describe the membrane physics satisfactorily (chapter 6),

the CFD model can be used to predict the mass transfer at the membrane for experimentally known membrane properties. However, an inversion of the problem should be possible as well determining the membrane properties from experimentally given mass transfer characteristics at the membrane. The integration of the CFD model into the revised LMPM allows not only to make use of local boundary layer data but also of global (surface integrated) permeate flux data to determine the membrane properties.

Referring to the literature review in section 1.1, collecting reliable data for the salt permeability constant B is most difficult. In contrast, the water permeability constant A can be determined more accurately and easy by means of pure water experiments. Therefore, it was decided to put the focus on the salt permeability constant in the following part of this study. Measuring the water permeability constant in the classical way, the only unknown parameter left for the determination via the CFD model is the membrane salt permeability constant.

The global permeate flux $\bar{j}_\mathrm{P}$ of the optical membrane test cell can be accurately measured. Also because of this, $\bar{j}_\mathrm{P}$ is best suited as target quantity for an iterative determination of the salt permeability constant B as sketched in figure 3.12.

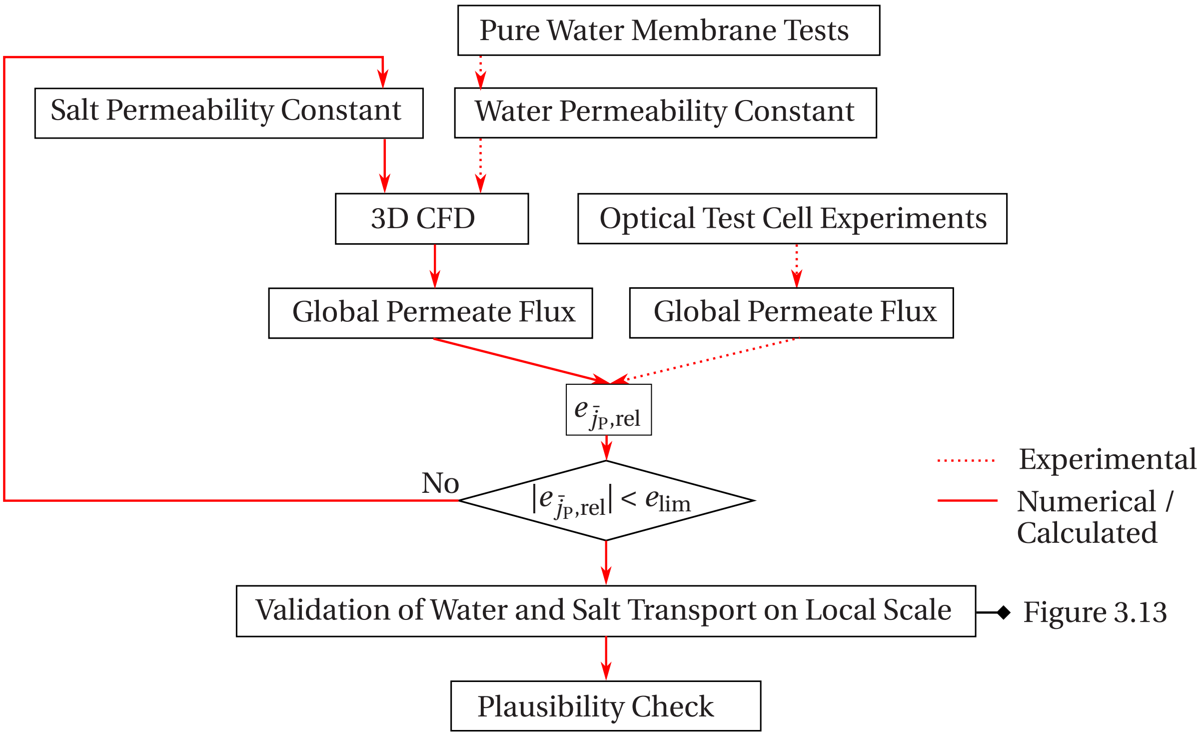

Figure 3.12: Determination of water and salt transport properties.

B is iteratively changed until the relative error

$$e_{\bar{j}_\mathrm{P},\mathrm{rel}} = \frac{\bar{j}_\mathrm{P}^\mathrm{CFD} - \bar{j}_\mathrm{P}^\mathrm{EXP}}{\bar{j}_\mathrm{P}^\mathrm{EXP}} \tag{3.13}$$

between numerical and experimental permeate flux is smaller than the threshold e_lim.

A reasonable value for e_lim can be assessed from the measurement accuracy estimation of the permeate flux (section 5.2.2). $e_\mathrm{lim} = 5\%$ is set in the present study.

After the iteration is finished, it is ensured that CFD simulation and experiment come to similar results for the global permeate flux. The preliminary results of the pure water experiment for A and of the iterative approach for B are uniform permeability constants for the entire membrane surface. As a next step, it needs to be checked if the local mass transport is already predicted well by these parameters.

To be able to validate both water and salt transport on a (line-of-sight) local scale, data of the concentration boundary layer experiments are used.

If the numerical and experimental boundary layer results are in good agreement, the membrane behaviour is obviously already described well. If not, the next step is to model local variations of the membrane properties by applying individual permeability constants to the cells on the membrane. This makes the lateral resolution of the revised LMPM dependent on the CFD mesh density on the membrane, see section 3.1.2. At measurement position, the rectangular cell surfaces can be approximated by circular areas with diameters between 10^{-5} and 10^{-4} m what is the minimum local resolution specified in section 1.2.

The implementation and testing of cell individual membrane parameters becomes easy if a modeling approach can be derived based on the outcome of the uniform permeability constants as it will be the case in the present study. A functional dependence for a locally varying B will be found. If this was not possible, a different modeling strategy would have been needed. This could be an iterative approach minimizing not only $e_{\bar{j}_\mathrm{P},\mathrm{rel}}$ but also the error between numerical and experimental boundary layer profiles. However, in this case the boundary layer data could not be used anymore for validation as described in the following.

In figure 3.13, a schematic overview is given of how the water and salt transport are to be validated on a local scale.

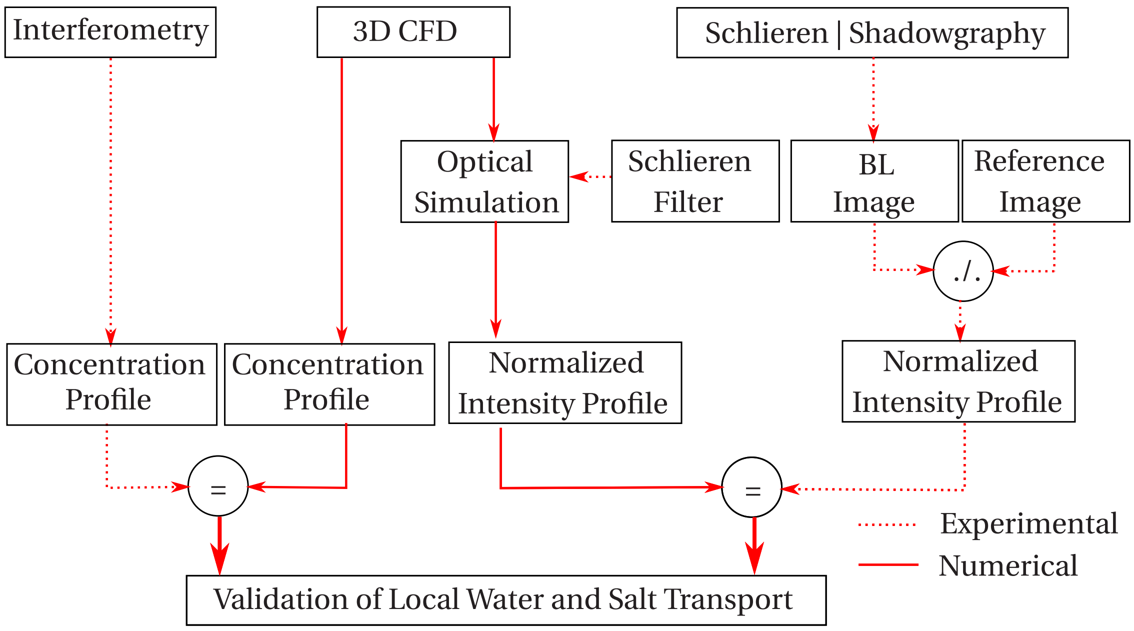

Figure 3.13: Validation of local water and salt transport by means of optical boundary layer (BL) measurements.

Interferometry, Schlieren and Shadowgraphy are combined in one setup. The simultaneous measurements of a boundary layer characteristic allows to validate the result of the optical methods with each other. Moreover, in section 6.2.2 it will turn out that the combination of the methods results in the extension of the overall measurement resolution.

For weak to moderate refractive index gradients, simultaneous Interferometry and Schlieren experiments are carried out. For strong refractive index gradients, the Schlieren experiment is substituted by Shadowgraphy to take care of the fanning effect which becomes more relevant with increasing gradients, see section 6.2.2. When the optical data are in good agreement, optical measurement errors can be assumed to be small. Precise optical measurements are seen as prerequisite for the validation of the salt and water mass transport by the boundary layer measurement.

The integration of the developed CFD model into the revised LMPM is also part of the solution to address the limits of the Schlieren and the Shadowgraphy method. Interferometry evaluation algorithms evaluate fringe patterns and are capable to minimize the influence of light intensity variations in the recorded image due to measurement noise and optical distortions, see TAKEDA ET AL. [165]. In contrast, classical Schlieren and Shadowgraphy evaluation algorithms directly evaluate the image intensity. Thus, they are limited in presence of optical distortions like fanning, spherical aberration and diffraction phenomena, which change the intensity distribution in the boundary layer image. Without accounting for these optical phenomena appropriately, the results of Schlieren and Shadowgraphy can be misleading. In case of both methods, the image intensity is directly linked to a derivative of the refractive index profile (section 2.2.3). Thus, error propagation of optical distortions and measurement noise during integration of the biased refractive index derivatives becomes a problem when calculating the boundary layer profile. The goal in this study is to compare the results of the optical measurements with CFD results. This comparison can be obviously done by means of concentration profiles. However, to avoid errors in case of Schlieren and Shadowgraphy the comparison of intensity profiles becomes more favorable instead. This requires a transformation of CFD concentration profiles to intensity profiles. Thus, the CFD model will be integrated in an optical ray tracing tool to simulate light propagation from the test cell to the camera chip.

The detailed evaluation strategy is sketched above in figure 3.13. The concentration distribution calculated by the 3D CFD model is fed into the optical simulation model. Further model inputs are the experimentally determined Schlieren filter transmittance curve $\tau(z)$ and properties of the optical setup and its components (section 5.1). The result of the optical ray tracing simulation is a light intensity profile at the location of the camera chip modeling the Schlieren or the Shadowgraphy experiment. The numerical light intensity is modeled as a relative quantity expressing an intensity change compared to an initial reference state with intensity one. In order to gain this relative intensity change from the experimental boundary layer image as well, an image of the optical target must be recorded without a boundary layer present, the so-called reference image. For comparison of boundary layer (BL) image and reference image, median intensity values of pixel rows are used.

After successful validation of global and local mass transport, the question remains whether the iteratively found membrane parameters truely represent the membrane behaviour under the applied experimental conditions. To answer that question a plausibility check is performed in the end (section 6.3). Membrane properties are indepenend from the membrane model. The plausibility check is successful when the same membrane properties result using different membrane modeling approaches which rely on different membrane parameters. Suitable membrane modeling approaches have been introduced in section 2.1.

4 Optical Ray Tracing

In this chapter, the developed optical ray tracing tool is described. First of all, the optical setup which needs to be modeled is introduced. Afterwards, an overview of the for modeling relevant optical phenomena is given. At the end, the ray tracing model itself is discussed.

4.1 Optical Setup

In figure 4.1, the combined setup of Interferometry, Schlieren and Shadowgraphy is presented.

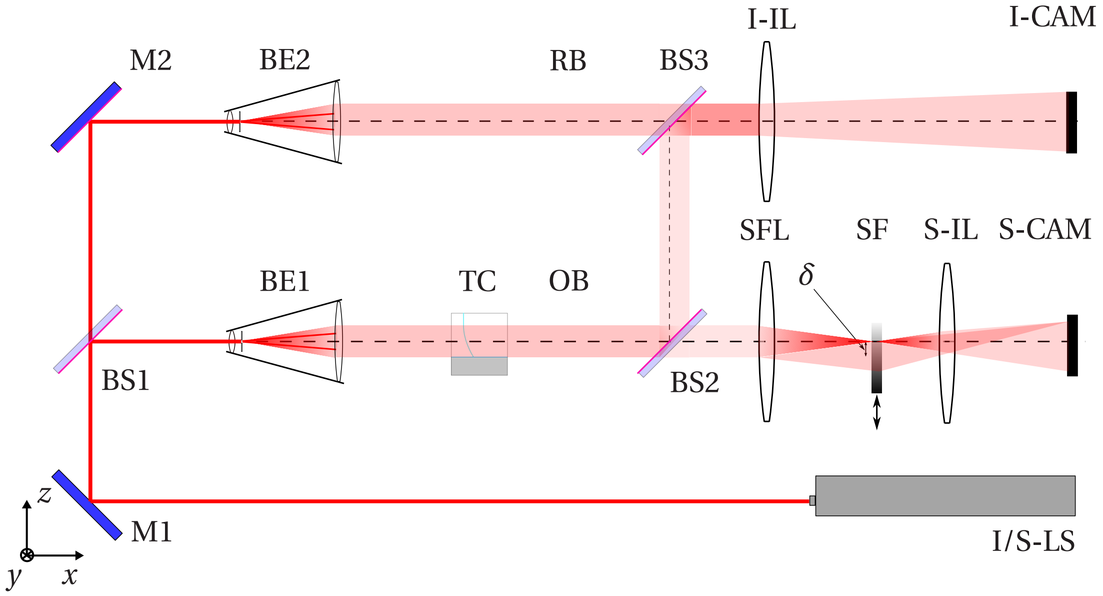

Legend:

Schlieren/Shadowgraphy S, Interferometry I, Light Source LS, Mirror M, Beam Splitter BS, Beam Expander BE, Test Cell TC, Reference Beam RB, Object Beam OB, Imaging Lens IL, Second Field Lens SFL, Schlieren Filter SF, Camera CAM

Figure 4.1: Scheme of the combined optical setup.

The setup was suggested in a previous publication [90]. It is similar to the patented setup of BLUE [18].

A 40 mW He-Ne-Laser provides coherent, monochromatic light at a wavelength of 632.8 nm. The laser beam is splitted into a reference beam RB and an object beam OB by beam splitter BS1, which are expanded by the beam expanders BE1 and BE2, respectively. The object beam propagates through the test section represented by the membrane test cell TC and is split into two parts by beam splitter BS2. One half of the beam propagates further through the subsequent Schlieren / Shadowgraphy components, the other half of the beam is united with the reference beam RB in beam splitter BS3. The latter beam splitter is also used to adjust the Finite Fringe pattern. The Interferometry setup part ends with its imaging lense I-IL and its camera I-CAM. The Schlieren setup consists of the second field lens SFL and a Schlieren filter SF plus an imaging lens S-IL and the camera S-CAM. The Shadowgraphy setup is identical to the Schlieren setup except for the Schlieren filter SF. Thus either Shadowgraphy or Schlieren can be combined with Interferometry for simultaneous measurements.

4.2 Obstructing Optical Phenomena

In the following, the optical phenomena are described, which were observed during experiments and which limit the applicability of the selected optical measurement techniques.

In figure 4.2, the cross section of the test cell at the measurement position is illustrated. Besides the focal planes of the optical setup (F1, F2), which will be discussed later on, different sections of the test cell are labeled which are crossed by the light propagating in positive x-direction. At the position of the membrane edge shown in figure 4.2 light is diffracted. HAUF ET AL. [66, p. 41] state that diffraction patterns caused by an opaque infinite half-plane like the membrane edge make a quantitative evaluation of Schlieren or Interferometry experiments impossible when the boundary layer height ranges in the same order of magnitude as the diffraction pattern. For channel heights of 1 mm, which is approximately the feed channel height in a commercial membrane module, such diffraction patterns become dominant. This could be observed in preliminary Schlieren experiments with a test configuration of 1 mm instead of 60 mm channel height (figure 4.3).

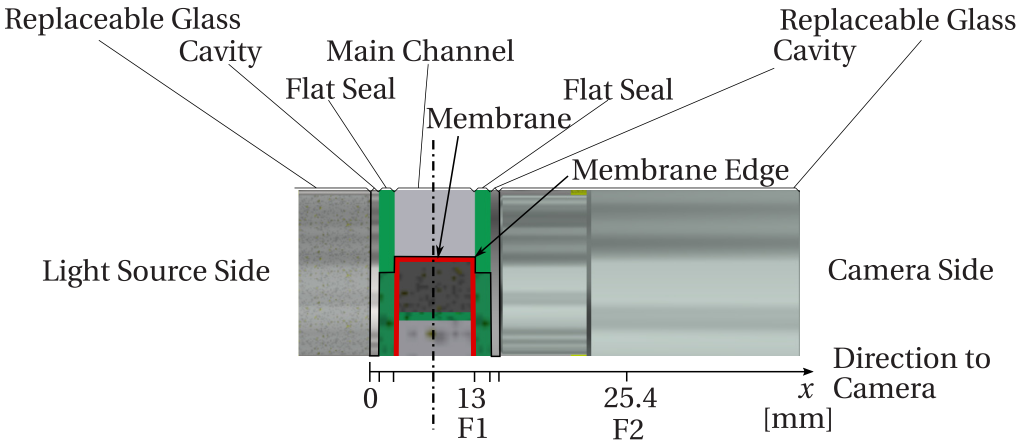

Figure 4.2: Cross section of test cell channel with different sections along the light path including real (F1) and virtual (F2) focal plane.

The left image in figure 4.3 denoted by CH1 shows a Schlieren reference image without concentration boundary layer. In the right image CH2 a boundary layer with height δ_C is depicted. The intensity distribution inside the boundary layer region is clearly obstructed by strong diffraction patterns.

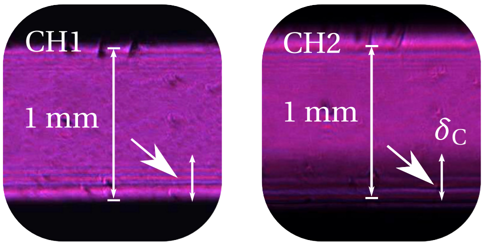

Figure 4.3: Limitation for slit-like test cell channels: diffraction patterns within boundary layer caused by opaque channel boundaries.

Even if a non-coherent white light source was used (figure 4.3) in contrast to the Laser Schlieren experiments of the present study (chapter 6), diffraction could not be avoided. In the Schlieren setup, spatial coherence was promoted by the source slit but also by the small feed channel height of 1 mm, which basically served as a second slit. At the same time, a high level of temporal coherence was achieved by a two-wavelength filter in the optical path in front of the optical test cell.

In order to minimize diffraction phenomena caused by the membrane edge (see figure 4.2) in the Laser Schlieren setup a small aperture due to small channel heights was avoided. In the high pressure test cell a maximum aperture with 8 mm is possible due to the geometry of the glass windows. With the channel height of 60 mm set in the present study, the channel geometry itself did not contribute to further increase spacial coherence of light.

However, diffraction phenomena still can significantly influence the optical measurement. With increasing refractive index gradients in the boundary layer, the boundary layer itself becomes what the membrane edge was before - a sharp change in refractive index causing diffraction patterns. In figure 4.4, an example is given for a Two-Wavelengths Schlieren experiment (D1) and a Digital Finite Fringe Interferometry experiment (D2).

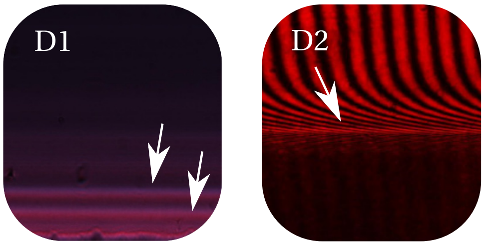

Figure 4.4: Limitation due to strong refraction index gradients: diffraction patterns caused by the boundary layer itself.

In the preliminary Schlieren experiment shown in D1, the transmittance of the Schlieren filter increases in negative z-direction. This means that the boundary layer appears bright as the light rays are deflected in negative z-direction by the refractive index gradient. In contrast, the bulk phase is darker. With this filter orientation, a better signal-to-noise ratio of the camera chip should be achieved. However, the reduced amount of light promoted diffraction. Therefore, it was decided to orientate the Schlieren filter such that its transmittance decreases in negative z-direction in the present study.

Another important issue concerns the adjustment of the focal plane of the optical system between test cell and camera. Focal plane and image plane at the camera chip form two conjugate optical planes [155, p. 35]. If there is more than one homogeneous medium (e.g. air) between these conjugated planes (e.g. air and glass windows) both a so-called virtual and a real focal plane have to be considered. If a further medium with a refractive index gradient is added, the focal plane turns from an even into a curved surface. Such a deformation of the focal plane can also be introduced by spherical aberration of the lenses used in the optics. In figure 4.5, a quantitative impression of the curved real and virtual focal planes of the Schlieren and the Interferometry setup is given for the experiment BW-P60.

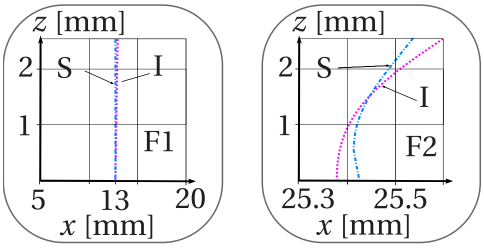

Figure 4.5: Curved real (F1) and virtual (F2) focal planes in an Interferometry (I) and Schlieren setup (S) for experiment BW-P60.

The real focal plane (F1) is adjusted such it contains the membrane edge shown in figure 4.2. The virtual focal plane (F2) lies within the step glass ($x \approx$ 25.4 mm in figure 4.2). As a camera chip is not curved, the curvature of the focal planes has to result in image distortions. To compensate such distortions is hardly possible without optical ray tracing. Image distortions due to spherical aberration (SA) of the lenses in the optical setup become prominent in particular in combination with strong refractive index gradients in the boundary layer. This is illustrated by means of a Shadowgraphy image in figure 4.6 (left image). Image distortions can be recognized best when comparing the diffraction patterns of small particles (impurities) on the optical glasses, see SA in figure 4.6. In the bulk region, these diffraction patterns are almost perfectly

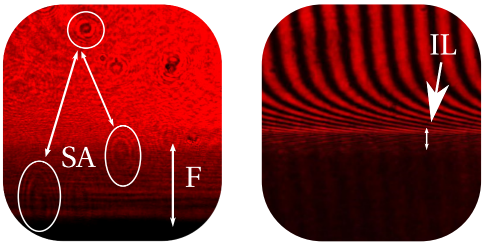

Figure 4.6: Image distortions due to spherical aberration (SA), attenuation of light intensity due to fanning (F) and loss of information (IL).

circular. At the bottom of the image, where high refractive index gradients are present, these diffraction patterns have an oval shape. Besides image distortion, the fanning effect (F) can be observed in the Shadowgraphy image on the left in figure 4.6. Due to fanning the recorded light intensity decreases in the boundary layer region. In the worst case, light intensity drops to zero before the membrane edge is reached. This loss of information makes a quantitative Schlieren or Shadowgraphy evaluation impossible.

Strong refractive index gradients can also limit the resolution of the Digital Interferometry measurements. An example is given in the right image of figure 4.6 denoted by IL. When the maximum frequency of the interference fringe pattern becomes higher than the sampling frequency of the digital camera chip [75, p. 27], the fringe pattern cannot be evaluated any more and information is lost. In addition, the fanning effect results in a decrease of the light intensity of the object beam. Ideally, the light intensity of reference and object beam should be the same to achieve maximum contrast of the interference pattern [152]. At high refractive index gradients, it can get difficult to distinguish between intensity maxima and minima. In addition, information can get lost also when the ray hits the membrane within the test cell. An example is illustrated later in figure 4.10 on page 105.

The optical simulation tool described in detail in the subsequent sections was developed to identify and quantify the observed optical phenomena. It will allow data analyses of Schlieren and Shadowgraphy experiments even in presence of strong refractive index gradients.

4.3 Optical Modeling

The optical simulation tool is described in the following. An illustrative overview of the numerical model is given below in figure 4.7. It is a model of the optical setup described in figure 4.1.

The 2D numerical ray tracing tool is implemented in MATLAB® R2016b [171]. The optical model consists of four main elements which are described in the following: the optical components, the optical system, the light rays and the so-called ray manipulator functions.

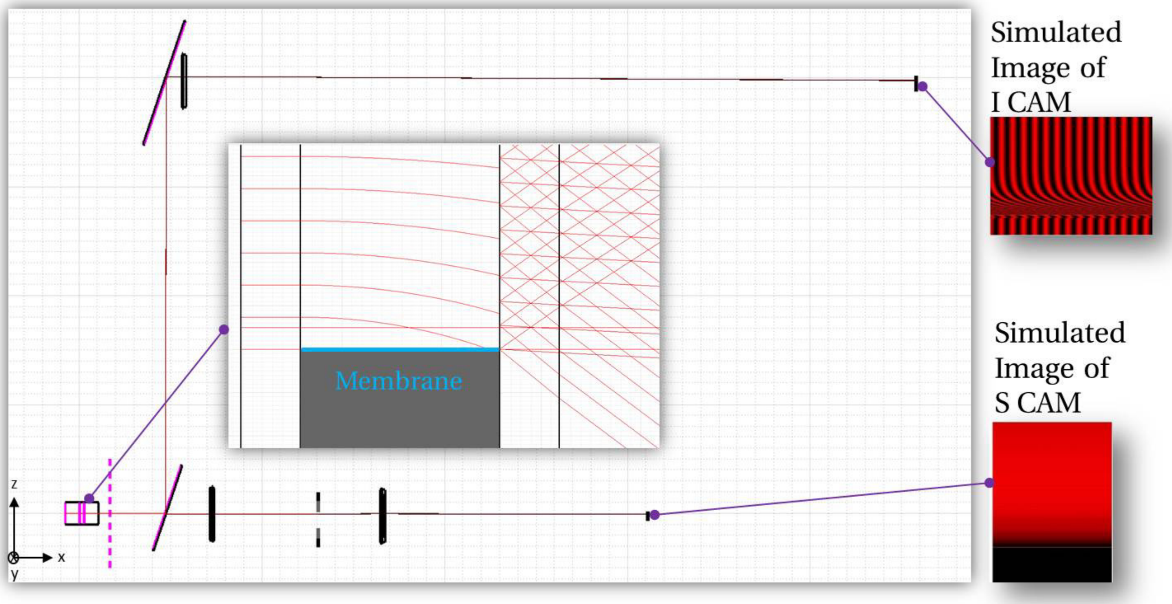

Figure 4.7: Ray tracing model of combined optical setup.

The Components

All relevant optical components are modeled. These are the light source, beam splitter, lens, lens mount, source slit, Schlieren filter, membrane test cell and camera. Each of these components has certain geometrical and optical properties, which are relevant for light propagation. To give a comprehensive overview of the all properties taken into account in the model, they are listed in table 4.1.

Table 4.1: Component properties.

Component	**Property**	**Symbol**
Light source	Number of sources	
	Number of rays per source	
	Max. opening angle of a source	
	Coherence / non-coherence	
	Wavelength(s)	λ_i
	Ray / wave optics model type	
Beam splitters, mirrors, windows, seals	Inclination angle relative to horizontal plane	α
	Trapezoid angle (see figure 4.8, $\beta = 0$ in present study)	β
	Thickness	d
	Length / height	l
	Reflecting surface (colored pink in the icon in figure 4.8)	
	Refractive index of material	
Lenses	Chromat / achromat	
	Radius 1 (crown)	r_1
	Radius 2 (crown / flint)	r_2
	Radius 3 (flint)	r_3
	Thickness 1	t_c
	Thickness 2	$t_{\mathrm{c},1}$
	Diameter	
	Refractive index of material 1 (crown)	
	Refractive index of material 2 (flint)	
Lense mounts	Type: tube or ring	
	Thickness	
	Thickness of lens holder	
	Diameter	
	Orientation of thread	
	Orientation of largest, outer lens radius (flint)	
Source slit	Opening width	
	Geometric dimensions of its mount	
Schlieren filter	Filter transmittance curve	$\tau(z)$
	Opaque filter frame geometry	
Test cell	Seal part in test cell channel → beam splitter	
	Cavity part in test cell channel → beam splitter	
	Membrane part in test cell channel with refractive index field (1D / 2D) → beam splitter	
	Height of optical access (aperture)	
	Inclination angle relative to optical axis: via coordinate-transformation	
Camera	Chip dimensions (vertical / horizontal)	
	Chip resolution (vertical / horizontal)	

In figure 4.8, the models of a beam splitter and a lens are shown to illustrate the geometric properties listed in table 4.1.

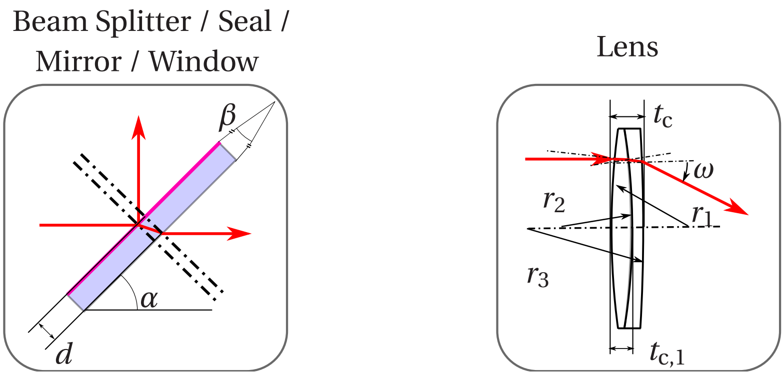

Figure 4.8: Geometric properties of components.

The Optical System

An optical system consists of different components and the media between them. The media modeled by their refractive indices. The components are linked by their spatial coordinates in x- and z-direction. For the model of the experimental setup, the exact positions of the components relative to each other have to be known. The position of a lens for example can be deduced easily from its location inside the mount. Such data are taken from CAD drawings provided by the supplier of the optomechanical components, THORLABS INC [173]. However, the measurement accuracy achieved for the x- and z-coordinate of each mount or other component relative to the membrane surface is hardly more than 1 mm, even if a laser rangefinder is used for distance measurements between the components.

Therefore, additional information is needed to model the experimental setup with high accuracy. To minimize inaccuracies of the x- and z-coordinate measurements of the optical components, a multi-parameter optimization with constraints is carried out using the MATLAB® built in solver `fmincon`. The spatial coordinates are the paramters to be optimized. The constraints are set by the measurement errors of the spacial coordinates. The solver aims to minimize the residuals of the model with respect to the following quality criteria:

- *z-coordinate of the image of the membrane edge along the ray path:* When no boundary layer is present, a screen is put into the ray path between test cell and camera. An image of the test cell aperture become visible on the screen. The membrane edge is part of the image frame. Its z-coordinate is measured at several x-positions along the ray path between test cell and camera. This needs to be done for both the Schlieren and the Interferometry setup.
- *Magnification:* Another quantity which determines the properties of the optical setup is its magnification. It is determined via a reference scale image recorded in both the Interferometry and the Schlieren setup, see figure 4.9 for illustration.

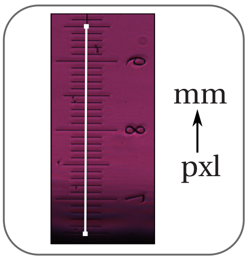

Figure 4.9: Reference scale image.

- *x-coordinate of the focal plane:* As it will be explained in more detail later in section 5.1, the experimental setup is designed such that it can be assured that the focal plane of both Interferometry and Schlieren is located at the membrane edge, see figures 4.2 and 4.5 for illustrations. Thus, the x-coordinate of the focal plane is well known and can be used as quality criterion.

Rays and Ray Manipulators Functions

A ray is mainly defined by spatial coordinates $(x,\ y)$, its inclination angle ω with respect to the optical axis (the horizontal plane) and its wavelength λ. It is initialized with a ray intensity $I = 1$ and a geometrical and optical path length $GPL = 0$ m and $OPL = 0$ m. An overview of all ray properties is given in table 4.2.

Table 4.2: Ray properties.

Ray	**Property**	**Symbol**
Ray	Spatial Coordinates	(x, z)
	Inclination Angle Relative to Horizontal Plane	ω
	Slope	$-\arctan(\omega)$
	Optical Path Length	OPL
	Sum of Optical Path Length	$\mathrm{sum}(OPL)$
	Geometrical Path Length	GPL
	Sum of Geometrical Path Length	$\mathrm{sum}(GPL)$
	Ray Intensity	I
	Wavelength	λ
	Ray Identifier	ID
	Reflectance Index	

The light source is modeled as a set of rays. This set of rays is bundled in a `struct`, which serves as input for the so-called ray manipulator functions. Such a function calculates the ray path through one or more components. A ray manipulator has its own coordinate system and is able to determine the relative position (west / east, north / south) of the entering ray. Depending on the properties of the component, the ray manipulator function modifies the ray properties according to geometrical and physical laws. The interfaces of the components are either even or spherically shaped surfaces. In the 2D model, they are modeled as mathematical functions of straight lines or circles. When a ray hits a transparent, non-reflecting interface, Snell's law

$$n_i \cdot \sin\omega_i = n_{i+1} \cdot \sin\omega_{i+1} \tag{4.1}$$

is applied resulting in a change of the ray slope at the interface. Note that the wavelength dependent refractive indices of all component materials need to be known. Information about the material of the optomechanical components are provided by THORLABS INC [173]. For these materials, wavelength dependent refractive index data can be obtained from glass manufacturers like SCHOTT AG [153]. If necessary, these wavelength dependent data can be interpolated to get data for the wavelength of interest.

When the ray hits a reflecting surface, the law of reflection is applied:

$$\alpha_{\mathrm{in}} = \alpha_{\mathrm{out}} \tag{4.2}$$

Here α is the angle between the normal of the reflecting surface and the ray. When the ray hits an opaque part, e.g. the frame of the source slit or of the Schlieren filter, the ray is simply deleted. The same applies for rays which do not enter the optical component. All media are assumed to be fully opaque or transparent, except for the Schlieren filter, which manipulates the intensity of the ray. The Schlieren filter transmittance function $\tau(z)$ is determined experimentally during a calibration procedure before the actual experiment. See section 5.1 for more details on calibration.

The most complex ray manipulator is the membrane test cell. It consists of seven main sections, see figure 4.2 on page 95. These are glass, cavity and seal section on the light source side, main channel with membrane on the bottom in the channel center, and seal section, cavity and glass on the camera side. The glass windows can be modeled by the beam splitter ray manipulator function. For the membrane channel, the 2D refractive index field normal to the membrane can be derived from the CFD model. For the seal and cavity part this is possible as well. In order to calculate the ray path within the test cell channel, the non-linear second order differential equation (2.75) needs to be solved. For this the standard MATLAB® solver `ode23tb` is used. For a small number of rays the ray path calculation is possible for the full 2D refractive index field at acceptable computational effort. However, about 1 million rays are necessary to gain a converged solution for a numerically generated image by the ray tracing simulation. In this case, a simulation with the 2D refractive index field takes too much calculation time. In order to reduce computational cost the refractive index field was approximated as follows:

On the light source side, both cavity and seal section are assumed to have bulk salt mass fraction. In the channel center, a uniform 1D refractive index profile is assumed using the data taken from the symmetry plane of the CFD model. On the camera side, in the seal and the cavity section as well the slopes of the respective rays are not changed after they exit the main channel region in the center with the membrane on the bottom. This procedure was best suited to approximate the ray path within the test cell with sufficient accuracy. In figure 4.10, the BW-P60 experiment (table 3.6, page 76) is shown, which exhibits strong gradients of salt mass fraction and refractive index.

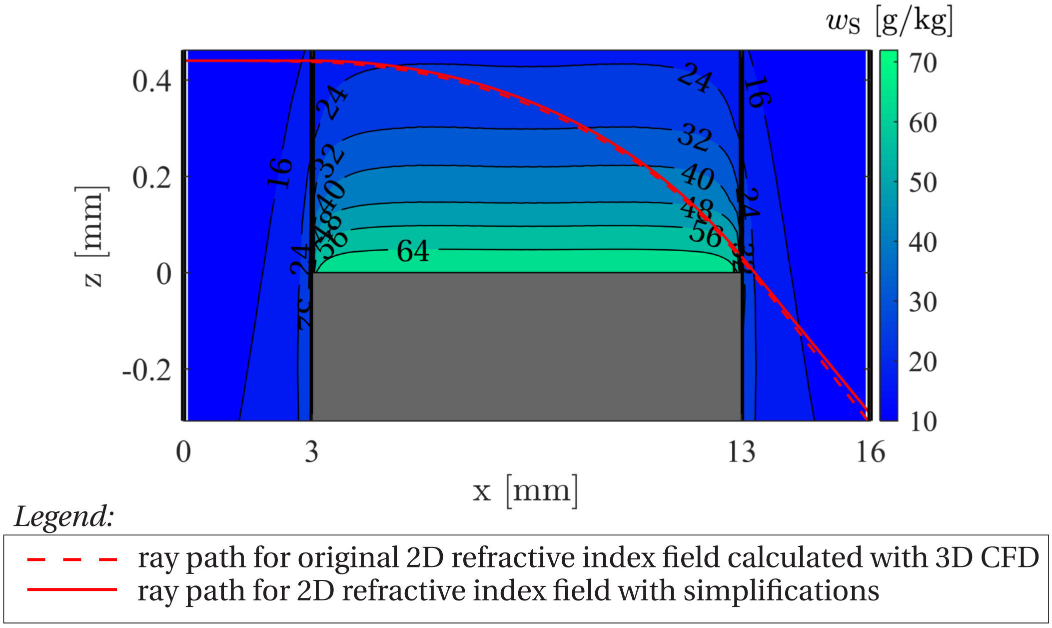

Figure 4.10: Ray path within test cell channel for experiment BW-P60 with a strong refractive index gradient in the boundary layer.

The path of the last light ray which does not hit the membrane is depicted for the two cases of a simplified (1D) and the original (2D) refractive index field. It can be seen that both ray deflection (relevant for Shadowgraphy) and ray exit angle (relevant for Schlieren) are in good agreement. In table 4.3 the relative difference $|e_{y,\mathrm{rel}}| = \left|\frac{y_{1\mathrm{D}}-y_{2\mathrm{D}}}{y_{2\mathrm{D}}}\right|$ is given for the most important ray properties at the channel exit, i.e. $x = 16$ mm in figure 4.10.

Table 4.3: Comparison of ray properties simulated with the simplified (1D) and the original (2D) refractive index field.

Relative Difference for	**Symbol**	**Value**
ray deflection	$\lvert e_{\Delta r,\mathrm{rel}}\rvert$	0.027
ray angle	$\lvert e_{\alpha,\mathrm{rel}}\rvert$	0.051
geometric ray path	$\lvert e_{GPL,\mathrm{rel}}\rvert$	$9.9 \cdot 10^{-5}$
optical path length	$\lvert e_{OPL,\mathrm{rel}}\rvert$	$4.0 \cdot 10^{-4}$
salt mass fraction on the membrane	$\lvert e_{w_{\mathrm{S,F,M}},\mathrm{rel}}\rvert$	0.032

Assuming an evaluation with Interferometry, the relative difference of the optical path length $|e_{OPL,\mathrm{rel}}|$ can be related to a relative difference of the feed salt mass fraction on the membrane:

$$|e_{w_{\mathrm{S,F,M}},\mathrm{rel}}| = f(|e_{n,\mathrm{rel}}|) = f(\frac{GPL_{\mathrm{2D}}}{GPL_{\mathrm{1D}}}\frac{OPL_{\mathrm{1D}}}{OPL_{\mathrm{2D}}} - 1) \approx f(|e_{OPL,\mathrm{rel}}|) \tag{4.3}$$

An error level of approximately 3.2% for the membrane salt mass fraction (see table 4.3) is obtained, which is a good compromise in exchange for lower computational effort.

Besides a significant reduction of computational time, the simplifications made for the 2D refractive index field have another advantage. The model of the seal/cavity channel section allows to easily account for small deviations of the seal width from the design specifications. These deviations occure due to compaction of the flat sheet seals during test cell assembling. But they can be easily measured. These measured data are used as input for the optical model.

The last ray manipulator to be described is the camera. When the rays reach the camera, they are clustered according to the pixels of the camera chip. In the ray optics model the intensities of the rays are summed up to determine the intensity distribution of the image.

As already indicated, for Schlieren and Shadowgraphy a total number of one million rays distributed over a height of 4.3 mm above the membrane were sufficient to achieve a converged numerical solution.

5 Experiments

In this chapter, an overview of the optical setup and the membrane test rig is given. The experimental data analysis is also addressed. This chapter concludes with membrane handling and testing procedures.

5.1 Combined Interferometry, Schlieren and Shadowgraphy

The focus of the following section is on the technical realization of the optical setup outlined in section 4.1.

5.1.1 Overview of Setup

Figure 5.1 gives an illustrative overview of the optical setup and table 5.1 provides the main technical details. For the successful implementation of the Interferometry setup the following was important:

- The difference of the geometric length between beam splitters BS1 and BS3 must be smaller than the coherence length of the applied laser, which is 0.316 m.
- The angle between reference beam RB and object beam OB needs to be as small as possible to be able to resolve the Interferometry fringes with the digital camera chip with limited spacial resolution [75, p. 34]. This is solved by aligning both beams via beam splitter BS3.
- The imaging lens I-IL is very helpful for the alignment of the optical setup, which needs to meet wavelength accuracy. Both reference beam RB and object beam OB are parallel when they are focussed on the same spot behind lens I-IL.

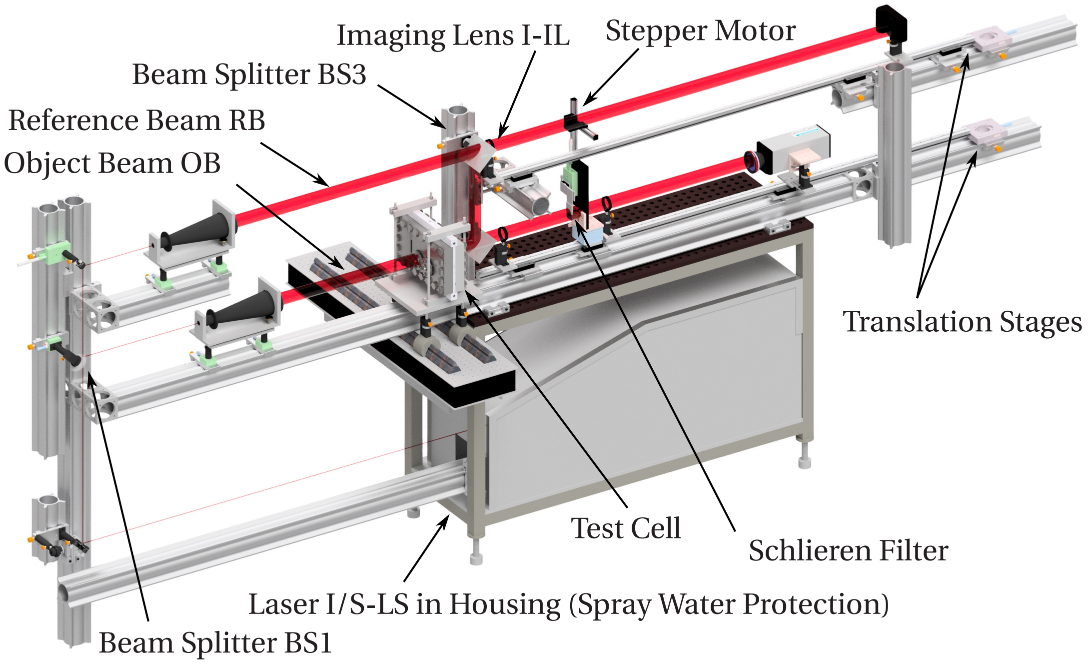

Figure 5.1: CAD model of the implemented optical setup.

Table 5.1: Properties of main optical components and setup.

Optical Component	**Index in Figure 4.1**	**Property**	**Value**
He-Ne-Laser	I/S-LS	Type	Siemens LGK 7626S
		Power	40 mW
		Wavelength	632.8 nm
		Coherence length	0.316 m
Interferometry	I-CAM	Type	Canon EOS 700D [60]
		Pixel size	4,3 μm x 4,3 μm [60]
	Setup	Magnification	3.01
		Resolution*	~ 8.4 μm
Schlieren / Shadowgraphy	S-CAM	Type	SVGA S/N 375LD0530 Sensicam [130]
		Pixel size	6,7 μm x 6,7 μm [130]
	Setup	Magnification	2.56
		Resolution*	~ 4.3 μm

(*) resolution $\frac{\lambda}{2n\sin\theta}$ according to ABBE [1]

Decisive for an efficient, reproducible and highly accurate experimental workflow for the conduction of the Schlieren experiment was the motion control of the Schlieren filter. The mount of the filter was equipped with a stepper motor, see figure 5.1. It was triggered with an Arduino control unit, integrated in the Labview Control software of the test rig. In order to gain the relationship between Schlieren filter transmittance and z-coordinate, images are recorded for several equally spaced z-positions (usually 200 steps). In order to compensate small intensity fluctuations of the laser, usually ten of such calibration sets are recorded and averaged afterwards. The sensitivity of the Schlieren measurement depends on the filter transmittance function, see e.g. [65, p. 11]. The choise of the Schlieren filter depends on the maximum refractive index gradient. Therefore, Schlieren filters tailored for the experimental needs were designed and manufactured.

Important in both beam paths is the determination and the proper adjustment of focal plane and optical magnification given by the optics behind the test cell. The lens systems and cameras were mounted on extra rails connected with translation stages (figure 5.1) to be able to adjust each rail position and thus each focal plane with micrometer accuracy. In order to be able to experimentally determine the optical magnification with a reference scale on the camera side of the installed test cell (figure 4.9), the optical system can be moved as a whole. In this way, the reference scale can be focussed without changing the sensitive optical setup itself.

5.1.2 Evaluation of Digital Finite Fringe Interferometry Data

While Shadowgraphy and Schlieren data are only evaluated in combination with optical ray tracing, Interferometry data are processed with an evaluation algorithm to directly determine the refractive index in the boundary layer. The evaluation algorithm needs to meet the following requirements:

1. Extract the target quantity $\Delta OPL = OPL_i - OPL_0$ from the interferogram with maximum sensitivity.
2. Avoid measurement inaccuracies due to unwanted intensity variations

in the recorded image. Such intensity variations can be caused by non-uniform light distribution within the reference or the object beam. Potential reasons are misalignment, dust particles on optical components, fanning or diffraction effects caused by the boundary layer itself.

3. Vibrations of the optical setup should not affect the accuracy of the evaluation result. As the test cell is part of both optical and hydraulic setup, vibrations caused by pumps in the hydraulic setup cannot be decoupled from the optical setup.

Evaluation algorithms applied for boundary layer investigations on desalination membranes often rely on the fringe counting method [23, 44, 142, 145, 146]. The refractive index profile can be determined via counting fringes from bulk phase to membrane as the difference of the optical path length ΔOPL is constant between two neighbouring fringes. In the present study fringe counting is avoided due to the following reasons:

1. The refractive index profile can be determined only in a discrete way with fixed discretization steps. This is a limitation especially for weakly pronounced boundary layers, which result in only a few fringes.
2. In the transition region from bulk phase to boundary layer the fringe counting method is limited by its rather poor sensitivity [165].

A methodology which meets the specified requiements and avoids the disadvantages of fringe counting methods goes back to TAKEDA ET AL. [165] in 1982. They rely on Finite Fringe Interferometry introducing a constant spacial carrier frequency into the Interferometry image. Tilting the beam splitter BS3 (figure 5.1) a uniform fringe pattern can be introduced which serves as carrier frequency, as it can be seen in the raw image depicted in the following figure 5.2.

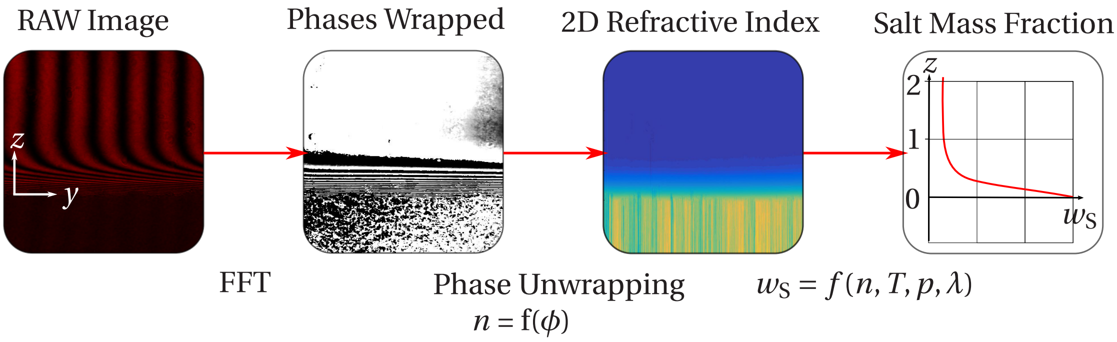

Figure 5.2: Evaluation of a Digital Finite Fringe Interferometry image.

JANG [76] implemented the method of TAKEDA ET AL. [165] in MATLAB® and published his code. With his permission, his code is integrated in the evaluation algorithm of the present study. In order to give an example of the Finite Fringe boundary layer evaluation, the main evaluation steps are presented in figure 5.2.

Instead of counting fringes to determine a discrete function of the optical path length OPL, the fringe pattern is analysed by a Fast Fourier Transform (FFT) to calculate a continuous function for OPL from the phase ϕ:

$$\phi = \frac{OPL}{\lambda} \cdot 2\pi \tag{5.1}$$

Numerically, phase ϕ cannot be extracted directly as a continuous function from the raw images. The so-called wrapped phase ϕ is limited to the range $[0{,}2\pi]$. In order to avoid discontinuities in the signal, phase ϕ needs to be unwrapped starting in the bulk phase by adding 2π at the discontinuities. Then the resulting, continuous phase $\phi(z)$ is related to its reference value in the bulk phase (index δ_C) to calculate $\Delta\phi = \phi(z) - \phi_{\delta_\mathrm{C}}$ and refractive index n:

$$n = n_{\delta_\mathrm{C}} + \frac{\Delta\phi}{2\pi}\frac{\lambda}{L} \tag{5.2}$$

The refractive index of the bulk phase can be calculated from the measured operating conditions $(w_\mathrm{S}, T, p, \lambda)$. The ray path in the test section is approximated by the main membrane channel width $L = 0.01$ m. This can result in a slight over-prediction of the refractive index profile if strong refractive index gradients are present (L is increased). A correction could be performed by means of the ray tracing tool but was avoided. Of course, boundary layers with strong refractive index gradients could be measured by means of Digital Interferometry but not to the full extend from bulk to membrane. Instead, only the upper part of the boundary layer was evaluated until the measurement resolution limit was reached, see section 4.2. In this upper boundary layer part ray deflection and its influence on the measurement result is small. Thus, in the analysis presented later in section 6, it was decided to perform the Interferometry evaluation without any manipulations.

5.2 Membrane Test Rig

The membrane test cell is embedded in a hydraulic loop equipped with measurement sensors and actuators for monitoring and automatic control. In the following, a brief overview of the test rig and the measurement accuracies of the most relevant sensors is given.

5.2.1 Overview of Setup

The flow chart of the test rig is presented in figure 5.3.

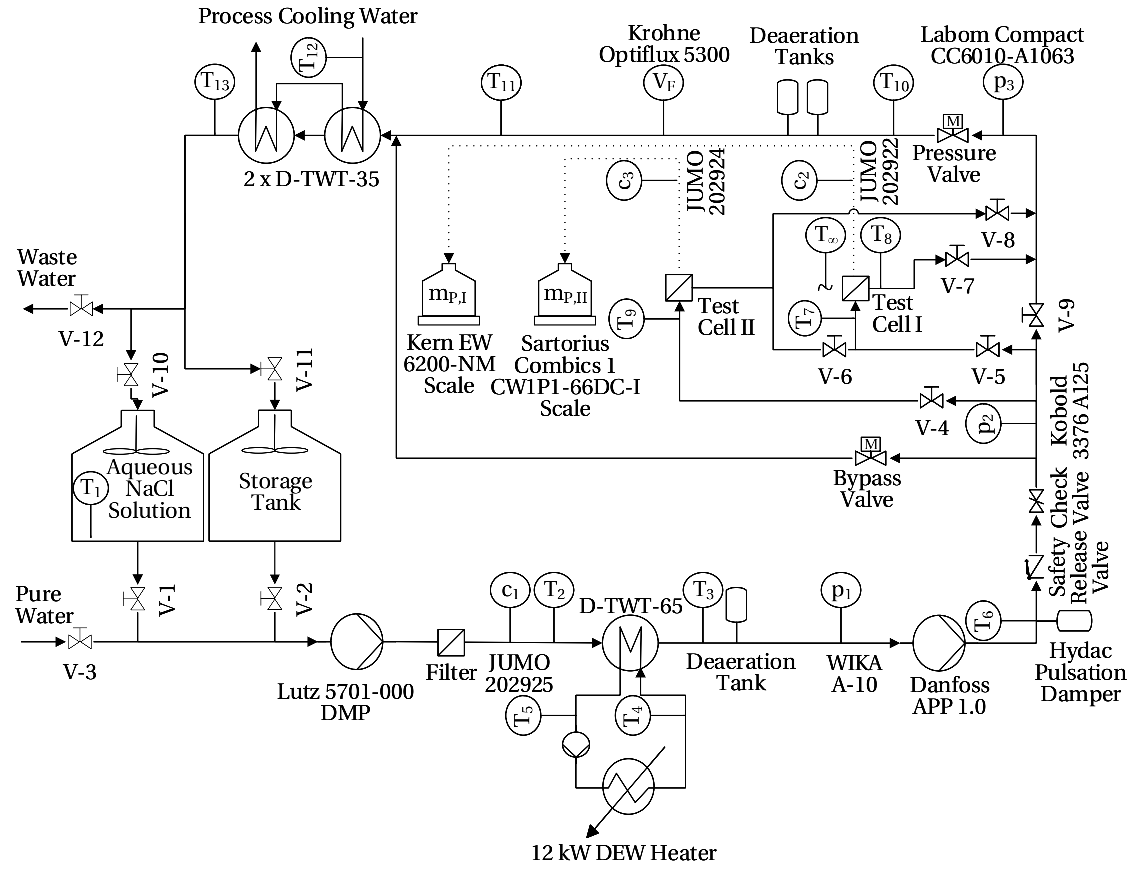

Figure 5.3: Schematic of the test rig.

These are the main requirements determining the design of the test rig:

- **Operation at typical RO operating pressures up to 60 bar:** A Danfoss APP 1.0 axial piston pump often used in RO applications [28] is fed by a double membrane piston pump DMP to provide the necessary operating pressures. The pressure level and the flow rate are adjusted by two needle valves, denoted by *bypass valve* and *pressure valve*. Both valves are equipped with a stepper motor and an electronic control via an Arduino microcontroller. Process inherent pulsations caused by the pumps are damped by an HYDAC pulsation damper after the high pressure pump.
- **Operation at temperatures up to 45°C:** A PID controller is designed to control the power input of the external heating cycle such that the temperature at the test cell inlet can be maintained at a constant temperature level. A mobile air conditioning system (not depicted in the flow chart) is used to control the ambient temperature inside the laboratory. An external cooling cycle after the test cell keeps the temperature in the feed tank at the constant laboratory temperature level.
- **Reproducibility of measurement results:** Two membrane test cells can be integrated within the setup, in series or parallel. Moreover, adjustment of (almost) identical operating conditions for different measurement campaigns was guaranteed. With a CompactRio 9074 from National Instruments [119] a fully automatized monitoring of sensors and control of actuators was achieved. The actuators include the stepper motors of valves and Schlieren filter, the heater, the stirrer in feed tank and the pumps. A LABVIEW control software was developed to allow data acquisition and data-logging, control of actuators, control of cameras, documentation of experiments and fail-safe operation.

Details about the investigated fluid can be found in appendix B. In order to keep the fluid pure from any deposits in the piping system, a pre-filtration unit with a 10 μm filter is installed after the double membrane piston pump DMP. The filter serves also as an additional damper for the DMP pump. Continuous stirring of the storage tanks avoided stratification inside the tanks and guaranteed a well-mixed feed solution throughout the experiments.

5.2.2 Sensors and Measurement Accuracies

An overview of sensors and actuators is given in figure 5.3. The measurement errors of the most important sensors are listed in table 5.2.

Table 5.2: Measurement errors of sensors. The nomenclature of the sensors is in accordance with the flow chart provided in figure 5.3.

Measurement Signal	**Description**	**#**	**Sensor Type**	**Error**	**Ref.**
Temperatures	TC feed inlet	T_7, T_9	PT-1000 1/3 DIN EN60751	±0.15 K*	DIN
	TC feed outlet	T_8	PT-1000 1/3 DIN EN60751	±0.15 K*	DIN
	ambient	T_∞	PT-100 A DIN EN60751	±0.21 K*	DIN
Pressures	TC feed inlet	p_2	Kobold 3376 A125	±0.5%	[85]
	TC feed outlet	p_3	Labom Compact CC6010-A1063	±0.2%	[95]
Salinity	feed	c_1	JUMO 202925 K-10 with ecoTRANS Lf 01/02	2% / 0.1 K	[79]
Mass	TC I permeate	$m_{\mathrm{P,I}}$	Kern EW 6200-2NM	0.01 g	[83]
	TC II permeate	$m_{\mathrm{P,II}}$	Sartorius Combics 1 CW1P1-66DC-I	±0.2 g	[147, p. 94]
Flow rate	feed ≈ brine volume flow	V_F	Krohne Optiflux 5300 DN 2.5	max. ±1.5%	[89]

(*) for $T = 303.15$ K

Accurate temperature measurements are necessary, especially to determine the fluid bulk temperature inside the test cell. It was tried to integrate uncoated, but small-scale PT1000 temperature sensors inside the test cell. However, their measurement signal was sensitive to the salt mass fraction in the fluid. Therefore, the fluid bulk temperature is approximated by the arithmetic average of the TC inlet and outlet temperatures. The ambient temperature was monitored in close vicinity to the test cell.

The pressure difference between TC inlet and outlet was negligibly small. Therefore, the arithmetic average between both signals was taken as hydrostatic feed pressure relative to the ambient pressure.

The feed salinity sensor is a conductivity meter and was calibrated in regular intervals. The permeate salinity sensors were used to detect membrane breakthrough or test-cell leakages but were not suitable to measure permeate salinity due to the small permeate production rates leading to a long dead-time from membrane to sensor. Permeate salinity is therefore determined from the boundary layer experiments (chapter 6).

Because of the small membrane area and thus small permeate production rates, the withdrawal of permeate from the feed has a negligible effect on the feed / brine volume flow rate. The effect is smaller than the measurement error of the flow rate sensor, compare tables 5.2 and 5.3.

Table 5.3: Error estimation.

Quantity	**Value**	**Unit**
minimum feed flow rate	3	kg/h
maximum permeate mass flux	23	kg/m^2h
membrane area (0.18 m x 0.01 m)	0.0018	m^2
error when neglecting permeate production	1.38	%

The measurement accuracy of the permeate mass flux depends on the permeate production itself, compare figure 5.4. The permeate is collected in a storage tank which is put on top of a scale. The weight of the permeate is measured over time, see figure 5.4. The slope of a least-square fit (FIT) determines the flux taking the membrane area into account. At low fluxes, there is no continuous flow of permeate into the storage tank. Only droplets of permeate reach the tank on the scale from time to time.Thus, the permeate flux measurement is less accurate at lower fluxes. For a qualitative estimate, hypothetical measurement errors of +/- 10% are added to the actual permeate flux result in figure 5.4 ($FIT_{+10\%}$, $FIT_{-10\%}$). To be able to measure also low fluxes at high accuracy the time interval for flux determination was increased from about 5 minutes at maximum flux levels to about 20 minutes at lowest flux levels.

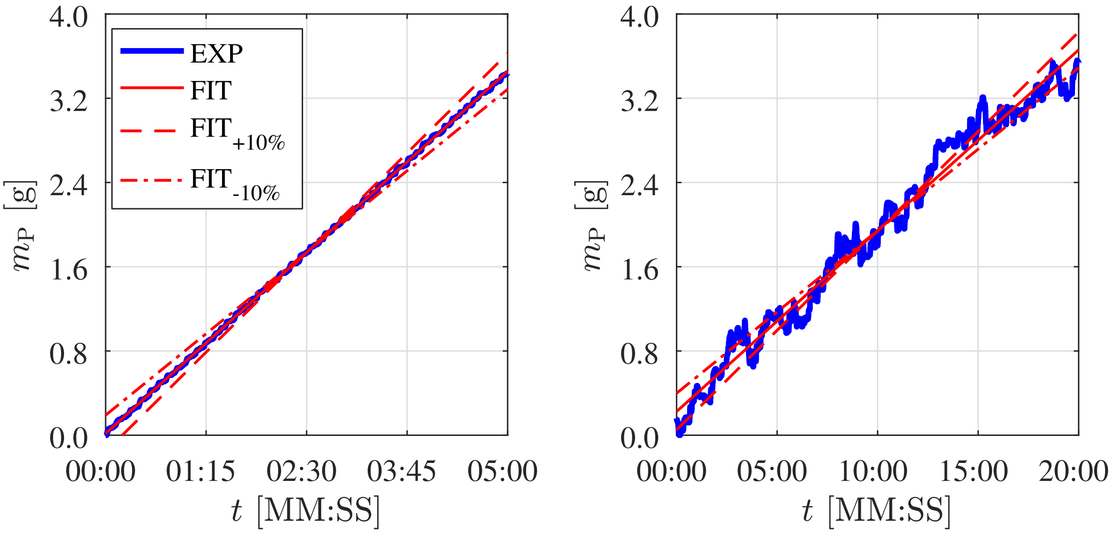

(a) High permeate flux: 22.89 kg/m^{2}h (b) Low permeate flux: 5.72 kg/m^{2}h

Figure 5.4: Permeate flux measurement.

5.2.3 Membrane Handling and Testing Procedure

The tested membrane samples originate from a commerically available membrane module with the product name TML10D [174] from TORAY INDUSTRIES, INC. The membrane module was opened to cut out samples from its membrane sheets. The samples were stored inside a refrigerator where a constant low temperature level and a dark environment was guaranteed to prevent biological growth during membrane storage. As additional measure, the membranes were stored in a one weight percent sodium bisulfite storage solution and vacuum packed in oxygen barrier bags, as recommended in the membrane module data sheet [174].

During test cell assembly, the membrane was continuously wetted with pure water.

Before a new membrane sample was tested, it was pre-compacted at a pressure level high enough to perform irreversible compaction, which is around 40 bar as experimentally determined by HUSSAIN ET AL. [73, p. 20]. In this way it is guaranteed that only reversible compaction occurs during membrane performance tests.

In order to check the integrity of the membrane sample installed inside the new high pressure membrane test cell, the water permeability tests were carried out with two test cells. Upstream in the hydraulic loop a conventional flat sheet membrane test cell [186] without optical access was installed in series to the new high pressure test cell. The membrane area of the conventional test cell was 0.0137 m^2. Its feed and the permeate channel was filled with spacers taken from the TML10D [174] membrane module. If one of the two tested membrane sheets were damaged, this would have been detected due to significantly different results for the water permeablity constants.

During the boundary layer experiments with saline water, only the high pressure test cell was used. In this case priority was set to be able to determine pressure, fluid temperature, flow rate and salinity in closest vicinity to the high pressure test cell to guarantee maximum accuracy of the input data to the CFD model. In this case, membrane integrity was monitored by the permeate salinity sensor (section 5.2.2).

Each experiment was run for one hour under the same test conditions before data were used for further analysis. A preliminary study of the boundary layer dynamics showed that one hour is sufficient to reach steady-state.

6 Results

In this chapter, the results of the revised LMPM introduced in section 3.3 are presented. In section 6.1, the pure water experiments for measuring the water permeability constant A are discussed. Afterwards in section 6.2, the salt permeability constant B is determined by means of boundary layer experiments. The results are checked for plausibility in section 6.3 before the most important findings are concluded in section 6.4.

6.1 Determination of the Water Permeability Constant

The water permeability constant A is a function of temperature and pressure, as introduced in section 2.1.4. With pure water, A can be determined measuring only water flux and hydrostatic pressure difference as the osmotic pressure difference is zero.

As outlined in section 5.2.3, the pure water experiments are run with two test cells in series (section 5.2.3). In the optical test cell, a new membrane (sample I) is installed. In the conventional flat sheet membrane test cell, a precompacted membrane is installed (sample II), which was already used in preliminary experiments at temperatures up to 40°C and pressures up to 40 bar.

In order to determine the temperature and pressure dependence coefficients α_T and α_p in equation (2.31), steady-state experiments are carried out at different temperature and pressure levels shown in figures 6.1(a) and 6.1(b). A maximum pressure level of 40 bar was chosen to obtain irreversible compaction of the new membrane (section 5.2.3) but to minimally stress the membrane before the boundary layer experiments. After irreversible compaction and a rest period of three days for the membrane, the experiment is repeated at the lowest temperature level of 24°C.

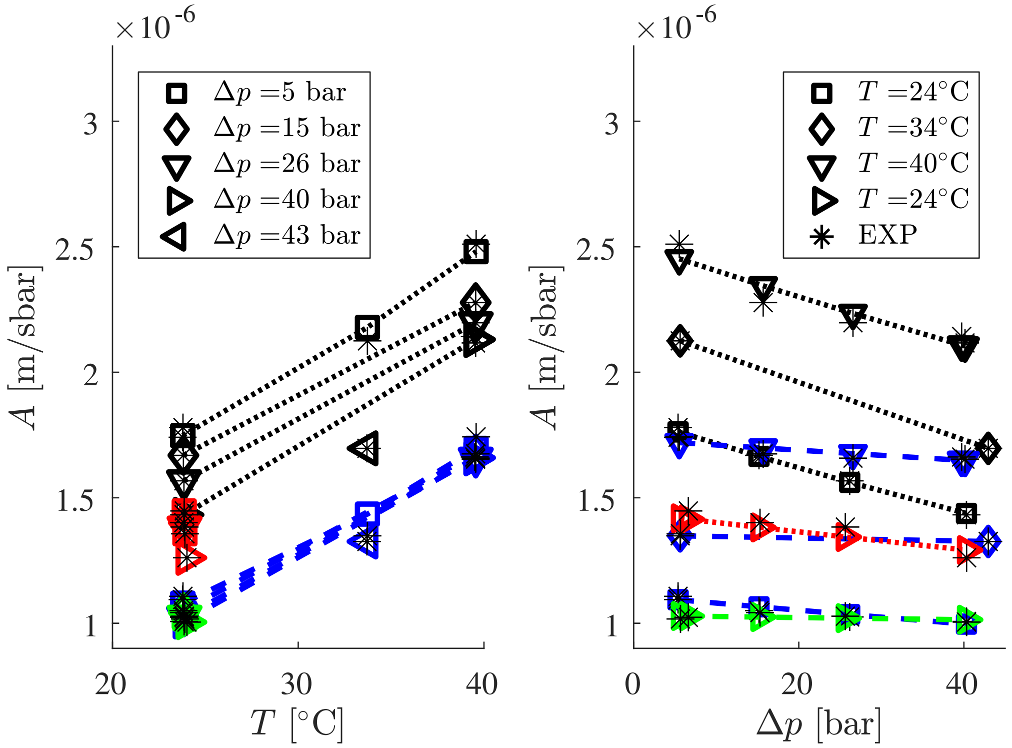

(a) Temperature dependence at different pressure levels.

(b) Pressure dependence at different temperature levels.

Figure 6.1: Experimental raw data ($*$ EXP) and least square fits (lines). Sample I pre-compaction (dotted, black) and post-compaction (dotted, red). Sample II post-compaction 1 (dashed, blue) and post-compaction 2 (dashed, green).

The following conclusions can be drawn from the results in figure 6.1(a) and 6.1(b).

- Discussing the results of the sample tested in the conventional test cell at $T = 24$°C (blue/green), it can be stated that after irreversible compaction the absolute value of A does not significantly change anymore. This is also true for its reversible dependence on pressure.
- Discussing the results of the sample tested in the new high pressure test cell at $T = 24$°C (black/red), a decrease of A can be observed between 10-15% at all pressure levels during irreversible compaction.

- While the temperature dependence is similar for both membrane samples, no matter if compacted or not, the pressure dependence is higher for the new membrane before irreversible compaction. This is plausible as irreversible and reversible compaction happen simultaneously for the new membrane, while only reversible compaction takes place for a compacted membrane. The pressure dependence is similar for both membrane samples after compaction. These results seem plausible and are in accordance with the experiments of HUSSAIN ET AL. [73, p. 20].
- In the compacted state, the absolute values of the water permeability constant are slightly different for the two membrane samples. However, the relative deviation is in a similar range as reported in literature (section 1.1). Thus, both membranes are assumed to be intact and undamaged.

In order to determine the correlation for A for the membrane sample in the high pressure test cell (sample I), the data collected after irreversible compaction were used to derive A_0 and α_p. The data collected before irreversible compaction could be used to calculate α_T as the temperature dependence appears to be independent of the compaction state anyway.

The results are summarized in table 6.1. The values of the different coefficients are similar to the ones from literature presented in section 2.1.4. These data are used to specify the water permeability constant in the CFD model used in the subsequent analyses.

Table 6.1: Water permeability characteristics of the membrane sample I according to equation (2.31).

Parameter	**Symbol**	**Value**	**Unit**
Temperature coefficient	α_T	6.6	-
Pressure coefficient	α_p	-0.0027	-
Reference water permeability constant	A_0	$1.45 \cdot 10^{-6}$	$\mathrm{m\,s^{-1}\,bar^{-1}}$
Reference pressure	p_0	1	bar
Reference temperature	T_0	298.13	K

6.2 Determination of the Salt Permeability Constant

After measuring the water permeability constant, the salt permeability constant can be determined according to the methodology described in section 3.3. The test conditions for the steady-state boundary layer experiments are given in table 3.6 on page 76. The test procedure is described in section 5.2.3.

6.2.1 Sensitivity Analysis

The methodology described in section 3.3 is based on an iterative determination of the salt permeability constant B. B is changed until the permeate flux of the CFD simulation corresponds to the measured permeate flux. In order to be able to interpret the results, a sensitivity study is carried out investigating the influence of the water and the salt permeability constant on the permeate flux. The study is done with the 2D CFD model (section 3.1.2) for the brackish water test conditions (table 3.6). Membrane boundary condition L is used, see section 3.1.4 on page 72.

In figure 6.2(a), the CFD results are depicted for three different salt permeability constants $B = 2 \cdot 10^{-7}$, $5 \cdot 10^{-7}$ and $8 \cdot 10^{-7}$ m/s. Each simulation is carried out four times increasing the water permeability constant A from $A = 1 \cdot 10^{-6}, 1.3 \cdot 10^{-6}, 1.7 \cdot 10^{-6}$ to $2 \cdot 10^{-6}$ m/sbar. The permeate flux increases with A in all cases. In figure 6.2(a), the range of the permeate flux change due to A is illustrated by means of error bars.

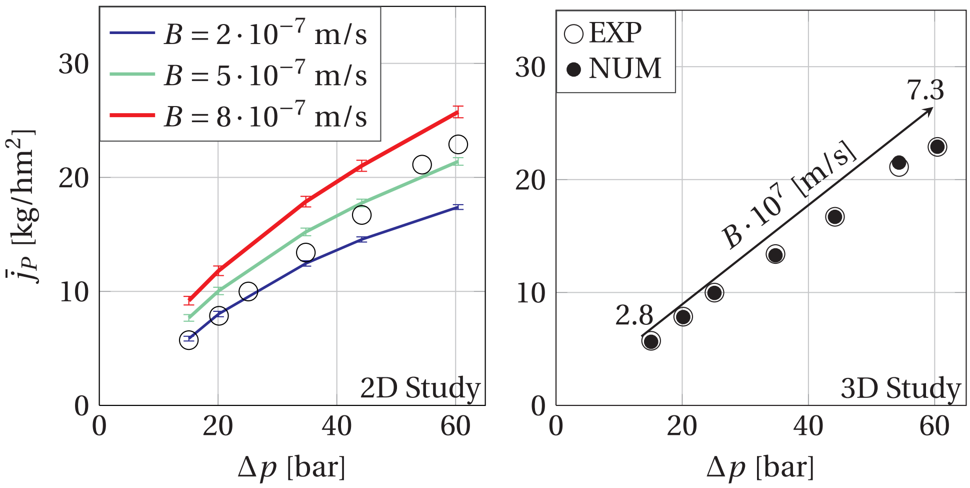

(a) 2D CFD study: sensitivity of permeate flux $\bar{j}_P$ on variations of B (solid lines) and on variations of A (error bars). Membrane boundary condition L is used.

(b) 3D CFD study: A from table 6.1 and B from iteration as explained in section 3.3. Membrane boundary condition M is used.

Figure 6.2: Sensitivity study and results.

From figure 6.2(a) several conclusions can be drawn: Firstly, the CFD curves for a specific B lets sense an interception with the Δp-axis, where $j_\mathrm{P} = \rho_\mathrm{W} A(\Delta p - \Delta\pi) = 0$. For a membrane with ideal separation characteristics, i.e. $B = 0$ m/s, Δp corresponds to the osmotic pressure of the fluid inlet $\pi_{\mathrm{F},0}$ which is around 8 bar for $w_{\mathrm{S,F},0}$ =10 g/kg. For increasing salt permeability constants $B > 0$ m/s this interception point is expected to be shifted to lower pressures, which corresponds with the results of figure 6.2(a). For constant B and increasing Δp, the permeate flux curve faces saturation. This means that the hydrostatic pressure increase is more and more compensated by a simultaneous increase of the osmotic pressure difference across the membrane due to a growing concentration boundary layer.

Secondly, while B has a significant influence on the overall permeate flux, the influence of A seems to play a minor role. In this case, the impact of a flux change caused by a changed net driving pressure across the membrane is higher than the one due to a change of the water permeability constant A.

A higher water permeability constant leads to higher fluxes, especially in close vicinity of the test cell inlet. Consequently, salt mass fractions increase more significantly in flow direction. The salt mass fraction in the permeate also increases but not to the same degree. Thus, the net driving pressure is reduced compensating the positive effect of an increased A.

In contrast to a higher water permeability constant, an increased salt permeability constant results in a reduced osmotic pressure difference and an increased net driving pressure across the entire membrane. This influence of the salt permeability constant on overall permeate flux depends on the impact of the permeate osmotic pressure on the total net driving pressure. It becomes more relevant the lower the net driving pressures and the higher the feed salt mass fractions on the membrane. In the present study, the salt mass fractions on the membrane become rather high due to the unobstructed channel geometry without spacers. Furthermore, net driving pressures are rather low compared to the hydrostatic pressures. To give an estimate of the net driving pressure levels occuring in this study, an example is given:

The net driving pressure can be easily estimated from the permeate flux for a known value of A and an approximate water density of 1000 kg/m^3:

$$\bar{j}_\mathrm{P}\ [\mathrm{kg/hm^2}] \xrightarrow{\cdot 0.2} NDP\ [\mathrm{bar}],\ \text{for}\ A = 1.4\cdot 10^{-6}\mathrm{m/sbar} \tag{6.1}$$

Considering the experimental fluxes presented in figures 6.2(a) and 6.2(b), the mean net driving pressure ranges between 1 and 5 bar, which is low.

Thirdly, comparing experimental and CFD results in figure 6.2(a), it becomes clear that the experimental results cannot be explained by a constant salt permeability constant. This observation is confirmed by the result of the iterative determination of B with 3D CFD according to the methodology described in section 3.3. B increases from BW-P15 to BW-P60, see figure 6.2(b). The iteration results are shown for membrane boundary condition M as they will be needed as reference later. However, the results for boundary condition L are similar and lead to the same conclusions. In order to double-check that a varying B is not a numerical artefact but an explanation for the experimental observation, the simulated mass transfer through the membrane is validated by boundary layer experiments. In section 6.2.5, the discussion will be whether hydrostatic pressure difference Δp or salt mass fraction on the membrane $w_{\mathrm{S,F,M}}$ has the main influence on B. In section 6.3, a physical explanation will be given.

To be able to estimate the sensitivity of the concentration boundary layer at the measurement position, the 3D CFD results are shown in dependence of B for BW-P60 in figure 6.3. Membrane boundary condition M was used.

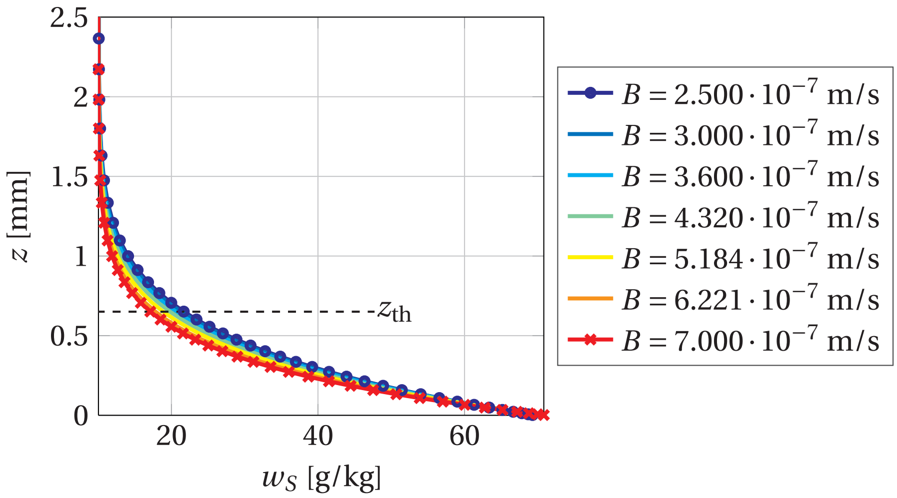

Figure 6.3: Concentration boundary layer from CFD in dependence of B at position P2 at the symmetry plane for BW-P60.

From $B = 2.5 \cdot 10^{-7}$ m/s to $B = 7 \cdot 10^{-7}$ m/s, the relative error drops to $e_{\bar{j}_\mathrm{P},\mathrm{rel}} = 0.3\%$ (see equation (3.13)). The boundary layer profile for $B = 7 \cdot 10^{-7}$ m/s (colored red in in figure 6.3) is taken as reference for two quality criteria. First, the mean relative deviation $e_{w_\mathrm{S},\mathrm{rel}}$ of the other boundary layer profiles $w_\mathrm{S}(\mathrm{z})$ from this reference profile is calculated. What turns out later is that below a certain threshold value z_th the Interferometry data cannot be evaluated anymore. For the considered experiment BW-P60, z_th is 0.66 mm. Therefore, $e_{w_\mathrm{S},\mathrm{rel}}$ takes only $w_\mathrm{S}(z)$ data for $z > z_\mathrm{th}$ into account. Second, the relative deviation $e_{w_\mathrm{S,th},\mathrm{rel}}$ of $w_\mathrm{S}(z_\mathrm{th})$ from the corresponding value at the reference profile is evaluated. The results for the different boundary layer profiles depicted in figure 6.3 are listed below in table 6.2. They are discussed later in context with the experimental boundary layer data.

It can be concluded from changes of the concentration boundary layer in dependence of B (figure 6.3 and table 6.2) that the boundary layer profile is a good validation criterion for the salt permeability property of the membrane. The achievable accuracy of the determination of B by means of the concentration boundary layer is estimated in the next section.

Table 6.2: Comparison of concentration boundary layer data in dependence of B.

$B \cdot 10^7$ [m/s]	$e_{B,\text{rel}}$ [-]	z_{th} [-]	$e_{w_{\text{S,th}},\text{rel}}$ [mm]	$e_{w_{\text{S}},\text{rel}}$ [-]
2.500	-0.64	0.66	26.67	11.48
3.000	-0.57	0.66	24.25	10.28
3.600	-0.49	0.66	20.42	8.44
4.320	-0.38	0.66	15.66	6.30
5.184	-0.26	0.66	10.13	3.95
6.221	-0.11	0.66	3.98	1.48
7.000$^{(*)}$	0.00	0.66	0.00	0.00

$^{(*)}$ Denotes the reference.

6.2.2 Brackish Water Conditions

The boundary layer results are discussed by means of raw images, normalized intensity profiles and salt mass fraction profiles depicted in figures 6.4 to 6.6. The raw images were recorded with the optical setup described in section 5.1. The normalized intensity profiles are determined as previously explained by means of figure 3.13. The experimental salt mass fraction profiles were derived from the Interferometry raw data, as described in section 5.1.2. The CFD salt mass fraction profiles were extracted at position P2 from the 3D data resulting after the iteration of B described in section 3.3. A was modeled with the parameters listed in table 6.1. Both membrane boundary conditions L and M were applied, however, only the results for M are discussed in the following as the results for L and M are similar.

In figure 6.4, the images recorded for the seven pressure levels of the BW series are presented. For the three lowest pressure levels BW-P15, BW-P20 and BW-P25 refractive index gradients in the boundary layer are rather weak. Therefore, Digital Finite Fringe Interferometry is combined with Schlieren. At higher pressure levels, which lead to stronger refractive index gradients, the Schlieren filter is left away. In these cases, the fanning effect is so prominent that it does not only significantly affect the Schlieren measurement. The intensity within the boundary layer drops to zero, even above the membrane. This means a loss of information, which has to be avoided. Therefore, Shadowgraphy is used instead of Schlieren for the measurement of these strong refractive index gradients.

For the Schlieren and Shadowgraphy results BW-P20 to BW-P60 image distortions close to the membrane are observed, as discussed in section 4.2. They can be explained by spherical aberration of the lenses in the optical setup. This is also the reason why the simulated intensity profiles in figure 6.5 continue for $z < 0$ mm. Such image distortions might have been difficult to compensate with classical evaluation methods which neglect ray deflection, see section 2.2.3.

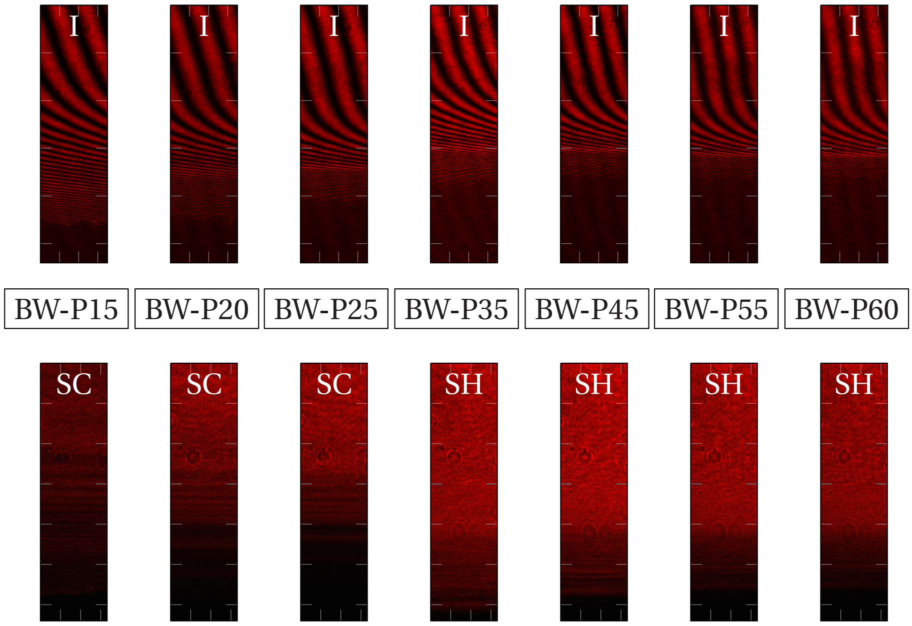

Figure 6.4: Raw data of Digital Finite Fringe Interferometry (index I), Schlieren (index SC) and Shadowgraphy (index SH).

Not only the intensity based methods face limitations. With increasing refractive index gradients, a bright horizontal intensity peak appears in the Interferometry boundary layer images at different heights above the membrane, see figure 6.4. By means of an optical ray tracing simulation based on wave theory (not scope of this study) it was found out that these intensity peaks can be explained by diffraction of light within the boundary layer itself. As already mentioned, it is possible to compensate such intensity variations with the Interferometry evaluation algorithm provided fringes are still detectable.

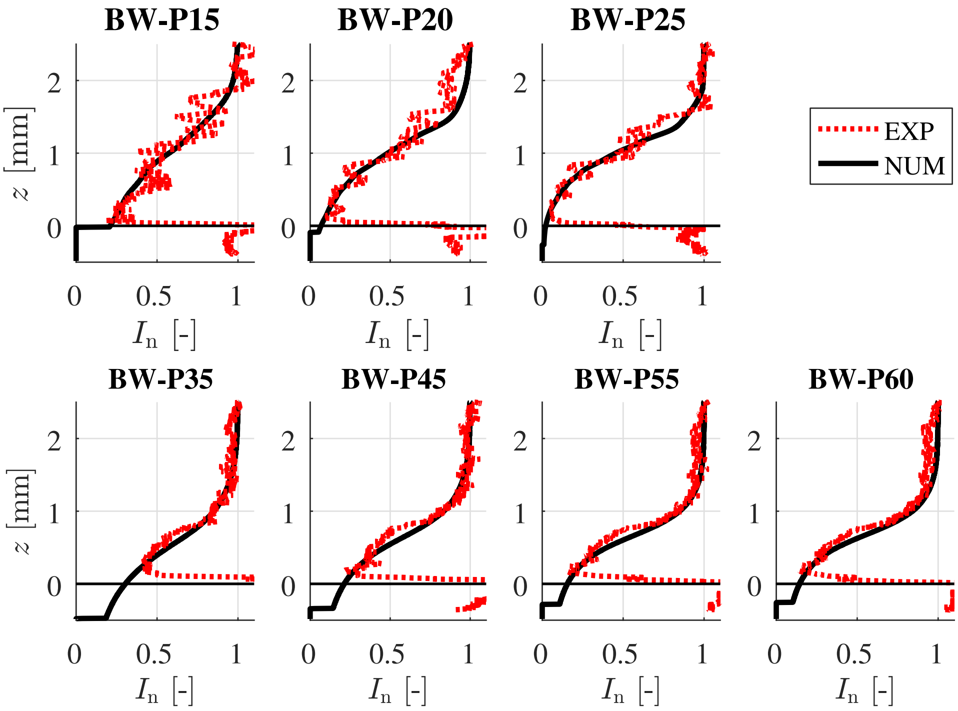

Figure 6.5: Experimental Schlieren (BW-P15 to BW-P25) and Shadowgraphy (BW-P35 to BW-P60) results (red, dotted lines) versus combined 3D CFD & optical ray tracing results (black, solid lines).

At strong refractive index gradients, the Interferometry measurement faces further limitations as explained section 4.2. They make a quantitative evaluation impossible below the threshold z_{th}, which was introduced in section 6.2.1. This becomes obvious looking at the concentration boundary layer profiles presented in figure 6.6 for BW-P25 to BW-P60. In this context, another advantage of combining different optical methods emerges. The combination of methods allows not only the validation of the results of the different methods with each other. In addition, the overall measurement resolution is extended. With the combined method, it is possible to investigate and validate the full boundary layer from bulk phase to membrane even in presence of strong refractive index gradients. Interferometry provides a direct measure of concentration in the boundary layer. Schlieren and Shadowgraphy validate the shape of the boundary layer profile measured with Interferometry for $z > z_{\mathrm{th}}$. And they provide further valuable information on the boundary layer development where Digital Finite Fringe Interferometry reaches its limits.

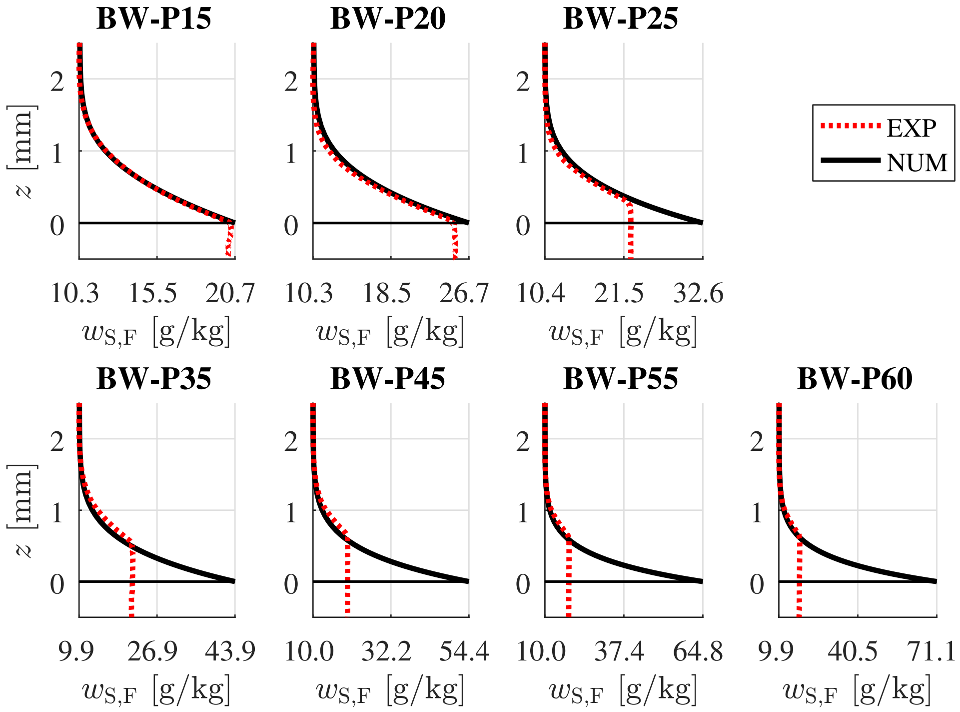

Figure 6.6: Experimental Digital Finite Fringe Interferometry results (red, dotted lines) versus 3D CFD results (black, solid lines).

Focusing on the quantitative results in figures 6.5 and 6.6, it can be stated that the experimental and numerical results are in good agreement. For quantification, the relative deviations between numerical and experimental results $|e_{w_{\mathrm{S}},\mathrm{rel}}|$, $|e_{w_{\mathrm{S,th}},\mathrm{rel}}|$ and $|e_{I_{\mathrm{n}},\mathrm{rel}}|$ are used. They are listed in the appendix in table C.2. Note that the relative deviation between numerical and experimental normalized image intensity I_{n} is determined for $z > 0.15$ mm only. Below this threshold, an interpretation of the *normalized* experimental intensity data does not make sense anymore (division by intensity values close zero due to diffraction patterns or the opaque test cell region). Furthermore, speckle noise in the boundary layer image and the according reference image promotes scattering of the normalized intensity data. The maximum relative deviation $|e_{I_{\mathrm{n}},\mathrm{rel}}|$ is less than 7.0%, which is observed for case BW-P25.

At the lowest pressure level BW-P15 the concentration profiles agree almost perfectly with each other ($|e_{w_{\mathrm{S}},\mathrm{rel}}| = 0.3\%$). For BW-P20 and BW-P25, the concentration profiles are in good agreement except for a small offset in z resulting in $|e_{w_{\mathrm{S}},\mathrm{rel}}| \approx 2.8\%$. A possible error source could be the accuracy of the determination of the exact membrane position $z = 0$ mm.

Also at higher pressure levels, for which a potential ray path increase in the boundary layer becomes more and more important, the Interferometry data are in good agreement with the numerical results ($|e_{w_{\mathrm{S}},\mathrm{rel}}| \leq 3.1\%$). It is concluded that the potential correction of a significantly increased ray path (section 5.1.2) does not become necessary as the boundary layer cannot be resolved where this correction might become relevant.

The Shadowgraphy data support the validity of the Interferometry measurements with $|e_{I_{\mathrm{n}},\mathrm{rel}}| < 3.8\%$. For BW-P60, the relative deviation of the salt mass fraction at the threshold $z_{\mathrm{th}} = 0.66$ mm is $|e_{w_{\mathrm{S,th}},\mathrm{rel}}| = 4.5\%$. According to table 6.2, such a relative deviation can originate from an inaccuracy of $|e_{B,\mathrm{rel}}| \approx 12\%$. The maximum relative deviation occurs for BW-P45 with $|e_{w_{\mathrm{S,th}},\mathrm{rel}}| = 9.1\%$, which corresponds to a possible inaccuracy of $|e_{B,\mathrm{rel}}| \approx 23\%$.

6.2.3 Sea Water Conditions

For further investigations, experiments were carried out with the same setup and the same membrane sample (sample I, see section 6.1) but with sea water at three different pressure levels. These test conditions were included already in table 3.6 on page 76. The main differences between the brackish and the sea water experiments are different feed salt mass fraction distributions on the membrane for similar pressure levels and higher salt mass fractions in the permeate.

Figure 6.7 shows the results of the quantitative evaluation of Digital Finite Fringe Interferometry as well as Shadowgraphy. The Schlieren technique was not applied here due to strong fanning.

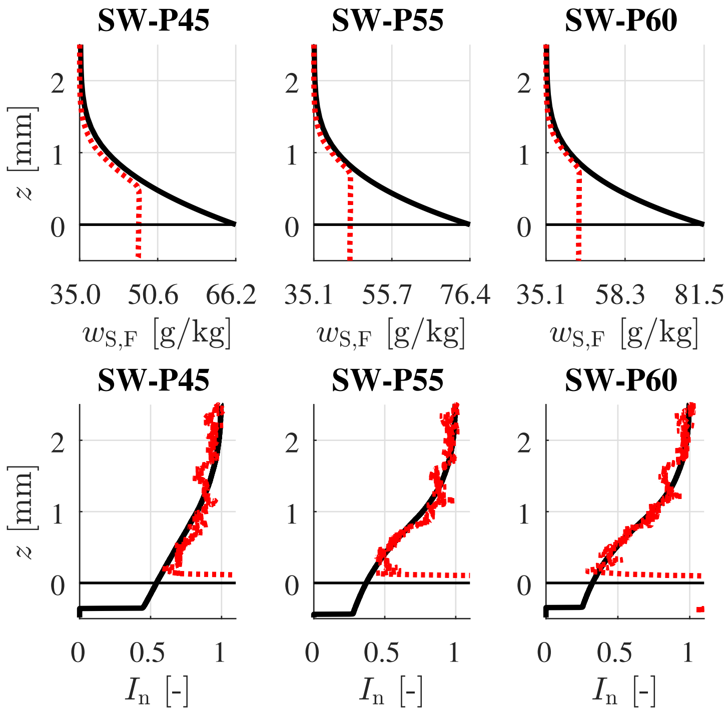

Figure 6.7: Experimental results (red, dotted lines) for Digital Finite Fringe Interferometry (top) and Shadowgraphy (bottom) versus combined 3D CFD & optical ray tracing results (black, solid lines).

At all pressure levels experimental and numerical results agree well for Interferometry and Shadowgraphy ($|e_{w_S,\mathrm{rel}}| < 2.6\%$ and $|e_{I_n,\mathrm{rel}}| < 4.7\%$). In the appendix, the data are listed for each experiment separately in table C.2 on page 170.

In the next section, an overview of the results of the brackish and sea water experiments is given including the salt permeability constant data.

6.2.4 Summary of Results

In order to validate the water and salt transport through the membrane, concentration boundary layer data from CFD and experiments were compared with each other. The mean relative deviation between CFD and Digital Finite Fringe Interferometry measurements is $|\bar{e}_{w_S,\mathrm{rel}}| = 0.4\%$. For a single experiment the maximum error is $|e_{w_S,\mathrm{rel}}| = 3.1\%$.

The comparison can also be made on the basis of normalized intensity profiles for Schlieren and Shadowgraphy. The mean relative deviation between the numerical and the experimental normalized intensities is $|\bar{e}_{I_\mathrm{n},\mathrm{rel}}| = 3.4\%$ for all experiments. For Schlieren the mean relative deviation $|\bar{e}_{I_\mathrm{n},\mathrm{rel}}| = 4.8\%$ is higher than for the Shadowgraphy $|\bar{e}_{I_\mathrm{n},\mathrm{rel}}| = 1.4\%$. The two main reasons for this difference might be the Schlieren filter as additional source of measurement noise and the lower absolute intensity level at the camera for the Schlieren experiments leading to lower signal to noise ratios. The good agreement between the results allows the statement that the optical measurement data serve well for validation for the CFD results.

In figure 6.8, the resulting salt permeability constant data of the brackish water and sea water pressure series are put in context and plotted in dependence of the mean feed salt mass fraction on the entire membrane. Besides, mean permeate salt mass fractions and hydrostatic pressure differences across the membrane are given. The results are discussed in the next section.

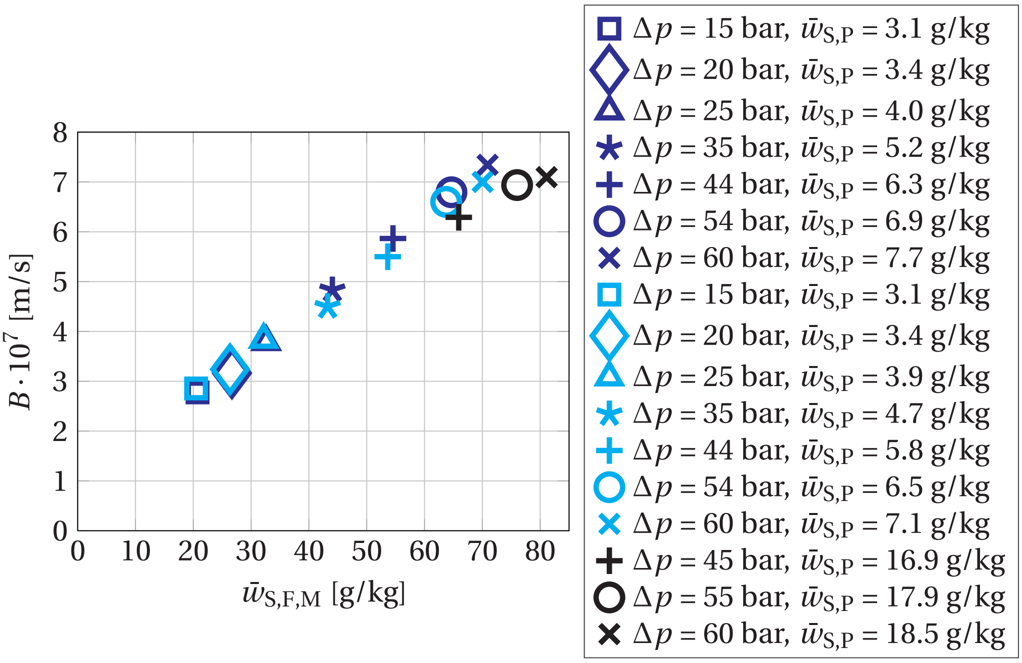

Figure 6.8: Brackish water results for membrane boundary condition L (blue) and M (cyan), sea water results for membrane boundary condition M (black).

6.2.5 Discussion of Results

The results shown in figure 6.8 allow to formulate two hypotheses.

6.2.5.1 Hypothesis I: Salt Permeability Constant as a Function of Pressure

A dependence of the salt permeability constant on pressure can be assumed taking only the brackish water (BW) pressure series into account, see figures 6.2(b) and 6.8. The salt permeability seems to increase almost linearly with pressure. If the tested membrane is not fully intact having imperfections like small holes, convective flow through these holes could occur. Parallel to the diffusive salt flux through the membrane, a convective flux could explain the pressure dependence of the salt flux. Modeling the membrane with the Solution-Diffusion model not taking into account membrane imperfections have to result in a salt permeability constant B increasing with pressure. However, this also means that B should be higher for higher feed salt mass fractions provided very similar driving forces for convective and diffusive transport, i.e. Δp and Δw_S across the membrane are similar. Taking the sea water results into account and comparing SW-P60 with BW-P60, which are most similar in Δp and $\Delta w_\mathrm{S} = \bar{w}_\mathrm{S,F,M} - \bar{w}_\mathrm{S,P}$, the hypothesis that pressure influences B can be rejected. For SW-60 the salt permeability constant B is not higher but at the same level as BW-P60, see figure 6.8.

The pure water membrane tests shown in figure 6.1(b) provide another reason to reject the hypothesis of abnormal membrane performance due to imperfections. If the membrane had imperfections allowing convective flow through the membrane, the pressure dependence of the water permeability constant would also show abnormal behaviour. However, this is not the case. The membrane sample tested in the optical test cell showed the same pressure dependence in the compacted state as the reference membrane sample tested simultaneously in a conventional flat sheet test cell, see section 6.1.

To further back up the assumption that membrane imperfections do not play a role in this study, a 2D CFD model was employed not taking into account the detailed inlet geometry of the test cell. The imperfections are modeled by seven membrane sections with elevated salt permeability constants (1 mm width). A local increase of B by a factor of 10 is assumed. This approach is certainly very simple but is considered suitable to get at least an estimate of the influence of imperfections on the boundary layer development. The result for BW-P60 is depicted in figure 6.9.

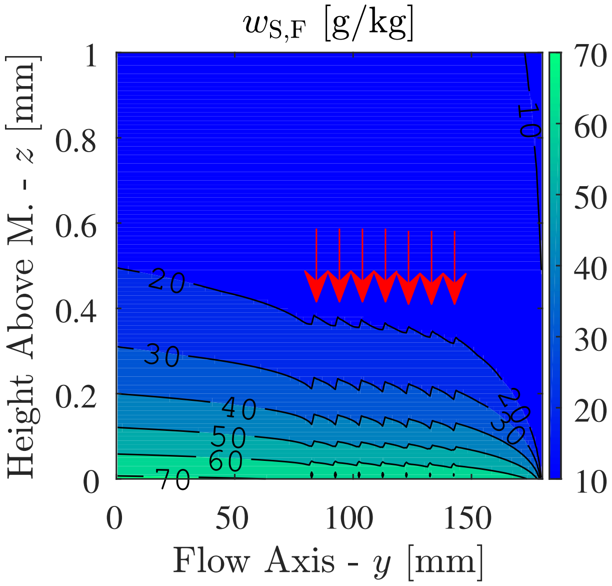

Figure 6.9: 2D CFD study on sensitivity of boundary layer to local imperfections modeled by a local increase of B by a factor of 10 in membrane sections of 1 mm width (highlighted by red arrows).

Figure 6.9 shows that the boundary layer development from channel inlet (y = 180 mm) to outlet is significantly obstructed by the seven regions with modeled imperfections. It may be reasonable to assume that boundary layer measurements can detect imperfections which have a significant influence on B, at least when they are located upstream of the actual optical measurement position. In this case experimental and numerical boundary layer results would not agree very well, which is not the case in the present study.

6.2.5.2 Hypothesis II: Salt Permeability Constant as a Function of Salinity

The interpretation of figure 6.8 allows a second hypothesis: There is a positive trend of the salt permeability constant for increasing feed salt mass fractions on the membrane. This would mean a local variation of membrane performance.

In section 2.1.4.4, three possible reasons were given for a dependence of the salt permeability constant on salinity. One of them was the concentration dependence of Fick's diffusivity which linearly contributes to the salt permeability constant. However, the low sensitivity of the thermodynamic correction factor on salinity shown in figure 2.9 cannot explain the large change of B presented in figure 6.8.

Another reason for a salinity dependent salt permeability constant can be membrane charge claimed by BARTELS ET AL. [10] and TORAY INDUSTRIES INC. [137]. The results depicted in figure 6.8 seem to complement the data of BARTELS ET AL. [10] shown in figure 2.8 with salt permeability constant data at higher salinities. BARTELS ET AL. [10] tested also a PA TFC membrane.

The third potential reason discussed in section 2.1.4.4 was the coupling of salt and water transport in the membrane. This phenomenon becomes more important with increasing salt mass fractions inside the membrane but is not taken into account by the SDM model.

Besides the membrane charge effect the coupling of salt and water transport is considered a possible physical explanation for a salinity dependence of the salt permeability constant. Which transport phenomenon is responsible for the results shown in figure 6.8 is analyzed by means of the Maxwell-Stefan modeling approach (section 2.1.5) in the following section.

6.3 Plausibility Check of Results

In section 2.1.5, the Maxwell-Stefan model was described including an approach for taking a salinity sensitive salt solubility into account. In total, nine parameters are necessary to describe membrane transport with this model. In section 2.1.6, an overview of literature data for these nine parameters is given. For the value of each Maxwell-Stefan membrane parameter only a value range can be given. In order to narrow down this range to a specific value for each membrane parameter, a multi-objective parameter optimization will be performed. It is described in detail in the following section.

It is important to mention here that the primary purpose of the following study is not to find the one unambigous solution for the set of nine Maxwell-Stefan membrane parameters. Instead, the question is to be answered if a set of nine membrane parameters exists which is able to describe the physics behind the experimental results presented in section 6.2.4. The results will allow to evaluate the two hypotheses:

1. The characteristic of the salt permeability constant B (section 6.2.4) can be explained by coupled salt and water mass transport.
2. The characteristic of the salt permeability constant B (section 6.2.4) can be explained by membrane charge effects.

6.3.1 Methodology

Figure 6.10 gives an overview of the multi-objective parameter optimization problem. The goal is to determine the nine membrane model parameters shown in the center of figure 6.10.

For known membrane model parameters and given boundary conditions (Δp, T, $w_{\mathrm{S,F}}$ and $w_{\mathrm{S,P}}$), salt and water mass flux j_{S} and j_{W} can be calculated. In this study, the nine Maxwell-Stefan membrane parameters are not known in contrast to the fluxes j_{S} and j_{W}, which are taken from the CFD results presented in section 6.2. The literature review in section 2.1.6 results in an a-priori knowledge about the realistic range of the membrane parameters. In figure 6.10, the membrane parameters $\mathfrak{D}_{\mathrm{SW}}$ to M_{M} are sorted from left to right according to the a-priori knowledge from high to low.

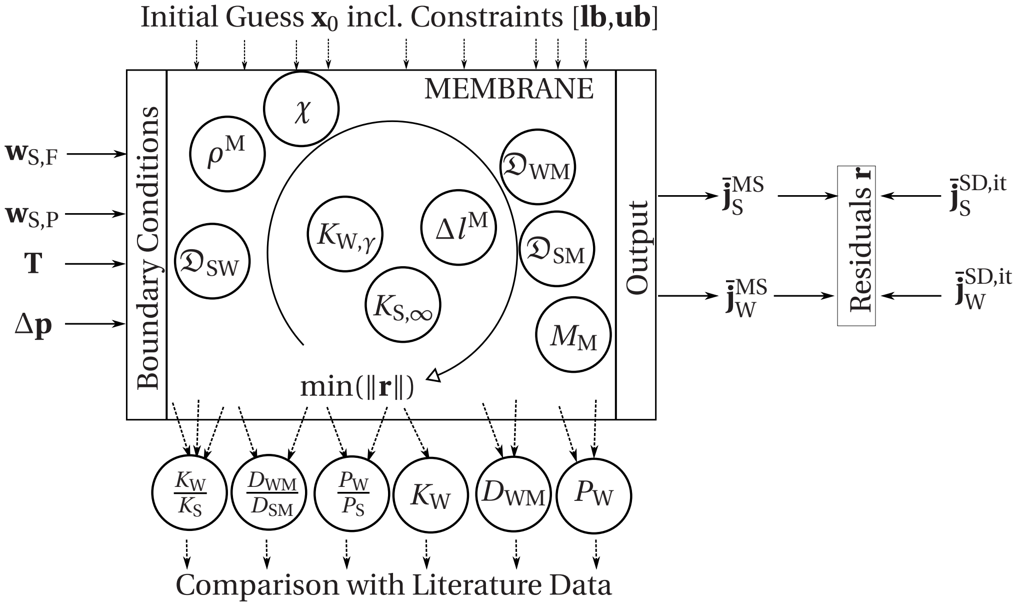

Figure 6.10: Overview of the multi-objective parameter optimization problem.

This allows to set upper and lower physically reasonable constraints for each of the nine membrane parameters [**lb**, **ub**]. Consequently, a solver is needed for a *constrained* optimization problem to access these membrane paramters. For this the MATLAB® solver `fmincon` is used. This solver is gradient-based and designed for constrained non-linear optimization problems [170]. It minimizes the scalar value of the residual R of a user-defined error function, which represents the membrane model in our case.

As input for the solver data of BW-P15 and SW-P60 are chosen, see table 3.6 on page 76. These two test cases represent the boundaries for salt permeability constants in the investigated salinity range, see figure 6.8 on page 133. The other eight test cases (BW-20 to BW-60, SW-P45 and SW-P50) are used to check the validity of the membrane parameters, which are determined by the multi-objective parameter optimization algorithm. The test conditions listed in table 3.6 as well as the CFD results for feed and permeate salt mass fraction on both sides of the membrane active layer are input for the optimization solver. For the analyses, surface-averaged values of the CFD results are used.

The global residual R, which is to be minimized, is based on the mean water and salt fluxes $\bar{j}_{\mathrm{W}}$ and $\bar{j}_{\mathrm{S}}$. The relative deviations between the Maxwell-Stefan model results $\bar{\mathbf{j}}_{\mathrm{W}}^{\mathrm{MS}}$ and $\bar{\mathbf{j}}_{\mathrm{S}}^{\mathrm{MS}}$ and the SDM CFD data $\bar{\mathbf{j}}_{\mathrm{W}}^{\mathrm{SD,it}}$ and $\bar{\mathbf{j}}_{\mathrm{S}}^{\mathrm{SD,it}}$ are used to calculate two residuals $r_{\bar{j}_{\mathrm{W}},i}$ and $r_{\bar{j}_{\mathrm{S}},i}$ for each test case i. Altogether, the single residual terms form the residual vector $\mathbf{r}$. Its second norm is the global residual $R = \|\mathbf{r}\|$. In figure 6.10, the circular arrow around the membrane parameters indicates their iterative optimization to reach the minimum of the global residual $\min(\|\mathbf{r}\|)$.

To evaluate if the constrained solver finds only the closest minimum to its arbitrary starting point instead of the global minimum, its solution is double-checked via the unconstrained solver `fminsearch` (not gradient based, direct search method [96, 169]). Furthermore, the absolute value of the global residual R is taken as indicator. When the residual reaches a value close to zero, a global minimum is likely. As additional quality check the determined membrane parameters are grouped to new sets of parameters, which are subsequently validated by literature data, see section 2.1.6 and appendix D. It is likely that mathematical artefacts would become apparent in this step but this cannot be not guaranteed.

The determination of the Maxwell-Stefan membrane model parameters is carried out for two model variants. The first variant takes charge effects into account ($\chi \neq 0$, $K_{\mathrm{S}} \neq \mathrm{const.}$). The second variant neglects charge effects ($\chi = 0$, $K_{\mathrm{S}} = K_{\mathrm{S},\infty} = \mathrm{const.}$). For both variants the coupled mass fluxes j_{W} and j_{S} can be compared with the decoupled ones $j_{\mathrm{W,WPart}}$ and $j_{\mathrm{S,SPart}}$ neglecting $j_{\mathrm{W,SPart}}$ and $j_{\mathrm{S,WPart}}$ (compare equations (2.43) to (2.50)).

Additionally, the Maxwell-Stefan model results will be compared to SDM results which are calculated with the 3D CFD model in combination with a salinity dependent salt permeability constant $B = f(w_{\mathrm{S,F,M}}^{\mathrm{E}})$. In this way, the step is made from uniform to locally varying membrane properties. From the results presented in figure 6.8 on page 133, a linear function for B was derived assuming saturation at $B = 7.344 \cdot 10^{-7}$ m/s. Note that the results calculated with membrane boundary condition L were used.

6.3.2 Physical Explanation for Results

In the following, the Maxwell-Stefan membrane model variants with and without charge effects are tested. It will turn out that the variant with membrane charge is capable to explain the dependence of the salt permeability constant B on salinity. This conclusion cannot be drawn from the variant without charge effects. The reasons supporting these statements are explained in the following.

First of all, the constraints for the nine membrane parameters are derived from the literature review results summarized in table 2.1 on page 42. Table 6.3 contains the initial guess and the lower and upper bounds for each parameter.

Table 6.3: Membrane parameters: initial guess $\mathbf{x}_0$, lower bound **lb**, upper bound **ub** and result $\mathbf{x}_\mathrm{R}$ for the Maxwell-Stefan model with charge effects.

Parameter	Unit	$\mathbf{x}_0$	lb	ub	$\mathbf{x}_\mathrm{R}$
$\mathfrak{D}_\mathrm{SM}$	$\frac{\mathrm{m}^2}{\mathrm{s}}$	$7 \cdot 10^{-14}$	$0.8 \cdot 10^{-14}$	$10.7 \cdot 10^{-14}$	$10.6396 \cdot 10^{-14}$
$\mathfrak{D}_\mathrm{WM}$	$\frac{\mathrm{m}^2}{\mathrm{s}}$	$2 \cdot 10^{-10}$	$1.2 \cdot 10^{-10}$	$8 \cdot 10^{-10}$	$1.2467 \cdot 10^{-10}$
$\mathfrak{D}_\mathrm{SW}$	$\frac{\mathrm{m}^2}{\mathrm{s}}$	$1.6119 \cdot 10^{-9}$	$1.6119 \cdot 10^{-9}$	$1.6119 \cdot 10^{-9}$	$1.6119 \cdot 10^{-9}$
$\bar{M}_\mathrm{M}$	$\frac{\mathrm{kg}}{\mathrm{mol}}$	0.6	0.03	10	0.0593
Δl^M	m	$100 \cdot 10^{-9}$	$10 \cdot 10^{-9}$	$200 \cdot 10^{-9}$	$85.8601 \cdot 10^{-9}$
$K_{\mathrm{S},\infty}$	-	0.1	0.0001	1	0.4552
$K_{\mathrm{W},\gamma}$	-	0.25	0.1	20	0.5974
χ	$\frac{\mathrm{mol}}{\mathrm{l}}$	0.3	0.2	0.35	0.3458
$\frac{\rho^\mathrm{M}}{\rho^\mathrm{E}}$	-	1.24	1.2	1.4	1.2275

Note that for the MATLAB® solver, scaling of the parameters in table 6.3 was required to avoid limitations due to machine precision.

For the model with charge effects, the residual R reaches almost zero ($R = 1.05 \cdot 10^{-5}$). For the case without charge effects, the minimum is several orders of magnitude higher ($R = 0.51$). To double-check the results, the unconstrained solver `fminsearch` was fed with the respective results of the constrained solver. For the model variant with membrane charge, the solution of the unconstrained solver is almost identical with the one of the constrained solver ($\mathbf{x}_R$, see table 6.3). The change of all parameters is negligibly small. The parameter which changes mostly with 2% of its the original value is the Maxwell-Stefan diffusivity $\mathfrak{D}_{SW}$. In the case without charge effects, the unconstrained solver ends up with $R = 0.50$, but with unreasonable results for some parameters. As the model without charge effects does account for coupled mass transport, this result is a first indicator that mass transport coupling might not be able to explain the change of B.

As next step, the determined membrane parameters are checked for validity. The optimization was carried out for BW-P15 and SW-P60. If the result $\mathbf{x}_R$ for the nine membrane model parameters is valid, it must be possible to predict the flux results of the other eight cases.

The results are shown in figure 6.11. BW-P15 and SW-P60, which served as input for the optimization, are also included (red circles). For water and salt flux, the relative deviation between the Maxwell-Stefan results and the original, iteratively determined Solution-Diffusion results (denoted by SD,it) are presented. Three Maxwell-Stefan (MS) model variants are considered:

- with charge and coupled (superscript MS,cc),
- with charge and decoupled (superscript MS,cd) and
- without charge and coupled (superscript MS,nc).

Moreover, the 3D CFD results calculated with the SDM model using a correlation for the salt permeability constant $B = f(w^{E}_{S,F,M})$ are included in figure 6.11. They have the superscript SD,ws. In order to put all results in context with the experimental permeate flux data, water and salt flux were calculated from the experimental permeate flux data and the simultated permeate salt mass fractions presented in section 6.2.4. These data are denoted by EXP in figure 6.11.

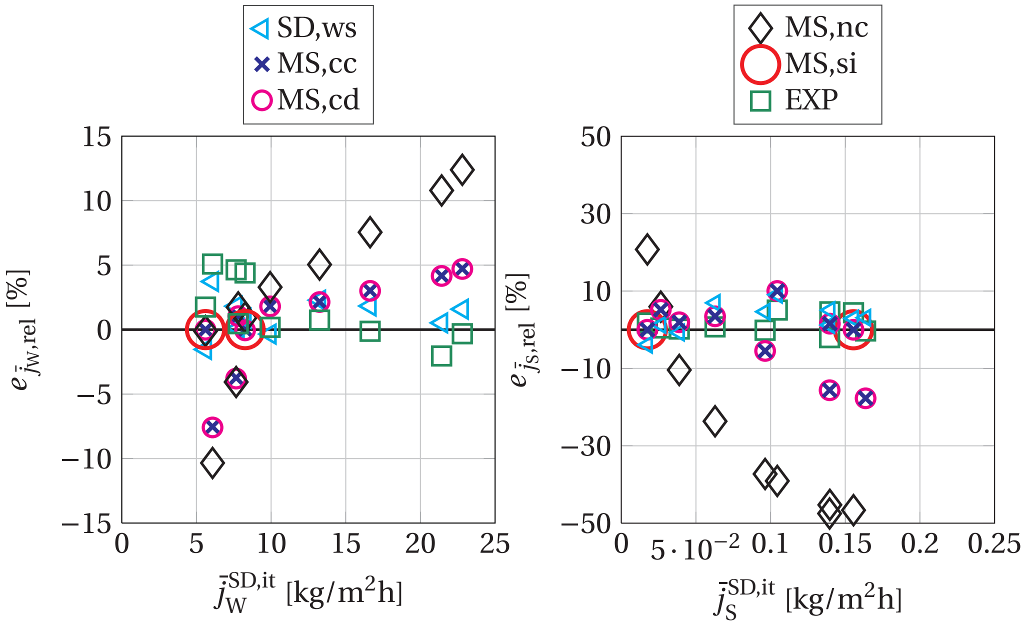

Figure 6.11: Relative deviation of different membrane modeling variants compared to the original 3D CFD results (superscript SD,it).

In the following, the results depicted in figure 6.11 are discussed.

Model Variant MS,cc

The average and the maximum error $|e_{\bar{j}_{W},rel}|$ of the water fluxes is 0.6% and 7.6%, respectively. The error of the salt fluxes $|e_{\bar{j}_{S},rel}|$ is 1.7% in average and maximum 17.7%. In comparison, the average error relative to the experimental data is 1.5%.

Model Variant MS,cd

The results for the Maxwell-Stefan model with coupled and decoupled mass flux are almost identical. Taking the coupling terms $j_{W,SPart}$ and $j_{S,WPart}$ into account in the calculation of the total fluxes j_W and j_S has no benefit, see equations (2.43) to (2.50). The influence of the coupling terms on the total flux is negligible small.

Model Variant MS,nc
The error of the water fluxes $|e_{\bar{j}_{\mathrm{W}},\mathrm{rel}}|$ is 2.7% in average and maximum 12.4%. The average and maximum error $|e_{\bar{j}_{\mathrm{S}},\mathrm{rel}}|$ of the salt fluxes is 27.4% and 50.5%, respectively. Both average and maximum error are high for this model variant, especially for the salt flux taking the experimental data EXP as reference. These high relative errors explain also the high residual R for this model variant, which was discussed above.

Concluding on the basis of the results above, it can be stated that it is likely that the results presented in section 6.2.4 can be explained membrane charge effects. For the model variant without charge effects the flux data are not predicted with acceptable accuracy. Taking into account mass transport coupling does not change the results. It can be concluded that coupled mass transport is unlikely to play a relevant for the modeling RO membranes, at least not for the investigated operation range. This finding supports the validity of the SDM assumption of binary mass transport inside the membrane. The data based on membrane charge effects are analyzed further in the following.

Model Variant SD,ws
The 3D CFD results calculated with the SDM model with the salinity dependent correlation for the salt permeability constant $B = f(w^{\mathrm{E}}_{\mathrm{S,F,M}})$ support the conclusions above. In figure 6.11, the error of the water fluxes $|e_{\bar{j}_{\mathrm{W}},\mathrm{rel}}|$ is 1.1% in average and the maximum is 3.7%. The error of the salt fluxes $|e_{\bar{j}_{\mathrm{S}},\mathrm{rel}}|$ is 3.7% in average and the maximum is 9.1%. Besides a comparison of numerical and experimental permeate flux data a validation based on boundary layer data is possible in this case, see tables C.1 and C.2 as well as figures C.1, C.2 and C.3 in the appendix. The errors are low: $|\bar{e}_{\bar{j}_{\mathrm{P}},\mathrm{rel}}| = 0.3\%$, $|e_{\bar{j}_{\mathrm{P}},\mathrm{rel}}| < 3.3\%$, $|\bar{e}_{w_{\mathrm{S}},\mathrm{rel}}| = 0.4\%$ and $|\bar{e}_{I_{\mathrm{n}},\mathrm{rel}}| = 3.6\%$. This further supports the hypothesis that there is a dependence of the salt permeability constant B on salinity.

Salt and Water Permeability Constants
In figure 6.12, the data for salt and water permeability constants are compared amongst each other. First of all, there are the salt permeability constant data denoted by SD,it. They were iteratively determined with the 3D CFD simulation using membrane boundary condition M. Second, there is the mentioned linear approximation function denoted by SD,ws with saturation at maximum

salt mass fractions. Third, there are the salt permeability constant data calculated from the Maxwell-Stefan model variants which include membrane charge effects. These results are presented for both coupled and decoupled mass transport.

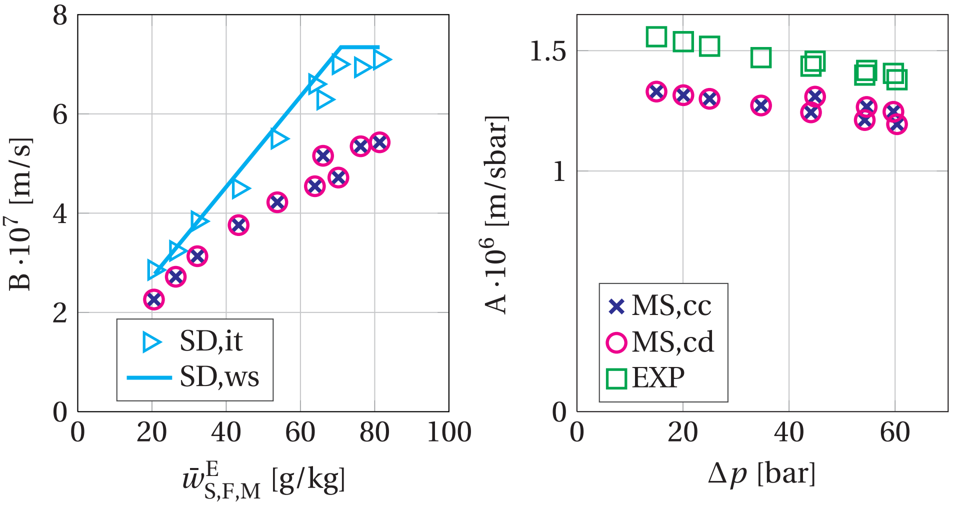

Figure 6.12: Comparison of salt and water permeability constants.

The salinity dependence of the salt permeability constant predicted by the Maxwell-Stefan membrane model with charge effects is not as strong as the original CFD data (SD,it) let assume. However, both data sets are in good agreement showing an average relative deviation $|\bar{e}_{B,\mathrm{rel}}| = 22.3\%$ between each other. A possible explanation for the apparent increasing deviation towards higher salt mass fractions might be that thermodynamic correction factors were not included in the model. Their relevance grows with increasing salt mass fraction.

An additional parameter suitable for validity checks is the water permeability constant A. It was also calculated from the Maxwell-Stefan model variant with charge effects and can be compared with the experimental data from section 6.1 (with superscript EXP). While the trends for experimental data and membrane model results are almost identical, an average deviation of 12.9% related to the experimental data is observed. This is still reasonable considering the low sensitivity of the permeate flux on A (section 6.2.1).

Derivation of New Parameter Sets

For the next validity check, the parameters used by GEISE ET AL. [55] are derived from the membrane parameters determined in this study.

In 2011, GEISE ET AL. [55] gave an overview of selected polymer membrane characteristics in desalination. They present the data in form of selectivities as it is known from gas separation literature [109, p. 449]. They assume that there is an empirical upper bound for salt and water separation characteristics of polymers due to a trade-off between permeability and selectivity [55, p. 135].

The data of GEISE ET AL. [55] are to be used in the following to validate the results for the MS model parameters. In accordance with GEISE ET AL. [55], selectivities are calculated (see appendix D for details). In figure 6.13, the water/NaCl solubility selectivity ($\frac{K_W}{K_S}$), the water/NaCl diffusivity selectivity ($\frac{D_W}{D_S}$) and the water/NaCl permeability selectivity ($\frac{P_W}{P_S}$) are presented. Furthermore, literature data of membranes with material properties similar to the membrane tested in this study are included. The upper bounds proposed by GEISE ET AL. [55] are also shown (black solid lines).

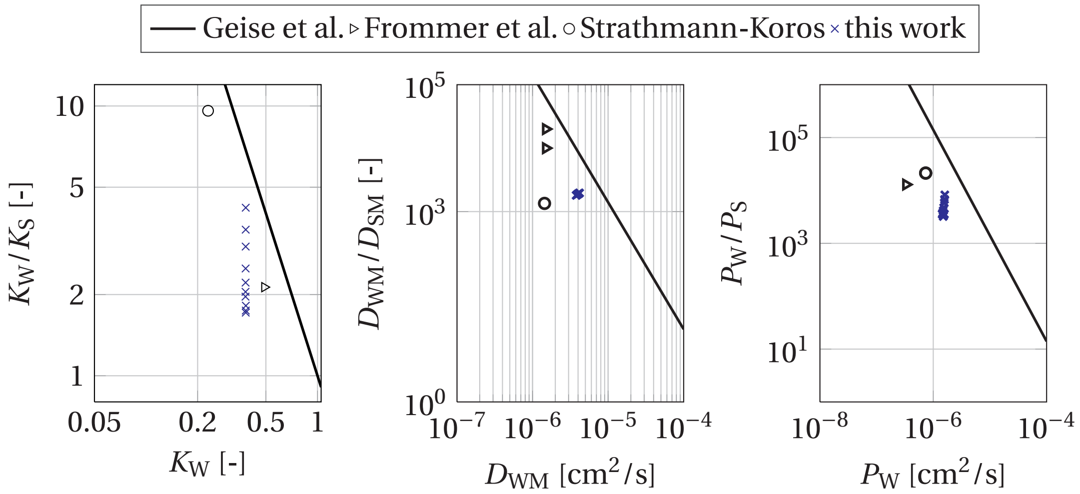

Figure 6.13: Modeling results determined with a Maxwell-Stefan approach including membrane charge effects in context with literature data.

The results presented in figure 6.13 allow to conclude that the membrane parameters determined in this study are in accordance with literature data. The depicted data do not exceed the empirical upper bounds proposed by GEISE ET AL. [55] and seem physically reasonable.

Salt Solubility

By means of salt solubility K_S the salinity dependent salt permeability constant can be explained. Based on the Maxwell-Stefan model data, it can be evaluated separately for the feed and the permeate side ($K_{S,F} = \frac{\gamma^E_{S,F}}{\gamma^M_{S,F}} \frac{c^M_F}{c^E_F}$ and $K_{S,P} = \frac{\gamma^E_{S,P}}{\gamma^M_{S,P}} \frac{c^M_P}{c^E_P}$). The resulting data are depicted in figure 6.14 in dependence of the salt mass fraction in the external solution, including both feed and permeate side.

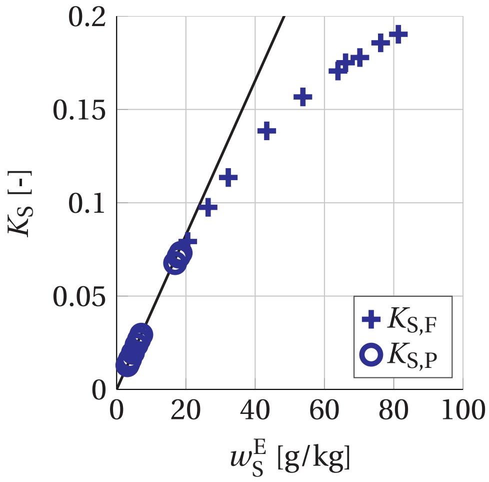

Figure 6.14: Salt solubility in dependence of salt mass fraction in the external solution.

The salinity range, for which data are available, reaches from the minimum permeate salt mass fraction to the maximum feed salt mass fraction ($w_S = 3.1 ... 81$ g/kg). In figure 6.14, a strong dependence of the salt solubility K_S on salinity can be seen. Furthermore, after an approximately linear increase for $w_S < 20$ g/kg, a trend towards saturation can be observed at higher salt mass fractions. Similarly, a saturation level seems to exist also for B at high salt mass fractions, see figure 6.8 (page 133), which might be explained by K_S. Moreover, the salt solubility results explain how the salt solubility data of FROMMER ET AL. [52] ($K_S = 0.23$) and STRATHMANN and MICHAELS [163]

($K_S = 0.024$) can be linked with each other. Assuming a salinity dependent salt solubility the difference of one order of magnitude between the salt solubility data of FROMMER ET AL. [52] and STRATHMANN and MICHAELS [163] can be reproduced.

6.4 Conclusion

Based on the outcome of the previous section the following conclusions with respect to the revised LMPM can be drawn:

It was shown that the membrane performance data determined by means of the method outlined in section 3.3 are physically correct. It can be concluded that the proposed method is suitable for membrane characterization. The integration of the CFD model in the revised LMPM allowed to account for local transport phenomena like a salinity sensitive salt permeability constant B. The CFD and experimental results agree well for both permeate fluxes and boundary layer profiles. The low errors of boundary layer profiles allow to state that validation of water and salt mass transport on a local scale (line-of-sight averaged) was successful.

A possible physical explanation for the dependence of the salt permeability constant on an operating parameter was found. All indications suggest that the electrical charge density of the investigated membrane type has to be taken into account. In the present study, a brackish water low fouling TFC polyamide RO membrane was tested. The results support the findings of BARTELS ET AL. [10], who investigated also a brackish water RO membrane but in a lower salinity range. The literature review presented in section 2.1.6 showed that the electrical charge density of cellulose acetate (CA) membranes is two orders of magnitude lower than of polyamide (PA) membranes. During the development of the SDM, only CA membranes were available. This might explain why charge effects are not standardly taken into account by the SDM.

The dependence of the salt permeability constant on salinity can be attributed to the salt solubility K_S. For the salinity range investigated in this study (w_S = 3.1...81 g/kg), it shows a linear increase for brackish water concentration levels

$w_S < 20$ g/kg and runs into saturation towards higher salt mass fractions. The positive effect of negative membrane charge on the membrane salt separation characteristic is increasingly compensated by an increasing amount of ions in the external solution. The salt solubility data determined in the present study are the link between the data of FROMMER ET AL. [52] and STRATHMANN and MICHAELS [163], which differ one order of magnitude.

It could be shown that detailed membrane modeling is not necessarily needed to take the charge effect into account. It can simply be integrated in the standard SDM by a salinity dependent correlation for the salt permeability constant B. The CFD results determined with this correlation were in good agreement with the measured permeate fluxes and concentration boundary layers.

Coupled water and salt mass transport was also investigated for the tested RO membrane. It was studied by means of a Maxwell-Stefan membrane modeling approach. Although it might not generally be concluded that coupled mass transport does not play a role in entire the RO operating window, no evidence for its relevance was found in the presented study.

7 Summary

The present study describes a new methodology for the inverse determination of RO membrane performance on a local scale. Motivation for this method was the local variation of RO membrane performance, which cannot be measured by means of conventional lab-scale membrane tests that provide only global, surface-averaged membrane performance data.

The main outcome of this study is the following:

- A membrane test cell design was introduced which allows to optically investigate concentration boundary layers at typical RO operating pressures around 60 bar.

- By means of boundary layer theory it was shown that the combination of Interferometry, Schlieren and Shadowgraphy is ideally suited to measure in-situ local mass transport (j_P and $w_{\mathrm{S,P}}$) and membrane parameters (A and B). Furthermore, the simultaneous application of multiple optical methods in one setup has the advantage of achieving higher measurement resolutions to quantify boundary layer profiles.

- The previously published LMPM [91] for the determination of membrane model specific local membrane parameters was tested in a proof of concept study. It was shown that the method has high potential to quantify local permeate fluxes j_P. However, only low accuracy was achieved for local permeate salt mass fraction data $w_{\mathrm{S,P}}$. With the pursued experimental methods and tools, an investigation of the local membrane parameters was not possible before a revision of the methodology.

- The revised LMPM combines the three optical methods with 3D computational fluid dynamics (CFD) and optical ray tracing. CFD is needed to inversely determine membrane properties from mass transport measurements. While surface-averaged permeate flux $\bar{j}_\mathrm{P}$ measurement data are used to determine membrane permeability constants, optical boundary layer measurements make a validation with line-of-sight averaged data possible. 3D CFD allows to study membrane transport phenomena at an even higher resolution depending on the mesh density. In the present study, the minimum local resolution ranges between 10^{-5} and 10^{-4} m.

- The developed optical ray tracing tool allowed to overcome limitations of classical Schlieren and Shadowgraphy. A quantitative comparison of numerical and experimental boundary layer data was possible even in presence of strong refractive index gradients in combination with obstructing optical phenomena (diffraction, fanning, spherical aberration). It was avoided to compare numerical concentration profiles with biased results derived from noisy light intensity measurements of Schlieren or Shadowgraphy experiments. Instead, normalized experimental and numerical light intensities were directly compared after simulating light propagation through the boundary layer to the camera.

- The revised LMPM was applied to a TCF PA brackish water RO membrane. Numerical and experimental data are in good agreement for both permeate flux and concentration boundary layer. Tests were carried out for brackish and sea water salinity conditions at pressures up to $\Delta p = 60$ bar and temperatures around $T = 30$°C. Sea water conditions are by definition not typical for brackish water membranes but allowed to study an interesting salt mass transport phenomenon. For the investigated operating conditions, salt permeability constants between $B \approx 3 \cdot 10^{-7}$ m/s and $B \approx 7 \cdot 10^{-7}$ m/s were determined. An almost linear dependence of B on salinity was observed with a trend towards saturation above brackish water salinities.

- By means of a Maxwell-Stefan modeling approach, different transport phenomena were investigated. While coupled salt and water mass transport inside the membrane played a minor role, the electrical charge density of the PA layer explained the observation made. The salt solubility results determined in the this study fill the data gap between FROMMER ET AL. [52] and STRATHMANN and MICHAELS [163], which differ one order of magnitude. The salt permeability constant results complement the findings of GEISE ET AL. [55] and BARTELS ET AL. [10].

8 Outlook

As an outlook on future work the following topics are to be mentioned:

- In this study, a membrane test cell design was presented which made optical investigations at high pressure possible without damaging the membrane during assembly. Based on the presented design solutions for the integration of the glass windows into a high pressure membrane test cell, future studies can focus on a test cell design with full optical access to the channel geometry. It is recommended to make two channel walls out of glass avoiding cavities and allowing quantitative boundary layer investigations along the entire channel length.

- The revised LMPM was applied to a rectangular, spacer-free channel geometry. However, the integration of CFD in the methodology allows the application of the method to any channel geometry and any membrane type provided that a boundary layer on the membrane can be measured. Thus optical access normal to the refractive index gradient in the boundary layer is needed.

- The applied optical methods are not only suited to quantify concentration or temperature boundary layers, respectively. The growth of opaque layers on the membranes can be detected as well. The simultaneous quantification of the growth of cake layers (UF/MF) or biofilms (any membrane process) as well as concentration boundary layers should be possible. This might provide valuable insight to coupled local mass transport phenomena in membranes.

- While working on the optical measurement of boundary layers, first steps were made with optical simulations based on wave theory. It is recommended to study diffraction patterns as actual measurement target for boundary layer measurements. These patterns are unique for the investigated boundary layer. The location and intensity of fringes caused by diffraction might serve as qualitative or even quantitative measurement data to characterize the boundary layer.

Appendix

A Chemical Potential at the Interface of External Solution and Membrane

The salt solubility is derived assuming that the chemical potential is a continuous function linking external solution and membrane phase. The sorption equilibrium for NaCl is [111, p. 41]:

$$\mathrm{Na}^{+^{\mathrm{E}}} + \mathrm{Cl}^{-^{\mathrm{E}}} \leftrightarrow \mathrm{Na}^{+^{\mathrm{M}}} + \mathrm{Cl}^{-^{\mathrm{M}}} \tag{A.1}$$

$$\mu^{\mathrm{E}}_{\mathrm{Na}^+} + \mu^{\mathrm{E}}_{\mathrm{Cl}^-} = \mu^{\mathrm{M}}_{\mathrm{Na}^+} + \mu^{\mathrm{M}}_{\mathrm{Cl}^-} \tag{A.2}$$

$$\ln a^{\mathrm{E}}_{\mathrm{Na}^+} + \ln a^{\mathrm{E}}_{\mathrm{Cl}^-} = \ln a^{\mathrm{M}}_{\mathrm{Na}^+} + \ln a^{\mathrm{M}}_{\mathrm{Cl}^-} \tag{A.3}$$

$$\ln(a^{\mathrm{E}}_{\mathrm{Na}^+} \cdot a^{\mathrm{E}}_{\mathrm{Cl}^-}) = \ln(a^{\mathrm{M}}_{\mathrm{Na}^+} \cdot a^{\mathrm{M}}_{\mathrm{Cl}^-}) \tag{A.4}$$

According to MERTEN [111, p. 41], the activity is substituted as follows:

$$\gamma^{\mathrm{E2}}_{\pm} \cdot c^{\mathrm{E2}}_{\mathrm{NaCl}} = \gamma^{\mathrm{M2}}_{\pm} \cdot c^{\mathrm{M}}_{\mathrm{Na}^+} \cdot c^{\mathrm{M}}_{\mathrm{Cl}^-} \tag{A.5}$$

However, the correct expression should read as follows:

$$\gamma^{\mathrm{E2}}_{\pm} \cdot x^{\mathrm{E2}}_{\mathrm{NaCl}} = \gamma^{\mathrm{M2}}_{\pm} \cdot x^{\mathrm{M}}_{\mathrm{Na}^+} \cdot x^{\mathrm{M}}_{\mathrm{Cl}^-} \tag{A.6}$$

$$\gamma^{\mathrm{E2}}_{\pm} \cdot \frac{c^{\mathrm{E2}}_{\mathrm{NaCl}}}{c^{\mathrm{E2}}} = \gamma^{\mathrm{M2}}_{\pm} \cdot \frac{c^{\mathrm{M}}_{\mathrm{Na}^+} \cdot c^{\mathrm{M}}_{\mathrm{Cl}^-}}{c^{\mathrm{M2}}} \tag{A.7}$$

B Fluid Properties

B.1 Correlation for Refractive Index

The refractive index correlation applied in this study was determined as follows:

1. Measurement of refractive index in dependence of salinity, temperature and wavelength according to table B.1.
2. Least-square fit of the experimental refractive index data to the polynomial of MILLARD and SEAVER [115] assuming that their correlation for sea water models the pressure dependence correctly also for an aqueous NaCl solution.

Table B.1: Test conditions for refractive index experiments.

Parameter	**Unit**	**Value**	**Repetitions**
Salt concentration	$\frac{g_{NaCl}}{kg_{H_2O}}$	0, 5, 10, ...40, 100, 150, ..., 300	-
Temperature	°C	15, 20, ..., 60	3
Wavelength	nm	435.9, 486.3, 513.2, 532.1, 546.9, 589.3, 633.1, 655.9	3

The measurements were conducted with an Abbemat MW Multiple Wavelengths refractometer [6]. The refractometer has a refractive index resolution of ±0.000001. Its Peltier thermostat maintained the temperature of the probes with an accuracy of ±0.03°C guaranteeing a stability of ±0.002°C [6]. The aqueous NaCl solutions were prepared by mixing NaCl and pure water samples weighed on a Sartorius scale of type MC1-RC-210-D-Typ-KB with an accuracy of 0.1 mg. The CAS-Nr. 7647-14-5 NaCl salt has chemically pure quality and was ordered from DIACLEAN GMBH [33].

The pure water used in the experiments was produced with a Trunz Brackish Water Box RO Plant [175] via desalination of the soft tap water available at the institute. The pure water quality was checked on a random basis. It can be stated that the average conductivity of the pure water was 16.4 μS/cm with a standard deviation of 13.0 μS/cm at an average temperature of 21.5 ± 2.7°C.

The 3600 experimental data points of the refractive index measurements were fitted to equation B.1.

$$\begin{aligned} n = a_1 - a_2 \cdot \lambda^2 + a_3 \cdot \frac{1}{\lambda^2} + a_4 \cdot \frac{1}{\lambda^4} + a_5 \cdot \frac{1}{\lambda^6} - a_6 \cdot T - a_7 \cdot T^2 + a_8 \cdot T^3 - a_9 \cdot T^4 \\ + a_{10} \cdot \lambda + a_{11} \cdot T^2 \cdot \lambda + a_{12} \cdot T^3 \cdot \lambda + a_{13} \cdot w_\mathrm{S} + a_{14} \cdot w_\mathrm{S} \cdot \frac{1}{\lambda^2} \\ + a_{15} \cdot w_\mathrm{S} \cdot T + a_{16} \cdot w_\mathrm{S} \cdot T^2 + a_{17} \cdot w_\mathrm{S} \cdot T^3 + a_{18} \cdot w_\mathrm{S} \cdot T \cdot \lambda \\ + a_{19} \cdot p + a_{20} \cdot p^2 + a_{21} \cdot p^2 \cdot \frac{1}{\lambda^2} + a_{22} \cdot p \cdot T + a_{23} \cdot p \cdot T^2 + a_{24} \cdot p^2 \cdot T^2 \\ + a_{25} \cdot p \cdot w_\mathrm{S} + a_{26} \cdot p \cdot w_\mathrm{S} \cdot T + a_{27} \cdot p \cdot w_\mathrm{S} \cdot T^2 \end{aligned} \quad \text{(B.1)}$$

The variables of this empirical equation have the following units: p [dbar], λ [μm], T [°C] and w_S [g/kg]. The resulting coefficients a_i are listed in table B.2. A correlation coefficient of $R = 99.99\%$ is achieved. The adjusted correlation coefficient, which additionally accounts for the number of terms in view of significance, is $R_\mathrm{adj} = 99.99\%$. Such a high value confirms that this equation is very well suited to describe both the refractive index of sea water and the deployed aqueous NaCl solution.

The mean standard deviation for the 1200 refractive index data sets with three repetitions each is $1.82 \cdot 10^{-6}$. The median standard deviation is $1.00 \cdot 10^{-6}$. Only for 11 data sets the deviation exceeded the magnitude of 10^{-5} with a maximum value of $2.01 \cdot 10^{-5}$.

Table B.2: Empirical coefficients of refractive index equation B.1.

Parameter	Millard and Seaver [115]	This Study
a_1	1.3280657	1.3285017
a_2	$4.554\cdot 10^{-3}$	$4.837\cdot 10^{-3}$
a_3	$2.547\cdot 10^{-3}$	$2.168\cdot 10^{-3}$
a_4	$7.502\cdot 10^{-6}$	$8.726\cdot 10^{-5}$
a_5	$2.803\cdot 10^{-6}$	$-3.335\cdot 10^{-6}$
a_6	$5.288\cdot 10^{-6}$	$-3.042\cdot 10^{-5}$
a_7	$3.074\cdot 10^{-6}$	$5.387\cdot 10^{-6}$
a_8	$3.012\cdot 10^{-8}$	$7.506\cdot 10^{-8}$
a_9	$2.088\cdot 10^{-10}$	$4.561\cdot 10^{-10}$
a_{10}	$1.051\cdot 10^{-5}$	$9.099\cdot 10^{-6}$
a_{11}	$2.128\cdot 10^{-7}$	$4.194\cdot 10^{-7}$
a_{12}	$1.706\cdot 10^{-9}$	$4.787\cdot 10^{-9}$
a_{13}	$1.903\cdot 10^{-4}$	$1.772\cdot 10^{-4}$
a_{14}	$2.424\cdot 10^{-6}$	$3.644\cdot 10^{-6}$
a_{15}	$7.396\cdot 10^{-7}$	$6.935\cdot 10^{-7}$
a_{16}	$8.982\cdot 10^{-9}$	$1.148\cdot 10^{-8}$
a_{17}	$1.208\cdot 10^{-10}$	$-6.936\cdot 10^{-11}$
a_{18}	$3.589\cdot 10^{-7}$	$-2.718\cdot 10^{-8}$
a_{19}	$1.587\cdot 10^{-6}$	$1.587\cdot 10^{-6}$
a_{20}	$1.574\cdot 10^{-11}$	$1.574\cdot 10^{-11}$
a_{21}	$1.071\cdot 10^{-8}$	$1.071\cdot 10^{-8}$
a_{22}	$9.483\cdot 10^{-9}$	$9.483\cdot 10^{-9}$
a_{23}	$1.010\cdot 10^{-10}$	$1.010\cdot 10^{-10}$
a_{24}	$5.809\cdot 10^{-15}$	$5.809\cdot 10^{-15}$
a_{25}	$1.118\cdot 10^{-9}$	$1.118\cdot 10^{-9}$
a_{26}	$5.731\cdot 10^{-11}$	$5.731\cdot 10^{-11}$
a_{27}	$1.546\cdot 10^{-12}$	$1.546\cdot 10^{-12}$

B.2 Correlation for Density

The density correlation applied in this study was determined as follows:

1. Measurement of density in dependence of salinity and temperature according to table B.3.
2. Least-square fit of the experimental density data to the polynomial of

SHARQAWY ET AL. [157] for the density of sea water at atmospheric pressure.

Table B.3: Test conditions for density experiments.

Parameter	**Unit**	**Value**	**Repetitions**
Salt concentration	$\frac{g_{\mathrm{NaCl}}}{kg_{\mathrm{H_2O}}}$	0, 5, 10, ...40, 100, 150, ..., 350	-
Temperature	°C	15, 20, ..., 60	3

The measurements were conducted with a DMA 4100 M density meter [168] which had an accuracy of 0.0001 $\mathrm{g/cm^3}$ for the density and 0.05 °C for temperature [7]. The same aqueous NaCl solution was used as for the refractive index measurments (section B.1).

The experimental data were fitted to equation B.2.

$$\begin{aligned}
\rho_{\mathrm{H_2O}} &= b_1 + b_2 \cdot T + b_3 \cdot T^2 + b_4 \cdot T^3 + b_5 \cdot T^4 \\
\rho_{\Delta} &= b_6 \cdot S_{\mathrm{R}} + b_7 \cdot S_{\mathrm{R}} \cdot T + b_8 \cdot S_{\mathrm{R}} \cdot T^2 + b_9 \cdot S_{\mathrm{R}} \cdot T^3 + b_{10} \cdot S_{\mathrm{R}}^2 \cdot T^2 \\
S_{\mathrm{R}} &= w_{\mathrm{S}} \cdot \frac{35165.04}{35000} \\
\rho &= \rho_{\mathrm{H_2O}} + \rho_{\Delta}
\end{aligned} \tag{B.2}$$

The variables of the empirical equation have the following units: reference salinity S_{R} [g/kg], w_{S} [g/kg], T [°C]. The resulting coefficients b_i are listed in table B.4 . A correlation coefficient of $R = 99.99\%$ is achieved. The adjusted correlation coefficient is $R_{\mathrm{adj}} = 99.98\%$ and the mean standard deviation is $7.8 \cdot 10^{-3}\ \mathrm{kg/m^3}$.

Table B.4: Empirical coefficients of the density equation B.2.

	SHARQAWY ET AL. [157]	**This Study**
b_1	$9.999229 \cdot 10^{2}$	$9.998626 \cdot 10^{2}$
b_2	$2.034118 \cdot 10^{-2}$	$1.187115 \cdot 10^{-1}$
b_3	$-6.162459 \cdot 10^{-3}$	$-1.262937 \cdot 10^{-2}$
b_4	$2.261466 \cdot 10^{-5}$	$1.623414 \cdot 10^{-4}$
b_5	$-4.657066 \cdot 10^{-8}$	$-1.025641 \cdot 10^{-6}$
b_6	$8.020024 \cdot 10^{2}$	$7.702272 \cdot 10^{2}$
b_7	-2.000518	$-9.535391 \cdot 10^{-1}$
b_8	$1.677102 \cdot 10^{-2}$	$-3.661409 \cdot 10^{-2}$
b_9	$-3.060054 \cdot 10^{-5}$	$2.252212 \cdot 10^{-4}$
b_{10}	$-1.613222 \cdot 10^{-5}$	$1.165671 \cdot 10^{-1}$

B.3 Correlation for Practical Osmotic Coefficient

The empirical coefficients of the equation for the practical osmotic coefficient were determined by means of a least square fit of data of CLARKE and GLEW [22] to equation (3.10). They are listed in table B.5.

Table B.5: Empirical coefficients of the practical osmotic coefficient equation (3.10).

	This Study
q_1	0.805973677117490
q_2	0.805765894410060
q_3	0.162449435049612
q_4	0.0905977224532414
q_5	1.04634733430156
q_6	-0.000252541737505390
q_7	1.05240369138876
q_8	0.972545671538487
q_9	0.253057549001445
q_{10}	0.00669306548570762

B.4 Correlation for Diffusivity

The diffusivity correlation applied in this study was determined as follows:

1. Measurement of diffusivity in dependence of salinity and temperature according to tables B.6 and B.7.
2. Identification of a diffusivity correlation from literature which predicts the experimental results within the order of measurement accuracy.

Table B.6: Test conditions for the determination the of concentration dependence of diffusivity.

Parameter	**Unit**	**Value**	**Repetitions**
Salt mass fraction (upper / lower cell half, see figure B.1)	$\frac{g_{NaCl}}{kg_{Sol.}}$	(0 / 1), (0 / 6), (0 / 10), (5 / 10), (5 / 15), (30 / 40), (45 / 55), (145 / 155), (220 / 230)	6
Temperature	°C	23	

Table B.7: Test conditions for the determination of the temperature dependence of diffusivity.

Parameter	**Unit**	**Value**	**Repetitions**
Salt mass fraction (upper / lower cell half, see figure B.1)	$\frac{g_{NaCl}}{kg_{Sol.}}$	(0 / 10)	6
Temperature	°C	14, 18, 23, 28, 35, 40	

For the measurements, the setup of REHFELDT [136, fig. 4.1, p. 24] was used having a flow junction cell tailored for diffusivity experiments, see figure B.1. The optical setup of REHFELDT [136] was changed from Holographic Interferometry to Digital Finite Fringe Interferometry allowing the efficient data analysis of TAKEDA ET AL. [165]. With JANG'S permission, his MATLAB® code implementation [76] of the algorithm of TAKEDA ET AL. [165] was integrated in the evaluation algorithm used in this study.

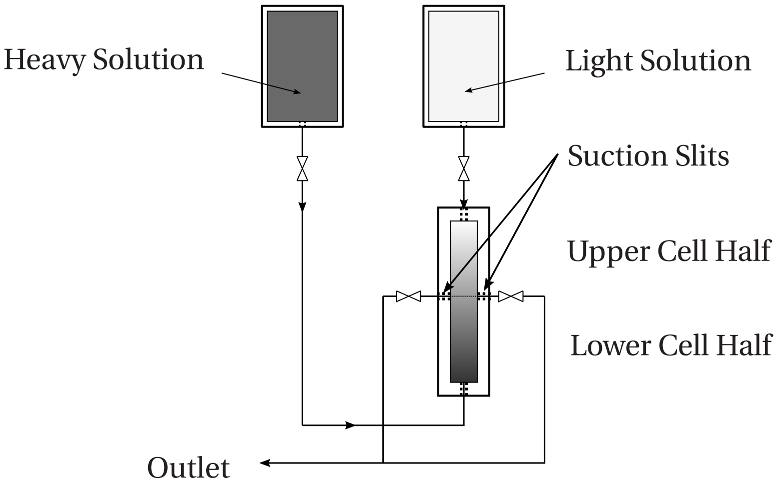

Figure B.1: Diffusivity experiment adapted from REHFELDT [136, fig. 4.2, p. 26] at the INSTITUTE OF PLANT AND PROCESS TECHNOLOGY [168].

The experimental results for diffusivity are depicted in figures B.2(a) and B.2(b).

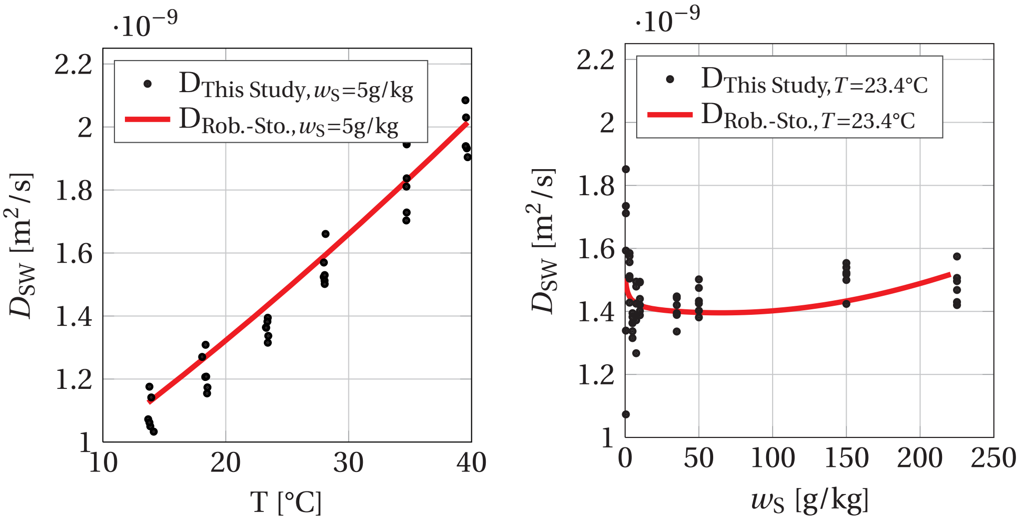

(a) Dependence of diffusivity on temperature.

(b) Dependence of diffusivity on salt mass fraction.

Figure B.2: Dependence of diffusivity on temperature and salt mass fraction: comparison of experimental results of this study with the correlation going back to ROBINSON and STOKES [141, p. 316].

The scattering of the experimental diffusivity results of $\pm 0.1 \cdot 10^{-9}$ gives a rough estimate for the achieved experimental accuracy. Note that this estimate only applies for solutions with salt mass fractions above $w_S > 0.5$ g/kg. For diffusivity experiments at concentrations lower than 5 g/kg, a lower concentration difference than 10 g/kg between upper and lower cell half had to be accepted. This lead to a lower total fringe number and to higher measurement inaccuracies.

In addition to the experimental diffusivity data, the theoretically motivated function of Robinson and Stokes [141, p. 316] is illustrated in figures B.2(a) and B.2(b):

$$D = \overbrace{(D^0 + \underbrace{\Delta_1}_{f_{\Delta_1}} + \underbrace{\Delta_2}_{f_{\Delta_2}})\underbrace{\left(1 + m\frac{d\ln\gamma}{dm}\right)}_{f_\Gamma}}^{\text{dilute solutions}}\overbrace{\underbrace{\left[1 + 0.036m\left(\frac{D^*_{\mathrm{H_2O}}}{D^0} - n\right)\right]}_{f_{\mathrm{H_2O}}}\underbrace{\frac{\mu^0}{\mu}}_{f_\mu}}^{\text{concentrated solutions}} \tag{B.3}$$

In order to derive an empirical correlation from tabulated data of Robinson and Stokes [141, p. 316], the terms f_{Δ_1}, f_{Δ_2}, $f_{\mathrm{H_2O}}$ and f_Γ were modeled according to equations (B.4) to (B.7):

$$f_{\Delta_1} = p_1 \cdot \frac{\sqrt{w_S}}{p_2 + p_3\sqrt{w_S}} \cdot 10^{-9} \tag{B.4}$$

$$f_{\Delta_2} = (p_4 \cdot w_S^{p_5} + p_6 \cdot w_S + p_7) \cdot 10^{-9} \tag{B.5}$$

$$f_{H_2O} = p_8 + p_9 \cdot w_S \tag{B.6}$$

$$\begin{aligned} f_\Gamma = 1 + w_S \cdot (p_{10} \cdot (p_{11} \cdot w_S^2 + p_{12} \cdot w_S + p_{13}) \\ + p_{10} \cdot w_S \cdot (2 \cdot p_{11} \cdot w_S + p_{12}) \\ - \frac{p_{14}}{2\sqrt{w_S} \cdot (p_{15}\sqrt{w_S} + p_{16})} + p_{14}\frac{p_{15}}{2(p_{15}\sqrt{w_S} + p_{16})^2}) \end{aligned} \tag{B.7}$$

The parameters for the correlations of f_{Δ_1} and f_{Δ_2} were determined by a least-square fit to tabulated concentration dependent data from Robinson and Stokes [141, tab. 11.4, p. 318]. The correlation for $f_{\mathrm{H_2O}}$ is based on the values $D^0 = 1.612 \cdot 10^{-9}$ m/s [141, p. 382], $D^*_{\mathrm{H_2O}} = 2.44 \cdot 10^{-9}$ m/s [141, p. 316] and hydration number $n = 1.12$ [141, p. 119]. The ratio $D^*_{H_2O}/D^0$ is assumed to be temperature independent. The parameters of the correction term f_Γ were determined via a least square fit to data of CLARKE and GLEW [22] consistent with the determination of the practical osmotic coefficient in section B.3. Also in this case, the validity range is 0 g/kg to 100 g/kg for salt mass fraction and 283.15 K to 323.15 for temperature. For viscosity $\mu(w_S, T)$ the correlation provided by SHARQAWY ET AL. [157] is used (section 3.1.5).

The experimental results presented in figures B.2(a) and B.2(b) agree well with the diffusivity equation of ROBINSON and STOKES [141] modeled with the derived empirical coefficients listed in table B.8. This result is an indicator for the validity of the diffusivity correlation decribed by equations (B.3) to (B.7) as well as for the validity of the used viscosity correlation.

Table B.8: Empirical coefficients of diffusivity equations (B.4) to (B.7).

	This Study
p_1	-0.271003032944101
p_2	1.82962943583334
p_3	10.3099517092153
p_4	0.191997848766897
p_5	0.246225039130240
p_6	-0.388200434246170
p_7	-0.0203899527095651
p_8	0.999546735813473
p_9	0.268871085854307
p_{10}	2.08238520676860
p_{11}	1.42157253344049
p_{12}	1.97683340362422
p_{13}	0.409006123046659
p_{14}	0.559413222954090
p_{15}	0.695554989336063
p_{16}	0.110121855758902
D^0	$1.612 \cdot 10^{-9}$

B.5 pH-Value

The pH-value of the pure water produced with a the Trunz Brackish Water Box RO Plant [175] was pH = 6.8 on average with a standard deviation of 0.3. During the measurements, the mean pure water temperature was 21.0 ±2.2°C. The pH-value of the aqueous NaCl solutions was pH = 7.1 on average with a standard deviation of 0.5, measured at a mean fluid temperature of 23.1 ± 2.1°C. For comparison, standard sea water has a pH-value of 8.1 according to MILLERO ET AL. [116, p. 63].

The measurements were carried out on a random basis by means of the PCE Instruments PCE-PH 22 [129] or the Mettler Toledo SevenExcellence [114] device. Significant changes of the pH-value were neither expected nor observed.

C 3D CFD Results for a Salinity Dependent Salt Permeability Constant

The 3D CFD results presented in the following are determined with the Solution-Diffusion model for the membrane based on a salinity dependent salt permeability constant $B = f(w^{\mathrm{E}}_{\mathrm{S,F,M}})$. The dependence of B on salinity is modeled by a linear function for brackish water salinities and a saturation level for higher salinities, see figure 6.12.

In contrast to the iterative determination of B, which guarantees a relative error $e_{\bar{j}_{\mathrm{P}},\mathrm{rel}}$ smaller than e_{lim} (see section 3.3), $e_{\bar{j}_{\mathrm{P}},\mathrm{rel}}$ depends now on the quality of the correlation for local variation of $B = f(w^{\mathrm{E}}_{\mathrm{S,F,M}})$. In table C.1, the results for $e_{\bar{j}_{\mathrm{P}},\mathrm{rel}}$ are listed. Note that $\bar{w}^{\mathrm{E}}_{\mathrm{S,F,M}}$ is the mean salt mass fraction on the entire membrane, while $w^{\mathrm{E}}_{\mathrm{S,F,M}}$ denotes the cell individual local salt mass fraction on the membrane.

Table C.1: Errors of 3D CFD with $B = f(w^{\mathrm{E}}_{\mathrm{S,F,M}})$ relative to experimental permeate flux data.

ID	$\bar{w}^{\mathrm{E}}_{\mathrm{S,F,M}}$ [g/kg]	$\bar{w}^{\mathrm{E}}_{\mathrm{S,P}}$ [g/kg]	$\bar{j}^{\mathrm{EXP}}_{\mathrm{P}}$ [kg/m^{2}h]	$\bar{j}^{\mathrm{CFD}}_{\mathrm{P}}$ [kg/m^{2}h]	$e_{\bar{j}_{\mathrm{P}},\mathrm{rel}}$ [%]
BW-P15	20.4	3.0	5.7	5.5	-3.2
BW-P20	26.4	3.4	7.9	7.8	-0.3
BW-P25	32.2	3.9	10.0	9.9	-0.5
BW-P35	43.4	4.9	13.4	13.6	1.6
BW-P45	53.7	5.9	16.7	17.0	2.0
BW-P55	63.8	6.5	21.1	21.7	2.6
BW-P60	70.1	7.2	22.9	23.3	1.9
SW-P45	66.6	17.7	6.5	6.4	-1.2
SW-P55	76.5	18.5	8.2	7.9	-2.6
SW-P60	81.4	18.8	8.8	8.5	-3.3
Average					-0.3

In table C.2, the relative errors of the boundary layer data are included for both the iterative determination of B and for the locally varying $B = f(w_{\text{S,F,M}}^{\text{E}})$.

Table C.2: Errors of 3D CFD relative to experimental boundary layer data.

Case ID	z_{th} [mm]	$e_{w_{\text{S,th}},\text{rel}}$ [%]	$e_{w_{\text{S}},\text{rel}}$ [%]	$e_{I_{\text{n}},\text{rel}}$ [%]	z_{th} [mm]	$e_{w_{\text{S,th}},\text{rel}}$ [%]	$e_{w_{\text{S}},\text{rel}}$ [%]	$e_{I_{\text{n}},\text{rel}}$ [%]
CFD	$B = f(\text{iteration})$				$B = f(w_{\text{S,F,M}}^{\text{E}})$			
BW-P15	0.04	1.0	0.3	-5.7	0.04	0.9	0.3	-5.6
BW-P20	0.04	4.0	2.8	-1.8	0.04	4.2	2.9	-2.0
BW-P25	0.30	6.1	2.8	-7.0	0.30	6.3	2.9	-7.1
BW-P35	0.55	-5.4	-3.1	-2.5	0.55	-6.1	-3.4	-2.7
BW-P45	0.66	-9.1	-3.1	-3.8	0.66	-10.0	-3.3	-3.9
BW-P55	0.65	-7.7	-1.8	-2.2	0.65	-8.0	-1.9	-2.2
BW-P60	0.66	-4.5	-0.5	-1.4	0.66	-5.6	-0.8	-1.3
SW-P45	0.58	5.1	2.6	-2.6	0.58	5.5	2.6	-3.4
SW-P55	0.78	4.3	2.2	-4.7	0.78	4.4	2.2	-5.3
SW-P60	0.83	3.9	2.1	-2.6	0.83	4.0	2.1	-3.1
Average		-0.2	0.4	-3.4		-0.4	0.4	-3.6

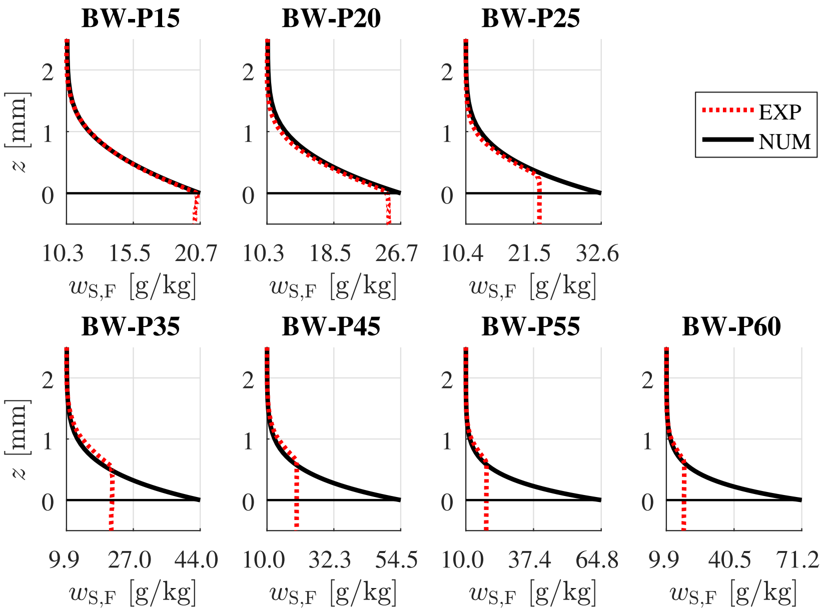

Figure C.1: BW experiments: Digital Finite Fringe Interferometry results versus 3D CFD data for $B = f(w_{\text{S,F,M}}^{\text{E}})$.

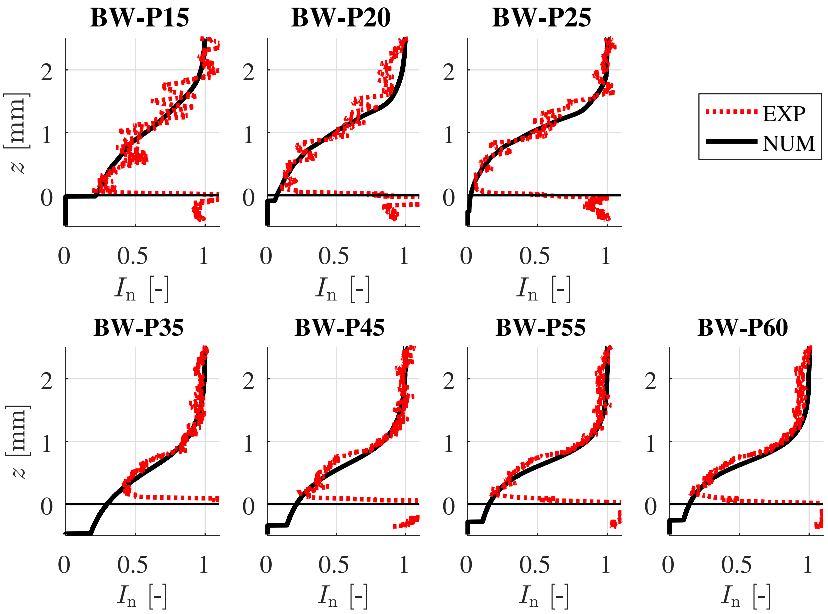

Figure C.2: BW experiments: Schlieren and Shadowgraphy results versus combined 3D CFD & optical ray tracing data for $B = f(w^{E}_{S,F,M})$.

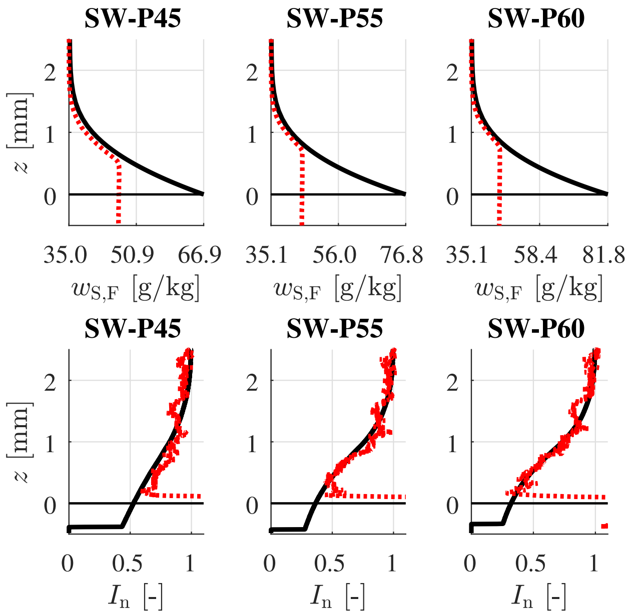

Figure C.3: SW experiments: Digital Finite Fringe Interferometry and Shadowgraphy results versus combined 3D CFD & optical ray tracing data for $B = f(w^{E}_{S,F,M})$.

D Conversion of Membrane Model Parameters

GEISE ET AL. [55] analyzed a wide range of membrane performance data from literature. This database appears to be well suited to benchmark the Maxwell-Stefan model results of this study. The data of GEISE ET AL. [55] are based on the SDM. Thus, the MS model parameters used in this study need to be converted to the key performance parameters used by GEISE ET AL. [55].

In the work of GEISE ET AL. [55], the water flux is defined as follows:

$$j_{\mathrm{W}} = \frac{1}{\Delta l^{\mathrm{M}}} \rho_{\mathrm{W}}^{\mathrm{E}} K_{\mathrm{W}} D_{\mathrm{WM}} \frac{\bar{V}_{\mathrm{W}}}{RT} (\Delta p - \Delta \pi) \tag{D.1}$$

GEISE ET AL. [55] express the water solubility K_{W} as concentration of water in the membrane [g H2O/cm^3] related to the concentration of water in the external solution:

$$K_{\mathrm{W}} = \frac{\rho_{\mathrm{W}}^{\mathrm{M}}}{\rho_{\mathrm{W}}^{\mathrm{E}}} \tag{D.2}$$

The water permeability is defined as [55]:

$$P_{\mathrm{W}} = K_{\mathrm{W}} \cdot D_{\mathrm{WM}} \tag{D.3}$$

Comparing these definitions with the model equations introduced in chapter 2, i.e. (2.17) and (2.19), the correlations for the water solubility seems different at first sight. However, the density of the membrane can be approximated by the density of the external solution [179]. Furthermore, the density of the external solution is approximately the one of the pure solvent which is valid for dilute solutions [127, p. 373], [135, p. 55]. Thus, it follows:

$$\rho^{\mathrm{M}} \approx \rho^{\mathrm{E}} \approx \rho_{W}^{\mathrm{E}} \tag{D.4}$$

Assuming continuous chemical potential at the interface of external solution and membrane phase, the water solubility K_W can be linked to the term $\frac{1}{\gamma_\mathrm{W}^\mathrm{M}}\frac{\bar{M}_\mathrm{W}}{\bar{M}^\mathrm{M}}$, see also [9, p. 27]. With equation (D.4) and the approximation of $\bar{M}_\mathrm{W}$ by $\bar{M}^\mathrm{E}$, K_W can be derived as follows:

$$\ln(\gamma_\mathrm{W}^\mathrm{E}\cdot x_\mathrm{W}^\mathrm{E}) = \ln(\gamma_\mathrm{W}^\mathrm{M}\cdot x_\mathrm{W}^\mathrm{M}) \tag{D.5}$$

$$x_\mathrm{W}^\mathrm{M} = \frac{\gamma_\mathrm{W}^\mathrm{E}}{\gamma_\mathrm{W}^\mathrm{M}}\cdot x_\mathrm{W}^\mathrm{E} \tag{D.6}$$

$$\frac{c_\mathrm{W}^\mathrm{M}}{c^\mathrm{M}} = \frac{\gamma_\mathrm{W}^\mathrm{E}}{\gamma_\mathrm{W}^\mathrm{M}}\cdot\frac{c_\mathrm{W}^\mathrm{E}}{c^\mathrm{E}} \tag{D.7}$$

$$\frac{\rho_\mathrm{W}^\mathrm{M}}{\bar{M}_\mathrm{W}\cdot c^\mathrm{M}} = \frac{\gamma_\mathrm{W}^\mathrm{E}}{\gamma_\mathrm{W}^\mathrm{M}}\cdot\frac{\rho_\mathrm{W}^\mathrm{E}}{\bar{M}_\mathrm{W}\cdot c^\mathrm{E}} \tag{D.8}$$

$$K_\mathrm{W} \overset{!}{=} \frac{\rho_\mathrm{W}^\mathrm{M}}{\rho_\mathrm{W}^\mathrm{E}} = \frac{\gamma_\mathrm{W}^\mathrm{E}}{\gamma_\mathrm{W}^\mathrm{M}}\frac{c^\mathrm{M}}{c^\mathrm{E}} = \frac{\gamma_\mathrm{W}^\mathrm{E}}{\gamma_\mathrm{W}^\mathrm{M}}\cdot\frac{\rho^\mathrm{M}}{\rho^\mathrm{E}}\cdot\frac{\bar{M}^\mathrm{E}}{\bar{M}^\mathrm{M}} \approx \underbrace{\frac{1}{\gamma_\mathrm{W}^\mathrm{M}}}_{K_{\mathrm{W},\gamma}}\cdot 1\cdot\frac{\bar{M}_\mathrm{W}}{\bar{M}^\mathrm{M}} \tag{D.9}$$

With equation (D.9), constraints related to $K_{\mathrm{W},\gamma} = \frac{1}{\gamma_\mathrm{W}^\mathrm{M}}$ can be estimated (section 6.3.2). The value of molar mass of the membrane solution $\bar{M}^\mathrm{M}$ should be at least as large as the one of the external solution $\bar{M}^\mathrm{E}$:

$$\bar{M}_\mathrm{M} > \bar{M}^\mathrm{M} \geq \bar{M}^\mathrm{E} \geq \bar{M}_\mathrm{W} \tag{D.10}$$

Thus, the lower constraint $K_{\mathrm{W},\gamma,\mathrm{min}}$ is equal to K_W (section 6.3.2). An upper constraint for $K_{\mathrm{W},\gamma}$ can be estimated by approximating the molar mass of the membrane solution $\bar{M}^\mathrm{M}$ by the molar mass of the membrane $\bar{M}_\mathrm{M}$:

$$K_{\mathrm{W},\gamma,\mathrm{max}} = K_\mathrm{W}\cdot\frac{\bar{M}_\mathrm{M}}{\bar{M}_\mathrm{W}} \tag{D.11}$$

To link the Maxwell-Stefan model results with the results of the GEISE ET AL. [55], the following expression for the water permeability can be used:

$$P_\mathrm{W}^\mathrm{MS} = \frac{\dot{j}_\mathrm{W}^\mathrm{MS}}{\frac{1}{\Delta l^\mathrm{M}}\rho^\mathrm{M}\frac{\bar{V}_\mathrm{W}}{RT}(\Delta p - \Delta\pi)} \tag{D.12}$$

The diffusivity of water in the membrane can be derived using K_W^{MS}, which was determined by means of the optimization algorithm in section 6.3.2:

$$D_{WM} = \frac{P_W^{MS}}{K_W} \tag{D.13}$$

In view of the salt properties, GEISE ET AL. [55] express the salt flux as well as the salt distribution coefficient in the same way as described in this study, see equations (2.18) and (2.21).

The salt permeability can be derived analogously:

$$P_S^{MS} = \frac{\dot{j}_S^{MS}}{\frac{\rho_{S,F}^E - \rho_{S,P}^E}{\Delta l^M}} \tag{D.14}$$

For the salt distribution coefficient, an effective parameter needs to be introduced in order to take not only feed but also permeate salinity into account. The salt solubility K_S in equation (2.18) can be calculated by relating the salt molar fraction difference inside the membrane ($x_{S,F}^M - x_{S,P}^M$) to the one in the external solution ($x_{S,F}^E - x_{S,P}^E$). For this purpose, the molar fractions inside the membrane where expressed as a function of the molar fractions in the external solution (equations (2.10) and (2.11)). Additionally, a constant ratio between the activity coefficients in the membrane and the external solution needed to be assumed (equation (2.15)), to be able to express ($x_{S,F}^M - x_{S,P}^M$) as $\frac{\gamma_S^E}{\gamma_S^M}(x_{S,F}^E - x_{S,P}^E)$. When transferring the Maxwell-Stefan model results to the SDM results, the assumption made in equation (2.15) is not valid any more. The ratio of activity coefficients $\frac{\gamma_S^E}{\gamma_S^M}$ needs to be derived differently. It links the molar fractions inside and outside the membrane:

$$\frac{\gamma_S^E}{\gamma_S^M} = \frac{x_{S,F}^M - x_{S,P}^M}{x_{S,F}^E - x_{S,P}^E} \tag{D.15}$$

To gain the salt solubility K_S, the ratio of activity coefficients (term A in equation (D.16)) needs to be multiplied by the ratio of molar concentrations in the membrane and the external solution (term B, resulting from transformation between concentration measures). Thus, the salt solubility can be calculated as follows, compare also equation (2.18):

$$K_{\mathrm{S}}^{\mathrm{MS}} = \underbrace{\frac{x_{\mathrm{S,F}}^{\mathrm{M}} - x_{\mathrm{S,P}}^{\mathrm{M}}}{x_{\mathrm{S,F}}^{\mathrm{E}} - x_{\mathrm{S,P}}^{\mathrm{E}}}}_{\mathrm{A}} \cdot \underbrace{\frac{c^{\mathrm{M}}}{c^{\mathrm{E}}}}_{\mathrm{B}} \tag{D.16}$$

Now, the corresponding diffusivity for salt in the membrane results:

$$D_{\mathrm{SM}} = \frac{P_{\mathrm{S}}^{\mathrm{MS}}}{K_{\mathrm{S}}^{\mathrm{MS}}} \tag{D.17}$$

Supervised Theses

More than 30 students have contributed with their term papers, diploma theses, bachelor's theses and master's theses to the research of the author. These students' contributions were provided to the Lehrstuhl für Thermodynamik in the years 2012 through 2016 under the close supervision of the author of this Ph.D. thesis with regard to all academic, professional, and context-related concerns. Various issues were investigated, contributing to solar powered desalination technology and fundamental research issues, in particular heat and mass transfer phenomena on Reverse Osmosis membranes. Results of the supervised theses were partly included in this Ph.D. thesis. The author would like to express his sincere gratitude to all formerly supervised students for their commitment and support of the research project and of the Ph.D. thesis at hand.

Student	Thesis	Reference
Hutter, Felix	Design of an Experimental Test Setup for a PV/T powered Reverse Osmosis Desalination Plant, Bachelor Thesis, 2012.	[74]
Hamberger, Stephan	Optimization of a Seawater Proof PV/T Collector, Term Paper, 2012.	[63]
Dürr, Holger	Modeling of a Reverse Osmosis Desalination Plant, Term Paper, 2012.	[34]
Shahrouri, Ahmad	Investigation of Influence Parameters on Long-Term Performance of PTFE-Membranes in Membrane Distillation, Master's Thesis, 2012.	[156]

Pinedo Engelmann, Pinedo	An Alternative Model to Describe a Reverse Osmosis Membrane - the Donnan Steric Pore Model, Term Paper, 2013.	[38]
Link, Moritz	Experimental Investigation of a Brackish Water Reverse Osmosis Desalination Plant, Bachelor's Thesis, 2013.	[100]
Wolf, Stephan	Modelling of a Reverse Osmosis Plant Driven by Hybrid Photovoltaic Thermal (PV/T) Collectors, Term Paper, 2013.	[183]
Schmidt, William	Techno-Economic Analysis of Solar Desalination Technologies, Term Paper, 2013.	[151]
Präbst, Alexander	A Bench-Scale Reverse Osmosis Plant - Experimental Setup and Numerical Modeling, Diploma Thesis, 2013.	[134]
Hamberger, Stephan	Design, Building and Testing of a Novel Photovoltaic System with Active Cooling, Master's Thesis, 2013.	[64]
Schmidt, Tobias	CFD Modeling of a Reverse Osmosis Desalination Membrane Test Cell, Term Paper, 2014.	[150]
Borgmann, Norbert	Conceptual Design and Implementation of a Modularised Dynamic Model Simulating a Desalination Plant, Term Paper, 2014.	[19]
Link, Moritz	Design, Implementation and Validation of a LabVIEW Measurement and Control System, Term Paper, 2014.	[101]
Marrero Diaz, Silvia	Experimental Investigation of Reverse Osmosis Membranes, Term Paper, 2014.	[31]
Thies, Cornelius	Numerical and Experimental Investigation of Concentration Polarisation in Membrane Desalination, Bachelor's Thesis, 2014.	[172]

Wolf, Stephan	Implementation of an Optical Measuring System for Investigation of Concentration Boundary Layers in Membrane Desalination, Master's Thesis, 2014.	[184]
Eyerer, Sebastian	Experimental Investigation of Boundary Layers in Membrane Desalination Using Quantitative Two-Wavelengths Schlieren, Diploma Thesis, 2014.	[39]
Bauer, Anna, Neudeck, Jan-Hendrick, Reibetanz, Lisa	Research on Refractive Index, Conductivity and pH-values of Ocean Water and other Salt Waters for a Reverse Osmosis Desalination Plant, Research Internship, 2014.	[11]
Altnöder, Maximilian	Experimental Investigation of Diffusive Coefficients of a NaCl-Water-Solution and Constructive Optimization of a Membrane Test Rig, Bachelor's Thesis, 2015.	[3]
Appel, Daniel	Optimization of a Test Rig Control Software and Review of Membrane Transport Phenomena in Reverse Osmosis Desalination, Bachelor's Thesis, 2015.	[8]
Meschenmoser, Matthias	Modelling Concentration Boundary Layers for Reverse Osmosis Desalination, Bachelor's Thesis, 2015.	[113]
Köhler, Franziska	Investigation on Evaluation Methods of Optical Experiments for Temperature and Concentration Boundary Layer Measurements, Term Paper, 2015.	[93]
Behnen, Tanja	Investigation of Algorithms to Determine and Evaluate Temperature and Concentration Boundary Layers in Membrane Desalination, Bachelor's Thesis, 2015.	[12]

Schreyer, Matthias	Numerical Investigation of a Reverse Osmosis Membrane Test Setup, Bachelor's Thesis, 2015.	[154]
Kuczaty, Julian	Application of Digital Holographic Interferometry for Analysis of Concentration Boundary Layers in Membran Desalination, Master's Thesis, 2015.	[92]
Heithorst, Bernd	Combined CFD and Optical Raytracing Simulation for a Reverse Osmosis Membrane Test Setup, Master's Thesis, 2015.	[68]
Zörntlein, Kilian	Design, Optimization and Experimental Investigation of Membrane Test Cells, Bachelor's Thesis, 2016	[186]
Altnöder, Maximilian	Application of Digital Interferometry for Investigation of Mass Transfer Boundary Layers, Term Paper, 2016	[4]
Hofmann, Michael	Experimental Investigations of Material Properties for Reverse Osmosis Membrane Desalination, Bachelor's Thesis, 2016	[70]
Körber, Stefan	Experimental Investigation and Optimization of a Schlieren Test Rig for Quantitative Boundary Layer Evaluations on Reverse Osmosis Membranes, Master's Thesis, 2016	[94]

Bibliography

[1] E. Abbe. Beiträge zur Theorie des Mikroskops und der mikroskopischen Wahrnehmung. *Archiv für mikroskopische Anatomie*, 9:413 – 468, 1873.

[2] A. Alexiadis, D. Wiley, A. Vishnoi, R. Lee, D. Fletcher, and J. Bao. CFD modelling of reverse osmosis membrane flow and validation with experimental results. *Desalination*, 217(1):242 – 250, 2007.

[3] M. Altnöder, A. Kroiß, M. Spinnler, and T. Sattelmayer. *Experimental investigation of diffusive coefficients of a NaCl-water-solution and constructive optimization of a membrane test rig*. Bachelor's Thesis, Technical University of Munich, 2015.

[4] M. Altnöder, A. Kroiß, M. Spinnler, and T. Sattelmayer. *Application of digital interferometry for investigation of mass transfer boundary layers*. Term Paper, Technical University of Munich, 2016.

[5] ANSYS, Inc. *ANSYS ICEM CFD 14.5 help manual*, 2012.

[6] Anton Paar GmbH. *Abbemat Series - the universal refractometer: the Abbemat MW Multiple Wavelengths*, 2016.

[7] Anton Paar GmbH. *Laboratory density and concentration meters: the DMA 4100 M*, 2016.

[8] D. Appel, A. Kroiß, M. Spinnler, and T. Sattelmayer. *Optimization of a test rig control software and review of membrane transport phenomena in reverse osmosis desalination*. Bachelor's Thesis, Technical University of Munich, 2015.

[9] R. W. Baker. *Membrane technology and applications*. John Wiley and Sons Ltd, 2nd edition, 2004.

[10] C. Bartels, R. Franks, S. Rybar, M. Schierach, and M. Wilf. The effect of feed ionic strength on salt passage through reverse osmosis membranes. *Desalination*, 184(1):185 – 195, 2005.

[11] A. Bauer, J.-H. Neudeck, L. Reibetanz, S. Eyerer, A. Kroiß, M. Spinnler, and T. Sattelmayer. *Research on refractive index, conductivity and pH-values of ocean water and other salt waters for a reverse osmosis desalination plant*. Research Internship, Technical University of Munich, 2014.

[12] T. Behnen, A. Kroiß, M. Spinnler, and T. Sattelmayer. *Investigation of algorithms to determine and evaluate temperature and concentration boundary layers in membrane desalination*. Bachelor's Thesis, Technical University of Munich, 2015.

[13] A. S. Berman. Laminar flow in channels with porous walls. *Journal of Applied Physics*, 24(9):1232–1235, September 1953.

[14] B. Bernales. *Modelisation de l'hydrodynamique et des transfers dans les procedes de filtration membranaire*. Ph.D. -Thesis, Universite d'Aix-Marseille, 2013.

[15] R. B. Bird, W. E. Stewart, and E. N. Lightfoot. *Transport phenomena*. John Wiley & Sons, Inc., 1st edition, 1960.

[16] R. B. Bird, W. E. Stewart, and E. N. Lightfoot. *Transport phenomena*. John Wiley & Sons, Inc., 2nd edition, 2002.

[17] J. G. A. Bitter. *Transport mechanisms in membrane separation processes (the plenum chemical engineering series)*. Plenum Press, 1991.

[18] R. Blue. Combination of Interferometer-Schlieren apparatus for density determination in non-homogeneous transparent fluids. United States Patent Office, No. 2,776,593, 1 1957.

[19] N. Borgmann, A. Kroiß, A. Präbst, M. Spinnler, and T. Sattelmayer. *Conceptual design and implementation of a modularised dynamic model simulating a desalination plant.* Term Paper, Technical University of Munich, 2014.

[20] T. Y. Cath, M. Elimelech, J. R. McCutcheon, R. L. McGinnis, A. Achilli, D. Anastasio, A. R. Brady, A. E. Childress, I. V. Farr, N. T. Hancock, J. Lampi, L. D. Nghiem, M. Xie, and N. Y. Yip. Standard methodology for evaluating membrane performance in osmotically driven membrane processes. *Desalination*, 312:31 – 38, 2013.

[21] V. Chen, H. Li, and A. Fane. Non-invasive observation of synthetic membrane processes – a review of methods. *Journal of Membrane Science*, 241(1):23 – 44, 2004.

[22] E. C. W. Clarke and D. N. Glew. Evaluation of the thermodynamic functions for aqueous sodium chloride from equilibrium and calorimetric measurements below 154°C. *Journal of Physical and Chemical Reference Data*, 14(2):489–610, 1985.

[23] C. Completo, V. Semiao, and V. Geraldes. Efficient CFD-based method for designing cross-flow nanofiltration small devices. *Journal of Membrane Science*, 500:190 – 202, 2016.

[24] O. Coronell, M. I. González, B. J. Mariñas, and D. G. Cahill. Ionization behavior, stoichiometry of association, and accessibility of functional groups in the active layers of reverse osmosis and nanofiltration membranes. *Environmental Science & Technology*, 44(17):6808–6814, 2010.

[25] O. Coronell, B. Mi, B. J. Mariñas, and D. G. Cahill. Modeling the effect of charge density in the active layers of reverse osmosis and nanofiltration membranes on the rejection of Arsenic(III) and Potassium Iodide. *Environmental Science & Technology*, 47(1):420–428, 2013.

[26] E. L. Cussler. *Diffusion - mass transfer in fluid systems.* Cambridge University Press, 3rd edition, 2009.

[27] W. Dahm. *Umkehrosmose und Gaspermeation - Untersuchungen zur Berechnung und Optimierung von Wickel- und Hohlfasermodulen*. Dissertation, Rheinisch-Westfälische Technische Hochschule Aachen, 1986.

[28] Danfoss A/S. Product specifications for Danfoss APP 1.0 axial piston pump. `http://high-pressurepumps.danfoss.com/products/high-pressure-pumps/app-pumps/app-pumps/#/`, Accessed: 2017-08-14.

[29] P. Debye and E. Hückel. Zur Theorie der Elektrolyte. I. Gefrierpunktserniedrigung und verwandte Erscheinungen. *Physikalische Zeitschrift*, 24(185):305, 1923.

[30] H.-U. Demisch and W. Pusch. Ion exchange capacity of cellulose acetate membranes. *Journal of the Electrochemical Society*, 123(3): 370–374, 1976.

[31] S. M. Diaz, A. Kroiß, M. Spinnler, and T. Sattelmayer. *Experimental investigation of reverse osmosis membranes*. Term Paper, Technical University of Munich, 2014.

[32] DOW Water Solutions. Product data sheet for membrane module type BW30-4040. `http://msdssearch.dow.com/PublishedLiteratureDOWCOM/dh_0973/0901b80380973b79.pdf?filepath=liquidseps/pdfs/noreg/609-00350.pdf&fromPage=GetDoc`, Accessed: 2017-06-22.

[33] Dr. Lohmann DIACLEAN GmbH . Product specifications for NaCl. `https://diacleanshop.com/natriumchlorid-1`, Accessed: 2017-09-11.

[34] H. Dürr, A. Kroiß, M. Spinnler, and T. Sattelmayer. *Modeling of a reverse osmosis desalination plant*. Term Paper, Technical University of Munich, 2012.

[35] H. Eckelmann. *Einführung in die Strömungsmeßtechnik*. Leitfäden der angewandten Mathematik und Mechanik - Teubner Studienbücher. Vieweg+Teubner Verlag, 1997.

[36] H. Eckelmann. Optische Messmethoden. In *Einführung in die Strömungsmesstechnik*, pages 142 – 230. Vieweg+Teubner Verlag, Wiesbaden, 1997.

[37] H. T. El-Dessouky and H. M. Ettouney. *Fundamentals of salt water desalination*. Elsevier Science B.V., 2002.

[38] M. P. Engelmann, A. Kroiß, M. Spinnler, and T. Sattelmayer. *An alternative model to describe a reverse osmosis membrane - the donnan steric pore model*. Term Paper, Technical University of Munich, 2013.

[39] S. Eyerer, A. Kroiß, M. Spinnler, and T. Sattelmayer. *Experimental investigation of boundary layers in membrane desalination using quantitative two-wavelengths Schlieren*. Master's Thesis, Technical University of Munich, 2014.

[40] A. Fane, R. Wang, and Y. Jia. Membrane technology: past, present and future. In L. Wang, J. Chen, Y.-T. Hung, and N. Shammas, editors, *Membrane and Desalination Technologies*. Elsevier Science B.V., 2011.

[41] J. Fernández-Sempere, F. Ruiz-Beviá, and R. Salcedo-Díaz. Measurements by holographic interferometry of concentration profiles in dead-end ultrafiltration of polyethylene glycol solutions. *Journal of Membrane Science*, 229(1):187 – 197, 2004. ISSN 0376-7388.

[42] J. Fernández-Sempere, F. Ruiz-Beviá, R. Salcedo-Díaz, and P. García-Algado. Diffusion studies in polarized reverse osmosis processes by holographic interferometry. *Optics and Lasers in Engineering*, 46(12):877 – 887, 2008.

[43] J. Fernández-Sempere, F. Ruiz-Beviá, P. García-Algado, and R. Salcedo-Díaz. Visualization and modelling of the polarization layer and a reversible adsorption process in PEG-10000 dead-end ultrafiltration. *Journal of Membrane Science*, 342(1):279 – 290, 2009.

[44] J. Fernández-Sempere, F. Ruiz-Beviá, P. García-Algado, and R. Salcedo-Díaz. Experimental study of concentration polarization in a crossflow reverse osmosis system using digital holographic interferometry. *Desalination*, 257(1):36 – 45, 2010.

[45] J. Fernández-Sempere, F. Ruiz-Beviá, R. Salcedo-Díaz, and P. García-Algado. Measurement of concentration profiles by holographic interferometry and modelling in unstirred batch reverse osmosis. *Industrial & Engineering Chemistry Research*, 45(21): 7219–7231, 2006.

[46] M. J. Fernández-Torres, F. Ruiz-Beviá, J. Fernández-Sempere, and M. López-Leiva. Visualization of the UF polarized layer by holographic interferometry. *AIChE Journal*, 44(8):1765–1776, 1998.

[47] J. H. Ferziger and M. Peric. *Numerische Strömungsmechanik*. Springer-Verlag Berlin Heidelberg, 2008.

[48] A. Fick. Ueber Diffusion. *Annalen der Physik*, 170(1):59–86, 1855. ISSN 1521-3889.

[49] G. Fimbres-Weihs and D. Wiley. Review of 3D CFD modeling of flow and mass transfer in narrow spacer-filled channels in membrane modules. *Chemical Engineering and Processing: Process Intensification*, 49(7):759 – 781, 2010.

[50] H. Flemming. *Biofouling bei Membranprozessen*. Springer Berlin Heidelberg, 2013.

[51] D. Fletcher and D. Wiley. A computational fluids dynamics study of buoyancy effects in reverse osmosis. *Journal of Membrane Science*, 245 (1-2):175–181, 2004.

[52] M. A. Frommer, J. S. Murday, and R. M. Messalem. Solubility and diffusivity of water and of salts in an aromatic polyamide film. *European Polymer Journal*, 9(4):367 – 373, 1973. ISSN 0014-3057.

[53] T. Fujioka, L. D. Nghiem, S. J. Khan, J. A. McDonald, Y. Poussade, and J. E. Drewes. Effects of feed solution characteristics on the rejection of N-nitrosamines by reverse osmosis membranes. *Journal of Membrane Science*, 409:66 – 74, 2012.

[54] G. M. Geise, H.-S. Lee, D. J. Miller, B. D. Freeman, J. E. McGrath, and D. R. Paul. Water purification by membranes: the role of polymer

science. *Journal of Polymer Science Part B: Polymer Physics*, 48(15): 1685–1718, 2010. ISSN 1099-0488.

[55] G. M. Geise, H. B. Park, A. C. Sagle, B. D. Freeman, and J. E. McGrath. Water permeability and water/salt selectivity tradeoff in polymers for desalination. *Journal of Membrane Science*, 369(1–2):130 – 138, 2011.

[56] V. Geraldes, V. Semião, and M. N. de Pinho. Flow and mass transfer modelling of nanofiltration. *Journal of Membrane Science*, 191(1):109 – 128, 2001.

[57] V. Geraldes and M. D. Afonso. Generalized mass-transfer correction factor for nanofiltration and reverse osmosis. *AIChE Journal*, 52(10): 3353–3362, 2006.

[58] N. Ghaffour, T. M. Missimer, and G. L. Amy. Technical review and evaluation of the economics of water desalination: current and future challenges for better water supply sustainability. *Desalination*, 309 (Supplement C):197 – 207, 2013.

[59] S. M. S. Ghiu. *Mass transfer of ionic species in direct and reverse osmosis processes*. Dissertation, University of South Florida, 2003.

[60] C. D. GmbH. Product specifications for Canon EOS 700D. `https://www.canon.de/for_home/product_finder/cameras/digital_slr/eos_700d/specification.aspx`, Accessed: 2017-10-09.

[61] L. M. Gowman and C. Ethier. Concentration and concentration gradient measurements in an ultrafiltration concentration polarization layer Part I: a laser-based refractometric experimental technique. *Journal of Membrane Science*, 131(1):95 – 105, 1997.

[62] P. Haldenwang, P. Guichardon, G. Chiavassa, and N. Ibaseta. Exact solution to mass transfer in Berman flow: application to concentration polarization combined with osmosis in crossflow membrane filtration. *International Journal of Heat and Mass Transfer*, 53(19):3898 – 3904, 2010.

[63] S. Hamberger, A. Kroiß, M. Spinnler, and T. Sattelmayer. *Optimization of a seawater proof PV/T collector.* Term Paper, Technical University of Munich, 2012.

[64] S. Hamberger, A. Kroiß, M. Spinnler, and T. Sattelmayer. *Design, building and testing of a novel photovoltaic system with active cooling.* Master's Thesis, Technical University of Munich, 2013.

[65] M. J. Hargather and G. S. Settles. A comparison of three quantitative Schlieren techniques. *Optics and Lasers in Engineering*, 50(1):8 – 17, 2012.

[66] W. Hauf, U. Grigull, and F. Mayinger. *Optische Meßverfahren der Wärme- und Stoffübertragung.* Wärme- und Stoffübertragung. Springer-Verlag Berlin Heidelberg, 1991.

[67] E. Hecht. *Optik.* Oldenburg Wissenschaftsverlag GmbH, 3rd edition edition, 2001.

[68] B. Heithorst, A. Kroiß, M. Spinnler, and T. Sattelmayer. *Combined CFD and optical raytracing simulation for a reverse osmosis membrane test setup.* Masters's Thesis, Technical University of Munich, 2015.

[69] M. Henmi, Y. Fusaoka, H. Tomioka, and M. Kurihara. High performance RO membranes for desalination and wastewater reclamation and their operation results. *Water Practice and Technology*, 4(4), 2009. ISSN 1751-231X.

[70] M. Hofmann, A. Kroiß, M. Spinnler, and T. Sattelmayer. *Experimental investigations of material properties for reverse osmosis membrane desalination.* Bachelor's Thesis, Technical University of Munich, 2016.

[71] T. Holzmann. Numerical schemes. `http://www.holzmann-cfd.de/index.php/en/numerical-schemes/`, Accessed: 2017-06-29.

[72] L. Y. Hung, C. C. Hu, W. S. Hung, and S. J. Lue. Probing free volume property of polyamide thin film composites with different cross-linking densities. *MOJ Polymer Science*, 2(2):1–4, 2018.

[73] Y. A. Hussain, M. H. Al-Saleh, and S. S. Ar-Ratrout. The effect of active layer non-uniformity on the flux and compaction of TFC membranes. *Desalination*, 328:17 – 23, 2013.

[74] F. Hutter, A. Kroiß, M. Spinnler, and T. Sattelmayer. *Design of an experimental test setup for a PV/T powered reverse osmosis desalination plant.* Bachelor's Thesis, Technical University of Munich, 2012.

[75] V. Ilchenko. *Digitale holographische Geschwindigkeitsmessung mittels Kreuzkorrelation und Partikelverfolgung.* Dissertation, Technical University of Munich, 2007.

[76] D.-G. Jang. Department of Physics and Photon Science, Gwangju Institute of Science and Technology, South Korea, 2015. Matlab function for extraction of phase from interferogram, version 1.0. `https://de.mathworks.com/matlabcentral/fileexchange/53421-matlab-function-for-extraction-of-phase-from-interferogram?focused=5643564&tab=function`, Accessed: 2017-08-15.

[77] X. Jin, A. Jawor, S. Kim, and E. M. Hoek. Effects of feed water temperature on separation performance and organic fouling of brackish water RO membranes. *Desalination*, 239(1):346 – 359, 2009.

[78] A. R. Johnson. Experimental investigation of polarization effects in reverse osmosis. *AIChE Journal*, 20(5):966–974, 1974.

[79] JUMO Instrument Co. Ltd. Product data sheet for ecoTRANS Lf 01/02. `https://www.jumo.net/attachments/JUMO/attachmentdownload?id=3456`, Accessed: 2017-08-05.

[80] S. Kakaç, A. Bergles, F. Mayinger, and H. Yüncü. *Heat transfer enhancement of heat exchangers.* Nato Science Series E:. Springer Netherlands, 1999.

[81] G. Kang and Y. Cao. Development of antifouling reverse osmosis membranes for water treatment: a review. *Water Research*, 46(3):584 – 600, 2012.

[82] O. Kedem and A. Katchalsky. Thermodynamic analysis of the permeability of biological membranes to non-electrolytes. *Biochimica et Biophysica Acta*, 27:229 – 246, 1958. ISSN 0006-3002.

[83] Kern & Sohn. Product data sheet for scale EW6200-2NM. `https://www.pkelektronik.com/media/downloads/k/e/kern%20&%20sohn%20praezisionswaage%20ew6200-2nm.pdf`, Accessed: 2017-08-05.

[84] S. Kimura and S. Sourirajan. Analysis of data in reverse osmosis with porous cellulose acetate membranes used. *AIChE Journal*, 13(3): 497–503, 1967. ISSN 1547-5905.

[85] KOBOLD Messring GmbH. Product data sheet for Kobold 3376 A125. `http://www.kobold.com/uploads/files/p2de_sen-3376-3377.pdf`, Accessed: 2017-08-05.

[86] Koch Membrane Systems. Product data sheet for membrane module type 8040-HR-400-34. `http://www.kochmembrane.com/PDFs/Data-Sheets/Spiral/RO/fluid-systems-tfc-hr-8-inch-400-440-datasheet.aspx`, Accessed: 2017-06-22.

[87] V. Kochkodan. Reduction of membrane fouling by polymer surface modification. In N. Hilal, M. Khayet, and C. Wright, editors, *Membrane Modification: Technology and Applications*. CRC Press, Taylor & Francis Group, LLC, 2012.

[88] W. Koros, G. Fleming, S. Jordan, T. Kim, and H. Hoehn. Polymeric membrane materials for solution-diffusion based permeation separations. *Progress in Polymer Science*, 13(4):339 – 401, 1988. ISSN 0079-6700.

[89] KROHNE Messtechnik GmbH. Product data sheet for Krohne Optiflux 5300. Measurement error estimation by Krone technical consultant for 3 l/h volume flow rate and DN 2.5. `http://cdn.krohne.com/dlc/AD_OPTIFLUX2x00_4x00_5x00_6x00_IFC300_Ex_de_090115.pdf`, Accessed: 2017-08-05.

[90] A. Kroiss, S. Eyerer, J. Kuczaty, C. Thies, A. Präbst, M. Spinnler, and T. Sattelmayer. Optical methods for simultaneous measurement of temperature and concentration polarization. In *Proceedings of the International Desalination Association World Congress on Desalination and Water Reuse*, 2015.

[91] A. Kroiss, M. Spinnler, and T. Sattelmayer. Method for determining local membrane parameters based on boundary layer investigations. In *Proceedings of the International Desalination Association World Congress on Desalination and Water Reuse*, 2015.

[92] J. Kuczaty, A. Kroiß, M. Spinnler, and T. Sattelmayer. *Application of digital holographic interferometry for analysis of concentration boundary layers in membrane desalination*. Masters's Thesis, Technical University of Munich, 2015.

[93] F. Köhler, A. Kroiß, M. Spinnler, and T. Sattelmayer. *Investigation on evaluation methods of optical experiments for temperature and concentration boundary layer measurements*. Term Paper, Technical University of Munich, 2015.

[94] S. Körber, A. Kroiß, M. Spinnler, and T. Sattelmayer. *Experimental investigation and optimization of a Schlieren test rig for quantitative boundary layer evaluations on reverse osmosis membranes*. Master's Thesis, Technical University of Munich, 2016.

[95] LABOM Mess- und Regeltechnik GmbH. Product data sheet for Labom Compact CC6010-A1063. `https://www.labom.com/files/downloads/technische_informationen/datenblaetter/D4-020-5__CC60xx-F__DE.pdf`, Accessed: 2017-08-05.

[96] J. C. Lagarias, J. A. Reeds, M. H. Wright, and P. E. Wright. Convergence properties of the Nelder–Mead simplex method in low dimensions. *SIAM Journal on Optimization*, 9(1):112–147, 1998.

[97] B. S. Lalia, V. Kochkodan, R. Hashaikeh, and N. Hilal. A review on

membrane fabrication: structure, properties and performance relationship. *Desalination*, 326:77 – 95, 2013.

[98] W. J. Lau, A. F. Ismail, N. Misdan, and M. A. Kassim. A recent progress in thin film composite membrane: a review. *Desalination*, 287:190 – 199, 2012. Special Issue in honour of Professor Takeshi Matsuura on his 75th Birthday.

[99] W. K. Lewis and W. G. Whitman. Principles of gas absorption. *Industrial & Engineering Chemistry*, 16(12):1215–1220, 1924.

[100] M. Link, A. Kroiß, M. Spinnler, and T. Sattelmayer. *Experimental investigation of a brackish water reverse osmosis desalination plant*. Bachelor's Thesis, Technical University of Munich, 2013.

[101] M. Link, A. Kroiß, M. Spinnler, and T. Sattelmayer. *Design, implementation and validation of a LabVIEW measurement and control system.* Term Paper, Technical University of Munich, 2014.

[102] H. K. Lonsdale, U. Merten, and R. L. Riley. Transport properties of cellulose acetate osmotic membranes. *Journal of Applied Polymer Science*, 9(4):1341–1362, 1965.

[103] H. K. Lonsdale, R. L. Riley, C. R. Lyons, and D. P. Carosella. Transport in composite reverse osmosis membranes. In M. Bier, editor, *Membrane Processes in Industry and Biomedicine*, pages 101–122. Springer US, Boston, MA, 1971.

[104] M. Luckas and J. Krissmann. *Thermodynamik der Elektrolytlösungen: Eine einheitliche Darstellung der Berechnung komplexer Gleichgewichte.* Springer Berlin Heidelberg, 2001.

[105] D. Mahlab, N. B. Yosef, and G. Belfort. Interferometric measurement of concentration polarization profile for dissolved species in unstirred batch hyperfiltration (reverse osmosis). *Chemical Engineering Communications*, 6(4-5):225–243, 1980.

[106] H. Mark, N. Gaylord, and B. M.N., editors. *Encyclopedia of polymer science and technology: plastics, resins, rubbers, fibers*, volume 10. Interscience Publishers a devision of John Wiley & Sons, Inc., 1969.

[107] T. Matsuura. *Synthetic membranes and membrane separation processes*. CRC Press, 1994.

[108] T. Matsuura and S. Sourirajan. Reverse osmosis transport through capillary pores under the influence of surface forces. *Industrial & Engineering Chemistry Process Design and Development*, 20(2):273–282, 1981.

[109] T. Melin and R. Rautenbach. *Membranverfahren - Grundlagen der Modul- und Anlagenauslegung*. Springer, 3rd edition edition, 2007.

[110] A. Mersmann. *Stoffübertragung*. Wärme- und Stoffübertragung. Springer Berlin Heidelberg, 1986.

[111] U. Merten. *Desalination by reverse osmosis - transport properties of osmotic membranes*. M.I.T. Press, 1966.

[112] W. Merzkirch. *Flow visualization*. Academic Press, Inc., 2nd edition edition, 1987.

[113] M. Meschenmoser, A. Kroiß, M. Spinnler, and T. Sattelmayer. *Modelling concentration boundary layers for reverse osmosis desalination*. Bachelor's Thesis, Technical University of Munich, 2015.

[114] Mettler Toledo. Product data sheet for SevenExcellence. `https://www.mt.com/dam/Analytical/pH-LabMeters/me-pdf/30046380A_V06.13_SevenExcellence_Broch_DE.pdf`, Accessed: 2017-10-17.

[115] R. C. Millard and G. Seaver. An index of refraction algorithm for seawater over temperature, pressure, salinity, densitiy, and wavelength. *Deep-Sea Research*, 37(12):1909 – 1926, 1990.

[116] F. J. Millero, R. Feistel, D. G. Wright, and T. J. McDougall. The composition of standard seawater and the definition of the

reference-composition salinity scale. *Deep-Sea Research I*, 55:50 – 72, 2008.

[117] F. Moukalled, L. Mangani, and M. Darwish. *The finite volume method in computational fluid dynamics: an advanced introduction with OpenFOAM and Matlab*. Springer International Publishing, 2016.

[118] Z. Murthy and S. K. Gupta. Estimation of mass transfer coefficient using a combined nonlinear membrane transport and film theory model. *Desalination*, 109(1):39 – 49, 1997.

[119] National Instruments. User manual and specifications for CompactRio 9074. `http://www.ni.com/pdf/manuals/374639f.pdf`, Accessed: 2017-10-09.

[120] Nitto Denko Hydranautics. Product data sheet for membrane module type CPA2-4040. `http://www.appliedmembranes.com/media/wysiwyg/pdf/membranes/hydranautics_cpa2-4040_ro_membrane_specifications.pdf`, Accessed: 2017-06-22.

[121] F. Nozaki. Documentation about buoyantPimpleFoam and buoyantSimpleFoam in OpenFOAM. `http://caefn.com/openfoam/solvers-buoyantpimplefoam`, Accessed: 2017-06-29.

[122] OpenCFD Ltd. OpenFOAM user guide - standard solvers. `http://www.openfoam.com/documentation/user-guide/standard-solvers.php`, Accessed: 2017-06-28.

[123] OpenCFD Ltd. OpenFOAM user guide - numerical schemes. `http://www.openfoam.com/documentation/user-guide/fvSchemes.php`, Accessed: 2017-06-29.

[124] OpenCFD Ltd. OpenFOAM documentation release 1.7. `https://openfoam.org/release/1-7-0./`, Accessed: 2017-06-29.

[125] OpenCFD Ltd. OpenFOAM solver documentation - buoyantSimpleFoam.

`http://www.openfoam.com/documentation/cpp-guide/html/buoyantSimpleFoam_8C.html`, Accessed: 2017-10-07.

[126] H. Ozbek, J. Fair, and S. Philips. *Viscosity of aqueous sodium chloride solutions from 0-150°C.* U.S. Department of Energy, 1977.

[127] D. R. Paul. Reformulation of the solution-diffusion theory of reverse osmosis. *Journal of Membrane Science*, 241(2):371 – 386, 2004.

[128] D. R. Paul and O. M. Ebra-Lima. Pressure-induced diffusion of organic liquids through highly swollen polymer membranes. *Journal of Applied Polymer Science*, 14(9):2201–2224, 1970. ISSN 1097-4628.

[129] PCE Deutschland GmbH. Product data sheet for PCE Instruments PCE-PH 22. `https://www.pce-instruments.com/deutsch/slot/1/download/16302/datenblatt-ph-tester-pce-ph-22.pdf`, Accessed: 2017-10-17.

[130] PCO AG. Product data sheet for Color Camera SVGA S/N 375LD0530. `http://www.leibniz-kis.de/fileadmin/user_upload/observatorien/manuals/anleitung_sensicam.pdf`, Accessed: 2017-08-14.

[131] M. T. M. Pendergast, J. M. Nygaard, A. K. Ghosh, and E. M. Hoek. Using nanocomposite materials technology to understand and control reverse osmosis membrane compaction. *Desalination*, 261(3):255 – 263, 2010. Special Issue in memory of Sidney Loeb (1917-2008).

[132] K. S. Pitzer, J. C. Peiper, and R. H. Busey. Thermodynamic properties of aqueous sodium chloride solutions. *Journal of Physical and Chemical Reference Data*, 13(1):1–102, 1984.

[133] A. Präbst, F. Kiefer, A. Kroiß, M. Spinnler, and T. Sattelmayer. Influence of dynamic operation of reverse osmosis systems on fluid dynamics and mass transfer by investigation of 2-D spacer filled channels. *Desalination and Water Treatment*, 73, Apr 2017.

[134] A. Präbst, A. Kroiß, M. Spinnler, and T. Sattelmayer. *A bench-scale reverse osmosis plant - experimental setup and numerical modeling*. Term Paper, Technical University of Munich, 2013.

[135] R. Rautenbach and R. Albrecht. *Membrane processes*. John Wiley and Sons Ltd., 1989.

[136] S. Rehfeldt. *Mehrkomponentendiffusion in Flüssigkeiten*. Dissertation, Technical University of Munich, 2009.

[137] R. Reisewitz. Membrane application types for reverse osmosis processes. Guest lecture in desalination course at Technical University of Munich., December 2014.

[138] H. F. Ridgway, J. Orbell, and S. Gray. Molecular simulations of polyamide membrane materials used in desalination and water reuse applications: recent developments and future prospects. *Journal of Membrane Science*, 524:436 – 448, 2017.

[139] P. J. Roache. Quantification of uncertainty in computational fluid dynamics. *Annual Review of Fluid Mechanics*, 29(1):123–160, 1997.

[140] P. J. Roache and P. M. Knupp. Completed Richardson extrapolation. *Communications in Numerical Methods in Engineering*, 9(5):365–374, 1993.

[141] R. A. Robinson and R. H. Stokes. *Electrolyte solutions*. Butterworths Publications Ltd., 1955.

[142] C. Rodrigues, P. Garcia-Algado, V. Semião, M. N. de Pinho, and V. Geraldes. Concentration boundary layer visualization in nanofiltration by holographic interferometry with light deflection correction. *Journal of Membrane Science*, 447:306 – 314, 2013. ISSN 0376-7388.

[143] S. Rosenbaum and O. Cotton. Steady-state distribution of water in cellulose acetate membrane. *Journal of Polymer Science Part A-1: Polymer Chemistry*, 7(1):101–109, 1969. ISSN 1542-9350.

[144] B. J. Rudie, T. A. Torgrimson, and D. D. Spatz. *Reverse osmosis and ultrafiltration membrane compaction and fouling studies using ultrafiltration pretreatment*, chapter 29, pages 403–414. 1985.

[145] R. Salcedo Díaz. *Aplicatión de la interferometriía holográfica al estudio de la capa de polarización en ósmosis inversa. Efecto de la convección natural.* Dissertation, Universidad de Alicante, 2006.

[146] R. Salcedo-Díaz, P. García-Algado, M. García-Rodríguez, J. Fernández-Sempere, and F. Ruiz-Beviá. Visualization and modeling of the polarization layer in crossflow reverse osmosis in a slit-type channel. *Journal of Membrane Science*, 456:21 – 30, 2014.

[147] Sartorius AG. Product data sheet for Sartorius Combics 1 CW1P1-66DC-I. `https://serviceshop.sartorius.com/fileadmin/fm-dam/DDM/Industrial-Weighing/Manuals/English/Combics/MAN-Combics_CompleteScale-e.pdf`, Accessed: 2017-08-05.

[148] E. M. Scattergood and E. N. Lightfoot. Diffusional interaction in an ion-exchange membrane. *Trans. Faraday Soc.*, 64:1135–1146, 1968.

[149] T. Schipolowski, A. Jezowska, and G. Wozny. Reliability of membrane test cell measurements. *Desalination*, 189(1):71 – 80, 2006.

[150] T. Schmidt, A. Kroiß, M. Spinnler, and T. Sattelmayer. *CFD modeling of a reverse osmosis desalination membrane test cell.* Term Paper, Technical University of Munich, 2014.

[151] W. Schmidt, P. Erroi, M. Geiger, A. Kroiß, and T. Sattelmayer. *Techno-economic analysis of solar desalination technologies*. Term Paper, Technical University of Munich, 2013.

[152] U. Schnars and W. Jueptner. *Digital holography: digital hologram recording, numerical reconstruction, and related techniques*. Springer, 2005.

[153] SCHOTT AG. Product data sheet for optical glasses. `http://www.schott.com/d/advanced_optics/ac85c64c-60a0-`

4113-a9df-23ee1be20428/1.1/schott-optical-glass-collection-datasheets-english-17012017.pdf, Accessed: 2017-08-15.

[154] M. Schreyer, A. Kroiß, M. Spinnler, and T. Sattelmayer. *Numerical investigation of a reverse osmosis membrane test setup*. Bachelor's Thesis, Technical University of Munich, 2015.

[155] G. S. Settles. *Schlieren and Shadowgraph techniques - visualizing phenomena in transparent media*. Experimental Fluid Mechanics. Springer-Verlag Berlin Heidelberg, 2001.

[156] A. Shahrouri, A. Klüpfel, M. Schröter, A. Kroiß, M. Spinnler, and T. Sattelmayer. *Investigation of influence parameters on long-term performance of PTFE-Membranes in membrane distillation*. Master's Thesis, Technical University of Munich, 2012.

[157] M. H. Sharqawy, J. H. Lienhard, and S. M. Zubair. Thermophysical properties of seawater: a review of existing correlations and data. *Desalination and Water Treatment*, 16(1-3):354–380, 2010.

[158] T. K. Sherwood, P. L. T. Brian, and R. E. Fisher. Desalination by reverse osmosis. *Industrial & Engineering Chemistry Fundamentals*, 6(1):2–12, 1967.

[159] T. Sherwood, R. Pigford, and C. Wilke. *Mass transfer*. McGraw-Hill chemical engineering series. McGraw-Hill, Inc., 1975.

[160] R. Singh. *Membrane technology and engineering for water purification*. Butterworth-Heinemann, second edition edition, 2015.

[161] S. Sourirajan. *Reverse osmosis*. Logos Press Limited, 1970.

[162] K. Spiegler and O. Kedem. Thermodynamics of hyperfiltration (reverse osmosis): criteria for efficient membranes. *Desalination*, 1(4):311 – 326, 1966. ISSN 0011-9164.

[163] H. Strathmann and A. Michaels. Polymer-water interaction and its relation to reverse osmosis desalination efficiency. *Desalination*, 21(2): 195 – 202, 1977.

[164] I. Sutzkover, D. Hasson, and R. Semiat. Simple technique for measuring the concentration polarization level in a reverse osmosis system. *Desalination*, 131(1):117 – 127, 2000.

[165] M. Takeda, H. Ina, and S. Kobayashi. Fourier-transform method of fringe-pattern analysis for computer-based topography and interferometry. *J. Opt. Soc. Am.*, 72(1):156–160, Jan 1982.

[166] A. Tamburini, P. Pitò, A. Cipollina, G. Micale, and M. Ciofalo. A thermochromic liquid crystals image analysis technique to investigate temperature polarization in spacer-filled channels for membrane distillation. *Journal of Membrane Science*, 447:260 – 273, 2013.

[167] R. Tauscher. *Wärmeübergang mit Turbulenzanregung bei niedrigen Reynoldszahlen*. Dissertation, Technical University of Munich, 2000.

[168] Technical University of Munich. Chair of Plant and Process Technology, Department of Mechanical Engineering. `https://www.apt.mw.tum.de/en/welcome-page/`, Accessed: 2017-09-11.

[169] The MathWorks, Inc. MATLAB fminsearch solver documentation. `https://de.mathworks.com/help/matlab/ref/fminsearch.html`, Accessed: 2017-06-30.

[170] The MathWorks, Inc. MATLAB fmincon solver documentation. `https://de.mathworks.com/help/optim/ug/constrained-nonlinear-optimization-algorithms.html#brnox01`, Accessed: 2017-06-30.

[171] The MathWorks, Inc. MATLAB 2016b. `https://de.mathworks.com/products/new_products/release2016b.html`, Accessed: 2017-08-15.

[172] C. Thies, A. Kroiß, M. Spinnler, and T. Sattelmayer. *Numerical and experimental investigation of concentration polarisation in membrane desalination*. Bachelor's Thesis, Technical University of Munich, 2014.

[173] Thorlabs Inc. Product specifications for achromatic doublets. `https://www.thorlabs.com/newgrouppage9.cfm?objectgroup_id=2696&pn=AC508-300-A-ML`, Accessed: 2017-08-14.

[174] Toray Industries, Inc. Product data sheet for membrane modul TML10D. `http://www.toraywater.com/products/ro/pdf/TML(D).pdf`, Accessed: 2017-08-14.

[175] Trunz Water Systems AG. Product specifications for Trunz Brackish Box. `http://www.trunzwatersystems.com/water-treatment/products/tbb-003/`, Accessed: 2017-10-17.

[176] V. Vilker, C. Colton, and K. Smith. Concentration polarization in protein ultrafiltration. Part I: an optical shadowgraph technique for measuring concenration profiles near a solution-membrane interface. *AIChE Journal*, 27(4):632–636, 1981. ISSN 1547-5905.

[177] V. Vilker, C. Colton, and K. Smith. Concentration polarization in protein ultrafiltration. Part II: theoretical and experimental study of albumin ultrafiltered in an unstirred cell. *AIChE Journal*, 27(4):637–645, 1981. ISSN 1547-5905.

[178] E. M. V. Wagner, A. C. Sagle, M. M. Sharma, and B. D. Freeman. Effect of crossflow testing conditions, including feed pH and continuous feed filtration, on commercial reverse osmosis membrane performance. *Journal of Membrane Science*, 345(1):97 – 109, 2009.

[179] T. Wei, L. Zhang, H. Zhao, H. Ma, M. S. J. Sajib, H. Jiang, and S. Murad. Aromatic polyamide reverse osmosis membrane: an atomistic molecular dynamics simulation. *The Journal of Physical Chemistry B*, 120(39):10311–10318, 2016.

[180] F. J. Weyl. *Analysis of optical methods*, pages 3–25. Princeton University Press, 1954.

[181] A. Wild. *Multicomponent diffusion in liquids*. Dissertation, Technical University of Munich, 2003.

[182] D. E. Wiley and D. F. Fletcher. Techniques for computational fluid dynamics modelling of flow in membrane channels. *Journal of Membrane Science*, 211(1):127 – 137, 2003.

[183] S. Wolf, A. Kroiß, M. Spinnler, and T. Sattelmayer. *Modelling of a reverse osmosis plant driven by hybrid photovoltaic thermal (PV/T) collectors*. Term Paper, Technical University of Munich, 2013.

[184] S. Wolf, A. Kroiß, M. Spinnler, and T. Sattelmayer. *Implementation of an optical measuring system for investigation of concentration boundary layers in membrane desalination*. Diploma Thesis, Technical University of Munich, 2014.

[185] X. Zhang, D. Cahill, O. Coronell, and B. Mariñas. Absorption of water in the active layer of reverse osmosis membranes. *Journal of Membrane Science*, 331(1-2):143–151, 4 2009.

[186] K. Zörntlein, A. Kroiß, M. Spinnler, and T. Sattelmayer. *Design, optimization and experimental investigation of membrane test cells*. Bachelor's Thesis, Technical University of Munich, 2016.